

Editorial corner – a personal view

Material circularity in rubber products

Alessandro Pegoretti*^{ID}

University of Trento, Department of Industrial Engineering Via Sommarive 9, 38123 Trento, Italy

The total rubber production worldwide in 2019 amounted to over 28.8 million tons, of which 13.6 million tons of natural rubber and 15.2 million tons of synthetic rubber (www.statista.com). Rubber products are used for various industrial applications, the most important in terms of volumes being tyres (accounting for about 70% of the total production), followed by other non-tyre automotive applications (such as seals, hoses, belts, anti-vibration mounts for about 13%) industrial applications (8%), footwear (7%) and other applications (2%). In most cases, for a good balance of mechanical strength and wear resistance, rubber products require a vulcanization process with sulfur (most common), peroxide or metal oxides, which ultimately leads to crosslinked polymers. This makes effective recycling and reuse of the scraps generated during the production of parts and rubber products at the end-of-life (EOL) a quite challenging issue (<https://doi.org/10.1515/9783110644142>). The main current EOL options for tyres are represented by i) stockpiling, ii) landfilling, iii) civil engineering applications (*i.e.* retention walls), iv) energy recovery (incineration), v) retreading, and vi) recycling or reuse. Despite the fact that in Europe and the USA the recovery rate of scrap tyres is around 90%, around 4 billion EOL tyres are still disposed in landfills and stockpiles worldwide and this amount will increase up to 5 billion by 2030 (<https://doi.org/10.1016/j.aiepr.2022.08.006>). In addition to the associated loss of valuable resources, stockpiles of waste tyres may also cause environmental problems due to the potential fire hazard and the proliferation of insects caused by water stagnation. Rubber recycling consists of the recovery of materials, converting rubber waste into an economically useful form that is achieved through a shredding process. For tyres, the removal of steel, fibres, and other non-rubber components is also re-

quired. Crumb rubber can be used for the production of rubber-modified-asphalt, playground surfaces, artificial turfs, insulating panels, and in small quantities (less than 20 wt%) mixed with virgin rubber for manufacturing of new products.

Reuse is the preferable EOL option since the material is returned to its original application, thus creating a virtual circularity in the materials used. Nevertheless, the reuse of rubber is an obstacle due to the cross-linked nature of rubber products.

Therefore, intense research efforts have been conducted in the last 50 years to find efficient devulcanization methods (<https://doi.org/10.1016/j.resconrec.2018.02.016>). In an ideal situation, the breakage of the sulfur-carbon or the sulfur-sulfur bonds is induced to obtain a polymer that can be handled and vulcanized similarly to virgin rubber. The principal devulcanization strategies include chemical, ultrasonic, microwave, biological and thermo-mechanical methods (<https://doi.org/10.3390/ma13051246>). A successful devulcanization allows the use of higher amounts of recovered rubber mixed with virgin rubber (<https://doi.org/10.1002/pen.25615>) or in brittle thermoplastic matrices to improve their fracture toughness (<https://doi.org/10.1007/s10924-020-01717-8>). Remarkable progress in the next ten years is expected in both chemical and thermo-mechanical devulcanization methods.



Prof. Alessandro Pegoretti
Member of the International Advisory Board

*Corresponding author, e-mail: alessandro.pegoretti@unitn.it
© BME-PT

Research article

Experimental studies on the absorption, swelling and erosion performance of hybrid woven Kevlar/hemp reinforced epoxy composites

Sangilimuthukumar Jeyaguru¹, Senthil Muthu Kumar Thiagamani¹,
Sanjay Mavinkere Rangappa^{2*}, Suchart Siengchin²

¹Department of Automobile Engineering, Kalasalingam Academy of Research and Education, Krishnankoil–626126, Tamil Nadu, India.

²Natural Composites Research Group Lab, Department of Materials and Production Engineering, The Sirindhorn International Thai-German Graduate School of Engineering (TGGs), King Mongkut's University of Technology North Bangkok (KMUTNB), Bangkok, Thailand

Received 31 July 2022; accepted in revised form 10 October 2022

Abstract. Hybridization of natural and synthetic fibers in a single composite material can be made by several means, and one of the best methods is the intra-ply in which both fibers are woven within a single layer. Through hybridization, the advantages of one type of fiber can improve the limitations of the other. Further the blending of natural and synthetic fibers leads to the fabrication of composites with higher mechanical performance. Hence, this work focuses on the fabrication of intra-ply Kevlar and hemp fiber reinforced epoxy hybrid composites with different weaving patterns such as plain weave, basket weave, and twill weave type. Yarns were woven by handloom technique to make intra-ply Kevlar and hemp fiber mats, and the composites were fabricated by compression molding. The water absorption, thickness swelling, and solid particle erosion characteristics of the composites were examined. The results of the experiments showed that the hemp fiber composites exhibited the least resistance (8.45% change in absorption and 4.34% change in thickness) towards the absorption and swelling, whereas pure epoxy (0.67% change in absorption and 0.31% change in thickness) and Kevlar (2.67% change in absorption and 1.67% change in thickness) composites possessed higher resistance. The absorption and swelling performance of all other hybrids was found to be in between the hemp and Kevlar composites hence proving the effectiveness of the hybridization. Further, Taguchi's experimental design results indicated that the basket weave type hybrid composites had a minimal erosion rate for 2 minutes of exposure duration and an impact angle of 90°. The morphological analysis of the eroded surfaces of composites revealed the presence of micro cavities, broken fibers, crater formation, and microcracks.

Keywords: polymer composites, hybridization, absorption and thickness swelling, solid particle erosion

1. Introduction

Natural fibers are environmentally favorable due to their low density, renewable nature, low cost, and biodegradability. Natural fibers such as kenaf, banana, jute, pineapple leaf fiber (PALF), hemp, sisal *etc.* are reinforced with polymer matrices to form polymer composites [1–7]. Polymer composites have found enormous applications in the field of automobiles

and are found to be more effective [8–15]. Natural fibers have many advantages, but they also have certain disadvantages, such as lower mechanical properties, high moisture absorption rate, uneven shapes with varied diameters, fiber and matrix incompatibility when compared to synthetic fibers [16–27]. A blend of natural/natural, natural/synthetic and synthetic/synthetic fibers in the same composite material

*Corresponding author, e-mail: mceems@gmail.com

© BME-PT

is called hybridization. Inter-ply and intra-ply are the two distinct kinds of hybridization where two or more layers placed in a homogeneous reinforcement are called inter-ply and two fibers integrated into one layer are called intra-ply hybrid composites. Composites using intra-ply are also referred to as intra-yarn [28–34]. Synthetic fibers, including carbon, Kevlar, and glass are employed in high-strength applications [35–41]. The advantages of synthetic fibers over natural fibers include their higher mechanical qualities, reduced moisture absorption, and compatibility with the polymer matrices [42–48]. They are frequently utilized in automobile applications such as engine covers and sports car components [49–54]. However, the cost of these composites is extremely high. On the other hand, natural fibers are extremely cost-effective [55–60]. Hybridized synthetic and natural fiber composites are created to compensate for the inadequacies of natural fiber-based polymer composites and synthetic fiber-based polymer composites [61–66]. Although the natural/synthetic fiber reinforced combination has more economical and cost-effective, it reduces the moisture absorption properties and enhances the properties of the composites [67–71].

Recently, polymer matrix composites have replaced metallic components in several applications. However, because the epoxy matrix is fragile, they are vulnerable to eroding wear. Numerous studies have examined the erosion wear behavior of polymer matrix composites to solve the disadvantages and improve the erosion resistance of polymer matrix composites. It is critical to investigate the erosion wear resistance of polymer matrix composites before they may be employed in a range of applications, particularly in the aerospace and automotive industries [72–80]. Gupta *et al.* [75] explored the influence of erosion wear performance on bamboo fiber-reinforced epoxy composites. It was revealed that composites with 40% bamboo fiber reinforcement have higher erosion resistance than composites with the 10, 20, and 30% of fiber loadings. Researchers found that the bamboo fiber reinforced epoxy composites with red mud filler added possess stronger erosion resistance compared to glass fiber reinforced epoxy composites [76]. The influence of erosion characteristics of composites made from lantana camara fiber and epoxy matrix was investigated experimentally [77]. According to the findings, increasing fiber loading and impact velocity results in higher composite

erosion rates. Mohanta and Acharya [78] examined the erosion behavior of luffa cylindrica fiber and glass fiber reinforced epoxy hybrid composites. The result showed that all laminate stacking sequences have an erosion rate that increases with impact velocity and peaks at an impact angle of 60°. This demonstrates the semiductile behavior of the luffa cylindrica fiber and glass fiber reinforced epoxy hybrid composites. Similarly, the investigation of hybrid Kevlar fiber and pineapple leaf fiber reinforced epoxy composites demonstrated a maximum erosion rate at 60° of impact angle, which implies a semi-ductile nature [79]. Statistical techniques are frequently employed to enhance the quality of a process. In an experiment with multiple variables, the user can select and assess the effect of each possible variable according to these statistical methodologies. In the instance of erosion rate, the experimental erosion technique is an illustration of a method where numerous control parameters interact to affect the performance output. The Taguchi's design involves using a robust design of tests to reduce the variability in a process. The method's predominant goal is to ensure high-quality of products at a cheap cost [80–83]. Vigneshwaran *et al.* [84] reported the Taguchi experimental design for erosion wear characteristics of sisal fiber and red mud filler reinforced epoxy hybrid composites. It was found that the erosion loss in the composites was mostly determined by the red mud particle, erodent velocity, and erodent feed rate. In another work, Johnson *et al.* [72] examined the erosion behavior of Sansevieria Cylindrica fiber-reinforced vinyl ester composites using Taguchi design. From the Taguchi experimental results, the optimal erosion process parameter was discovered from the data.

The effects of moisture absorption properties on a hybrid of flax-hemp-epoxy composites were studied by Saha *et al.* [85]. The results showed that hybrid composites absorbed the least amount of water when compared to pure hemp and pure flax composites. The effects of Kevlar fiber and *cocos nucifera* sheath hybridization reinforced with epoxy matrix composites were examined [86]. The results showed that composites with a higher percentage of (75 wt%) Kevlar had improved water absorption capabilities. Behera *et al.* [87] investigated the Luffa-coir-epoxy hybrid composites, and they concluded that the hybrid composites showed higher moisture resistance than pure composites. Yahaya *et al.* [88] examined the moisture absorption behavior of kenaf-kevlar-epoxy

hybrid composites. In comparison to other hybrid compositions, hybrid composites with higher Kevlar fiber content exhibited lower water absorption and thickness swelling.

Many investigations have been performed on the swelling, absorption, and erosion properties of natural-synthetic fibre reinforced inter-ply hybrid composites, however, research on intra-ply hybrid composites is limited when compared with inter-ply hybrid composites [52, 79]. Hence, in this research, the moisture absorption, swelling, and erosion performance of intra-ply hybrid Kevlar and hemp fiber reinforced epoxy matrix composites with different weaving patterns such as plain (1×1), twill (2×2), and basket (3×3) were studied.

2. Materials and methods

2.1. Materials

The hemp and Kevlar fibers were procured from Go Green Products in Chennai, Tamil Nadu. The matrix materials, epoxy resin (LY556) and hardener (HY951) were supplied by Vasavibala Resins Pvt Ltd., Chennai, Tamil Nadu. Table 1 lists the mechanical properties of fibers and matrix used in this study.

2.2. Methods

2.2.1. Fabrication of woven fabric mats

The Kevlar and hemp fibers were weaved using hand-loom technique. Pure kevlar (K) and hemp (H)

woven fabric mats were prepared by weaving separate kevlar and hemp fibers. On the other hand, the kevlar and hemp fibers were inserted in warp and weft direction to obtain the intra-ply 1×1 plain (KH1), 2×2 twill (KH2) and 3×3 basket (KH3) type woven fabrics. The same quantity of Kevlar and hemp yarn were used for the weaving of different woven fabrics with the varied design of weaving patterns. Figure 1 and Figure 2 depicts the pure and intra-ply woven fabrics employed in this research.

2.2.2. Preparation of composites

The pure composites and intra-ply hybrid composites were fabricated using a compression moulding machine. The woven fabrics with a thickness ranging from 0.9 and 1.1 mm were placed on a steel mould having a size of 300×300×3 mm. A 10:1 ratio of epoxy resin to hardener was used to fabricate the composites. The mould cavity was filled with 3 layers of woven fabrics, and then the matrix was poured and spread along the cavity. Air bubbles were carefully eliminated during the fabrication of composites using a roller. Finally, the mould was closed and compressed at a pressure of 200 bar for 12 hrs at room temperature. After removing the mould from the compression moulding machine, the laminates were subjected to post curing at 110 °C for about 15 minutes. The cured composites were then cut as per ASTM standards for of testing.

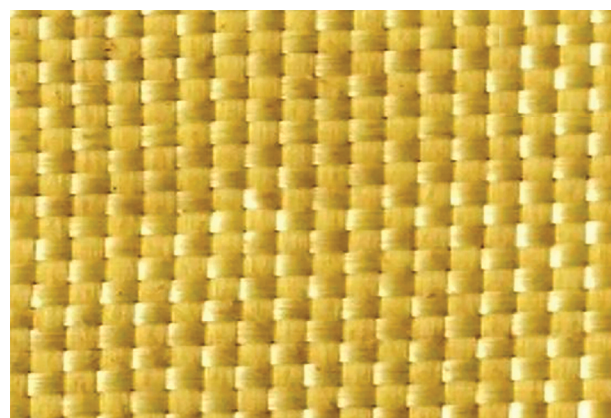
2.3. Characterization

2.3.1. Moisture absorption test

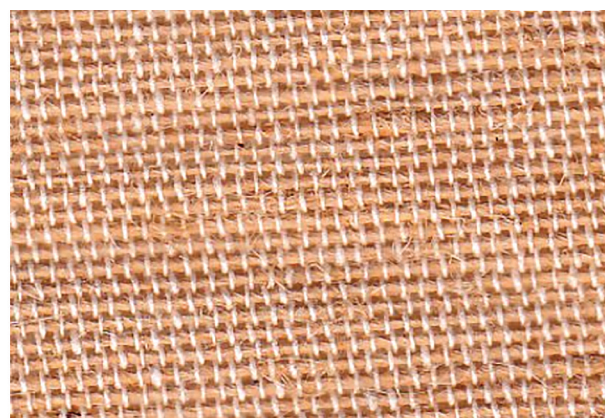
The developed Kevlar-hemp fiber-reinforced epoxy-based hybrid composites were tested for water absorption behaviour as per the ASTM D 570 standard. Three composite specimens in each composition

Table 1. Mechanical properties of fibers and matrix.

Mechanical properties	Hemp fiber	Kevlar fiber	Epoxy	References
Density [g/cm ³]	1.50	1.76	1.16	[9], [10], [13], [88–90]
Tensile strength [MPa]	550–900	4500	31	
Young's modulus [GPa]	70	250	4	
Elongation at break[%]	1.6	3.3	5.0	



a)



b)

Figure 1. Pure woven mats a) Kevlar (K), b) Hemp (H).

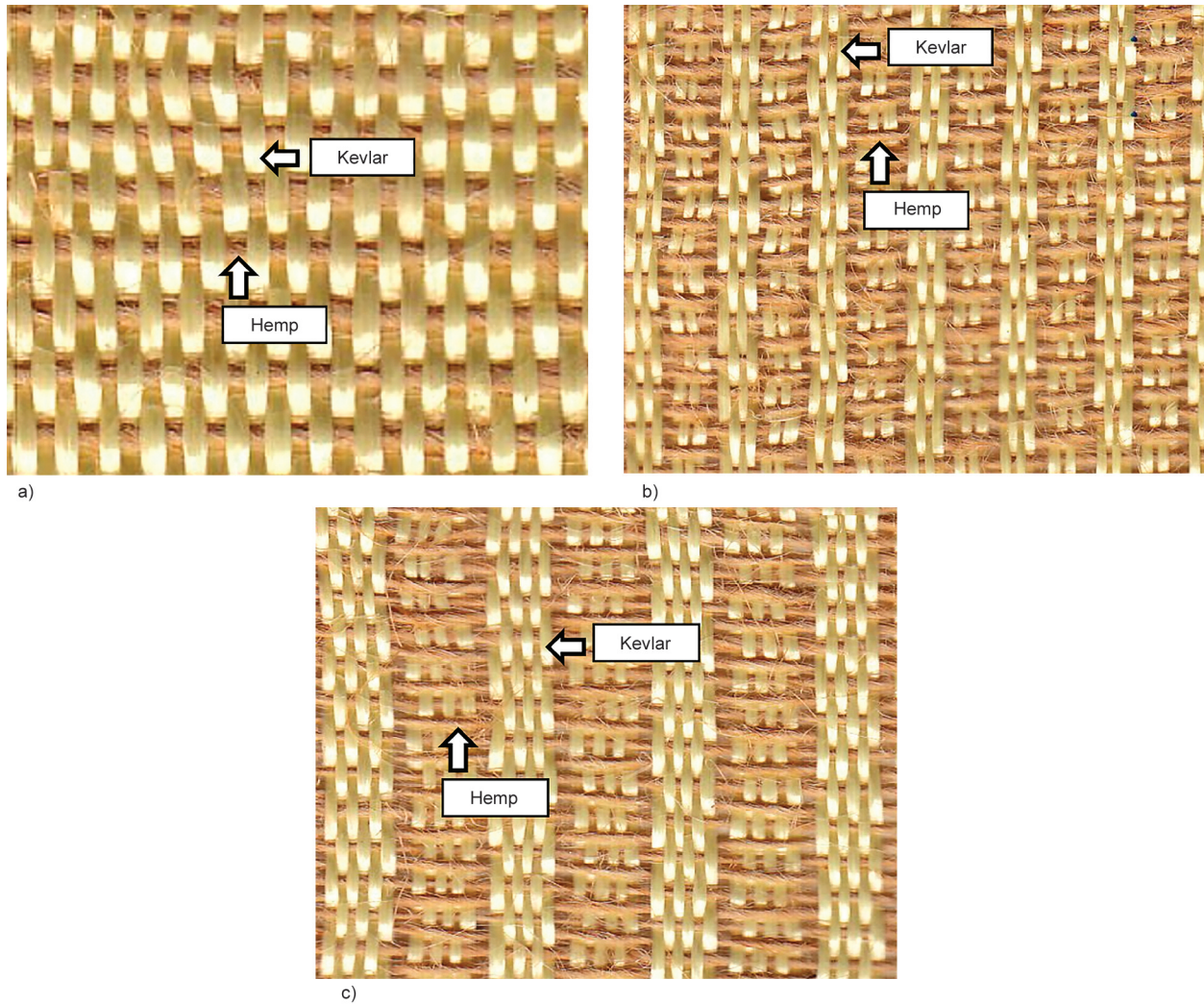


Figure 2. Intra-ply woven mats a) plain weave (KH1), b) twill weave (KH2), c) basket weave (KH3).

were soaked in distilled water at room temperature. Composite specimens were weighed initially prior to soaking in distilled water. After soaking in distilled water, the weight of each specimen was measured every 24 hours until a constant weight was reached. The percentage of moisture absorbed for each composite sample was determined using the Equation (1) [21, 25, 79, 104]:

$$\begin{aligned} \text{Percentage of water absorbed [\%]} &= \\ &= \frac{W_f - W_i}{W_i} \cdot 100 \end{aligned} \quad (1)$$

where W_f is the final weight and W_i is the initial weight of the composite specimen.

2.3.2. Thickness swelling test

The Kevlar-hemp fiber reinforced epoxy hybrid composites were measured for thickness swelling behaviour according to the ASTM D 570 standard. Three

specimens were measured for each composition, and the average value was reported. The initial thickness of the specimens was weighed before immersion in pure water. After 24 hours, the specimens were taken out of pure water and were scrubbed gently using a soft tissue paper in order to remove the water particles on the surface of the specimen before being measured on a digital vernier scale. The specimen's secondary thickness was then measured every 24 hours for several days until a constant thickness value was reached. Based on Equation (2) [21, 25, 79, 104] the percentage of thickness swelling behaviour was estimated.

$$\begin{aligned} \text{Percentage of thickness swelling [\%]} &= \\ &= \frac{T_f - T_i}{T_i} \cdot 100 \end{aligned} \quad (2)$$

where T_f represents the final thickness of the composite specimen, T_i is the initial thickness of the composite specimen.

2.3.3. Erosion test

An air jet erosion machine (R-470 DUCOM) was utilized to perform the erosion wear test. Figure 3 depicts the machine used to carry out the erosion test. Figure 4 shows the composite specimens having dimensions of 25×25×3 mm used for the erosion wear test in accordance with ASTM G76 standards. The erosion test process variables and their levels are listed in Table 2. The erosion wear rate was estimated from the Equation (3) [74, 79, 84, 102]:

$$\text{Erosion wear rate [g/g]} = \frac{\text{Specimen weight before wear} - \text{Specimen weight after wear}}{\text{Erodent feed rate} \cdot \text{time}} \quad (3)$$

2.3.4. Taguchi’s design of experiment

The Taguchi technique was employed to examine the effects of erosion process factors on the Kevlar-hemp-epoxy hybrid composites with various weaving patterns. The Minitab 17 software was used for this Taguchi analysis. The significance of the control elements on output parameters was designed using Taguchi experimental design. The experiment was carried out using a conventional Taguchi L27 (3^3) design. The chosen control variables were weaving patterns, impact angle, exposure time and working levels (Table 2). To study the erosion process parameters at the working conditions in a typical full factorial test, 3^3 = 27 runs were taken [78]. The experimental values are then used to estimate signal-to-noise (S/N) ratios. Regarding the S/N ratio for a low

Table 2. Erosion process variables and working levels.

Erosion process variables	Symbols	Operating levels
Impingement angle [°]	A	30, 60, 90
Erodent size [μm]	ES	50
Exposure duration [min]	B	2, 4, 6
Erodent	E	Alumina powder
Weaving	C	1, 2, 3
Erodent feed rate [g/min]	EFR	3.3
Impact velocity [m/s]	IV	100

wear rate, ‘smaller is better.’ Equation (4) was used to compute the S/N ratio [91]:

$$S/N = -10 \log \frac{1}{n} \sum y^2 \quad (4)$$

where *n* denotes the number of observations, *y* is the observed data.

3. Results and discussions

3.1. Moisture absorption properties

Figure 6 illustrates the moisture absorption properties of Kevlar-hemp-epoxy hybrid composites. It can be seen from Figure 6 that the absorption property of the intra-ply hybrid composites showed a linear increase during the first several days of soaking in water. This may be due to the quick penetration of water into the composites through the hydrophilic hemp fiber. As the soaking days increased, the intra-ply hybrid composites’ ability to absorb water declined until they were saturated. The pure Kevlar composites had the lowest water absorption percentage of 2.6% after 30 days of soaking among all types of composites. On the other hand, pure epoxy resin composites possessed the lowest water absorption percentage (0.67%). In contrast to fiber-reinforced composites, epoxy resin restricts water absorption by creating a matrix that is water-resistant. Moreover, specimens of pure hemp fiber reinforced composites had the highest moisture absorption percentage of 8.4%, higher than all other composites. This could be attributed to the hydrophilic nature of the hemp fiber. The various weaving patterns affected the moisture absorption behaviour of hybrids. Results showed substantial differences in water absorption behaviour between kevlar-hemp-epoxy hybrid composites with various weaving patterns. Nevertheless, hybrid composites of the basket weave type (KH3) showed

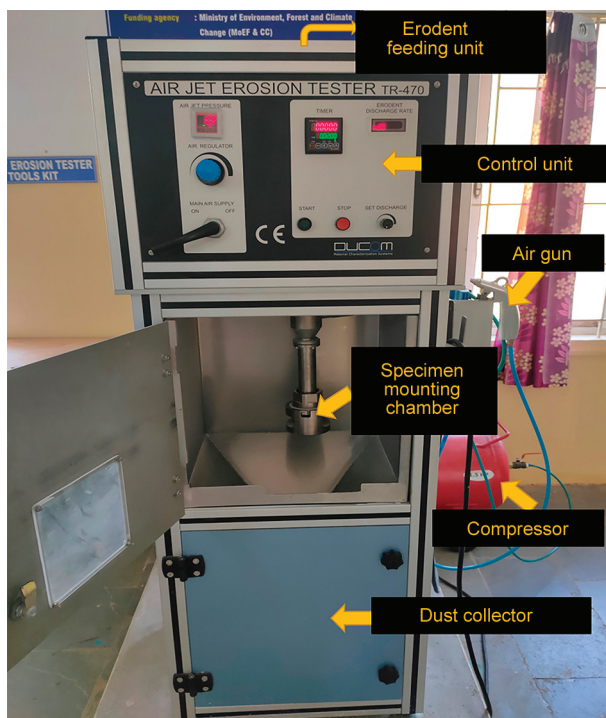


Figure 3. Air jet erosion tester used in the study.

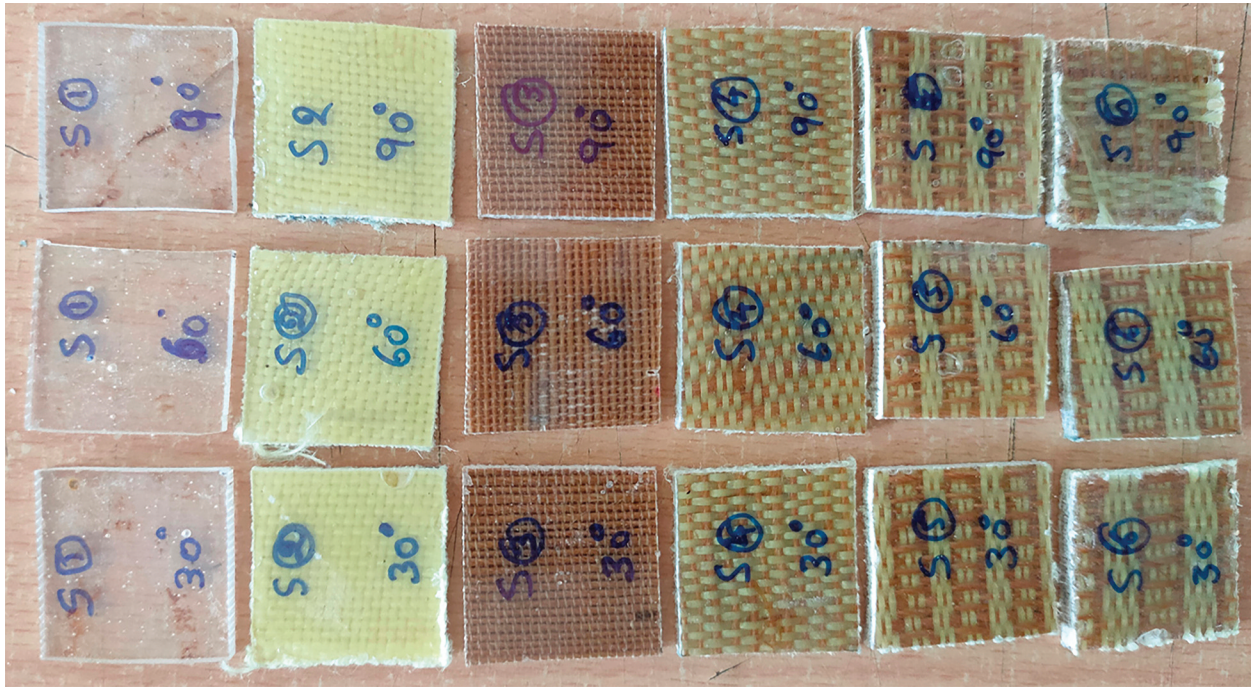


Figure 4. Erosion test specimens.

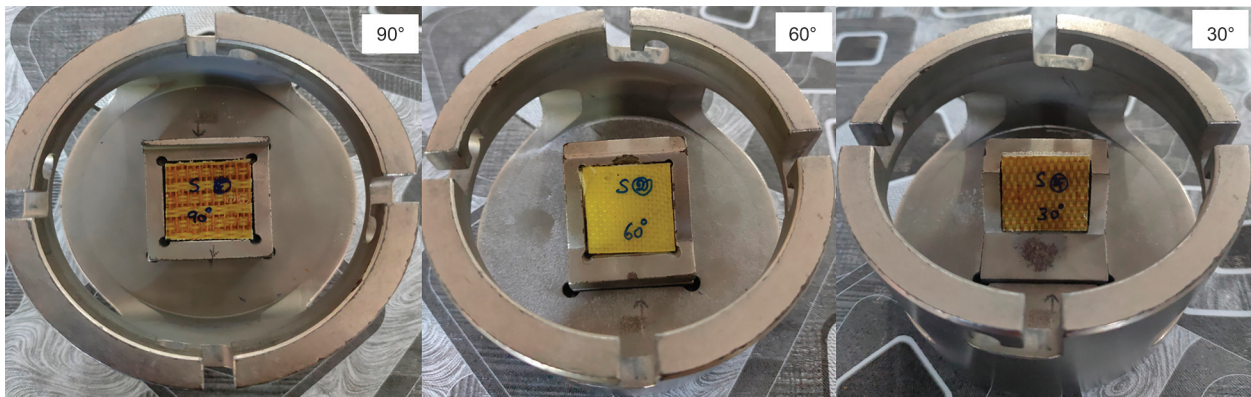


Figure 5. Specimen holders with various impact angles.

minimum water absorption of 4.4%. Alternatively, hybrid composites of plain weave (KH1) demonstrated a maximum water absorption of 5.3%. The twill weave type (KH2) hybrid composites were observed with an intermediate water absorption value of 4.8%. Following are the order of the examined composites increased water absorption percentages: Hemp > KH1 > KH2 > KH3 > Kevlar > Epoxy. The findings showed that, with the exception of hemp fiber composites, pure Kevlar, pure epoxy, and intra-ply Kevlar-hemp hybrid composites have better water absorption capabilities. Similar research was conducted on hybrid composites with jute and empty fruit bunch reinforced epoxy matrix, and they discovered that hybrid composites had better water absorption characteristics than pure composites [92, 93]. Another study that examined the hybrid of jute/Kevlar/epoxy composites concluded that all hybrid composites, with the

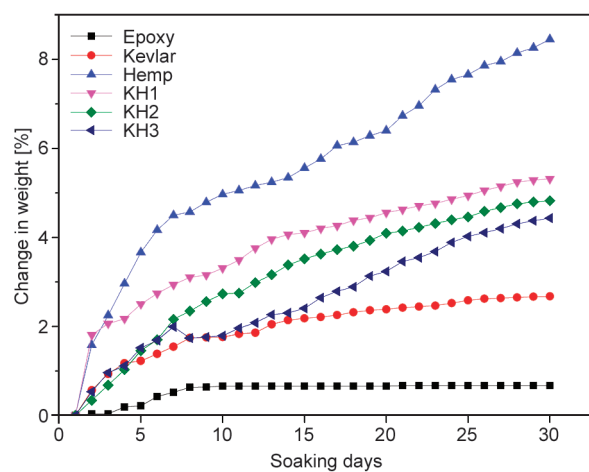


Figure 6. Water absorption behaviour of various composite specimens.

exception of JKJK type hybrid composites, had better water absorption resistance [94].

3.2. Thickness swelling properties

Figure 7 illustrates the findings from an investigation into the effect of thickness swelling behaviour of various Kevlar-hemp hybrid and pure composites. From the Figure 7 it can be observed that the thickness swelling of composites was increased with an increase in the soaking days. According to the results, the basket weave type KH3 hybrid composites (1.76%) and pure Kevlar composites (1.67%) possessed lower thickness swelling behaviour. This could be ascribed to the influence of the hybridization in which the hydrophobic Kevlar fiber restricted the moisture absorbance and hence resisted the swelling of the composites. A similar trend was also seen in the twill weave type KH2 (2%) and plain weave KH1 composites (2.3%), respectively. However, the pure hemp fiber reinforced epoxy composites exhibited higher thickness swelling behaviour (4.3%). It might be because of the existence of polar groups and hydrogen bonding, that natural fiber-based composites had lower water resistance. In this occurrence, moisture formed in the cell walls of composites made of natural fibers [95–97].

In contrast, pure epoxy matrix showed the least (0.3%) swelling behaviour. This is due to the hydrophobic nature of epoxy resin [93]. All composites exhibited a swelling behaviour in the following sequence: Hemp > KH1 > KH2 > KH3 > Kevlar > Epoxy. A study done earlier on Kevlar-PALF-Epoxy hybrid composites exhibited a similar trend [79]. The effect of moisture absorption and swelling characteristics of hybrid composites with lyocell and basalt fiber-reinforced with acrylated epoxidized soybean oil were examined [98]. The results found that hybrid

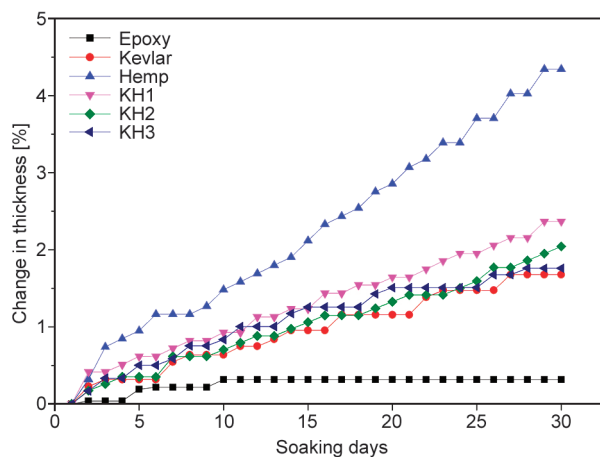


Figure 7. Thickness swelling characteristics of various hybrid composite specimens.

composites with basket weave type showed lower moisture absorption and thickness swelling.

3.3. Erosion experiment

3.3.1. Effects of different impact angle

The angle between the particle's trajectory and the degraded surface right before impact is referred to as the angle of impact [99]. The erosion experiment was carried out for different impact angles 30, 60, 90° by varying the exposure time of 2, 4, and 6 min at a constant velocity and feed rate of 100 m/s and 3.3 g/min, respectively. Figure 5 shows a sample holder with various impact angles. The erosion rate of the composite specimens under varied impact angles is shown in Figure 8. Different process variables and operation levels had an impact on the erosion rate of the composite specimens. The findings demonstrated that the epoxy matrix exhibited a maximum erosion wear rate of $9.0909 \cdot 10^{-4}$ g/g than all other composites at an impact angle of 60°. Similarly, among the composites, pure hemp fiber composites showed a maximum erosion wear rate of $7.5757 \cdot 10^{-4}$ g/g at 60° impact angle. The lowest erosion rate of $1.0101 \cdot 10^{-4}$ g/g was observed for pure Kevlar fiber reinforced composites at 90° impact angle. This could be attributed due to the good bonding between the fiber and matrix. For basket weave type (KH3) and plain weave type (KH1) composites, the minimum and maximum values of erosion wear rate were found to be $1.0606 \cdot 10^{-4}$ and $4.5454 \cdot 10^{-4}$ g/g at impact angles of 90 and 60°. If the maximum erosion rate ranges from 15 to 30°, it is ductile in nature, while it goes above 90° it is brittle in nature [100–102]. In our research, the maximum erosion wear

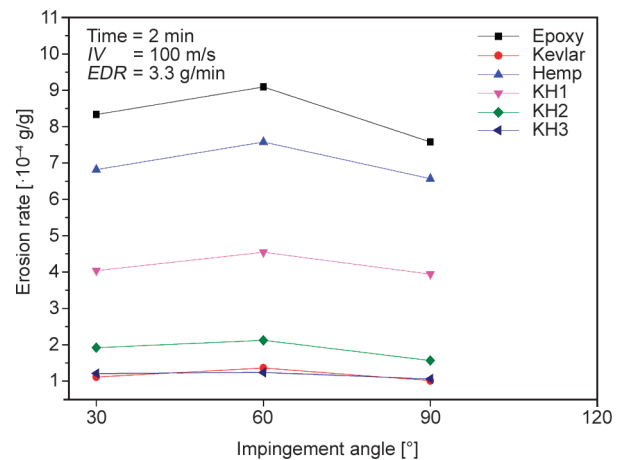


Figure 8. Impact angle versus erosion rate of various hybrid composite specimens

rate was 60° impact angle. Hence it is semi-ductile in nature. After 2 minutes of exposure, the erosion rate significantly expanded from 30 to 60° of impact angle while declining slightly to 90° impact angle for all composite specimen types. Similarly, numerous researchers have reported the erosion behaviour of Kevlar-PALF fiber reinforced epoxy hybrid composites and hence concluded that 60° of impact angle was found to have the maximum wear rate, suggesting the composites' semi-ductile nature [79]. Dalbehera *et al.* [103] investigated the erosion performance of hybrid with jute and glass fiber epoxy matrix composites and the results concluded that semi-ductile character of the composites is shown by the maximum erosion wear rate at 45 to 60° impact angles.

3.3.2. Effects of different exposure time

Exposure time is known as a measurement of cumulative exposure to an erosive or abrasive environment [99]. Erosion experiments for several impact angles (30, 60, and 90°), impact velocity 100 m/s, constant erosion feed rate of 3.3 g/min and the impacts of varied exposure intervals (2, 4, 6 minutes)

were examined. Figure 9 illustrates the exposure duration and rate of erosion at different impact angles. The epoxy matrix and hemp composites showed the maximum rate of erosion between the different impact angle and exposure times. Moreover, the kevlar composites exhibited a minimum erosion rate of $1.0101 \cdot 10^{-4}$ g/g at an impact angle of 90° with an exposure time of 2 min. The highest rate of erosion $4.6666 \cdot 10^{-4}$ g/g in hybrid composites was attained for plain weave (KH1) composites at 90° impact angle and 2 minutes exposure duration. Furthermore, the basket weave type (KH3) hybrid composites showed the lowest rate of erosion ($1.0606 \cdot 10^{-4}$ g/g) at 90° impact angle with 2 minutes of exposure. The findings suggest that, aside from pure Kevlar composites, every hybrid composite had improved erosion properties than non-hybrid composites.

3.3.3. Effects of different weaving patterns

Results showed that basket weave type (KH3) had greater erosion resistance at all exposure times and impact angles than all other weaving types of intra-ply Kevlar-hemp-epoxy hybrid composites. This

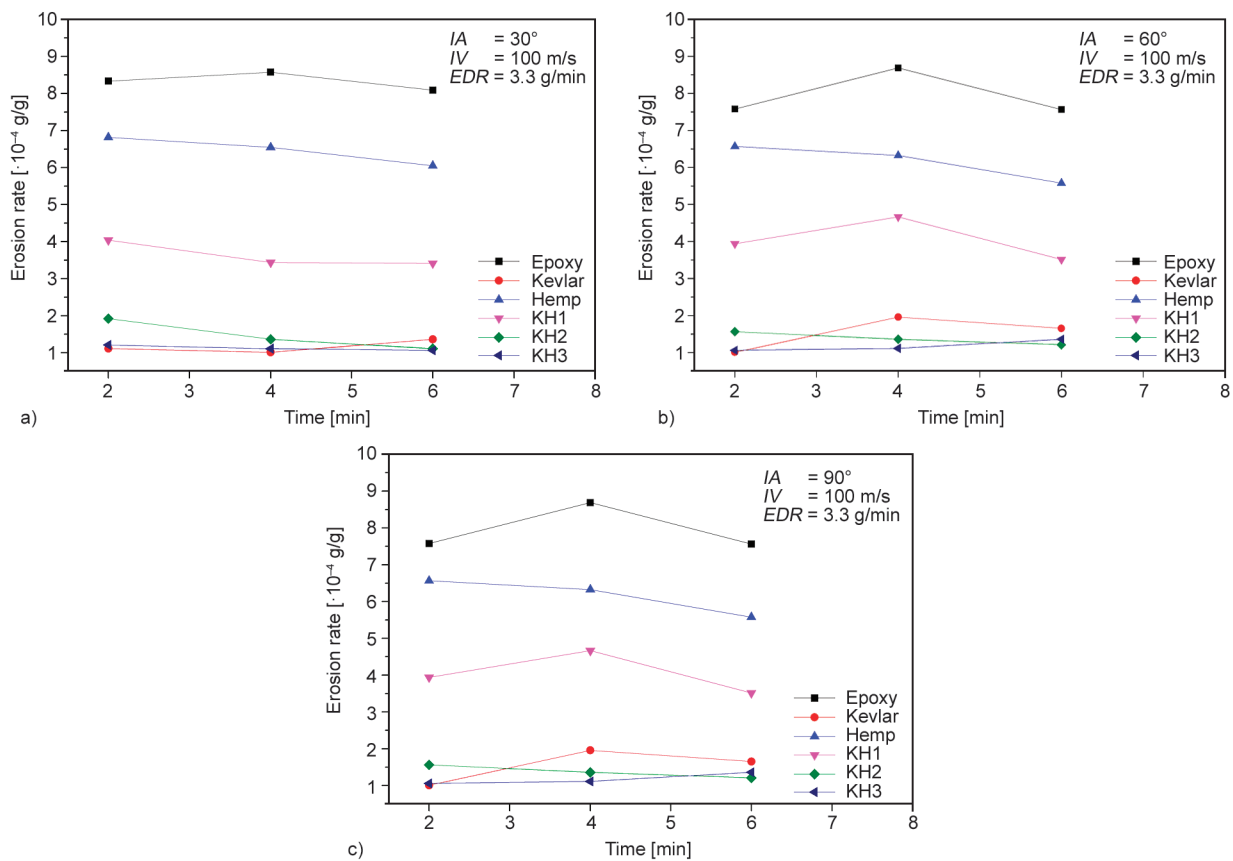


Figure 9. a) Erosion wear rate as a function of exposure duration at an impact angle of 30° of various hybrid composite specimens. b) Erosion wear rate as a function of exposure duration at an impact angle of 60° of various hybrid composite specimens. c) Erosion wear rate as a function of exposure duration at an impact angle of 90°.

could be attributed to the effect of the hybridizing where the hydrophobic Kevlar fiber dominated the hybrid composites. However, plain weave type (KH1) composites with various exposure times and impact angles demonstrated poor wear resistance behaviour. For plain weave type patterns, the highest wear rate was seen at an impact angle of 60° and various exposure time. This might be due to manufacturing flaws that result in the creation of micro voids in the composite specimens. Moreover, the twill weave type (KH2) displayed the middle of the wear resistance behaviour for all weaving designs. This is a result of the woven fabrics strong adhesion to the twill Kevlar and hemp fibers. The order of wear resistance to erosion at various composite weaving patterns was basket weave type (KH3) > Twill weave type (KH2) > plain weave type (KH1).

3.4. Taguchi method

The influence of different control variables on the rate of erosion wear of the Kevlar-hemp-epoxy hybrid

composites was investigated through the analysis of experiments using Taguchi method. Using 27 different combinations of the control parameters, experiments were run in accordance with the Taguchi analysis design. There were three levels, three factors, and 27 experimental runs in the Taguchi L27 (3³) orthogonal array. Table 3 lists the erosion rate and accompanying S/N ratios. The MINITAB 17 software was used to analyse the rate of erosion wear for Kevlar-hemp hybrid epoxy composites. The erosion wear rates mean signal-to-noise ratio was found to be -5.6854 dB.

The effects of different variables on the Signal to Noise ratio and mean of erosion wear rate are graphically depicted in Figures 10 and 11. The interaction plot of exposure time, impact angle, and various weaving patterns on the Kevlar-hemp fiber reinforced epoxy intra-ply hybrid composites are also shown in Figures 12 and 13. Both figures make it simple to comprehend how various control elements affect erosion wear rate. Additionally, Table 4 shows

Table 3. L27 Experimental design.

Experimental run	Impact angle [°]	Exposure duration [min]	Weaving patterns	Erosion wear rate [$\cdot 10^{-4}$ g/g]	S/N ratio [dB]
1	30	2	1	4.0404	-12.1285
2	30	4	1	3.4393	-10.7294
3	30	6	1	3.4141	-10.6655
4	60	2	1	4.5454	-13.1514
5	60	4	1	4.4949	-13.0544
6	60	6	1	4.4454	-12.9582
7	90	2	1	3.9393	-11.9084
8	90	4	1	4.6666	-13.3800
9	90	6	1	3.5151	-10.9188
10	30	2	2	1.9191	-5.6620
11	30	4	2	1.3636	-2.6937
12	30	6	2	1.1111	-0.9151
13	60	2	2	2.1212	-6.5316
14	60	4	2	1.9595	-5.8429
15	60	6	2	1.5656	-3.8936
16	90	2	2	1.5656	-3.8936
17	90	4	2	1.3636	-2.6937
18	90	6	2	1.2121	-1.6708
19	30	2	3	1.2121	-1.6708
20	30	4	3	1.1110	-0.9143
21	30	6	3	1.0606	-0.5110
22	60	2	3	1.2360	-1.8404
23	60	4	3	1.2121	-1.6708
24	60	6	3	1.0101	-0.0873
25	90	2	3	1.0606	-0.5110
26	90	4	3	1.1111	-0.9151
27	90	6	3	1.3636	-2.6937

the *S/N* ratio values. According to these results, the weaving pattern characteristic has the greatest impact

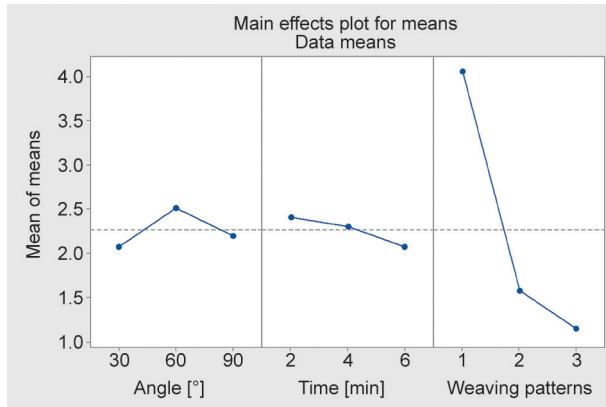


Figure 10. Mean erosion rate and erosion parameter main effect chart.

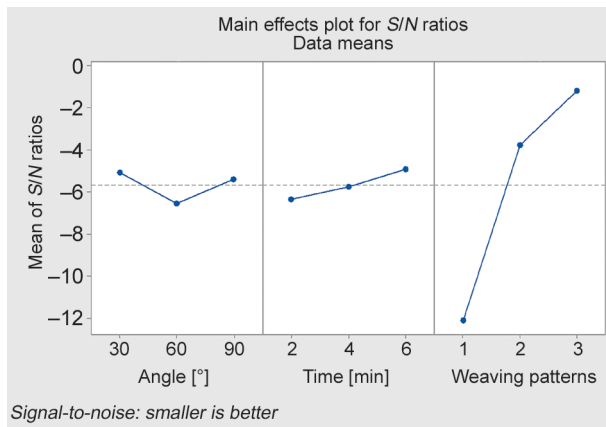


Figure 11. *S/N* ratio and erosion parameter main effect chart.

on the erosion wear rate for Kevlar-hemp-epoxy intra-ply hybrid composites. The remaining control variables, such as exposure time and impact angle, only slightly affect the erosion wear rate.

The highest and lowest erosion rates for each experimental factor are shown in Figure 11. This investigation led to the conclusion that the control factor combination A3B1C3 resulted in the prepared sample's erosion rate to be the lowest. The basket type weave pattern, 90° impact angle, and 2 posture time were found to have the lowest erosion wear rates of hybrid composites.

3.4.1. ANOVA regression analysis

In this work, an effort has been made to identify the ideal control factor values for the lowest erosion wear rate. For single-objective optimization, the connection between the rate of erosion wear and control variables must be quantified. The analysis of variance (ANOVA) findings for the erosion rate at a 5% level

Table 4. Signal-to-noise (*S/N*) ratio response table.

Level	Impact angle [°]	Exposure time [min]	Weaving patterns
1	-5.009	-6.366	-12.099
2	-6.559	-5.766	-3.755
3	-5.398	-4.924	-1.202
Delta	1.460	1.443	10.898
Rank	2	3	1

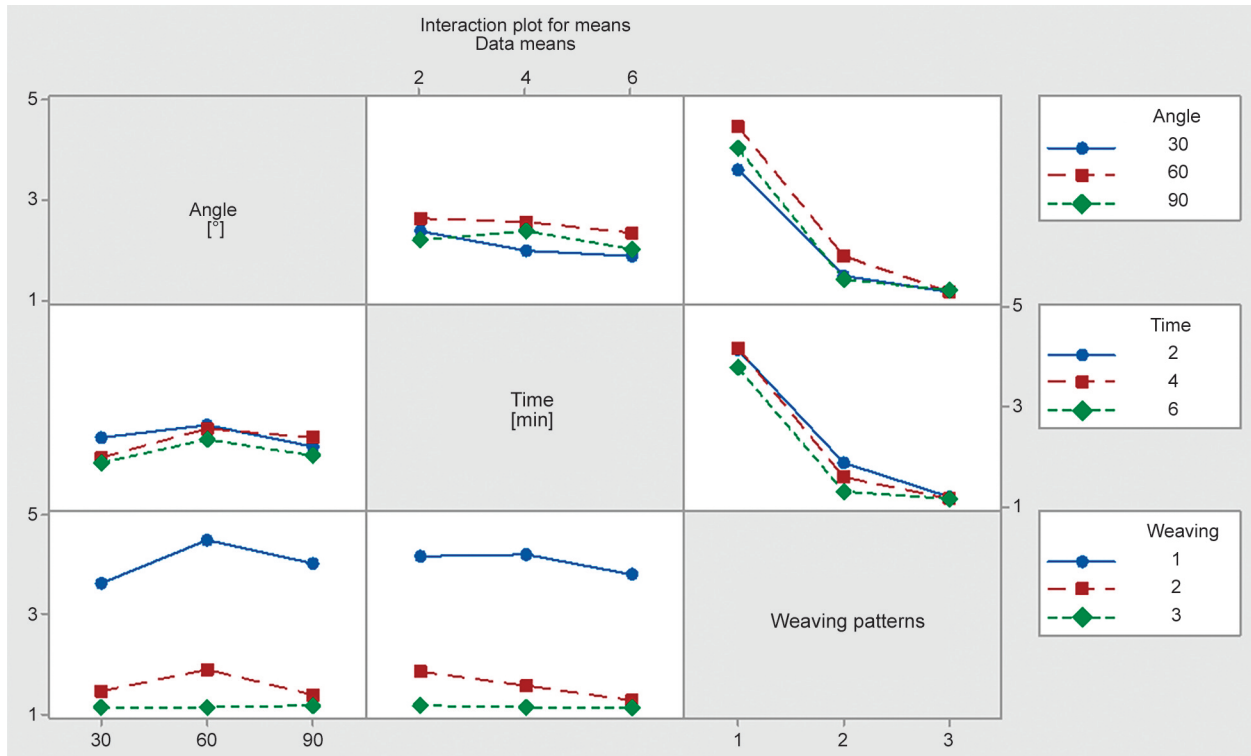


Figure 12. Erosion rate and process parameter interaction chart.

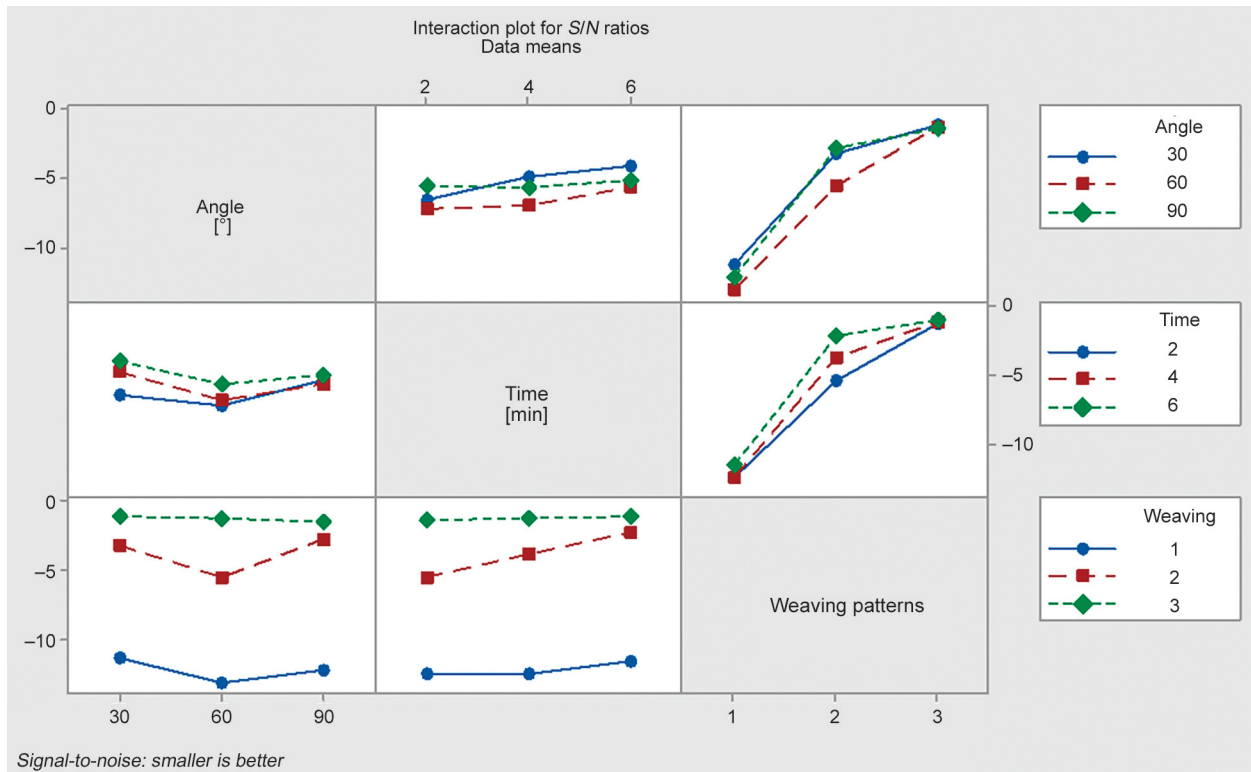


Figure 13. S/N ratio and process parameter interaction chart.

of significance are shown in Table 5. According to the findings, exposure time ($p = 0.278$) impingement angle ($p = 0.674$) had a less significant impact on the erosion rate. They also contribute less percentage significantly to the rate of erosion 1.01 and 0.15%, respectively. The weaving patterns exhibit a higher level of significance ($p = 0.000$) and a greater impact (79.96%) to the erosion wear rate. Regression analysis had utilized to calculate the theoretical erosion rate for using MINITAB software, yielding the following regression Equation (5):

$$\text{Erosion wear rate} = 5.366 + 0.00209 \cdot \text{Angle} - 0.0817 \cdot \text{Time} - 1.451 \cdot \text{Weaving} \quad (5)$$

The erosion wear rate for Kevlar-hemp-epoxy hybrid composites is compared in Table 6 with theoretical and experimental results, with the percentage error being within an acceptable range of 0 to 20%.

3.4.2. Confirmation test

The confirmation test is the last step in the process of designing an experiment. The goal of the confirmation test is to confirm the outcomes of the analytical phase. In the confirmation experiment, a fresh set of factor settings A3B1C3 is utilised to accurately predict the erosion rate. Taguchi analysis can be used to calculate a predicted value and the erosion wear rate's S/N ratio. The wear rate is predicted using the Taguchi approach employing a new predicted parameter of A3B1C3, and the S/N ratio is discovered to be -0.5177 dB. As stated in Table 7, an experiment was conducted utilising the combination factor A3B1C3, along the outcomes which had been compared to the results predicted. This created model seems to be able to predict erosion rate with accuracy. There is a 1.31% error in the S/N ratio of erosion rate. Nevertheless, the error can be decreased if the number of measurements has risen. As a result, the

Table 5. Results of an ANOVA on the erosion wear rate.

Source	Degree of freedom	Sequential sum of square	Percentage of contribution [%]	Adjusted sum of square	Adjusted mean square	F value	p value
Regression	3	38.4639	81.12	38.4639	12.8213	32.94	0.000
Angle	1	0.0705	0.15	0.0705	0.0705	0.18	0.674
Time	1	0.4809	1.01	0.4809	0.4809	1.24	0.278
Weaving	1	37.9126	79.96	37.9126	37.9126	97.40	0.000
Residual error	23	8.9525	18.88	8.9525	0.3892	–	–
Total	26	47.4164	100.00	–	–	–	–

Table 6. The outcome of experimental and theoretical comparison.

Ex No.	Erosion wear rate for theoretical values, E_{th} [$\cdot 10^{-4}$ g/g]	Erosion wear rate for experimental values, E_{ex} [$\cdot 10^{-4}$ g/g]	Error [%]
1	3.923670	4.0404	-2.88906
2	3.631670	3.4393	5.59330
3	3.338459	3.4141	-2.21554
4	4.595870	4.5454	1.11036
5	4.644404	4.4949	3.32607
6	4.245426	4.4454	-4.49845
7	4.005559	3.9393	1.68201
8	4.324726	4.6666	-7.32598
9	3.790715	3.5151	7.84088
10	1.930504	1.9191	0.59422
11	1.306870	1.3636	-4.16028
12	1.156426	1.1111	4.07937
13	2.156237	2.1212	1.65176
14	1.873137	1.9595	-4.40740
15	1.616926	1.5656	3.27836
16	1.519159	1.5656	-2.96632
17	1.506693	1.3636	10.49374
18	1.115448	1.2121	-7.97392
19	1.317426	1.2121	8.68954
20	0.975359	1.1110	-12.20890
21	1.090915	1.0606	2.85827
22	1.150493	1.2360	-6.91808
23	1.148959	1.2121	-5.20920
24	1.158748	1.0101	14.71618
25	1.040781	1.0606	-1.86861
26	1.309881	1.1111	17.89051
27	1.184637	1.3636	-13.12430

Table 7. Confirmation tests for erosion wear rate.

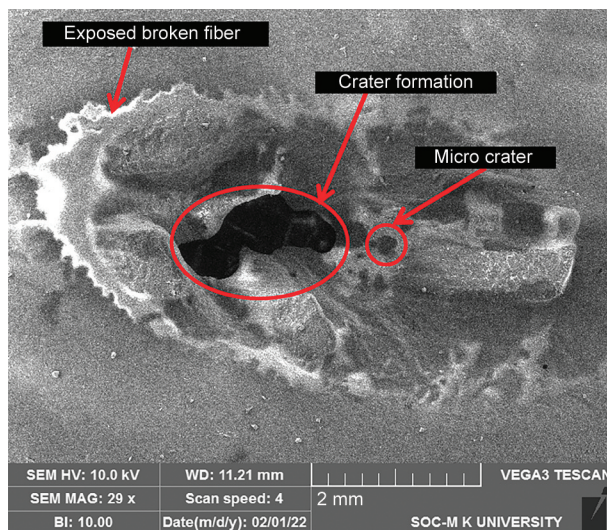
	Optimal control variables		Percentage error
	Prediction	Experiment	
Operating levels	A3B1C3	A3B1C3	1.31%
Erosion rate [$\cdot 10^{-4}$ g/g]	1.0909	1.0606	
S/N ratio [dB]	-0.5177	-0.5110	

Taguchi method of estimating the outcome measures were based on input variables.

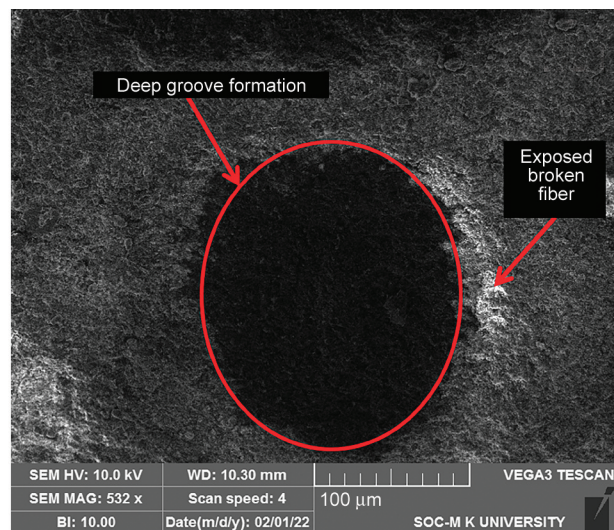
3.5. Morphological analysis of eroded surfaces

In this investigation of eroded composite, the eroded surface failure mechanism of intra-ply hybrid composite samples was observed by using the SEM (scanning electron microscope, performed with a Tescan Vega3 SEM) analysis. Figure 14 illustrate the eroded surfaces of plain and twill weave type intra-ply hybrid composites at 30 and 60° impact angle of 2 min exposure time. It clearly demonstrates the local loss of matrix material from the surface caused by eroded particles. Fiber breakages can also be seen on the damaged surfaces. Further on the surfaces of composite, micro cavities are also formed. This could have occurred as a result of compressive stresses developing on the composite’s surface due to alumina particle indentation. Fibers were also broken as a result of the impact. After the breaking of the fibers, they become detached from the surface, resulting in the creation of cavities.

Figure 15 shows the same microscopy image at a higher magnification, revealing the grooves and broken



a)



b)

Figure 14. Eroded surfaces of a) plain (KH1) and b) twill (KH2) type woven fabric composites.

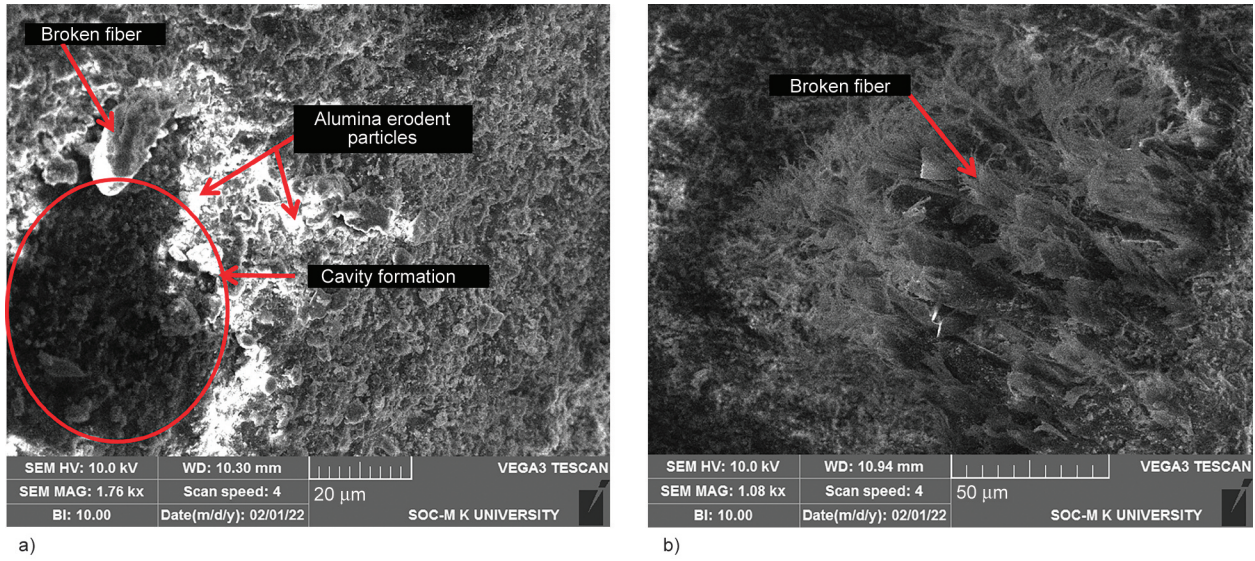


Figure 15. Eroded surfaces of a) plain (KH1) and b) twill (KH2) type woven fabric composites at higher magnification.

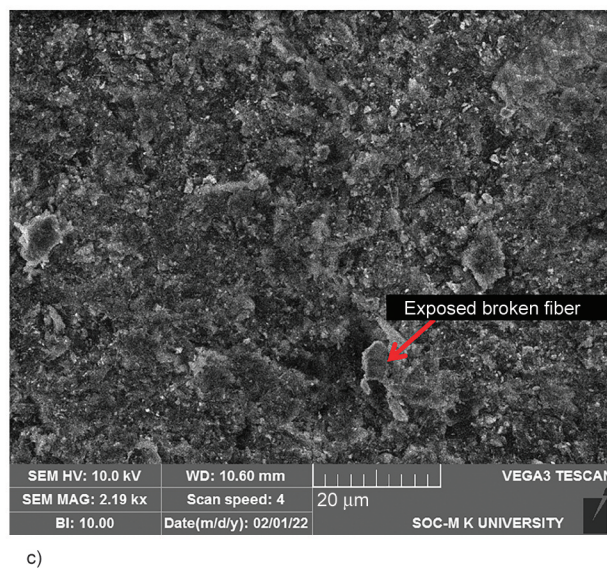
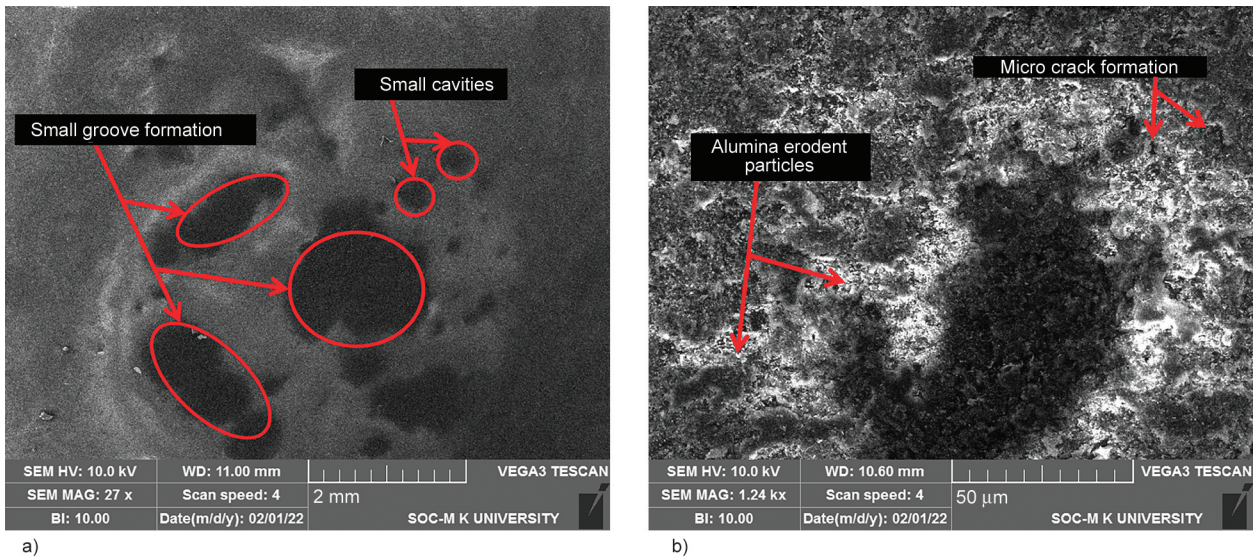


Figure 16. Eroded surfaces of basket (KH3) weave composites at higher magnification. a) 27×, b) 1240×, c) 2190×.

fibers clearly. Figures 16a and 16b displays a microscopy image of intra-ply hybrid Kevlar/hemp epoxy composite with a basket type weaving pattern at 90° of impact angle and 2 min exposure time. Local matrix removal occurred here as well, but the creation of cavities was smaller. Fiber breakage and matrix removal are also reduced, as shown in Figure 16c. This could have happened because the addition of Kevlar fiber good bonding between the woven fabrics of the composites, limiting the impact of eroding the surface. As a result, the resistance of the composites improves.

In comparison to Figure 14, Figures 16a and 16b depicts the same microscopy image at a higher magnification, revealing the creation of smaller and fewer grooves. Table 8 represents the eroded surface failure mechanism of hybrid composites using SEM analysis.

4. Conclusions

The effect of swell thickness, water absorption, and erosion property in intra-ply composites with Kevlar-hemp fiber reinforced epoxy matrix has been investigated experimentally. The following observations are:

- The moisture absorption and thickness swelling of hybrid composites showed greater resistance than hemp composites and epoxy matrix composites.
- The basket weave composites exhibited minimum absorption of moisture of 4.8% and thickness of swelling of 1.7%. Although, Kevlar composites had minimum water absorption of 2.6% and swelling thickness of 1.6% percentages.
- The basket weave composites and kevlar composites were discovered to have increased erosion resistance behaviour among all types of composites with a variety of control parameters.
- In comparison with our previous study of Kevlar-PALF-epoxy hybrid composites, the Kevlar-hemp-epoxy hybrid composites have better erosion resistance properties. Moreover, the min-

imum erosion wear rate of Kevlar-hemp-epoxy hybrid composites is $1.0606 \cdot 10^{-4}$ g/g.

- The Taguchi design analyses revealed that the hybrid composites' optimal control parameters were 90° impact angle and 2 minute exposure time for a basket type weaving pattern.
- ANOVA results showed that weaving types contributed more significantly while impact angle contributed less significantly.
- According to the results of the confirmation test, the improved parameter can offer superior resistance to erosion on the hybrids of Kevlar-hemp-epoxy composites.
- From the SEM study of eroded surfaces, it was evident that the fiber breakages, micro cavities, crater formation, small grooves were the failure mechanisms of material removal for the intra-ply hybrid composites.

Based on the literature and the investigations carried out so far by the researchers, there is a necessity to detect the defects in the intra layers in the hybridized composite materials for the performance improvement, and this could be seen as a future perspective.

Acknowledgements

The authors thank the management of KARE, India and KMUTNB for providing fabrication and testing facilities for this research work.

This research was funded by National Science, Research and Innovation Fund (NSRF), and King Mongkut's University of Technology North Bangkok with Contract no. KMUTNB-FF-66-14.

References

- [1] Rangappa S. M., Siengchin S.: Moving towards bio-fiber-based composites: Knowledge gaps and insights. *Express Polymer Letters*, **16**, 451–452 (2022). <https://doi.org/10.3144/expresspolymlett.2022.33>
- [2] Senthil Kumar K., Siva I., Rajini N., Jappes J. T. W., Amico S. C.: Layering pattern effects on vibrational behavior of coconut sheath/banana fiber hybrid composites. *Materials and Design*, **90**, 795–803 (2016). <https://doi.org/10.1016/j.matdes.2015.11.051>
- [3] Singh T., Patnaik A., Ranakoti L., Dogosy G., Lendvai L.: Thermal and sliding wear properties of wood waste-filled poly(lactic acid) biocomposites. *Polymers*, **14**, 2230 (2022). <https://doi.org/10.3390/polym14112230>
- [4] Sanjay M. R., Siengchin S.: Exploring the applicability of natural fibers for the development of biocomposites. *Express Polymer Letters*, **15**, 193 (2021). <https://doi.org/10.3144/expresspolymlett.2021.17>

Table 8. Eroded surfaces failure mechanism of hybrid composites using SEM analysis.

Hybrid composites	Erosion failures
Plain weave type hybrid composites	Micro cavities, broken fibers, crater formation
Twill weave type hybrid composites	Small cavities, smaller and fewer grooves
Basket weave type hybrid composites	Small cavities, disposed fibers, crater formation, micro crack

- [5] Singh T., Pattnaik P., Kumar S. R., Fekete G., Dogossy G., Lendvai L.: Optimization on physicochemical and wear properties of wood waste filled poly(lactic acid) biocomposites using integrated entropy-simple additive weighting approach. *South African Journal of Chemical Engineering*, **41**, 193–202 (2022).
<https://doi.org/10.1016/j.sajce.2022.06.008>
- [6] Puttegowda M., Pulikkalparambil H., Rangappa S. M.: Trends and developments in natural fiber composites. *Applied Science and Engineering Progress*, **14**, 543–552 (2021).
<https://doi.org/10.14416/j.asep.2021.06.006>
- [7] Singh T.: Optimum design based on fabricated natural fiber reinforced automotive brake friction composites using hybrid CRITIC-MEW approach. *Journal of Materials Research and Technology*, **14**, 81–92 (2021).
<https://doi.org/10.1016/j.jmrt.2021.06.051>
- [8] Jeyaguru S., Thiagamani S. M. K., Pulikkalparambil H., Siengchin S., Subramaniam J., Rangappa S. M., Muthukumar C., Krishnasamy S.: Mechanical, acoustic and vibration performance of intra-ply kevlar/PALF epoxy hybrid composites: Effects of different weaving patterns. *Polymer Composites*, **43**, 3902–3914 (2022).
<https://doi.org/10.1002/pc.26665>
- [9] Rangappa S. M., Siengchin S., Parameswaranpillai J., Jawaaid M., Ozbakkaloglu T.: Lignocellulosic fiber reinforced composites: Progress, performance, properties, applications, and future perspectives. *Polymer Composites*, **43**, 645–691 (2022).
<https://doi.org/10.1002/pc.26413>
- [10] Sanjay M. R., Madhu P., Jawaaid M., Senthamarikannan P., Senthil S., Pradeep S.: Characterization and properties of natural fiber polymer composites: A comprehensive review. *Journal of Cleaner Production*, **172**, 566–581 (2018).
<https://doi.org/10.1016/j.jclepro.2017.10.101>
- [11] Puttegowda M., Rangappa S. M., Jawaaid M., Shivanna P., Basavegowda Y., Saba N.: Potential of natural/synthetic hybrid composites for aerospace applications. in ‘Sustainable composites for aerospace applications’ (eds.: Jawaaid M., Thariq M.) Elsevier, Amsterdam, 315–351 (2018).
<https://doi.org/10.1016/B978-0-08-102131-6.00021-9>
- [12] Atiqah A., Chandrasekar M., Kumar T. S. M., Senthilkumar K., Ansari M. N.: Characterization and interface of natural and synthetic hybrid composites. in ‘Encyclopedia of renewable and sustainable materials’ (eds.: Hashmi S., Choudhury I. A.) Elsevier, Amsterdam, Vol. 4, 389–400 (2020).
<https://doi.org/10.1016/B978-0-12-803581-8.10805-7>
- [13] Sanjay M. R., Siengchin S., Parameswaranpillai J., Jawaaid M., Pruncu C. I., Khan A.: A comprehensive review of techniques for natural fibers as reinforcement in composites: Preparation, processing and characterization. *Carbohydrate Polymers*, **207**, 108–121 (2019).
<https://doi.org/10.1016/j.carbpol.2018.11.083>
- [14] Chandrasekar M., Shahroze R. M., Ishak M. R., Saba N., Jawaaid M., Senthilkumar K., Kumar T. S. M., Siengchin S.: Flax and sugar palm reinforced epoxy composites: Effect of hybridization on physical, mechanical, morphological and dynamic mechanical properties. *Materials Research Express*, **6**, 105331 (2019).
<https://doi.org/10.1088/2053-1591/ab382c>
- [15] Nagarajan K. J., Ramanujam N. R., Sanjay M. R., Siengchin S., Surya Rajan B., Sathick Basha K., Madhu P., Raghav G. R.: A comprehensive review on cellulose nanocrystals and cellulose nanofibers: Pretreatment, preparation, and characterization. *Polymer Composites*, **42**, 1588–1630 (2021).
<https://doi.org/10.1002/pc.25929>
- [16] Shahroze R. M., Muthukumar C., Krishnasamy S., Senthilmuthukumar T., Ishak M. R., Asyraf M. R. M.: A review on the various fibre treatment techniques used for the fibre surface modification of the sugar palm fibres. in ‘Proceedings of the Seminar Enau Kebangsaan 2019. Bahau, Malaysia’, 48–52 (2019).
- [17] Mohit H., Rangappa S. M., Siengchin S., Gorbatyuk S., Manimaran P., Alka Kumari C., Khan A., Doddamani M.: A comprehensive review on performance and machinability of plant fiber polymer composites. *Polymer Composites*, **43**, 608–623 (2022).
<https://doi.org/10.1002/pc.26403>
- [18] Krishnasamy S., Muthukumar C., Nagarajan R., Thiagamani S. M. K., Saba N., Jawaaid M., Siengchin S., Ayrimis N.: Effect of fibre loading and Ca(OH)₂ treatment on thermal, mechanical, and physical properties of pineapple leaf fibre/polyester reinforced composites. *Materials Research Express*, **6**, 085545 (2019).
<https://doi.org/10.1088/2053-1591/ab2702>
- [19] Vinod A., Sanjay M. R., Suchart S., Jyotishkumar P.: Renewable and sustainable biobased materials: An assessment on biofibers, biofilms, biopolymers and biocomposites. *Journal of Cleaner Production*, **258**, 120978 (2020).
<https://doi.org/10.1016/j.jclepro.2020.120978>
- [20] Jagadeesh P., Puttegowda M., Rangappa S. M., Siengchin S.: Influence of nanofillers on biodegradable composites: A comprehensive review. *Polymer Composites*, **42**, 5691–5711 (2021).
<https://doi.org/10.1002/pc.26291>
- [21] Thiagamani S. M. K., Krishnasamy S., Muthukumar C., Tensuthiwat J., Nagarajan R., Siengchin S., Ismail S. O.: Investigation into mechanical, absorption and swelling behaviour of hemp/sisal fibre reinforced bio-epoxy hybrid composites: Effects of stacking sequences. *International Journal of Biological Macromolecules*, **140**, 637–646 (2019).
<https://doi.org/10.1016/j.ijbiomac.2019.08.166>
- [22] Radoor S., Karayil J., Rangappa S. M., Siengchin S., Parameswaranpillai J.: A review on the extraction of pineapple, sisal and abaca fibers and their use as reinforcement in polymer matrix. *Express Polymer Letters*, **14**, 309–335 (2020).
<https://doi.org/10.3144/expresspolymlett.2020.27>

- [23] Parameswaranpillai J., Jacob J., Dominic C. D. M., Muthukumar C., Thiagamani S. M. K., Jayakumar A., Siengchin S., Radoor S.: Effect of water absorption on the tensile, flexural, fracture toughness and impact properties of biocomposites. in ‘Aging effects on natural fiber-reinforced polymer composites’ (eds.: Muthukumar C., Krishnasamy S., Thiagamani S. M. K., Siengchin S.) Springer, Singapore, 35–50 (2022).
https://doi.org/10.1007/978-981-16-8360-2_3
- [24] Ramesh M., Deepa C., Kumar L. R., Sanjay M. R., Siengchin S.: Life-cycle and environmental impact assessments on processing of plant fibres and its biocomposites: A critical review. *Journal of Industrial Textiles*, **51**, 5518S–5542S (2020).
<https://doi.org/10.1177/1528083720924730>
- [25] Thiagamani S. M. K., Pulikkalparambil H., Siengchin S., Ilyas R. A., Krishnasamy S., Muthukumar C., Radzi A. M., Rangappa S. M.: Mechanical, absorption, and swelling properties of jute/kenaf/banana reinforced epoxy hybrid composites: Influence of various stacking sequences. *Polymer Composites*, in press (2022).
<https://doi.org/10.1002/pc.26999>
- [26] Girijappa Y. G. T., Rangappa S. M., Parameswaranpillai J., Siengchin S.: Natural fibers as sustainable and renewable resource for development of eco-friendly composites: A comprehensive review. *Frontiers in Materials*, **6**, 226 (2019).
<https://doi.org/10.3389/fmats.2019.00226>
- [27] Senthilkumar K., Saba N., Rajini N., Chandrasekar M., Jawaid M., Siengchin S., Othman Y., Alotman Y.: Mechanical properties evaluation of sisal fibre reinforced polymer composites: A review. *Construction and Building Materials*, **174**, 713–729 (2018).
<https://doi.org/10.1016/j.conbuildmat.2018.04.143>
- [28] Chandrasekar M., Siva I., Kumar T. S. M., Senthilkumar K., Siengchin S., Rajini N.: Influence of fibre inter-ply orientation on the mechanical and free vibration properties of banana fibre reinforced polyester composite laminates. *Journal of Polymers and the Environment*, **28**, 2789–2800 (2020).
<https://doi.org/10.1007/s10924-020-01814-8>
- [29] Rangappa S. M., Parameswaranpillai J., Siengchin S., Jawaid M., Ozbakkaloglu T.: Bioepoxy based hybrid composites from nano-fillers of chicken feather and lignocellulose ceiba pentandra. *Scientific Reports*, **12**, 397 (2022).
<https://doi.org/10.1038/s41598-021-04386-2>
- [30] Senthilkumar K., Subramaniam S., Ungtrakul T., Kumar T. S. M., Chandrasekar M., Rajini N., Siengchin S., Parameswaranpillai J.: Dual cantilever creep and recovery behavior of sisal/hemp fibre reinforced hybrid biocomposites: Effects of layering sequence, accelerated weathering and temperature. *Journal of Industrial Textiles*, **51**, 2372S–2390S (2022).
<https://doi.org/10.1177/1528083720961416>
- [31] Athith D., Sanjay M. R., Yashas Gowda T. G., Madhu P., Arpitha G. R., Yogesha B., Omri M. A.: Effect of tungsten carbide on mechanical and tribological properties of jute/sisal/E-glass fabrics reinforced natural rubber/epoxy composites. *Journal of Industrial Textiles*, **48**, 713–737 (2018).
<https://doi.org/10.1177/1528083717740765>
- [32] Shaik S., Reddy D. R. R., Kornipalli A., Kasam A., Aravind D., Krishnasamy S., Muthukumar C., Thiagamani S. M. K.: Influencing effects of hybridization and addition of fillers on the viscoelastic properties of reinforced polymer-based composites. in ‘Vibration and damping behavior of biocomposites’ (eds.: Thiagamani S. M. K., Hoque E., Krishnasamy S., Muthukumar C., Siengchin S.) CRC Press, Boca Raton, 189–200 (2022).
- [33] Arpitha G. R., Sanjay M. R., Senthamaraiannan P., Barile C., Yogesha B.: Hybridization effect of sisal/glass/epoxy/filler based woven fabric reinforced composites. *Experimental Techniques*, **41**, 577–584 (2017).
<https://doi.org/10.1007/s40799-017-0203-4>
- [34] Sanjay M. R., Yogesha B.: Studies on hybridization effect of jute/kenaf/E-glass woven fabric epoxy composites for potential applications: Effect of laminate stacking sequences. *Journal of Industrial Textiles*, **47**, 1830–1848 (2018).
<https://doi.org/10.1177/1528083717710713>
- [35] Joshi S. V., Drzal L. T., Mohanty A. K., Arora S.: Are natural fiber composites environmentally superior to glass fiber reinforced composites? *Composites Part A: Applied Science and Manufacturing*, **35**, 371–376 (2004).
<https://doi.org/10.1016/j.compositesa.2003.09.016>
- [36] Jothibas S., Mohanamurugan S., Vijay R., Lenin Singaravelu D., Vinod A., Sanjay M. R.: Investigation on the mechanical behavior of areca sheath fibers/jute fibers/glass fabrics reinforced hybrid composite for light weight applications. *Journal of Industrial Textiles*, **49**, 1036–1060 (2020).
<https://doi.org/10.1177/1528083718804207>
- [37] Begum K., Islam M.: Natural fiber as a substitute to synthetic fiber in polymer composites: A review. *Research Journal of Engineering Sciences*, **2**, 46–53 (2013).
- [38] Ganesan K., Kailasanathan C., Sanjay M. R., Senthamaraiannan P., Saravanakumar S. S.: A new assessment on mechanical properties of jute fiber mat with egg shell powder/nanoclay-reinforced polyester matrix composites. *Journal of Natural Fibers*, **17**, 482–490 (2020).
<https://doi.org/10.1080/15440478.2018.1500340>
- [39] John K. M., Kumaran S. T., Kumar K. S., Kumar S. S., Aslan M. U., Alver Ü. M.: Mechanical and vibrational behavior of twill woven carbon fiber reinforced composites. *International Polymer Processing*, **35**, 203–210 (2020).
<https://doi.org/10.3139/217.3918>

- [40] Bharath K. N., Sanjay M. R., Jawaid M., Harisha, Basavarajappa S., Siengchin S.: Effect of stacking sequence on properties of coconut leaf sheath/jute/E-glass reinforced phenol formaldehyde hybrid composites. *Journal of Industrial Textiles*, **49**, 3–32 (2019). <https://doi.org/10.1177/1528083718769926>
- [41] Sangilimuthukumar J., Jappes J. T. W., Siva I., Brintha N. C.: The low-cost, high-performance material for automotive application. *International Journal of Innovative Technology and Exploring Engineering*, **9**, 1084–1087 (2019). <https://doi.org/10.35940/ijitee.B1428.1292S219>
- [42] Madhu P., Sanjay M. R., Senthamaraiannan P., Pradeep S., Saravanakumar S. S., Yogesha B.: A review on synthesis and characterization of commercially available natural fibers: Part-I. *Journal of Natural Fibers*, **16**, 1132–1144 (2018). <https://doi.org/10.1080/15440478.2018.1453433>
- [43] Shahzad A., Nasir S. U.: Mechanical properties of natural fiber/synthetic fiber reinforced polymer hybrid composites. in ‘Green biocomposites’ (eds.: Jawaid M., Sapuan S., Allothman O.) Springer, 355–396 (2017). https://doi.org/10.1007/978-3-319-46610-1_15
- [44] Gowda T. G. Y., Sanjay M. R., Bhat K. S., Madhu P., Senthamaraiannan P., Yogesha B., Pham D.: Polymer matrix-natural fiber composites: An overview. *Cogent Engineering*, **5**, 1446667 (2018). <https://doi.org/10.1080/23311916.2018.1446667>
- [45] Vinod A., Gowda T. Y., Vijay R., Sanjay M. R., Gupta M. K., Jamil M., Kushvaha V., Siengchin S.: Novel *Muntingia Calabura* bark fiber reinforced green-epoxy composite: A sustainable and green material for cleaner production. *Journal of Cleaner Production*, **294**, 126337 (2021). <https://doi.org/10.1016/j.jclepro.2021.126337>
- [46] Vignesh V., Balaji A. N., Nagaprasad N., Sanjay M. R., Khan A., Asiri A. M., Ashraf G. M., Siengchin S.: Indian mallow fiber reinforced polyester composites: Mechanical and thermal properties. *Journal of Materials Research and Technology*, **11**, 274–284 (2021). <https://doi.org/10.1016/j.jmrt.2021.01.023>
- [47] Kavya H. M., Bavan S., Sanjay M. R., Siengchin S., Gorbatyuk S.: Effect of coir fiber and inorganic filler on physical and mechanical properties of epoxy based hybrid composites. *Polymer Composites*, **42**, 3911–3921 (2021). <https://doi.org/10.1002/pc.26103>
- [48] Yorseng K., Rangappa S. M., Pulikkalparambil H., Siengchin S., Parameswaranpillai J.: Accelerated weathering studies of kenaf/sisal fiber fabric reinforced fully biobased hybrid bioepoxy composites for semi-structural applications: Morphology, thermo-mechanical, water absorption behavior and surface hydrophobicity. *Construction and Building Materials*, **235**, 117464 (2020). <https://doi.org/10.1016/j.conbuildmat.2019.117464>
- [49] Dér A., Kaluza A., Kurlé D., Herrmann C., Kara S., Varley R.: Life cycle engineering of carbon fibres for lightweight structures. *Procedia CIRP*, **69**, 43–48 (2018). <https://doi.org/10.1016/j.procir.2017.11.007>
- [50] Prabhu L., Krishnaraj V., Gokulkumar S., Sathish S., Sanjay M. R., Siengchin S.: Mechanical, chemical and sound absorption properties of glass/kenaf/waste tea leaf fiber-reinforced hybrid epoxy composites. *Journal of Industrial Textiles*, **51**, 1674–1700 (2022). <https://doi.org/10.1177/1528083720957392>
- [51] Zhang J., Chaisombat K., He S., Wang C. H.: Hybrid composite laminates reinforced with glass/carbon woven fabrics for lightweight load bearing structures. *Materials and Design* (1980–2015), **36**, 75–80 (2012). <https://doi.org/10.1016/j.matdes.2011.11.006>
- [52] Jeyaguru S., Thiagamani S. M. K., Pulikkalparambil H., Siengchin S., Krishnasamy S., Rajkumar A. G., Muthukumar C., Rangappa S. M.: Effects of different weaving patterns on thermomechanical and dynamic mechanical properties of kevlar/pineapple leaf fiber hybrid composites. *Polymer Composites*, **43**, 4979–4997 (2022). <https://doi.org/10.1002/pc.26764>
- [53] Muthukumar C., Krishnasamy S., Thiagamani S. M. K., Jeyaguru S., Siengchin S., Nagarajan R.: Polymers in aerospace applications. in ‘Encyclopedia of materials: Plastics and polymers’ (eds.: Hashmi J.) Elsevier, Vol. 4, 382–389 (2022). <https://doi.org/10.1016/B978-0-12-820352-1.00077-8>
- [54] Sanjay M. R., Arpitha G. R., Senthamaraiannan P., Kathiresan M., Saibalaji M. A., Yogesha B.: The hybrid effect of jute/kenaf/E-glass woven fabric epoxy composites for medium load applications: Impact, inter-laminar strength, and failure surface characterization. *Journal of Natural Fibers*, **16**, 600–612 (2018). <https://doi.org/10.1080/15440478.2018.1431828>
- [55] Sharma P., Bhanot V. K., Singh D., Undal H. S., Sharma M.: Research work on fiber glass wool reinforced and epoxy matrix composite material. *International Journal of Mechanical Engineering and Robotics Research*, **2**, 106–124 (2013).
- [56] Stalin A., Mothilal S., Vignesh V., Sanjay M. R., Siengchin S.: Mechanical properties of hybrid vetiver/banana fiber mat reinforced vinyl ester composites. *Journal of Industrial Textiles*, **51**, 5869S–5886S (2022). <https://doi.org/10.1177/1528083720938161>
- [57] Krishnasamy S., Thiagamani S. M. K., Muthukumar C., Tensuthiwat J., Nagarajan R., Siengchin S., Ismail S. O., Brintha N. C.: Effects of stacking sequences on static, dynamic mechanical and thermal properties of completely biodegradable green epoxy hybrid composites. *Materials Research Express*, **6**, 105351 (2019). <https://doi.org/10.1088/2053-1591/ab3ec7>

- [58] Kavya H. M., Bavan S., Yogesha B., Sanjay M. R., Suchart S., Sergey G.: Effect of coir fiber and inorganic filler hybridization on Innegra fiber-reinforced epoxy polymer composites: Physical and mechanical properties. *Cellulose*, **28**, 9803–9820 (2021).
<https://doi.org/10.1007/s10570-021-04140-x>
- [59] Senthilkumar K., Ungtrakul T., Chandrasekar M., Kumar T. S. M., Rajini N., Siengchin S., Pulikkalparambil H., Parameswaranpillai J., Parameswaranpillai J., Ayrilmis N.: Performance of sisal/hemp bio-based epoxy composites under accelerated weathering. *Journal of Polymers and the Environment*, **29**, 624–636 (2021).
<https://doi.org/10.1007/s10924-020-01904-7>
- [60] Ramachandran A., Rangappa S. M., Khan A., Seingchin S., Dhakal H. N.: Modification of fibers and matrices in natural fiber reinforced polymer composites: A comprehensive review. *Macromolecular Rapid Communications*, **43**, e2100862 (2022).
<https://doi.org/10.1002/marc.202100862>
- [61] Yashas Gowda T. G., Madhu P., Kushvaha V., Rangappa S. M., Siengchin S.: Comparative evaluation of areca/carbon/basalt fiber reinforced epoxy/bio epoxy based hybrid composites. *Polymer Composites*, **43**, 4179–4190 (2022).
<https://doi.org/10.1002/pc.26680>
- [62] Suriani M. J., Radzi F. S. M., Ilyas R. A., Petru M., Sapuan S. M., Ruzaidi C. M.: Flammability, tensile, and morphological properties of oil palm empty fruit bunches fiber/PET yarn-reinforced epoxy fire retardant hybrid polymer composites. *Polymers*, **13**, 1282 (2021).
<https://doi.org/10.3390/polym13081282>
- [63] Mukesh S. K., Bettagowda N., Praveenkumara J., Girijappa Y. G. T., Puttegowda M., Rangappa S. M., Gorbatyuk S.: Influence of stacking sequence on flax/kevlar hybrid epoxy composites: Mechanical and morphological studies. *Polymer Composites*, **43**, 3782–3793 (2022).
<https://doi.org/10.1002/pc.26655>
- [64] Yorseng K., Rangappa S. M., Parameswaranpillai J., Siengchin S.: Towards green composites: Bioepoxy composites reinforced with bamboo/basalt/carbon fabrics. *Journal of Cleaner Production*, **363**, 132314 (2022).
<https://doi.org/10.1016/j.jclepro.2022.132314>
- [65] Puttegowda M., Rangappa S. M., Khan A., Al-Zahrani S. A., Otaibi A. A., Shivanna P., Liu Y., Siengchin S.: Effect of layering sequence on impact properties of alkali treated phoenix pusilla fibers-glass-carbon fabrics reinforced hybrid composite laminates. *Journal of Natural Fibers*, in press (2022).
<https://doi.org/10.1080/15440478.2021.1932683>
- [66] Praveenkumara J., Vidya Sagar H. N., Madhu P., Gowda Y., Rangappa S. M., Khan M. R., Khan I., Siengchin S.: Pongamia pinnata (PP) shell powder filled sisal/kevlar hybrid composites: Physico-mechanical and morphological characteristics. *Research Square*, in press (2021).
<https://doi.org/10.21203/rs.3.rs-273651/v1>
- [67] Jagadeesh P., Puttegowda M., Girijappa Y. G. T., Rangappa S. M., Siengchin S.: Carbon fiber reinforced areca/sisal hybrid composites for railway interior applications: Mechanical and morphological properties. *Polymer Composites*, **43**, 160–172 (2022).
<https://doi.org/10.1002/pc.26364>
- [68] Arpitha G. R., Verma A., Sanjay M. R., Siengchin S.: Preparation and experimental investigation on mechanical and tribological performance of hemp-glass fiber reinforced laminated composites for lightweight applications. *Advances in Civil Engineering Materials*, **10**, 427–439 (2021).
<https://doi.org/10.1520/ACEM20200187>
- [69] Madhu P., Sanjay M. R., Khan A., Otaibi A. A., Al-Zahrani S. A., Pradeep S., Boonyasopone P., Siengchin S.: Hybrid effect of PJFs/e-glass/carbon fabric reinforced hybrid epoxy composites for structural applications. *Journal of Natural Fibers*, **19**, 3742–3752 (2020).
<https://doi.org/10.1080/15440478.2020.1848724>
- [70] Puttegowda M., Rangappa S. M., Khan A., Al-Zahrani S. A., Al Otaibi A., Shivanna P., Moure M. M., Siengchin S.: Preparation and characterization of new hybrid polymer composites from *Phoenix pusilla* fibers/e-glass/carbon fabrics on potential engineering applications: Effect of stacking sequence. *Polymer Composites*, **41**, 4572–4582 (2020).
<https://doi.org/10.1002/pc.25734>
- [71] Omri M. A., Sanjay M. R., Triki A., Yogesha B., Kallel A.: Dielectric properties and interfacial adhesion of jute, kenaf and E-glass fabrics reinforcing epoxy composites. *Polymer Composites*, **40**, 2142–2153 (2019).
<https://doi.org/10.1002/pc.25001>
- [72] Johnson R. D. J., Arumugaprabu V., Uthayakumar M., Vigneshwaran S., Manikandan V., Bennet C.: Erosion performance studies on sansevieria cylindrica reinforced vinylester composite. *Materials Research Express*, **5**, 035309 (2018).
<https://doi.org/10.1088/2053-1591/aab412>
- [73] Das G., Biswas S.: Erosion wear behavior of coir fiber-reinforced epoxy composites filled with Al₂O₃ filler. *Journal of Industrial Textiles*, **47**, 472–488 (2017).
<https://doi.org/10.1177/1528083716652832>
- [74] Muthusamy A. R., Thiagamani S. M. K., Krishnaswamy S., Muthukumar C., Pulikkalparambil H., Subramanian J., Madasamy N.: Erosion performance of natural fiber reinforced vinyl ester hybrid composites: Effect of layering sequences. *Materials Today: Proceedings*, **64**, 200–206 (2022).
<https://doi.org/10.1016/j.matpr.2022.04.365>
- [75] Gupta A., Kumar A., Patnaik A., Biswas S.: Effect of different parameters on mechanical and erosion wear behavior of bamboo fiber reinforced epoxy composites. *International Journal of Polymer Science*, **2011**, 592906 (2011).
<https://doi.org/10.1155/2011/592906>

- [76] Biswas S., Satapathy A.: A comparative study on erosion characteristics of red mud filled bamboo–epoxy and glass–epoxy composites. *Materials and Design*, **31**, 1752–1767 (2010).
<https://doi.org/10.1016/j.matdes.2009.11.021>
- [77] Deo C., Acharya S. K.: Solid particle erosion of lantana camara fiber-reinforced polymer matrix composite. *Polymer-Plastics Technology and Engineering*, **48**, 1084–1087 (2009).
<https://doi.org/10.1080/03602550903094340>
- [78] Mohanta N., Acharya S. K.: Implementations of the Taguchi design for the erosive wear of *Luffa cylindrica* fiber-reinforced epoxy hybrid composite. *Journal of Polymer Engineering*, **35**, 391–399 (2015).
<https://doi.org/10.1515/polyeng-2014-0235>
- [79] Jeyaguru S., Thiagamani S. M. K., Rajkumar A. G., Rangappa S. M., Siengchin S.: Solid particle erosion, water absorption and thickness swelling behavior of intra-ply kevlar/PALF fiber epoxy hybrid composites. *Polymer Composites*, **43**, 3929–3943 (2022).
<https://doi.org/10.1002/pc.26667>
- [80] Patnaik A., Tejyan S., Rawal A.: Solid particle erosion behavior of needlepunched nonwoven reinforced composites. *Research Journal of Textile and Apparel*, **14**, 12–22 (2010).
<https://doi.org/10.1108/RJTA-14-03-2010-B002>
- [81] Mishra S. C., Praharaj S., Satapathy A.: Evaluation of erosion wear of a ceramic coating with Taguchi approach. *Journal of Manufacturing Engineering*, **4**, 241–246 (2009).
- [82] Sathishkumar T. P., Satheeshkumar S., Bhuvaneshkumar K., Sanjay M. R., Siengchin S.: Crashworthiness characterization of jute fiber woven mat reinforced epoxy composite tube for structural application using Taguchi’s method. *International Journal of Crashworthiness*, **27**, 1351–1367 (2021).
<https://doi.org/10.1080/13588265.2021.1926861>
- [83] Rajan B. M. C., Kumar S. A., Sornakumar T., Senthamaraikannan P., Sanjay M. R.: Multi response optimization of fabrication parameters of carbon fiber-reinforced aluminium laminates (CARAL): By taguchi method and gray relational analysis. *Polymer Composites*, **40**, E1041–E1048 (2019).
<https://doi.org/10.1002/pc.24815>
- [84] Vigneshwaran S., Uthayakumar M., Arumugaprabu V.: Solid particle erosion study on redmud – An industrial waste reinforced sisal/polyester hybrid composite. *Materials Research Express*, **6**, 065307 (2019).
<https://doi.org/10.1088/2053-1591/ab0a44>
- [85] Saha A., Kumar S., Zindani D.: Investigation of the effect of water absorption on thermomechanical and viscoelastic properties of flax-hemp-reinforced hybrid composite. *Polymer Composites*, **42**, 4497–4516 (2021).
<https://doi.org/10.1002/pc.26164>
- [86] Naveen J., Jawaid M., Zainudin E. S., Sultan M. T. H., Yahaya R.: Mechanical and moisture diffusion behaviour of hybrid kevlar/*Cocos nucifera* sheath reinforced epoxy composites. *Journal of Materials Research and Technology*, **8**, 1308–1318 (2019).
<https://doi.org/10.1016/j.jmrt.2018.07.023>
- [87] Behera A., Dehury J., Thaware M. M.: A comparative study on laminated and randomly oriented luffa-kevlar reinforced hybrid composites. *Journal of Natural Fibers*, **16**, 237–244 (2019).
<https://doi.org/10.1080/15440478.2017.1414653>
- [88] Yahaya R., Sapuan S. M., Jawaid M., Leman Z., Zainudin E. S.: Water absorption behaviour and impact strength of kenaf-kevlar reinforced epoxy hybrid composites. *Advanced Composites Letters*, **25**, 99–102 (2016).
<https://doi.org/10.1177/096369351602500403>
- [89] Karimzadeh A., Yahya M. Y., Abdullah M. N., Wong K. J.: Effect of stacking sequence on mechanical properties and moisture absorption characteristic of hybrid PALF/glass fiber composites. *Fibers and Polymers*, **21**, 1583–1593 (2020).
<https://doi.org/10.1007/s12221-020-9640-2>
- [90] Suresha K. V., Shivanand H. K., Amith A., Vidyasagar H. N.: Evaluation of mechanical properties of hybrid fiber (hemp, jute, kevlar) reinforced composites. *AIP Conference Proceedings*, **1943**, 020109 (2018).
<https://doi.org/10.1063/1.5029685>
- [91] Colomer-Romero V., Rogiest D., García-Manrique J. A., Crespo J. E.: Comparison of mechanical properties of hemp-fibre biocomposites fabricated with biobased and regular epoxy resins. *Materials*, **13**, 5720 (2020).
<https://doi.org/10.3390/ma13245720>
- [92] Patnaik A., Satapathy A., Mahapatra S. S., Dash R. R.: Implementation of Taguchi design for erosion of fiber-reinforced polyester composite systems with SiC filler. *Journal of Reinforced Plastics and Composites*, **27**, 1093–1111 (2008).
<https://doi.org/10.1177/0731684407087688>
- [93] Khalil H. A., Jawaid M., Bakar A. A.: Woven hybrid composites: Water absorption and thickness swelling behaviours. *BioResources*, **6**, 1043–1052 (2011).
- [94] Rahman M. A., Mia S., Rana M. S., Ferdous M. S.: Experimental investigation on mechanical characterization of jute-kevlar hybrid composites. in ‘International Conference on Mechanical, Industrial and Energy Engineering, Khulna, Bangladesh’, Vol. 93, 1–6 (2020).
- [95] Ashori A., Sheshmani S.: Hybrid composites made from recycled materials: Moisture absorption and thickness swelling behavior. *Bioresource Technology*, **101**, 4717–4720 (2010).
<https://doi.org/10.1016/j.biortech.2010.01.060>
- [96] Khalil H. A., Hanida S., Kang C. W., Fuaad N. N.: Agro-hybrid composite: The effects on mechanical and physical properties of oil palm fiber (EFB)/glass hybrid reinforced polyester composites. *Journal of Reinforced Plastics and Composites*, **26**, 203–218 (2007).
<https://doi.org/10.1177/0731684407070027>

- [97] Nourbakhsh A., Ashori A.: Particleboard made from waste paper treated with maleic anhydride. *Waste Management and Research*, **28**, 51–55 (2010).
<https://doi.org/10.1177/0734242X09336463>
- [98] Adekunle K., Cho S-W., Patzelt C., Blomfeldt T., Skrifvars M.: Impact and flexural properties of flax fabrics and lyocell fiber-reinforced bio-based thermoset. *Journal of Reinforced Plastics and Composites*, **30**, 685–697 (2011).
<https://doi.org/10.1177/0731684411405874>
- [99] Tewari U. S., Harsha A. P., Häger A. M., Friedrich K.: Solid particle erosion of carbon fibre– and glass fibre–epoxy composites. *Composites Science and Technology*, **63**, 549–557 (2003).
[https://doi.org/10.1016/S0266-3538\(02\)00210-5](https://doi.org/10.1016/S0266-3538(02)00210-5)
- [100] Barkoula N-M., Karger-Kocsis J.: Effects of fibre content and relative fibre-orientation on the solid particle erosion of GF/PP composites. *Wear*, **252**, 80–87 (2002).
[https://doi.org/10.1016/S0043-1648\(01\)00855-9](https://doi.org/10.1016/S0043-1648(01)00855-9)
- [101] Rattan R., Bijwe J.: Influence of impingement angle on solid particle erosion of carbon fabric reinforced polyetherimide composite. *Wear*, **262**, 568–574 (2007).
<https://doi.org/10.1016/j.wear.2006.07.001>
- [102] Sangilimuthukumar J., Thiagamani S. M. K., Kumar C. M., Krishnasamy S., Arpitha G. R., Mayakannan S.: Erosion characteristics of epoxy-based jute, kenaf and banana fibre reinforced hybrid composites. *Materials Today: Proceedings*, **64**, 6–10 (2022).
<https://doi.org/10.1016/j.matpr.2022.03.469>
- [103] Dalbehera S., Acharya S. K.: Impact of cenosphere on the erosion wear response of woven hybrid jute–glass epoxy composites. *Advances in Polymer Technology*, **37**, 240–246 (2018).
<https://doi.org/10.1002/adv.21662>
- [104] Nasimudeen N. A., Karounamourthy S., Selvarathinam J., Thiagamani S. M. K., Pulikkalparambil H., Krishnasamy S., Muthukumar C.: Mechanical, absorption and swelling properties of natural fibre-based vinyl ester hybrid composites. *Applied Science and Engineering Progress*, **14**, 680–688 (2021).
<https://doi.org/10.14416/j.asep.2021.08.006>

Research article

Mechanical, thermal and rheological investigation of poly(lactic acid) (PLA)/poly(3-hydroxybutyrate-co-hydroxyvalerate) (PHBV) blend within its synergistic elongation effect region

Hosein Pouriman^{1,2*}, Richard Lin¹, Kevin Graham², Krishnan Jayaraman¹

¹Centre for Advanced Composite Materials, Department of Mechanical and Mechatronics Engineering, The University of Auckland, 1142 Auckland, New Zealand

²Friendlypak Ltd Corporation, 51b Rosebank Road, Avondale, 1026 Auckland, New Zealand

Received 3 July 2022; accepted in revised form 4 November 2022

Abstract. A mathematical Design of Experiments (DOE) was structured to consider the interactive effects of poly(lactic acid) (PLA), poly(3-hydroxybutyrate-co-hydroxyvalerate) (PHBV), triethyl citrate (TC) plasticiser, and epoxy functionalised styrene acrylate (ESA) within the synergistic elongational region of the PLA-PHBV blend (PLA/PHBV of 70/30 to 90/10 ratios). Twelve blends were prepared via twin screw extrusion process. Mixture design showed that PLA and TC content has the highest and ESA content has the lowest total effectiveness. The optimal values for the lowest cost and highest elongation at break and the elongational viscosity were reached at PLA/PHBV/plasticiser/ESA content of 0.574/0.3/0.113/0.012 wt%. Rheological studies showed the blends with the highest elongational viscosity were suitable for blown film extrusion.

Keywords: biodegradable polymers, polymer blends, and alloys, mechanical properties, PLA-PHBV blend, synergistic elongational effect

1. Introduction

Poly(lactic acid) (PLA) and poly(3-hydroxybutyrate-co-hydroxyvalerate) (PHBV) are biodegradable polymers produced from non-petrochemical and sustainable resources with the largest global production amongst biopolymers. PLA is an aliphatic homopolymer produced via ring opening polymerisation of lactide or via polycondensation of lactic acid [1–3]. The methyl side group and the short repeat unit make PLA slow to crystallise and intrinsically a brittle polymer [4]. In addition, PLA has poor impact-energy absorption and barrier properties to aroma, oxygen, and water vapour compared to other widely used thermoplastics for packaging applications [5]. For these reasons, PLA is typically blended

with other biopolymers and additives, such as nucleating agents, before processing.

PHBV is the copolymer of polyhydroxy butyrate (PHB) with hydroxy valerate (HV), a subset of polyhydroxyalkanoates (PHAs). In contrast to PLA, which is produced via chemical synthesis, PHAs can be produced from algae or bacteria [6–8]. PHBV has poor tensile strength but excellent gas barrier properties and an impact strength four times greater than PLA [9–12]. Because the mechanical and barrier properties of PLA and PHAs can complement one another, many researchers have investigated the properties and behaviour of PLA/PHA blends at various polymer and additives ratios as a cost-effective method to benefit from the superior properties of each polymer in the

*Corresponding author, e-mail: mpou994@aucklanduni.ac.nz

© BME-PT

blend [13]. One of the caveats of polymer blending is that improving one property could sometimes result in the deterioration of another [14, 15].

Researchers have investigated the PLA-PHBV blend with and without incorporating compatibilisers. In practice, the absence of a compatibiliser results in the break-up, dispersion, and coalescence of the minor polymer phase in the major phase [16–19]. This behaviour is attributed to the low interfacial adhesion between two polymer phases. The in situ reactive extrusion method has improved the miscibility and compatibility between PLA and PHBV [20]. Researchers have reported a synergistic elongational increase in the PLA/PHBV ratio from 70/30 to 95/10 percent [21–24]. This synergistic effect has often been addressed as an unusual blend behaviour that resulted in elongational increases up to 1056% (from 4.8 to 50.7%) [21].

Among the literature, Zhao *et al.* [24] reported an increase of about 250% in the strain at the break at the PLA/PHBV ratio of 85/15 and about 50% at the PLA/PHBV ratio of 70/30 compared to pristine PLA. Noda *et al.* [25] reported that the addition of 10 wt% PHA to PLA increased the elongation of the blend by 100% and attributed this behaviour to the presence of the amorphous phase in the blend. They further discuss that the deformation mechanism is different within this region compared to the rest of the blend ratio. The failure points are localised without propagating to sudden sample failure. Nanda *et al.* [26] found a 110 and 250% increase in elongation at break at PLA/PHBV 60/40 and 70/30, respectively. Although the biggest elongational increase happened in the synergistic region, the elongation at break of all samples processed at the same screw speed (150 rpm) was reported to be higher than that of the pristine polymers. In another study, Ma *et al.* [23] found that the incorporation of 10 to 30% PHBV into PLA significantly increased the ductility of PLA. They report that at the PLA/PHBV ratio of 80/20, the increase of elongation at break is 5750% (from 4 to 230%). Han *et al.* [27] also blended 5 to 30% PHBV with PLA and reported a 317% increase of elongation at break in PLA/PHBV 80/20. This value is 57 times greater than that of PLA. And again, with the linear increase of PHBV content in the blend, the elongation at break decreased. Gérard *et al.* [21] reports similar results and an increase of 204 and 50.7% at the 90/10 and 80/20 ratios, respectively. Liu *et al.* [28] also noticed the elongation increase in the 70/30 to 90/10 region,

with the 80/20 having a 500% increase compared to pure PLA. In more recent studies, researchers have incorporated PLA and PHBV with other polymers and additives [29–31], which makes the synergistic region non-conclusive to the effect of PLA and PHBV polymers only. However, an outlier elongational increase at high PLA content can be seen. The decrease in tensile strength due to the addition of PHBV content within the synergistic elongational region of the PLA-PHBV blend reported in the literature is between 5 to 10% compared to pristine PLA [26, 32].

The elongational increase and relative tensile strength stability within the synergistic region promise further investigation, specifically for flexible packaging applications. At the time of writing this paper, we have not found any journal article specifically investigating the synergistic elongational region in PLA/PHBV blend with a systematic ‘Design of Experiments’ approach. In this research, a mixture design has been defined within the PLA/PHBV ratio of 70/30 to 90/10 to count for the interactive effect of each blend component. A plasticiser and epoxy functionalised styrene acrylate (ESA) chain extender were added to the blend to enhance the elongation at break further and improve the melt strength.

2. Materials and methodology

2.1. Materials

To improve the miscibility of PLA and PHBV, the polymer grades with a minimum difference between their melting temperatures were selected. For PLA, Ingeo™ Biopolymer 2003D (melt flow rate (MFR), 6 g/10 min, 210 °C, 2.16 kg) with $T_m = 160$ °C was supplied from NatureWorks (Minnesota, USA). For PHBV polymer, ENMAT™ Thermoplastics Resin Y1000P (MFR = 8–15 g/10 min, 180 °C, 2.16 kg) was supplied from TianAn Biopolymer (Ningbo, China). For the ESA chain extender, Joncryl ADR 4468 was provided by BASF, Singapore. Triethyl citrate (TC) plasticiser ($C_{12}H_{20}O_7$) with a molecular weight of 276.28 g/mol (CAS-No 77-93-0) was supplied by Sigma Aldrich (Milwaukee, USA). All materials were consumed as received.

2.2. Methodology

The candidate batches to proceed further to blown film extrusion were chosen based on exhibiting the highest values of elongational viscosity and elongational strain.

As mentioned earlier, a synergistic effect between the blend constituents at PLA/PHBV ratios of 70/30 to 90/10 is expected; hence the mixture design statistical analysis was employed to analyse the interactive effects of each mixture component on different properties of the blends. Mixture design is typically utilised when the only intended variable in the manufacturing of one mixture is the content ratio of its constituent, and other factors that could contribute to the manufacturing, *e.g.*, process temperature, process time, etc., remain unchanged. Hence in mixture design, responses only depend on the relative proportion of components. Minitab software was used to generate the material proportions of all testing batches (Table 1).

Twelve different batches were manufactured based on mixture design. In addition, three batches with pristine PLA to PHBV ratios of 70/30, 80/20, and 90/10 (A70, A80, A90) with no plasticiser and chain extender were manufactured to draw a comparison with other samples containing plasticiser and chain extender. Extreme vertices design was chosen with a linear constraint of $0.82 < \text{PLA} + \text{PHBV} < 0.95$ and quadratic model type. In quadratic models, if, for example, A, B, and mixture components, the model will calculate the linear as well as the AB, AC, and BC relationships. Extreme vertices of the constraint design space using the XVERT algorithm were generated, as shown in Figure 1. Using Piepel’s CONAEV algorithm, the centroid points can be calculated up to the specified degree.

Table 1. The weight percent materials of testing batches based on mixture design.

Batch	Weight percent of component			
	PLA	PHBV	Triethyl citrate	ESA
1	83.8	8.2	5.0	3.0
2	76.8	8.2	15.0	0.0
3	73.8	8.2	15.0	3.0
4	66.5	28.5	5.0	0
5	63.5	28.5	5.0	3.0
6	85.5	8.2	5.0	1.3
7	85.5	8.2	6.3	0
8	85.5	9.5	5.0	0
9	57.4	28.5	14.1	0
10	57.4	27.6	15.0	0
11	57.4	28.5	11.1	3.0
12	57.4	24.6	15.0	3.0
A70	70.0	30.0	0	0
A80	80.0	20.0	0	0
A90	90.0	10.0	0	0

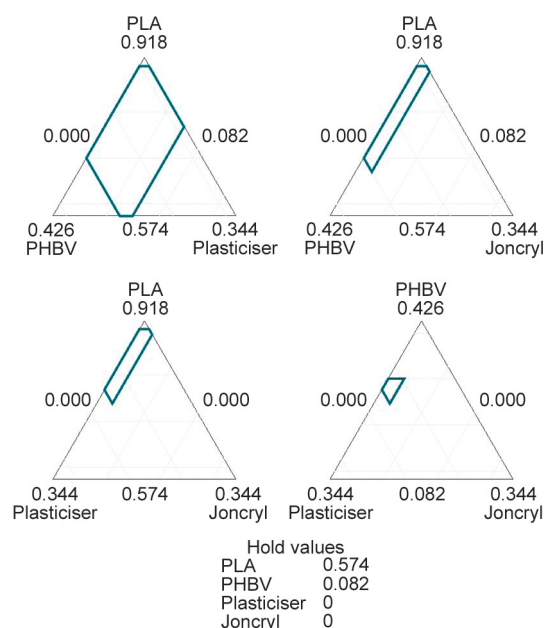


Figure 1. Matrix of simplex design plots in amounts.

The Cox response trace plots were used to examine the effect of each component on the response. The trace curves depict the impact of changing a component’s value along an imaginary line connecting the reference blend and the vertex. The following were considered when interpreting the response trace plots:

- The steeper the response traces, the greater the effect on the response.
- Components were analysed relative to the reference mixture.
- Longer response traces are indicative of the components with larger widths (upper and lower bounds), and shorter response traces are indicative of the components with the smaller width.
- The total influence of a component is determined by the component’s range as well as the steepness of its response trace.
- The total influence is determined by the difference in response between where the effect direction point in the component is at its lower bound and the effect direction point where the component is at its upper bound.
- Components with response traces that are nearly horizontal have almost no effect on the response.
- Components that have similar response traces have a similar impact on the specified response.

In this analysis, all residuals were standardised. A residual is a difference between a fitted value (\hat{y}) and its corresponding observed value (y); in other words, it identifies how accurately a model describes the variance in the observed data. To obtain the standardised

residual, the value of the residual was divided by the estimation of its standard deviation. The standardised residuals less than -2 or greater than 2 are generally considered large.

2.2.1 Sample manufacturing

Extruding filaments

Virgin PLA and PHBV pellets were dried at 90°C for 3 hours, and the moisture content was recorded to be less than 0.025% (250 ppm). PLA, PHBV, and ESA proportions were premixed and fed to the extruder through the hopper section. TC was proportionally and continuously fed to the extruder through a tube attached to a multi-syringe-equipped liquid pump (Cole-Parmer, IL, USA) equipped with a 60 ml syringe. Each batch was extruded via a co-rotating twin screw extruder (Brabender, Duisburg, Germany) with an L/D ratio of 40:1, screw diameter of 25 mm, a rotation speed of 75 rpm (delivering a varying torque of 9.5 to 10 N·m) and a temperature profile of 160–180–185–190–185–180 °C from feeding to metering zone and utilising a 4-mm die. The extrudates that were in the form of filaments were cooled down via a downstream air-cooling line and then wound to a filament spool. For further mechanical characterisation, samples of adequate lengths were separated in filament form. The rest of the filaments were pelletised via a pelletiser (Labtech, Samut Prakan, Thailand) to produce samples for rheological studies.

2.2.2. Rheology studies

The rheological behaviour of manufactured batches was studied via a dual-barrel capillary rheometer (Rheo-Tester 2000, Göttfert, Buchen, Germany). An isothermal test was conducted at 180°C with varying apparent shear rates of 100, 200, 500, 1000, 2000, 5000, 6000, and 9000 s^{-1} . Barrels were equipped with two capillary dies with 30 and 10 mm lengths and an equal hole diameter of 1 mm. Two pressure transducers capable of 500 and 1000 bar read the die pressures during the test, and the results were recorded by Göttfert's proprietary software WinRheo in real time. Each batch was tested twice, and the results were averaged.

Apparent shear stress (τ_a) was calculated based on Equation (1), where R is the radius of the capillary, L is the capillary length (30 mm), and P_1 and P_2 are the pressure readings from capillary 1 (30 mm) and capillary 2 (10 mm), respectively:

$$\tau_a = \frac{P_1}{2\frac{L}{R}} \quad (1)$$

By dividing the apparent shear stress by the apparent shear rate (γ_a), the apparent viscosity (η_a) can also be calculated [33] (Equation (2)):

$$\eta_a = \frac{\tau_a}{\dot{\gamma}_a} \quad (2)$$

Based on Bagley correction [34], the corrected shear stress can be calculated as shown in Equation (3):

$$\tau_w = \frac{P_1 - P_2}{2\frac{L}{R}} \quad (3)$$

The Rabinowitsch correction was then used to account for the effect of the non-Newtonian behaviour of molten polymers in the corrected shear rates. Based on this correction, a power-law correlation between γ_a and τ_w (Equation (4)) is drawn. The pseudo plasticity index (n) can then be determined as the slope of a double logarithmic plot of τ_w versus γ_a (Equation (4)):

$$\tau_w = k\dot{\gamma}_a^n \quad (4)$$

The Rabinowitsch correction can then be incorporated into values of γ_a , and then the true shear rate ($\dot{\gamma}_w$) can be calculated as in Equation (5), and the true viscosity (η_w) as in Equation (6):

$$\dot{\gamma}_w = \dot{\gamma}_a \frac{3n+1}{4n} \quad (5)$$

$$\eta_w = \frac{\tau_w}{\dot{\gamma}_w} \quad (6)$$

The Cogswell Equations, Equations (7), (8), and (9), were used to calculate the elongational viscosity of the manufactured batches [35]:

$$\sigma_E = \frac{3}{8}(n+1)P_2 \quad (7)$$

$$\dot{\epsilon} = \frac{4}{3} \frac{\eta_a \dot{\gamma}_a^2}{(n+1)P_2} \quad (8)$$

$$\eta_e = \frac{\sigma_E}{\dot{\epsilon}} \quad (9)$$

where σ_E denotes the average extensional stress, and the extensional viscosity (η_e) was calculated via extensional strain ($\dot{\epsilon}$).

2.2.3. Differential scanning calorimetry (DSC)

Thermal analysis was conducted via a differential scanning calorimeter (Q1000™, TA Instruments, DE, USA) at standard mode with a heat/cool/heat cycle. The temperature profile was programmed to cover –50 to 200 °C, with the starting temperature of ambient temperature, heating and cooling rate of 20 K/min, and nitrogen gas purging rate of 50 ml/min. Perforated aluminium pans were used to rid the samples of possible trapped moisture in the first heating cycle. All samples have equal weights of 10±0.1 mg. The melting temperature (T_m), glass transition temperature (T_g), the onset of crystallisation temperature, and the enthalpy of fusion from recorded thermographs were calculated via the DSC's proprietary software.

2.2.4. Mechanical properties characterisation

Tensile strength and elongation at break

Tensile strength and elongation at break tests were conducted via a universal tensile testing machine (Instron 5567, Instron, Massachusetts, USA). Single-bolt-type grips were used to hold the filament samples in place. The gauge length of all samples was set to 5 mm and the crosshead speed to 50 mm/min. The gauge length increment was measured and recorded

via a high-precision camera. The tensile strength measurements were automatically calculated via Bluhill software, proprietary software for Instron, by reading directly from the testing machine. At least five specimens were tested for each testing sample, and the results were averaged.

3. Results and discussion

3.1. Mathematical model analysis

The measured results for tensile stress, elongation at break, glass transition temperature, and enthalpy of fusion are presented in Table 2. To determine the accuracy of the models and whether the regression assumptions are met, the plot of residuals vs percent, fitted value, frequency, and observation order was drawn. Probing the residual plots can determine whether the ordinary least square assumptions are met. If these assumptions are met, unbiased coefficient estimates with a minimum difference are produced by the ordinary least square regression. Residual plots are shown in Figures 2 to 5.

The generated fitted values for tensile stress, elongation at break, glass transition temperature, and the onset of crystallisation temperature versus the deviation from reference blend in proportion are depicted in Figure 6. Before individual analysis of each

Table 2. Results from mechanical properties tests, thermal analysis, and cost estimation for mathematical model analysis.

Sample name	PLA	PHBV	Plasticiser	ESA	Cost [NZD/kg]	σ_u [MPa]	σ_b [MPa]	ϵ [%]	T_g [°C]	T_c [°C]	T_m [°C]	ΔH_{fus} [J/g]
1	0.838	0.082	0.050	0.030	10.2	46.80	35.8	54	50.67	51.28	142.5	16.68
2	0.768	0.082	0.150	0	13.4	33.70	29.1	196	39.61	44.68	140.4	21.86
3	0.738	0.082	0.150	0.030	14.6	5.44	5.0	190	36.26	43.62	135.1	35.47
4	0.665	0.285	0.050	0	10.3	45.90	41.6	53	53.21	53.01	171.6	31.52
5	0.635	0.285	0.050	0.030	11.5	44.30	36.5	164	48.07	52.32	167.5	29.23
6	0.855	0.082	0.050	0.013	9.5	45.70	32.9	113	51.08	54.61	142.9	20.06
7	0.855	0.082	0.063	0	9.5	38.60	29.3	135	51.16	52.98	144.5	12.84
8	0.855	0.095	0.050	0	9.1	52.10	38.2	52	53.03	54.69	168.4	13.70
9	0.574	0.285	0.141	0	14.3	34.30	34.0	189	38.05	45.90	165.1	31.74
10	0.574	0.276	0.150	0	14.6	34.20	33.8	199	38.34	42.98	167.2	33.10
11	0.574	0.285	0.111	0.030	14.2	34.70	31.2	206	43.79	45.66	167.0	30.66
12	0.574	0.246	0.150	0.030	15.6	27.40	27.1	197	40.15	43.54	165.4	33.73
13/A70	0.700	0.300	0	0	8.2	45.90	42.7	52	60.5	60.17	171.9	26.04
14/A80	0.800	0.200	0	0	7.6	52.50	51.5	54	59.85	60.95	170.5	21.66
15/A90	0.900	0.100	0	0	6.99	49.60	49.3	51	59.95	60.87	149.7	12.80

σ_u is the ultimate tensile stress,
 σ_b is the tensile stress at the break,
 ϵ is the elongation at the break,
 T_g is the glass transition temperature,
 T_c is the onset of cold crystallisation temperature,
 T_m is the temperature at the melting point,
 ΔH_{fus} is the enthalpy of fusion

response, a common trend that could be identified among all responses is that PLA and TC components have the longest response range (upper and lower bounds); therefore, the highest total effectiveness, and ESA has the shortest range, hence the lowest total

effectiveness. The total efficiency of PLA relative to other components is high with respect to its range and steepness, albeit the PLA graph isn't the steepest one in any of the responses. TC for the specified responses may be the most effective component in the blend

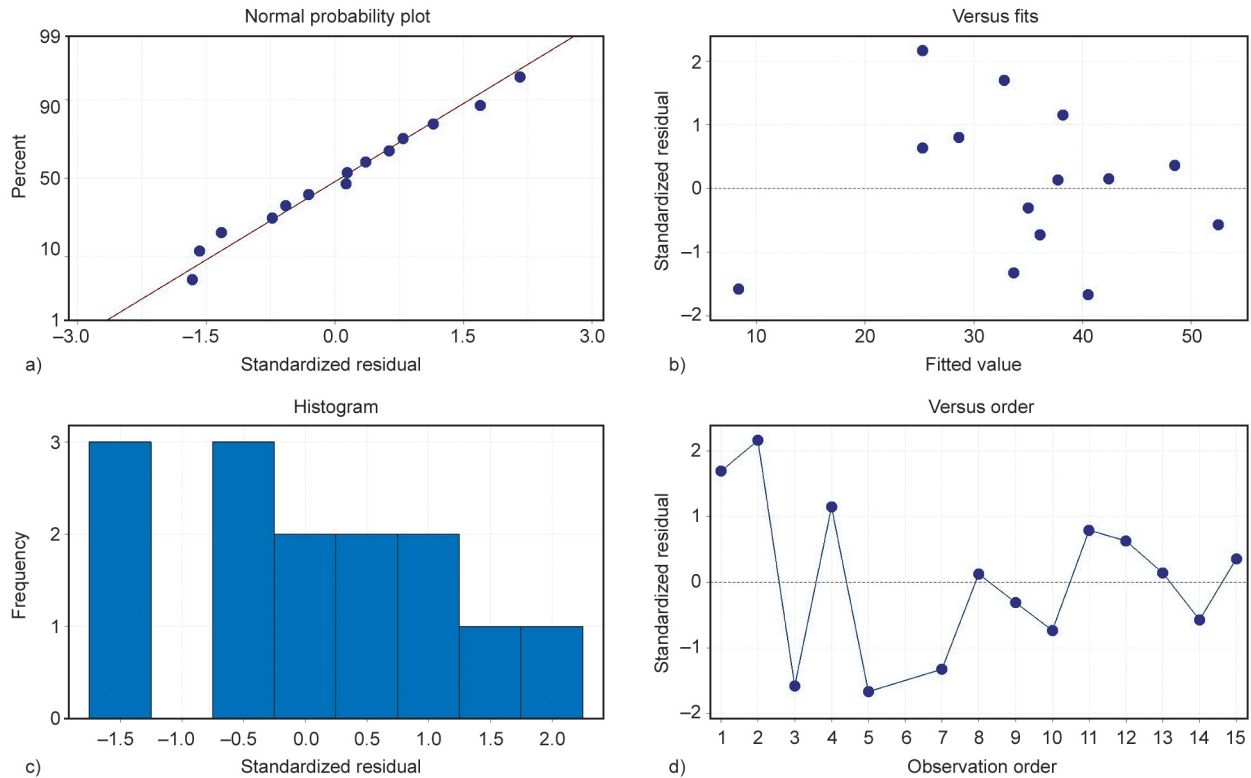


Figure 2. Residual plots for tensile stress at break. a) Normal probability plot, b) versus fits, c) histogram, d) versus order.

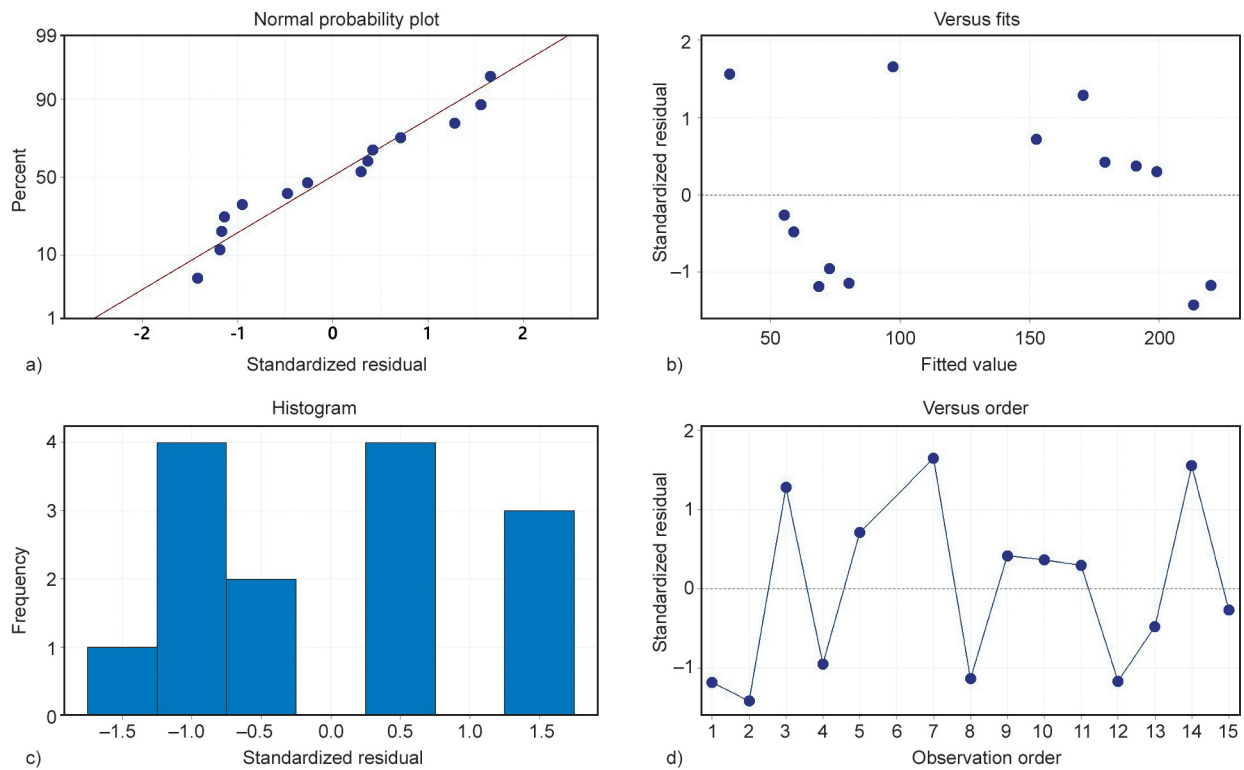


Figure 3. Residual plots for elongation at break. a) Normal probability plot, b) versus fits, c) histogram, d) versus order.

due to its steep presence in all response graphs and an extended range of upper and lower bounds. It can be seen from the tensile stress response plot (Figure 6a) that PLA and PHBV have a similar

response trace but at a different range. With the proportional increase of these components, the tensile stress increases and then decreases. PHBV with a steeper presence denotes higher effectiveness among

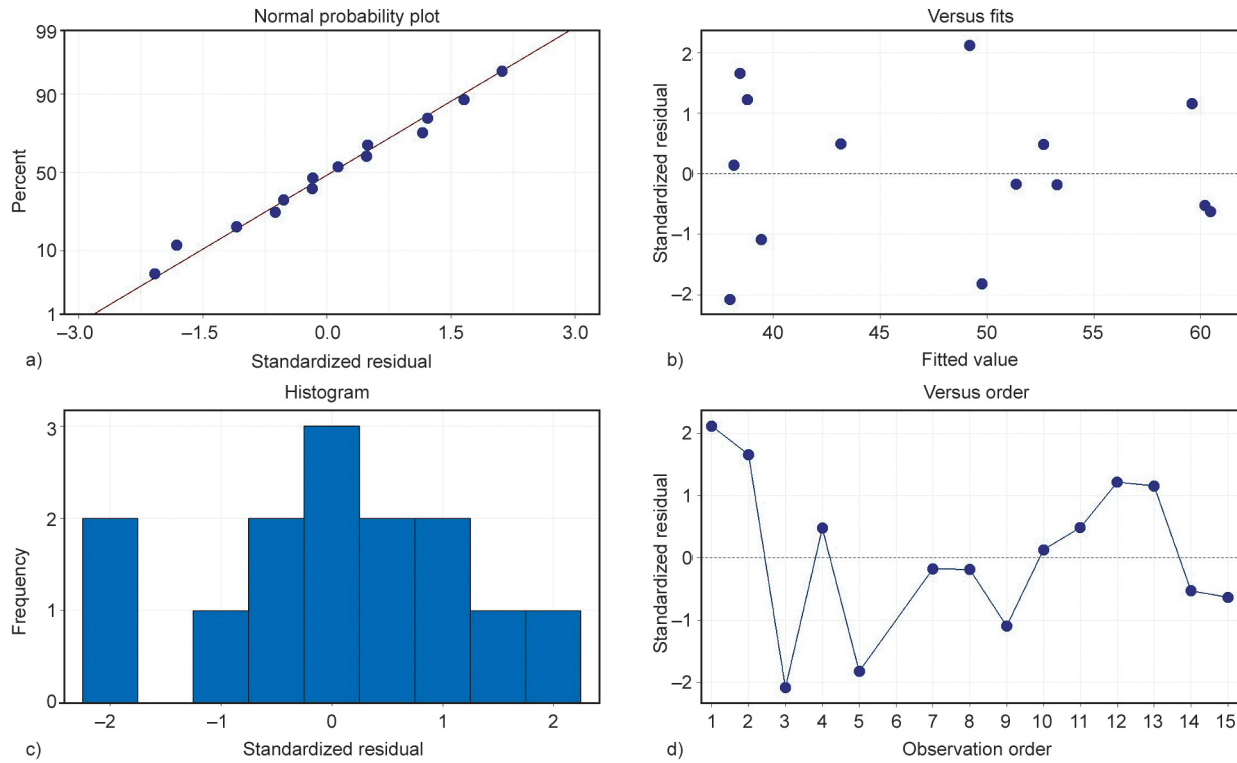


Figure 4. Residual plots for glass transition temperature. a) Normal probability plot, b) *versus* fits, c) histogram, d) *versus* order.

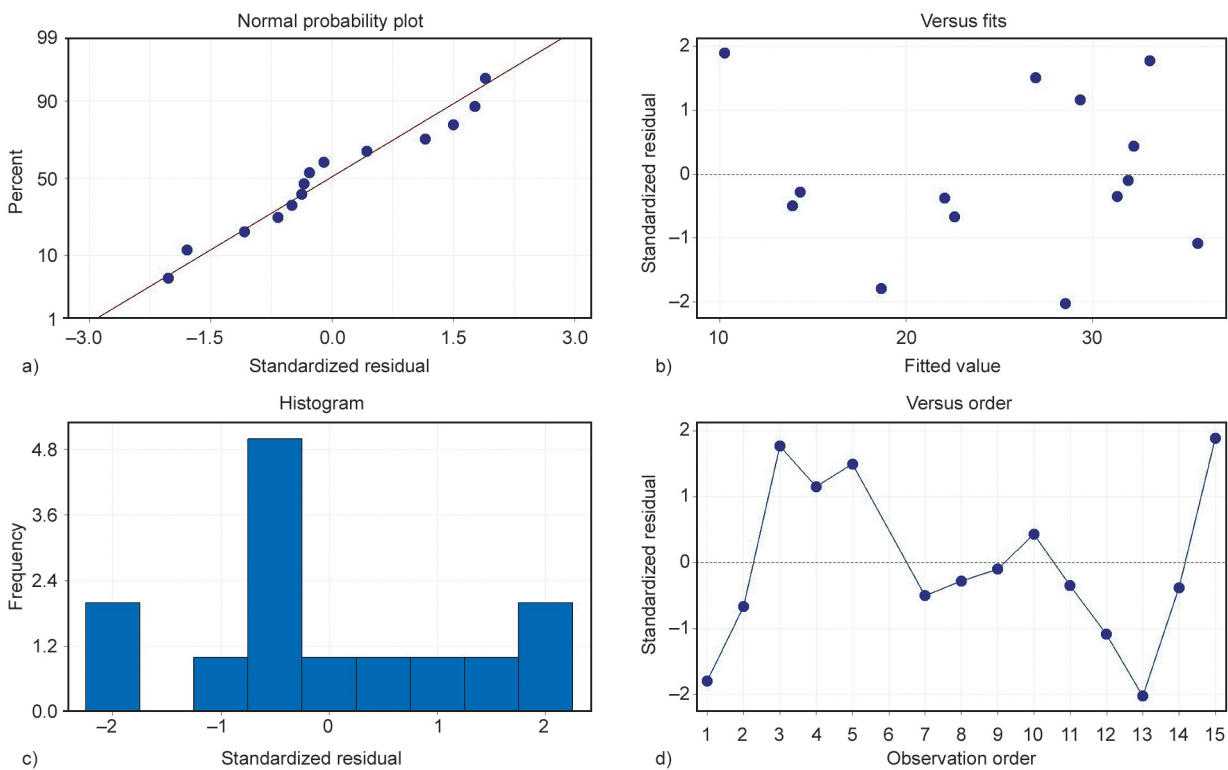


Figure 5. Residual plots for enthalpy of fusion. a) Normal probability plot, b) *versus* fits, c) histogram, d) *versus* order.

the two thermoplastics but at a lower range. The TC plasticiser with the steepest line among all components indicates a continuous decline in tensile stress with its proportional addition to the blend. This behaviour can be explained by the function of most plasticisers in the polymer blend. TC molecules with low vapour pressure and molecular weight place themselves among polymer molecules, providing a lubricating effect between polymer chains. This leads to an increase in chain mobility, hence facilitating molecular separation at higher stress loads. The ESA chain extender's low range and short upper and lower bounds indicate its low total effectiveness. The increase of ESA content proportional to other blend components slightly decreases and then increases the tensile stress. ESA chain extender is used in trace contents in the mixture and here shows, it does not have a significant interactive effect with other components in terms of tensile stress.

As shown in Figure 6b, PLA has the longest response trace for the elongation at break response. The proportional increase of PLA content in the blend leads to a rapid and almost linear decrease of the elongational strain of the samples from around 220 to 100%. The high brittleness of PLA can explain this direct correlation between PLA content and elongational strain. In contrast, as expected, the addition of TC led to a linear increase of elongational strain in the samples indicating a non-interactive effect of plasticiser with respect to the increase of other blend components. PHBV and ESA content show a reversed interactive effect on the blend. An increase in PHBV slightly decreases the elongational strain from 140 to 120% and then back to about 150%. PHBV has the lowest response range and the most temperate slope between all components. This indicates that PHBV content is not a significant contributor but has a synergistic effect on the elongational

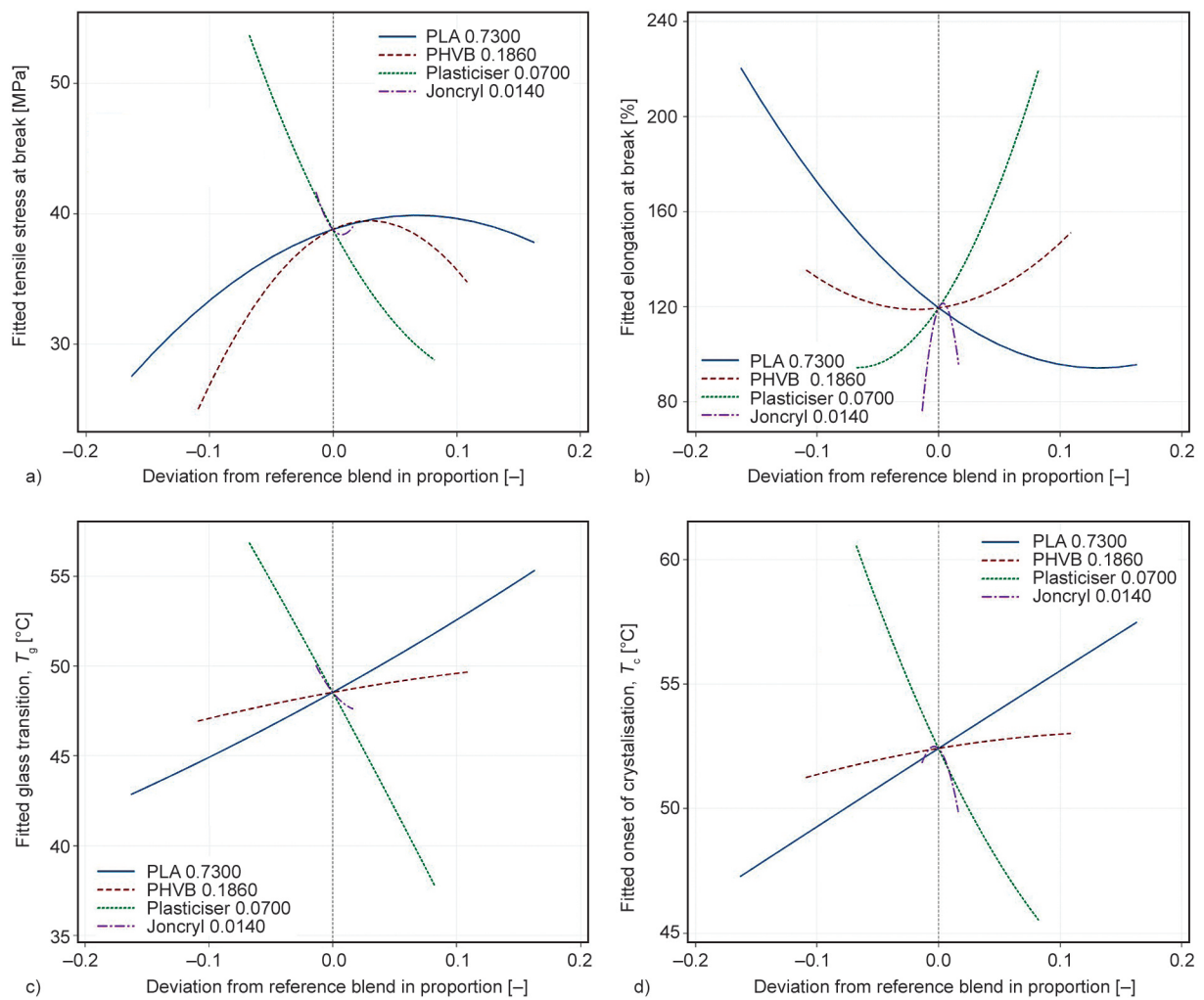


Figure 6. Cox response trace plots for a) tensile stress at break, b) elongation at break, c) glass transition temperature and d) the onset of crystallisation.

strain of the compound. ESA content with high effectiveness (steep trace line) at a short response range has a counter effect with PHBV content. It initially increases the strain rate from 80 to 120% at a rapid rate and then declines. These interactive effects justify the importance of mixture design analysis and call for an optimisation study when different properties are to be reached simultaneously.

For the glass transition temperature (Figure 6c), all components show an almost linear response trace signifying a direct relationship with their proportional content increase. The increase of PLA and PHBV contents leads to an increase in the T_g . However, PLA has a more significant effect where the effect of PHBV is subdued. The direct correlation between the increase in TC content and the decrease of T_g can be explained as the main functionality of plasticisers in polymer blends, which is to place itself between polymer chains. This affects the intensity of the secondary bonding forces between the polymer chains, decreasing the glass transition temperature, among other effects. ESA chain extender, albeit with low total effectiveness, acts as a plasticiser in glass transition temperature response.

The response trace graphs from the onset of crystallisation temperature (T_c) (Figure 6d) are closely similar to the T_g graphs except for the chain extender

content. The increase of ESA content shows an interactive effect in the blend with a sudden rise and fall of T_c . Although, in this case, the effect of the chain extender is not significant compared to the total effectiveness of other contributors, it can be concluded that ESA could be used in optimum contents to have a maximised T_c response.

The matrixes of cost per material of components were visualised by drawing surface response plots for the main contributing components, as presented in Figure 7. ESA chain extender was omitted from the plots due to its trivial contribution to the overall cost. In surface plots, the mixture components are represented in x and y-axes, the cost on z-axis, and the response on the meshed surface. Overall, it can be concluded that the cost of manufacturing the range of these mixture compositions is highly dependent on the price of PLA and, after that, PHBV, then the plasticiser. This conclusion could change based on the selection of different grades of materials, the year of production, and the market price.

Multiple variables often must be considered when a compound is designed for a real-time application. For this study, the optimisation goals were to lower the cost and increase the elongation at break and the apparent elongational viscosity. The weight and importance of responses were equally distributed. The

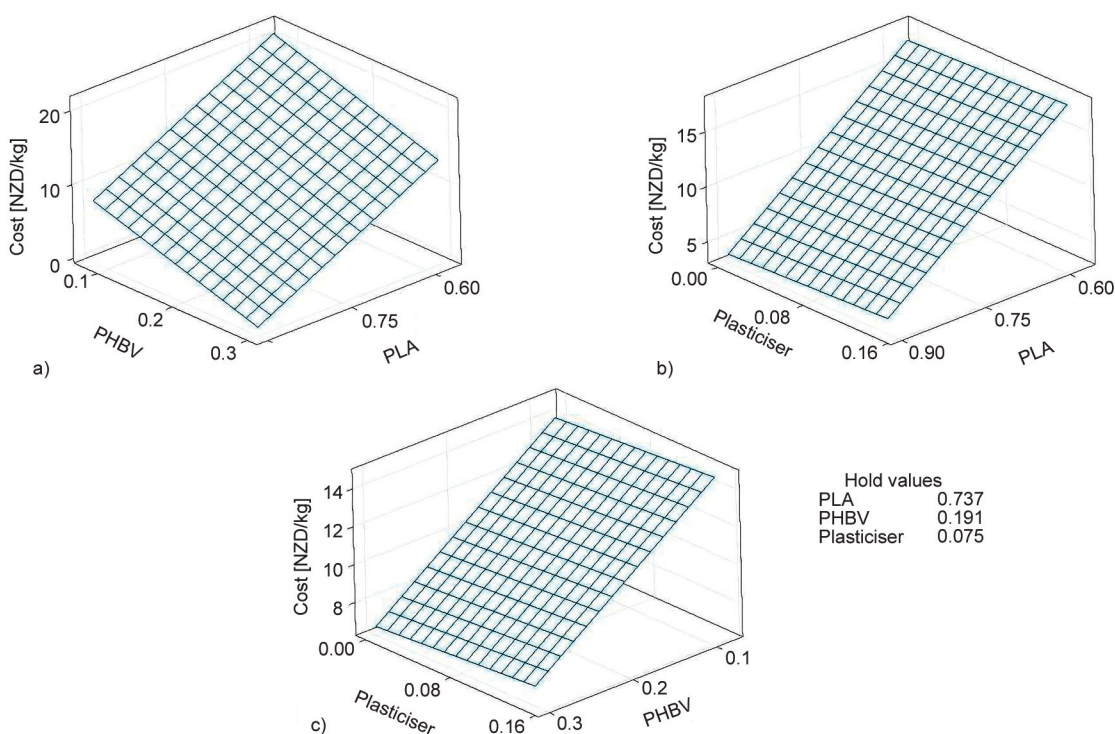


Figure 7. Matrix of surface response plots for the cost [NZD/kg] for a) PHBV-PLA, b) plasticiser-PLA and c) plasticiser-PHBV

collected experimental results were used for sensitivity analysis to find the optimal responses and compound values. The goal, the target, and the lower and the higher values of the mentioned properties are presented in Table 3. The tensile stress values were omitted from the optimisation because the tensile stress results were within the desired range.

Individual desirability was calculated for each response. The optimal values were generated when the maximum composite desirability of 0.363988 was reached. The optimal calculated component content and the predicted responses are presented in Table 4. The results of embedding these values in the response optimisation plot are shown in Figure 8. Red vertical lines represent optimal compositions. One can control how the changes affect the response by adjusting the variable settings.

3.2. Mechanical properties

The yield stress, ultimate tensile stress, and tensile stress at break follow almost a similar trend from one sample to another, which is quite different from the strain at break. These two results were separated into different figures, as presented in Figure 9 and Figure 10. The deepest dive in the tensile properties among samples happen as proceeding consecutively from sample 1 to sample 3. The PHBV content among these three samples is identical, and the PLA content is nearly identical. Hence the decrease in stress is attributed to the increase of the plasticiser content from samples 1 to 3. However, from samples 2 to 3, the plasticiser content is constant. Hence it could be concluded that in sample 3 the ESA content act as a plasticiser. This could also indicate that sample 3 could contain excess ESA that has not reacted with

Table 3. Optimisation parameters.

	Goal	Lower	Target	Upper	Weight	Importance
Elongation at break [%]	Maximum	100	500	500	1	1
Cost [NZD/kg]	Minimum	10	10	15	1	1
η_e at γ_a	Maximum	1400	3660	3660	1	1

Table 4. Predicted optimal component compositions for a targeted response setting.

Component	Percentage	Predicted response	Value	Desirability
PLA	57.40	Elongation at break [%]	206.83	0.267076
PHBV	30.00	Cost [NZD/kg]	13.67	0.266246
Plasticiser	11.36	η_e at γ_a	2932.68	0.678175

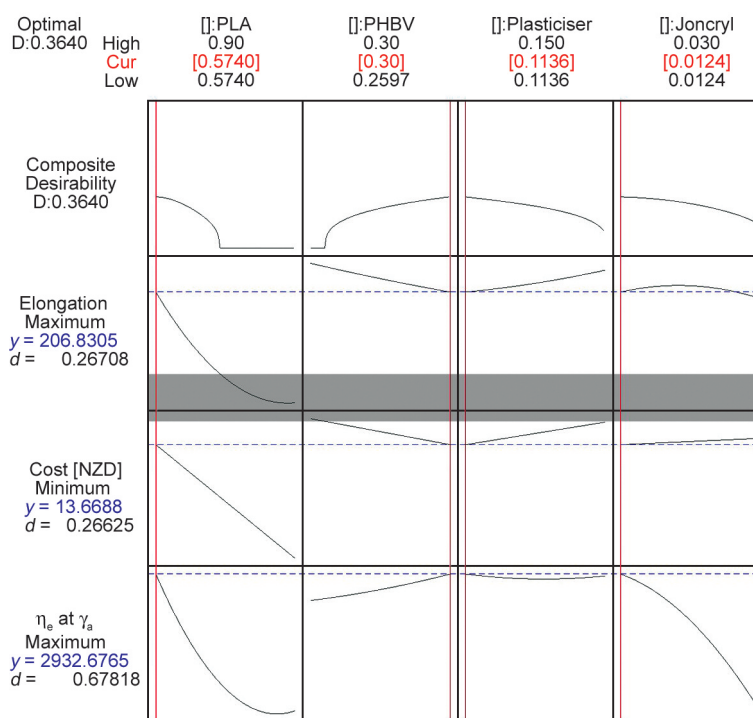


Figure 8. Response optimisation plot.

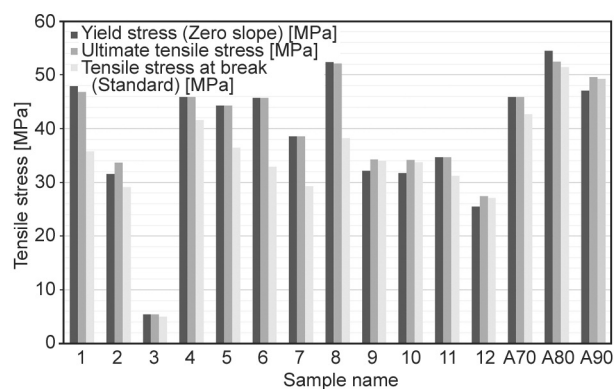


Figure 9. Tensile stress, yield, and ultimate tensile stress of the filament-like extruded samples.

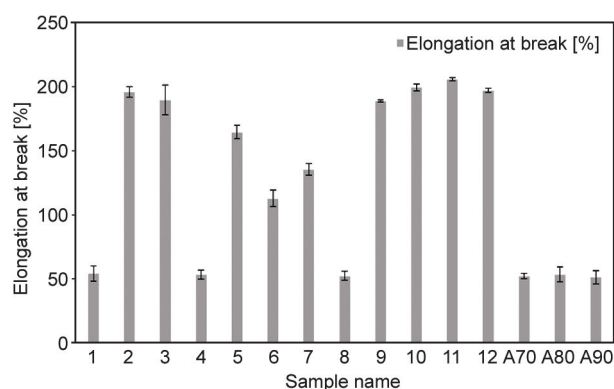


Figure 10. Elongation at break of the filament-like extruded samples.

the terminal hydroxyl and carboxylic acid groups in PLA and PHBV polymer chains. Samples 2 and 3 both have significantly higher percent elongation at breaks, corroborating the plasticising effect of TC and ESA.

From sample 4, the tensile stress properties are back to a 40 to 50 MPa range again, and then it declines as proceeds to sample 7. It is understandable that in sample 4, the lack of ESA [36] and the lower TC contents [11] leads to a more brittle blend, possessing a percent elongation at break of only 50% with high tensile stress properties among all samples. It is also interesting to see that sample 4 and sample 1 can withhold almost the same ultimate tensile stress (about 46 MPa) while containing completely different component proportions. This could be of interest in a practical application where cost optimisation is necessary. Sample 5, similar to sample 4 in polymer and plasticiser composition, has only the addition of ESA content. As discussed earlier, the excess (or unreacted) ESA content can act as a plasticiser in the blend, increasing the ductility while reducing the tensile stress of the compound relative to the sample 4 values.

Samples 6 and 7 possess equal contents of PLA and PHBV and varying contents of TC and ESA. In these two compounds, the PLA content is higher than samples 4 and 5 by around 20 to 25%, projecting a slightly different synergistic effect on their tensile properties. As a result, samples 6 and 7 have lower tensile stress than 4 and 5. Another characterisation of the blend that could be identified from the results can be seen in the contrasting results of samples 7 and 3. In sample 3, the tensile stress, ultimate tensile stress, and yield stress all have nearly the same value, whereas, in sample 7, the tensile stress sits about 25% lower on the stress axes than ultimate tensile and yield

stress. This is indicative that sample 3, under axial stress, does not enter plastic deformation; hence the material experiences a continuous elastic stretch from the onset until the breaking point. However, samples 7 (as well as 4, 5, 6, and 8) experience plastic deformation, presenting different values of yield stress and tensile stress at break.

Sample 8 shows similar results to sample 4. They both have some of the highest tensile properties and low (about 50%) strain at break among all. These two samples have equal plasticiser and chain extenders and varying polymer contents. The higher PLA content explains the higher yield stress in sample 8. It also becomes apparent that sample 4 experiences a shorter elastic deformation than sample 8. There is not much compositional difference between sample 9 and sample 10. These compositions were mathematically generated to take account of all plausible interactive effects incurred by variation of composition content. Sample 9 has only 1% more PHBV content (less plasticiser content) in its composition. This slight material difference manifests its effect in a 10% increase in elongation at the break of sample 10.

zilar condition in comparison, except here, with the presence of an ESA chain extender. Sample 12 possessed 4% less PHBV content and was replaced by plasticiser. As a result, sample 12 have about 10 MPa lower tensile stress, ultimate, and yield stress than sample 10 and 9% lower strain at break. It could also be concluded that sample 12 experienced a lower plastic deformation than sample 11.

Samples A90, A80, and A70, contain no plasticiser nor chain extender and a PLA/PHBV ratio of 90/10, 80/20, and 70/30, respectively. The first noticeable result from these compositions is the higher values of tensile stress (in the 45 to 55 MPa region) and low elongation at break (in the 50% region) among all

samples. The strain at break remains almost the same as proceeding consecutively from A70 to A90. This indicates that if no additives are used, the incorporation of even up to 30% PHBV content in a blend with PLA cannot reduce the rigidity of the blend and increase its ductility. The tensile strength properties show a nonlinear relationship between PHBV content and tensile strength; hence a synergistic effect is identified. The synergistic effect is manifested in sample A80 as it possesses a higher stress value than A70 and A90.

3.3. Thermal properties

The melting temperature of pristine PLA and PHBV used in the sample compositions were separately measured to be 150.2 and 175.1 °C, respectively. The lower melting temperature values of PLA explain the lower T_m values of samples 1, 2, 3, 6, and 7, as these samples contain the largest contents of PLA. This applies to sample A90 as well. The rest of the samples have a T_m in a narrow range of 165 to 172 °C, indicating the trivial effect of TC and ESA on the melting behaviour of the compounds.

As can be seen in Figure 11, a range of enthalpy-of-fusion values is obtained for the samples, indicating that a different crystalline structure is formed for each mixture composition. PLA has a slow crystallisation rate [37]. Therefore, when a sample containing PLA content goes through the manufacturing process and then cools down to environment temperature, its PLA content holds a lower ΔH_{fus} than the PLA material before the process. This is because the lactide polymers need a longer time to arrange and form crystal lamellae [38].

In this test, the thermal properties were calculated from the second heating cycle of the DSC thermographs. Therefore, PLA polymer contents had a

narrow window to fully crystallise. The lower degrees of crystallinity and slow crystallisation rate results in the formation of shorter crystal structures in processed PLA compared to processed PHBV. This incurs lower enthalpy of fusion values. Therefore, this could be associated with the lower ΔH_{fus} values of samples 1, 7, 8, and A90 due to their high PLA contents. This trend is followed by samples 2, 6, and A80 for having proportionally higher PLA contents. It can also be deduced that the presence of a chain extender can result in the formation of new and larger crystal structures. This can be seen in comparing the enthalpy of fusion in sample 3 with samples 9 and 10. Sample 3 contains 16% higher PLA contents; hence it is expected to present lower ΔH_{fus} values than samples 9 and 10. But on the contrary, it has a higher value. This could be associated with the ESA content that is absent in samples 9 and 10 and present in sample 3. ESA is a multifunctional component that can react with the terminal carboxylic acid and hydroxyl groups in polyesters [39]. This extends the polymer chains, which increases the polymer's molecular mass. The molecular mass increase ensues under different conditions in molecular arrangement conditions when the polymer is being cooled. Therefore, a larger crystal structure could be formed.

All the glass transition temperatures (T_g) and the onset of crystallisation temperatures (T_c) in Figure 11 are indicative of PLA because PHBV has a T_g and T_c in the range of -10 to 20 °C [40], and these two polymers are immiscible. T_g and T_c have almost the same value in samples A70, A80, and A90. These samples contain only polymers and no additives. Compared with the rest of the samples, this means the addition of plasticiser and chain extender has a higher effect on changing the glass transition and crystallisation temperature of PLA. Samples 2, 3, 9, 10, 11, and 12

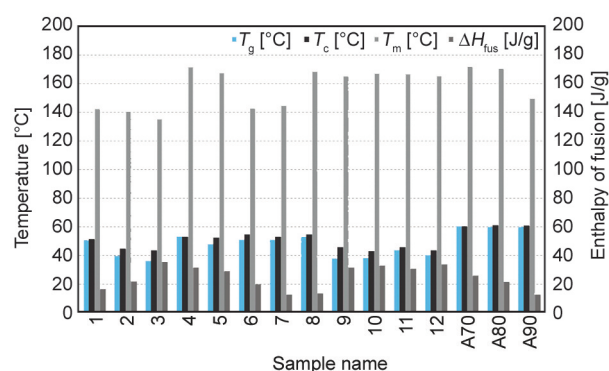


Figure 11. Thermal properties of the rod-like extruded samples obtained by differential scanning calorimetry.

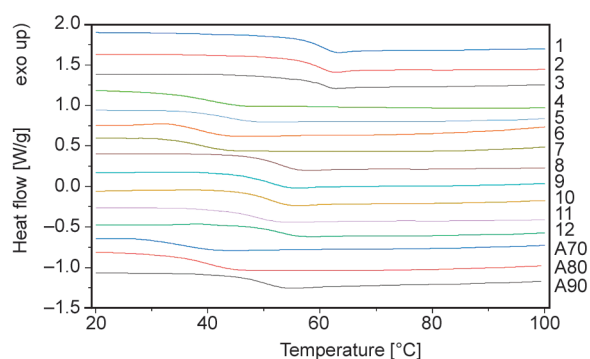


Figure 12. Thermograms of all samples from the second heating cycle obtained from DSC test.

specifically have the lowest T_g and T_c among all samples due to the highest plasticiser contents. Figure 12 shows the behaviour of thermograms near the glass transition region of each sample in their second heating cycle.

3.4. Rheology studies

Figure 13 depicts the rheology graphs obtained from the different blends. A non-Newtonian behaviour is observed for all samples; in other words, shear viscosity decreases with the increase of the shear rate. To further investigate the results, first, the pristine blends were assessed to identify whether the increase of PHBV content directly relates to the decrease of shear viscosity. As seen in Figure 13, it cannot be concluded that the increase of PHBV leads to a lower shear viscosity at any given shear rate value because the shear viscosity values of the A70 blend stand between the A80 and A90. The polymer chains typically stretch out in the machine direction during the processing stage due to the existing shear stress in the barrel and slide on one another. At this stage, the molecular structure and presence of additives or other blend components affect the chain mobility, hence affecting the shear viscosity of the blend. This synergistic effect has been reported by other researchers working with different grades of PLA and PHBV.

The synergistic rheological interaction between PLA and PHBV in a pristine blend (only at the PLA/PHBV ratio of 90/10, 80/20, and 70/30) is once more pronounced in Figure 14. This time it can be seen that with the increase in extensional strain rate, the A70 blend shows higher extensional viscosity values, specifically when the strain rate is in the $3.11 \cdot 10^7$ to $5.00 \cdot 10^8 \text{ s}^{-1}$ range. This means that at identical processing conditions, the A70 blend at the given strain

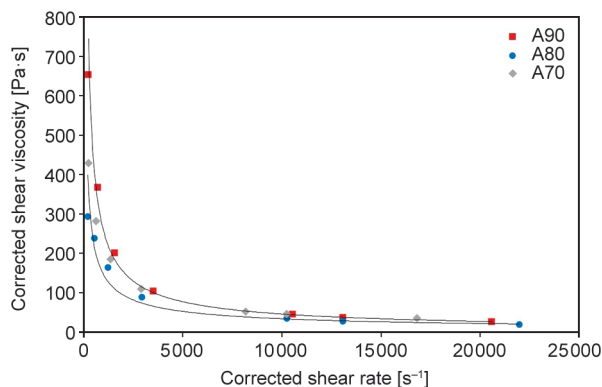


Figure 13. Comparison of shear thinning behaviour of pristine PLA/PHBV blends with a PLA to PHBV ratio of 90/10, 80/20, and 70/30.

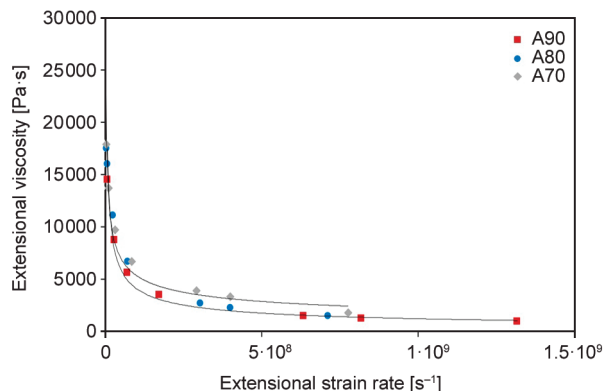


Figure 14. The extensional viscosity vs. extensional strain rate graph of pristine PLA/PHBV blends with a PLA to PHBV ratio of 90/10, 80/20, and 70/30.

rate could provide a more stable bubble as extensional viscosity directly affect bubble stability in the blown film extrusion process. Generally, the higher the extensional viscosity, the more stable the bubble. However, for every polymer, extensional viscosity needs to reach a point from which the bubble could be formed (if the polymer is capable of being blown), and this value changes with the change in strain rate. If a blend's extensional viscosity is below the bubble formation viscosity, the bubble stability would not be a concern.

One reason batches 2, 3, 10, and 12 were chosen to be blown to films was their highest values of extensional viscosities among all manufactured blends. Figure 15 provides a better understanding of the change in shear viscosity with the increase in shear rate. It can be seen that sample 3, followed closely by sample 12, presents the highest extensional viscosities among the blends along the shear rate axes. Sample 12 also offers the highest extensional viscosity at any given extensional strain rate (Figure 16). This was expected because both of these samples

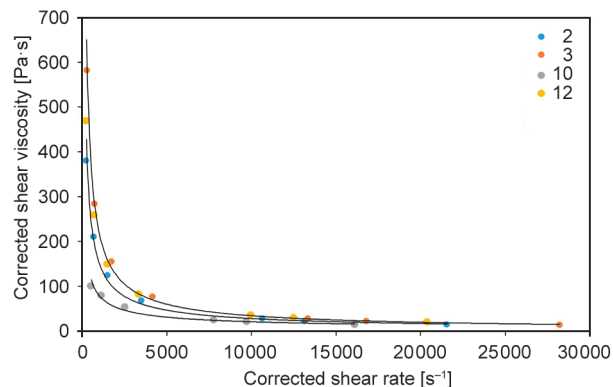


Figure 15. Comparison of the shear thinning behaviour of the chosen blends made into blown films.

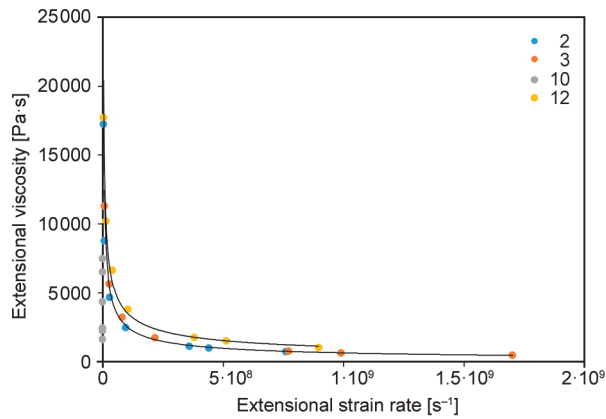


Figure 16. The extensional viscosity vs. extensional strain rate graph of the chosen blends that were made into blown film.

contained an ESA chain extender, contrary to the other two samples. The primary application of using chain extenders is to increase the melt viscosity in polymer blends. This, as explained earlier, is achieved by the reaction of the chain extender with the terminal $-OH$ functional groups in PLA and PHBV polyesters, extending the chain length and hence restricting the molecular mobility of the polymers. Samples 3 and 12 have equal percent contents of ESA (chain extender) and TC (plasticiser), but sample 3 has lower PLA content. It can be concluded that in the manufacturing of blown films, in processing conditions, when the strain rate is below $1.0 \cdot 10^9 \text{ s}^{-1}$, the blend with the lower PLA content could offer better bubble stability where the chain extender and plasticiser are equal proportions.

Batch 10 brings about some complexity to Figure 16. The only difference between batches 10 and 12 is ESA content. One can conclude that the lack of a chain extender in sample 10 results in plummeting extensional viscosity at very early values of strain rates. This is visible as the η_e values of sample 10 stack up on the $\eta_e = 0$. This is, of course, not the case, but it appears this way when the extensional strain rate is logarithmically plotted. This rheological behaviour could also mean that the increase of extensional viscosity is more dependent on the chain extender content (in this case, the presence and lack thereof of ESA) than the PLA content. This is deduced from the direct comparison of sample 2 and sample 10. PHBV polymer, due to having high degrees of crystallinity, has a low extensional viscosity at any given strain rate. Literature also shows that PHBV could not be blown into the film when not blended with another polymer with higher extensional viscosity and melt stress values. This means that PHBV percent content in a polymer blend acts as a bottleneck in the blown film extrusion process, given that other blend constituents have extensional viscosity and melt stress values higher than the point the bubble forms (depending on the processing temperature and screw speed).

To have a clear view of how the shear thinning behaviour of all mixture formulations compares with one another, a summary of the elongational viscosity vs. apparent shear rate of all samples is presented in Figure 17.

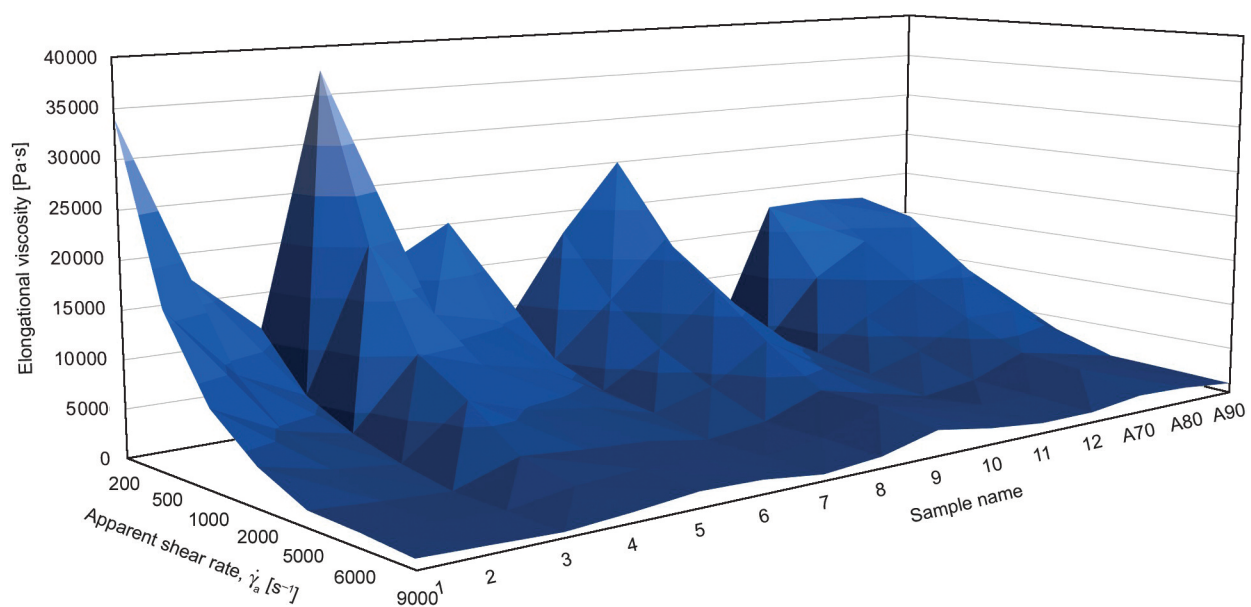


Figure 17. Summary of the differences in shear thinning behaviour of all blends compared with one another.

4. Conclusions

PLA and TC contents have the highest, and ESA content has the lowest total effectiveness in the blends. ESA content shows a nonlinear and interactive effect in responses as its linear content increase leads to the sudden rise and fall of crystallisation temperature, elongation at break, and tensile stress. The optimal values for the lowest cost and highest extension at break and the elongational viscosity were reached at PLA/PHBV/plasticiser/chain extender content of 0.574/0.3/0.113/0.012 wt%. The sample with the highest PLA content possessed the highest tensile stress. Also, the unreacted ESA content can act as a plasticiser in the blend, increasing the ductility and reducing the tensile strength of the compound. Finally, it cannot be simply concluded from rheology studies that the increase of PHBV leads to a lower shear viscosity at any given shear rate because the shear viscosity values of the A70 blend stood between the A80 and A90. This substantiates the synergistic effect of the PLA/PHBV blend in this range.

Acknowledgements

The authors warmly acknowledge the financial support of Callaghan Innovation in New Zealand during the course of this research.

References

- [1] Dusselier M., van Wouwe P., Dewaele A., Jacobs P. A., Sels B. F.: Shape-selective zeolite catalysis for bioplastics production. *Science*, **349**, 78–80 (2015).
<https://doi.org/10.1126/science.aaa7169>
- [2] Penczek S., Szymanski R., Duda A., Baran J.: Living polymerization of cyclic esters—A route to (bio) degradable polymers. Influence of chain transfer to polymer on livingness. in ‘Macromolecular symposia. Vol. 201, 261–270 (2003).
<https://doi.org/10.1002/masy.200351129>
- [3] Yu Y., Storti G., Morbidelli M.: Ring-opening polymerization of L,L-lactide: Kinetic and modeling study. *Macromolecules*, **42**, 8187–8197 (2009).
<https://doi.org/10.1021/ma901359x>
- [4] Li Z., Yang J., Loh X. J.: Polyhydroxyalkanoates: Opening doors for a sustainable future. *NPG Asia Materials*, **8**, e265 (2016).
<https://doi.org/10.1038/am.2016.48>
- [5] García-Campo M. J., Boronat T., Quiles-Carrillo L., Balart R., Montanes N.: Manufacturing and characterization of toughened poly(lactic acid) (PLA) formulations by ternary blends with biopolyesters. *Polymers*, **10**, 3 (2017).
<https://doi.org/10.3390/polym10010003>
- [6] Mendhulkar V. D., Shetye L. A.: Synthesis of biodegradable polymer polyhydroxyalkanoate (PHA) in cyanobacteria *Synechococcus elongates* under mixotrophic nitrogen- and phosphate-mediated stress conditions. *Industrial Biotechnology*, **13**, 85–93 (2017).
<https://doi.org/10.1089/ind.2016.0021>
- [7] Koller M., Salerno A., Tuffner P., Koinigg M., Böchzelt H., Schober S., Pieber S., Schnitzer H., Mittelbach M., BrauneGG G.: Characteristics and potential of microalgal cultivation strategies: A review. *Journal of Cleaner Production*, **37**, 377–388 (2012).
<https://doi.org/10.1016/j.jclepro.2012.07.044>
- [8] Singh A. K., Sharma L., Mallick N., Mala J.: Progress and challenges in producing polyhydroxyalkanoate biopolymers from cyanobacteria. *Journal of Applied Phycology*, **29**, 1213–1232 (2017).
<https://doi.org/10.1007/s10811-016-1006-1>
- [9] Siracusa V., Rocculi P., Romani S., Dalla Rosa M.: Biodegradable polymers for food packaging: A review. *Trends in Food Science Technology*, **19**, 634–643 (2008).
<https://doi.org/10.1016/j.tifs.2008.07.003>
- [10] Fabra M. J., Lopez-Rubio A., Lagaron J. M.: Nanostructured interlayers of zein to improve the barrier properties of high barrier polyhydroxyalkanoates and other polyesters. *Journal of Food Engineering*, **127**, 1–9 (2014).
<https://doi.org/10.1016/j.jfoodeng.2013.11.022>
- [11] Crétois R., Follain N., Dargent E., Soulestin J., Bourbigot S., Marais S., Lebrun L.: Microstructure and barrier properties of PHBV/organoclays bionanocomposites. *Journal of Membrane Science*, **467**, 56–66 (2014).
<https://doi.org/10.1016/j.memsci.2014.05.015>
- [12] Jost V., Langowski H-C.: Effect of different plasticisers on the mechanical and barrier properties of extruded cast PHBV films. *European Polymer Journal*, **68**, 302–312 (2015).
<https://doi.org/10.1016/j.eurpolymj.2015.04.012>
- [13] Liu H., Zhang J.: Research progress in toughening modification of poly(lactic acid). *Journal of Polymer Science part B: Polymer Physics*, **49**, 1051–1083 (2011).
<https://doi.org/10.1002/polb.22283>
- [14] Acha B., Marcovich N., Reboredo M.: Lignin in jute fabric–polypropylene composites. *Journal of Applied Polymer Science*, **113**, 1480–1487 (2009).
<https://doi.org/10.1002/app.29999>
- [15] Al-Itry R., Lamnawar K., Maazouz A.: Biopolymer blends based on poly (lactic acid): Shear and elongation rheology/structure/blowing process relationships. *Polymers*, **7**, 939–962 (2015).
<https://doi.org/10.3390/polym7050939>
- [16] Tang W., Wang H., Tang J., Yuan H.: Polyoxymethylene/thermoplastic polyurethane blends compatibilized with multifunctional chain extender. *Journal of Applied Polymer Science*, **127**, 3033–3039 (2013).
<https://doi.org/10.1002/app.37538>

- [17] Chen X-H., Yu P., Kostromin S., Bronnikov S.: Minor-phase particles evolution in a polyethylene/ethylene-propylene copolymer (80/20) blend across mixing: Breakup and coalescence. *Journal of Applied Polymer Science*, **130**, 3421–3431 (2013).
<https://doi.org/10.1002/app.39373>
- [18] Zuev V., Steinhoff B., Bronnikov S., Kothe H., Alig I.: Flow-induced size distribution and anisotropy of the minor phase droplets in a polypropylene/poly(ethylene-octene) copolymer blend: Interplay between break-up and coalescence. *Polymer*, **53**, 755–760 (2012).
<https://doi.org/10.1016/j.polymer.2011.12.046>
- [19] Zuev V. V., Bronnikov S. V.: Statistical analysis of morphology of low density polyethylene/polyamide 6 blends with addition of organoclay and maleic anhydride-grafted polystyrene-*b*-poly(ethylene-*co*-butene-1)-*b*-polystyrene copolymer as compatibilizers. *Journal of Macromolecular Science Part B*, **51**, 1558–1565 (2012).
<https://doi.org/10.1080/00222348.2012.656008>
- [20] Quiles-Carrillo L., Montanes N., Lagaron J. M., Balart R., Torres-Giner S.: *In situ* compatibilization of biopolymer ternary blends by reactive extrusion with low-functionality epoxy-based styrene-acrylic oligomer. *Journal of Polymers and the Environment*, **27**, 84–96 (2019).
<https://doi.org/10.1007/s10924-018-1324-2>
- [21] Gérard T., Budtova T., Podshivalov A., Bronnikov S.: Polylactide/poly(hydroxybutyrate-*co*-hydroxyvalerate) blends: Morphology and mechanical properties. *Express Polymer Letters*, **8**, 609–617 (2014).
<https://doi.org/10.3144/expresspolymlett.2014.64>
- [22] Li L., Huang W., Wang B., Wei W., Gu Q., Chen P.: Properties and structure of polylactide/poly(3-hydroxybutyrate-*co*-3-hydroxyvalerate) (PLA/PHBV) blend fibers. *Polymer*, **68**, 183–194 (2015).
<https://doi.org/10.1016/j.polymer.2015.05.024>
- [23] Ma P., Spoelstra A. B., Schmit P., Lemstra P. J.: Toughening of poly(lactic acid) by poly(β -hydroxybutyrate-*co*- β -hydroxyvalerate) with high β -hydroxyvalerate content. *European Polymer Journal*, **49**, 1523–1531 (2013).
<https://doi.org/10.1016/j.eurpolymj.2013.01.016>
- [24] Zhao H., Cui Z., Sun X., Turg L-S., Peng X.: Morphology and properties of injection molded solid and microcellular polylactic acid/polyhydroxybutyrate-valerate (PLA/PHBV) blends. *Industrial and Engineering Chemistry Research*, **52**, 2569–2581 (2013).
<https://doi.org/10.1021/ie301573y>
- [25] Noda I., Satkowski M. M., Dowrey A. E., Marcott C.: Polymer alloys of Nodax copolymers and poly(lactic acid). *Macromolecular Bioscience*, **4**, 269–275 (2004).
<https://doi.org/10.1002/mabi.200300093>
- [26] Nanda M. R., Misra M., Mohanty A. K.: The effects of process engineering on the performance of PLA and PHBV blends. *Macromolecular Materials and Engineering*, **296**, 719–728 (2011).
<https://doi.org/10.1002/mame.201000417>
- [27] Han L., Han C., Zhang H., Chen S., Dong L.: Morphology and properties of biodegradable and biosourced polylactide blends with poly(3-hydroxybutyrate-*co*-4-hydroxybutyrate). *Polymer Composites*, **33**, 850–859 (2012).
<https://doi.org/10.1002/pc.22213>
- [28] Liu Q., Wu C., Zhang H., Deng B.: Blends of polylactide and poly(3-hydroxybutyrate-*co*-3-hydroxyvalerate) with low content of hydroxyvalerate unit: Morphology, structure, and property. *Journal of Applied Polymer Science*, **132**, 42689 (2015).
<https://doi.org/10.1002/app.42689>
- [29] Hedrick M. M., Wu F., Mohanty A. K., Misra M.: Morphology and performance relationship studies on biodegradable ternary blends of poly(3-hydroxybutyrate-*co*-3-hydroxyvalerate), polylactic acid, and polypropylene carbonate. *RCS Advances*, **10**, 44624–44632 (2020).
<https://doi.org/10.1039/D0RA07485C>
- [30] Gong J., Qiang Z., Ren J.: *In situ* grafting approach for preparing PLA/PHBV degradable blends with improved mechanical properties. *Polymer Bulletin*, **79**, 9543–9562 (2021).
<https://doi.org/10.1007/s00289-021-03958-6>
- [31] Yang M., Hu J., Xiong N., Xu B., Weng Y., Liu Y.: Preparation and properties of PLA/PHBV/PBAT blends 3D printing filament. *Materials Research Express*, **6**, 065401 (2019).
<https://doi.org/10.1088/2053-1591/ab06cf>
- [32] Kanda G. S., Al-Qaradawi I., Luyt A. S.: Morphology and property changes in PLA/PHBV blends as function of blend composition. *Journal of Polymer Research*, **25**, 196 (2018).
<https://doi.org/10.1007/s10965-018-1586-3>
- [33] Huang J-C., Leong K-S.: Shear viscosity, extensional viscosity, and die swell of polypropylene in capillary flow with pressure dependency. *Journal of Applied Polymer Science*, **84**, 1269–1276 (2002).
<https://doi.org/10.1002/app.10466>
- [34] Bagley E.: End corrections in the capillary flow of polyethylene. *Journal of Applied Physics*, **28**, 624–627 (1957).
<https://doi.org/10.1063/1.1722814>
- [35] Cogswell F.: Measuring the extensional rheology of polymer melts. *Transactions of the Society of Rheology*, **16**, 383–403 (1972).
<https://doi.org/10.1122/1.549257>
- [36] Li H., Huneault M. A.: Effect of chain extension on the properties of PLA/TPS blends. *Journal of Applied Polymer Science*, **122**, 134–141 (2011).
<https://doi.org/10.1002/app.33981>

- [37] Müller A., Ávila M., Saenz G., Salazar J.: Crystallization of PLA-based materials. in 'Poly(lactic acid) science and technology: Processing, properties, additives and applications' (eds.: Jiménez A., Peltzer M., Ruseckaite R.) The Royal Society of Chemistry, London, Vol. 12, 66–98 (2015).
<https://doi.org/10.1039/9781782624806-00066>
- [38] Xu S., Li X., Sun C., Ni L., Xu W., Yuan W., Zheng Y., Yu C., Pan P.: Controllable crystallization and lamellar organization in nucleobase-functionalized supramolecular poly(lactic acid)s: Role of poly(lactic acid) stereostructure. *Polymer*, **232**, 124148 (2021).
<https://doi.org/10.1016/j.polymer.2021.124148>
- [39] Coltelli M-B., Bertolini A., Aliotta L., Gigante V., Vannozzi A., Lazzeri A.: Chain extension of poly(lactic acid) (PLA)-based blends and composites containing bran with biobased compounds for controlling their processability and recyclability. *Polymers*, **13**, 3050 (2021).
<https://doi.org/10.3390/polym13183050>
- [40] Mofokeng J. P., Luyt A. S.: Dynamic mechanical properties of PLA/PHBV, PLA/PCL, PHBV/PCL blends and their nanocomposites with TiO₂ as nanofiller. *Thermochimica Acta*, **613**, 41–53 (2015).
<https://doi.org/10.1016/j.tca.2015.05.019>

Research article

Influence of 3D printed structures on energy absorption ability of brittle polymers under dynamic cyclic loading

Mohit Sood¹, Chang-Mou Wu^{*1}

Department of Materials Science and Engineering, National Taiwan University of Science and Technology, 10607 Taipei, Taiwan, R.O.C

Received 25 August 2022; accepted in revised form 10 November 2022

Abstract. Structural change can alter the energy absorption ability of constituent materials. Carbon organic framework (COF)-inspired structures printed with fusion deposition modeling (FDM) using polylactic acid (PLA) and acrylonitrile butadiene styrene (ABS) polymers are used to analyze the structural effect. Structures were characterized for specific energy absorption under static compression. The best structures from the static testing results were further characterized for dynamic compression using sinusoidal displacement to calculate the dynamic elastic recovery (DER), hysteresis work, and $\tan \delta$. Based on the results, the bending-dominated structure absorbed the highest energy, and the surface structure provided the best DER. The structure which failed by the pure collapsing of the layer showed the best specific values. The delamination of printed layers during loading reduced the performance of structures despite of the materials.

Keywords: processing technologies, mechanical properties, material testing, fusion deposition modeling, polymer

1. Introduction

Several manufacturing techniques for instant casting, forging, welding, and forming have been used for decades. However, industries are now shifting their focus toward additive manufacturing (AM) because of its ability to manufacture lightweight and structural designs [1, 2]. Currently, AM has been employed to fabricate numerous engineering components using polymers and metallic materials. Vat photopolymerization, material jetting, material extrusion, sheet lamination [3, 4], direct energy deposition binding jets, and powder bed fusion [5–10] are examples of commercially applied AM processes.

Among the processes, fusion deposition modeling (FDM) is widely used to create three-dimensional (3D)-printed structures using thermoplastic filaments [11]. FDM provides manufacturing with greater autonomy to control mechanical properties [12]. These properties are easy to alter by changing

some parameters, such as the extrusion and printing bed temperature, printing speed [12–15], resolution of the extruded layer, infill density, and pattern [15, 16]. This makes FDM more suitable for fabricating lattice structures. Polylactic acid (PLA) and acrylonitrile butadiene styrene (ABS) are abundantly available commercial polymeric materials [17–21]. These polymers are well known for their high mechanical strength, better printability at a low cost, and biodegradable nature for PLA, which make them suitable candidates for lattice structure fabrication using FDM [22–25].

In recent years, researchers have fabricated traditional structures and analyzed their compression properties. Dalaq *et al.* [26] fabricated a triply periodic minimal surface (TPMS) of the Schwarz structure, diamond rhombic, Schoen, Neovius, and Fischer–Koch types using Tango- and Vero-plus material and evaluated the mechanical properties under uniaxial compression.

*Corresponding author, e-mail: cmwu@mail.ntust.edu.tw
© BME-PT

They concluded that the Schwarz primitive showed the best mechanical properties because of least debonding under static loading [26]. Honeycomb structures using thermoplastic polyurethanes were manufactured by Bates *et al.* [27]. They concluded that the energy absorption ability of these structures depended on the strain rate and cell orientation of the structure under the static compression load. Li *et al.* [28] proposed truss, conventional honeycomb, and re-entrant honeycomb structures and evaluated their bending behavior. Owing to the localized stress concentration in the truss and conventional honeycomb structures, they showed an early catastrophic failure. Hence, the energy absorption and mechanical properties were less than that of the re-entrant structure. Abueidda *et al.* [29] printed Schwarz, Schoen, and Neovius structures with polyamide-12 and evaluated their compressive strength, modulus, and energy absorption with static loading. The Neovius structure provided the highest results because it retained the geometrical structure until the compression ended [29]. Cubic, octet, and Isomax structures were characterized by quasi-static bending and dynamic low-velocity impact. The Isomax with cubic meta sandwich beam provided the highest energy absorption under bending as well as impact [30]. Al-Ketan *et al.* [31] evaluated the mechanical properties of the strut base, skeletal-TPMS, and sheet-TPMS structures under uniaxial static compression, and the high relative density of the sheet-based TPMS structures outperformed that of the other structures. Another report by Abueidda *et al.* [32] evaluated the mechanical properties of the gyroid surface structure under a uniaxial static test and demonstrated that the highest relative density absorbed the highest amount of energy under static compression. Similarly, octet structures composed of PLA were found to absorb more specific energy at a higher relative density under quasi-static compression [33]. Evidently, most studies were performed using static loading compression, and none has yet used dynamic compression yet, particularly not with sinusoidal displacement for the characterization of the proposed structures.

Most studies have focused on traditional TPMS and octet structures, and for these structures, relative density is the most effective criterion for good energy absorption. However, if a greater number of strut arrangements are provided in the loading direction, the energy absorption ability of the structure may also be enhanced. Carbon organic framework (COF)

compounds have some unique two-dimensional and 3D atom arrangements that can be used as inspiration for designing novel structure arrangements because they can provide more struts in the loading direction [34–37]. These COF-inspired structures fabricated using FDM with PLA and ABS have never been reported. The main aim of this study is to fabricate the proposed COF-inspired structures printed with hard materials (PLA and ABS) and characterize the effect of these structure arrangements on the energy absorption ability of the materials under static and dynamic sinusoidal cyclic loading compression.

2. Experimental procedure

2.1. Design of structures

The design concept for the new type of structure was inspired by the COF compounds shown in Figure 1. The major advantage of COF-inspired structures is their ability to change the density of unit cells without changing in diameter, and all inspired structures can provide more struts in the loading direction.

The lattice structures are either strut or surface-based and show stretch or bending domination behaviors [2]. COF compounds have an unpteen type of atomic arrangements that can be used to fabricate both types of structures. The first structure (S1) was drawn from the sp^2 carbon conjugate COF. This compound can provide the stretch domination behavior (Maxwell number (M) = 5) by dividing the load on the two struts. The S2 and S3 structures were adopted from the boronic ester and tetrathiafulvalene COFs. These arrangements were selected because they can provide the bending domination behavior ($M = -6$ for S2 and $M = -12$ for S3). To compare the strut-based structure with surface-typed structures, periodic surface-based structures (SS) were designed by mimicking the zeolitic imidazolate framework (ZIF-8). The SS can provide better foam-like properties. Another reason for the selection of these COF compounds was their printability with the FDM printer. All unit cells of the inspired structures carry loads, as shown in Figure 2.

Solidworks 2019 (SP5, Dassault Systèmes, Vélizy-Villacoublay, France) was used to illustrate the CAD files of the structures. The structures were formed according to the hybrid connection approach as outlined in Figure 3. A unit cell of $10 \times 10 \times 10$ mm was formed in two manners: with an external connector and with self-connection. This approach can control the density of the unit cell without changing the diameters of the struts. The external connector made

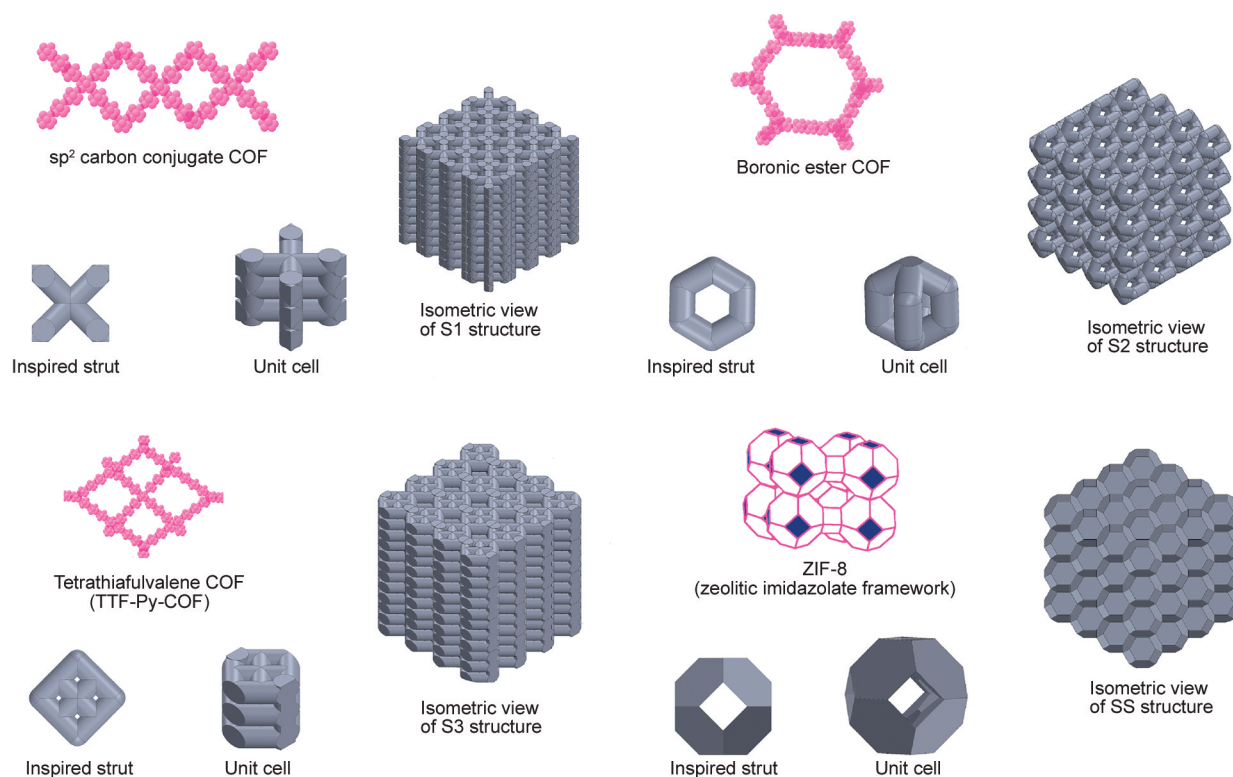


Figure 1. Unit cells inspired by the different carbon organic frameworks, along with final structural arrangements.

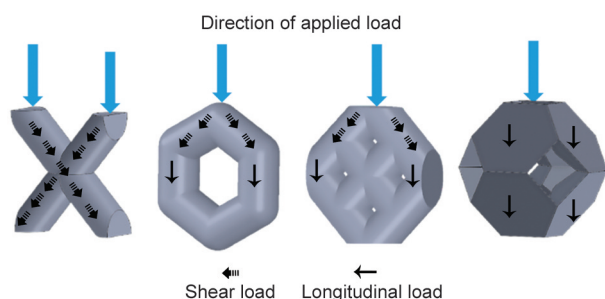


Figure 2. Direction and distribution of the load in the struts and shell-type unit cells under the compression loading.

the unit cell denser, whereas self-connection made the unit cell more porous. Unit cells were repeated in the 3D space to form $40 \times 40 \times 40$ mm [35] structures. All unit cells were connected with the surfaces in the 3D structure. The diameter for the struts was selected to be 3.00 mm, which is the minimum diameter that prints at an acceptable quality. Similarly, the SS was printed with a 3.00 mm shell.

2.2 Manufacturing samples

All printing filament materials: ABS (PA-756, POLYLAC[®], Chimei Corporation, Tainan, Taiwan) and PLA (4032D, IngeoTM, NatureWorks, Minnesota, USA; having D-lactic content of 1.4%), were purchased from XYZ Printing Company, Taipei, Taiwan, with a diameter of 1.75 mm. The CAD drawing of

these samples was saved in STL format and sliced using Ultimaker Cura 4.13 software (Ultimaker B.V., Massachusetts, USA). The G-codes, generated with Cura, were sent to the 3D printer (Ender-3 Max, Creality 3D technology corporation limited, Shenzhen, China) with a nozzle diameter of 0.4 mm. Table 1 lists the optimized printing parameters.

2.3. Morphology of structures

To verify the printing quality and layer adhesion of the manufactured samples, one unit of each type of structure was examined randomly under an optical microscope (SV-55, Sage Vision, Pennsylvania, USA). For further investigation of the quality of fabricated structures, the higher magnification images were captured by a scanning electron microscope (SEM, 6390 LV, JEOL, Tokyo, Japan). As all the samples were non-conductive, hence, before keeping them inside the SEM chamber, the platinum coating was applied by using an automatic spin coater (JFC-1300, JEOL, Tokyo, Japan).

2.4. Energy absorption characterization under static loading

Uniaxial quasi-static compression was performed with a universal testing machine (MTS 810, Capacity 100 kN, MTS Systems Corporation, Minnesota,

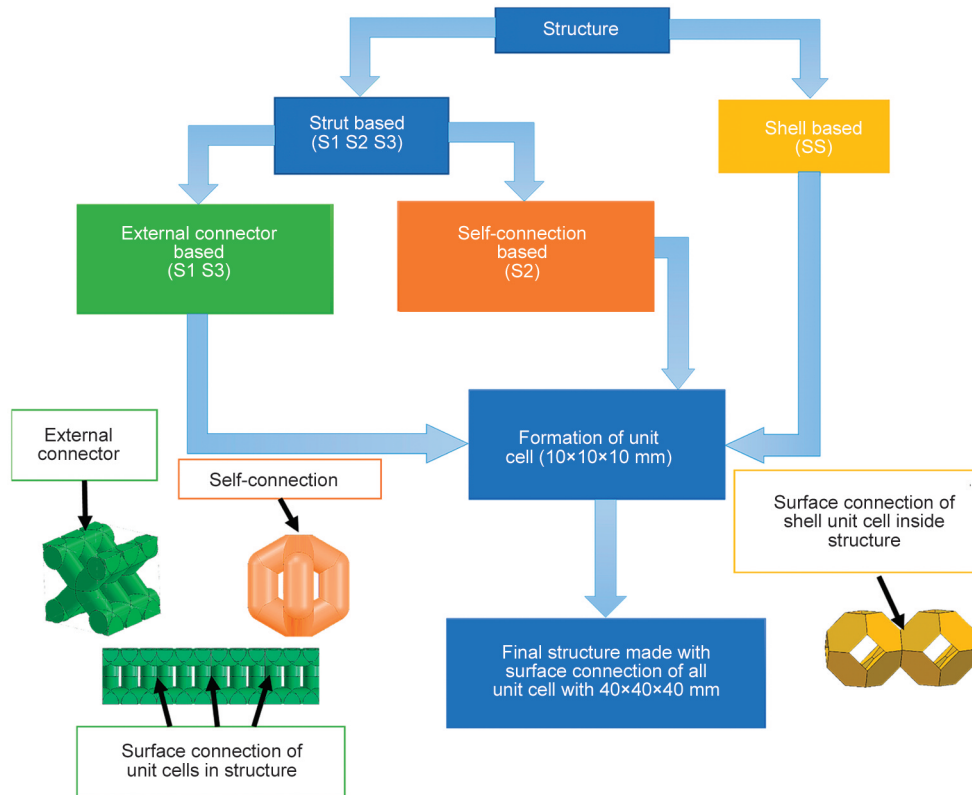


Figure 3. Unit cell assembly approach and final structure dimension.

Table 1. Optimized printing parameters used for manufacturing structures with FDM.

Material	Nozzle temperature [°C]	Printing speed [mm/s]	Heating bed temperature [°C]	Layer height [mm]	Infill density	Infill pattern
ABS	235	20	100	0.2	10%	Cubic
PLA	190	20	45	0.2	10%	Cubic

USA) to obtain the energy absorption capacity. All samples were compressed until failure. Here the meaning of failure is till the structure is delaminated or compressed to half of its depth. Compression plates were polished with oil to avoid samples sticking during compression. The test was conducted according to ASTM D1621 with a steady crossed-head speed of 3 mm/min under room temperature conditions [38]. All samples were compressed in the printing direction. To minimize biasing in the experiment, all structures were fabricated in large quantities, and three units of each structure were randomly tested. The energy absorption was calculated from the area under the load-displacement curve with OriginPro 2021 software (OriginLab Corporation, Northampton, USA). The value of the specific energy absorption (SEA) was calculated according to Equation (1) [39, 40]. Furthermore, the load-displacement data was converted into stress and strain to calculate the modulus. For further comparison purposes, these values were also normalized by relative density ($\bar{\rho}$),

which normalized the effect of materials and structural density. The relative density is defined as the ratio of structural density to the parent material density and is calculated as per Equation (2) [41]. The modulus per unit relative density is called relative modulus. Similarly, initial peak stress and energy absorbed per unit relative density is known as the relative initial peak stress and relative energy absorption, respectively.

$$SEA [J/g] = \int_0^{\delta} \frac{F \cdot d\delta}{w} \quad (1)$$

where w is the mass of the sample in grams, F is the compression force and $d\delta$ is the displacement.

$$Relative\ density, \bar{\rho} = \frac{\rho}{\rho_s} \quad (2)$$

where ρ is the structural density, calculated with the ratio of the mass of the structure to the volume of the structure and ρ_s is the density of the parent material. The density of ABS and PLA was taken at 1.05 and

Table 2. Mass, volume, and relative density of FDM printed structures.

Material	Sample	Mass [g]	Volume [cm ³]	Structure density [g/cm ³]	Relative density, $\bar{\rho}$ [-]
ABS	S1	24.9	35.7	0.70	0.66
	S2	16.2	21.4	0.75	0.72
	S3	28.9	41.5	0.69	0.66
	SS	19.0	24.2	0.78	0.74
PLA	S1	29.0	35.7	0.81	0.66
	S2	19.0	21.4	0.89	0.72
	S3	33.6	41.5	0.81	0.66
	SS	22.6	24.2	0.93	0.75

1.24 g/cm³, respectively, from the literature [22]. Table 2 provides the mass of each sample, the material volume of the structures (calculated with Solidworks 2019), and structural and relative densities.

2.5. Dynamic compression

Because the structures were brittle and hard, sustaining the structures for repeated cycles was difficult. Hence, to perform the repeated compression, the cyclic displacement was required to be below the first peak point in the load-displacement curve during static testing. Moreover, during static testing, the displacement value of the first peak was considered to decide the range of the dynamic displacement. The displacement was given in the form of a sinusoidal wave using the same machine used for static compression. The range of the sinusoidal displacement

was from 30 to 50% of the displacement value of the first peak for each load-displacement curve of a static test. The range was selected after many trial experiments to prevent the plate and sample from detaching during the cycle. The cyclic test was performed only on samples that provided higher energy absorption in the static test. Ten cycles were applied, and the 10th cycle was considered for further calculations. The sin wave displacement was generated at three different frequencies, and all structures were tested at frequencies of 0.1 Hz (low), 1.0 Hz (base), and 4.0 Hz (high). The dynamic elastic recovery (DER) ratio of the area under the unloading curve to the loading curve was calculated for each 10th cycle along with the hysteresis work (the area enclosed by the cyclic curve).

3. Results and discussion

3.1. Surface integrity of the 3D-printed structure

To determine the integrity of the extruded layers, all samples were enlarged under an optical microscope. As observed in Figure 4, all layers were well connected and aligned. This shows that the quality of the 3D-printed structures was appropriate for compression testing. None of the samples demonstrated any visible type of void under extrusion, void cracking, or printing misalignment. For further verification, the samples were magnified under SEM. As can be seen from the SEM images, the extruded layers are

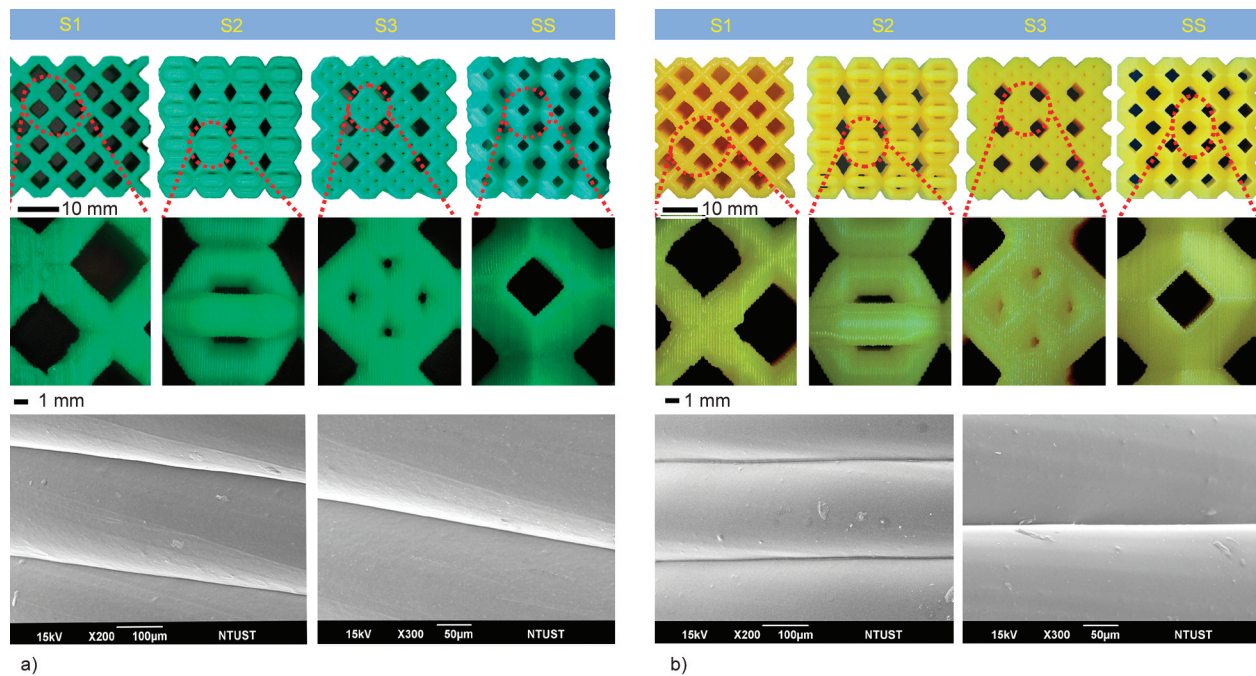


Figure 4. Layer integrity and quality of the extruded layers under high magnification SEM a) ABS, b) PLA.

firmly fused together at the interface without any delamination. At 200× magnification, the structure looks similar to an image captured by a light microscope. Further magnified to 300 times, the interface between the layers is still well bonded, and there are no microcracks and microvoids on the surface of the layer. This indicates that the print quality is fully up to standard and the sample is well-qualified for further testing. However, the interlayer adhesion strength of the samples needs to be tested under a universal testing machine.

3.2. Specific energy absorption under static loading

All structures exhibited different SEAs and initial peak values in load-displacement curves despite being composed of the same materials. Figure 5 depicts the load displacement of the S1 structures. Both material structures provided similar fluctuating curves

regardless of the material. The PLA structure absorbed 4.71 J/g energy, whereas the ABS structure absorbed 1.99 J/g. The SEA for the PLA structure was 58% more than that of the ABS structure. The S1 structures (ABS and PLA) exhibited dominating stretching. Both structures experienced a cross-shear failure until the first curve, but this failure was more severely pronounced in the ABS structure owing to the delamination of the layers. The first peak for the PLA structure was higher than that of ABS because, until the first peak in the PLA structure, only some cracks were evident, in contrast, with ABS, the delamination had already started. After the first peak, the PLA structure showed cross-shear failure, which caused the large drop in the curve. However, subsequently, the structural part below the shear line exhibited resistance to the subsequent load. Therefore, the structure could sustain and carry the additional load. Owing to this, the PLA structure showed the second peak.

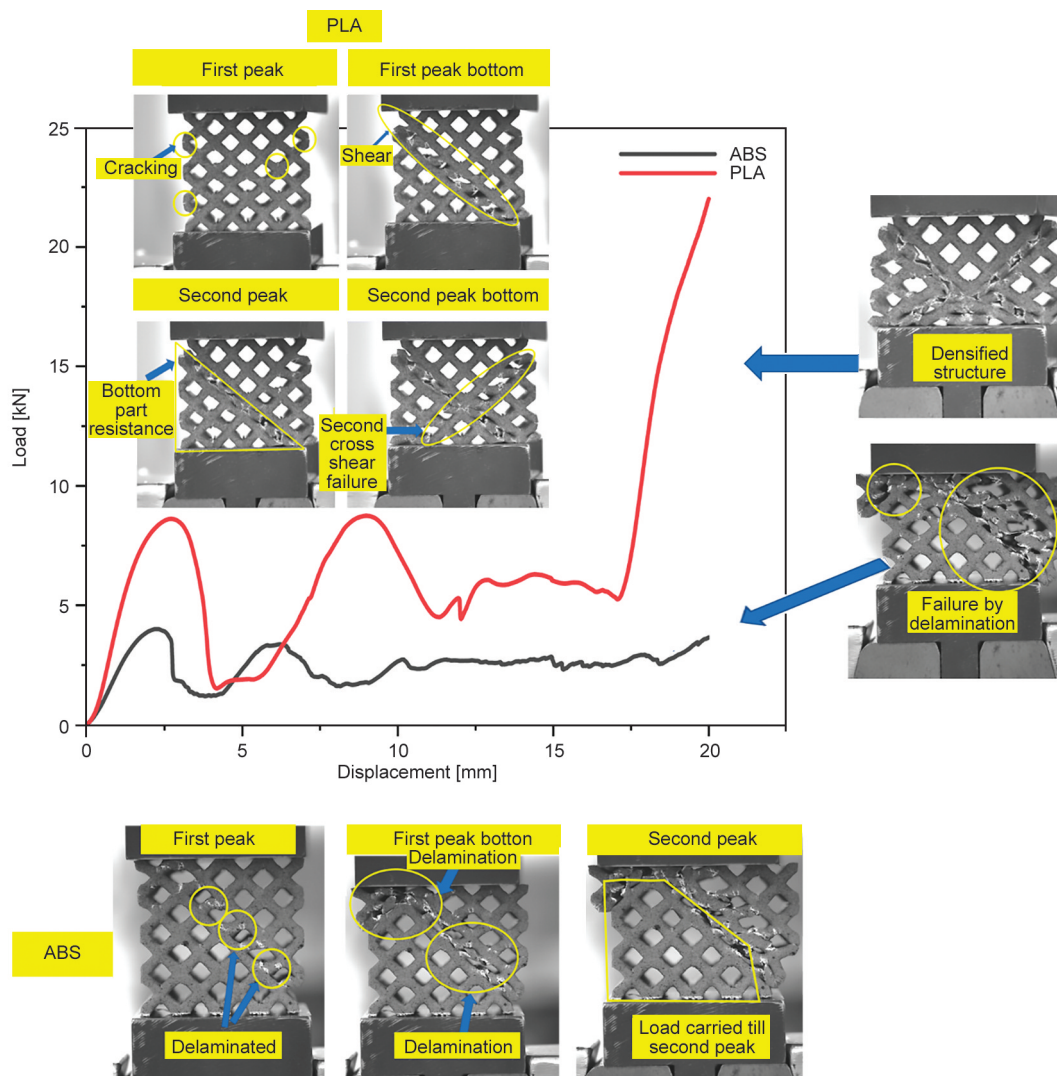


Figure 5. Load-displacement curve of S1 structure for ABS and PLA materials along with failure images at the different stages of static displacement.

After the second peak, one more cross-shear failure occurred, causing the second peak drop. After this point, the structure had already failed, but the debris of the structure carried the additional load from the bottom of the second peak and fully densified until the end.

For the ABS structure, after the first peak, the curve drop was a straight line because of the fatal delamination. Subsequently, the remaining structure was able to carry the load, thereby showing the second peak, but the structure failed with delamination. After the second drop in the peak, the next curve was caused by the debris of the structure. The delamination of the printed layer was the primary reason for the poor performance of the S1 structure with ABS.

A similar tendency was observed for the S2 structure, as shown by Figure 6, where the PLA structure had an of 6.87 J/g, which was 78% higher than that of the ABS structure, which was 1.51 J/g. However, the structures showed no fluctuations in the curve after the first peak. The ABS structure had broken from the bottom side until the first peak, whereas the PLA structure showed only some cracking, which caused a higher first-peak value for the PLA structure than that of the ABS structures. After the first peak, the

ABS structure was fully delaminated and could barely sustain until the 20 mm displacement owing to a complete debonding of the printed layer, whereas the PLA structure demonstrated a layer collapse.

For the S3 structures, as shown in Figure 7, regardless of the materials, both structures (ABS and PLA) showed the highest SEAs with 15.16 and 10.07 J/g for PLA and ABS, respectively. However, PLA still absorbed 34% more specific energy than the structures composed of ABS. These structures carried the load with a bending domination behavior in both materials. From the failure images, cracking and delamination started in the ABS structures until the first peak, whereas the PLA structure exhibited no signs of delamination. As the displacement progressed, the cracks formed in more areas in the ABS structure, whereas PLA deformed with collapsing layers. At the 20 mm displacement, the ABS structure showed a delamination failure, whereas the PLA structure failed by only a layer collapse. Here, layer debonding was also the cause of less energy absorbed by the ABS-printed structures.

Similarly, for the SS structures, the energy absorption was 6.29 and 3.16 J/g for the PLA and ABS structures, respectively. The SEA for PLA was still

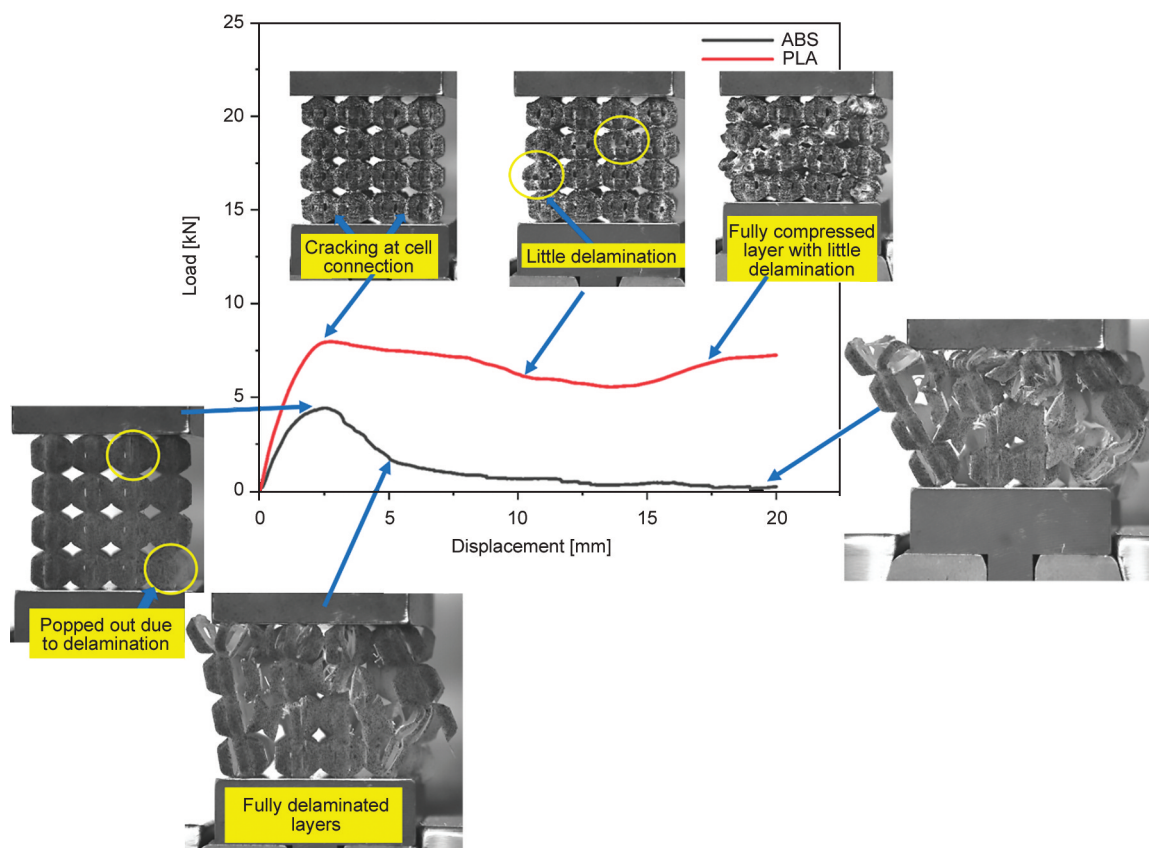


Figure 6. The load-displacement curve of S2 structure for ABS and PLA materials, along with failure images at the different stages of static displacement.

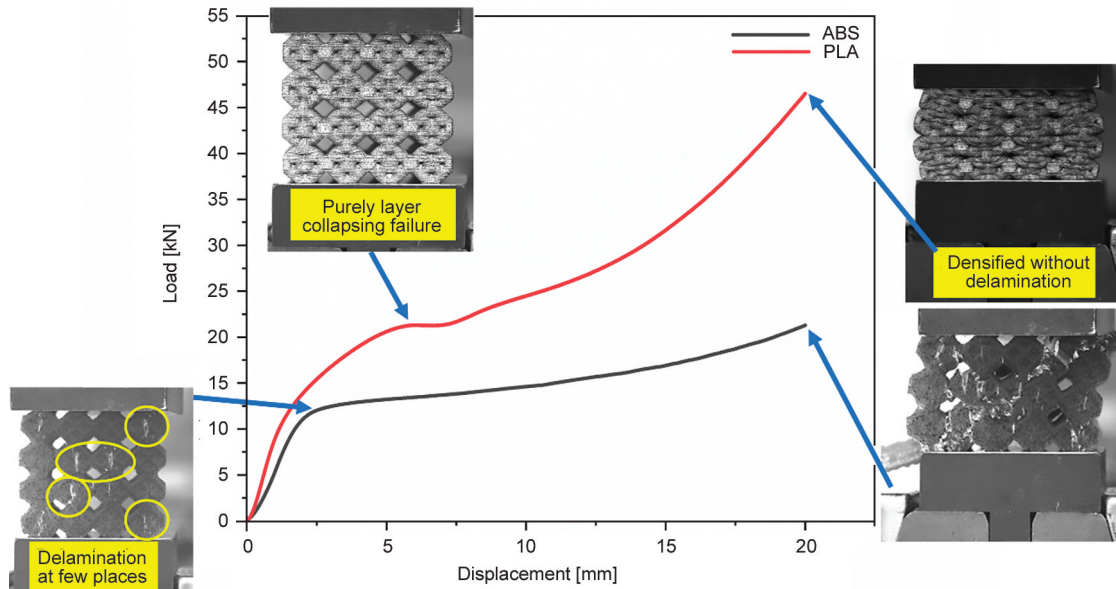


Figure 7. Load-displacement curve of S3 structure for ABS and PLA materials along with failure images at the different stages of static displacement.

50% higher than that of ABS. As shown in [Figure 8](#), the structural effect provided the bending domination behavior. From the failure images until the first peak, the PLA structure failed because the bottom layers collapsed, but ABS had already delaminated severely. The PLA structure showed mostly layer-collapsing failures with small cracks. Hence, it was able to absorb more energy. In this case, the ABS structure demonstrated poor energy absorption because of the delamination. A small fluctuation was observed at the end of the ABS curve caused by the instability of the delaminated structure during compression.

To analyze the unit load required for unit displacement, the specific elastic constant of all structures was calculated from their respective load-displacement diagrams, as shown in [Figure 9](#). The S3 structure had the highest specific elastic constant among all the PLA structures, followed by the S2 and SS structures, regardless of the material, and the S1 structure had the lowest specific elastic constant for both materials. Comparing the materials, the PLA structure had higher specific elastic constant values than those of the ABS structures. The poor interlayer adhesion for the ABS structure led to lower specific

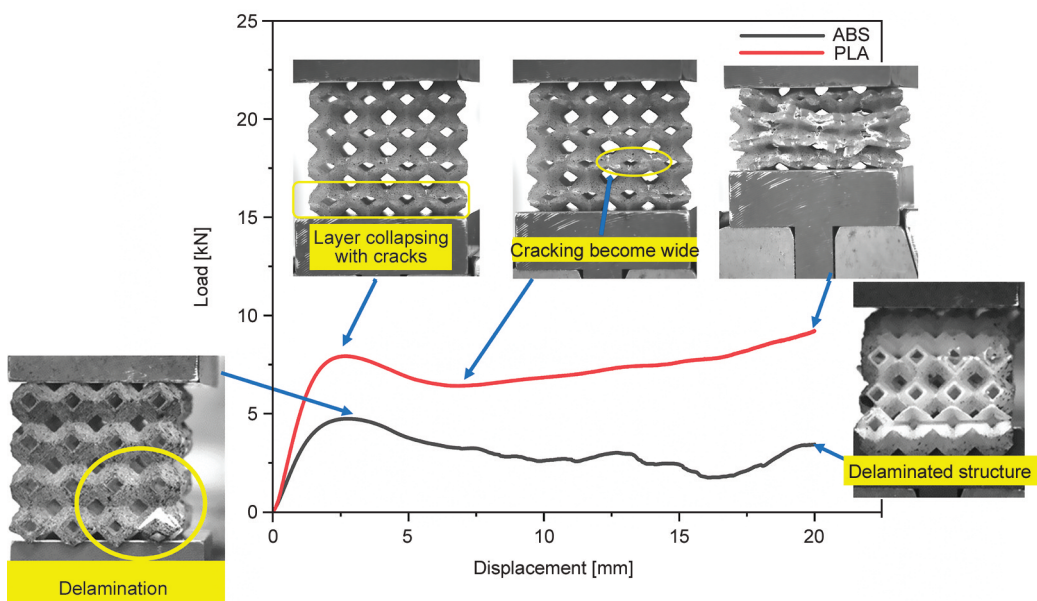


Figure 8. The load-displacement curve of SS structure for ABS and PLA materials, along with failure images at the different stages of static displacement.

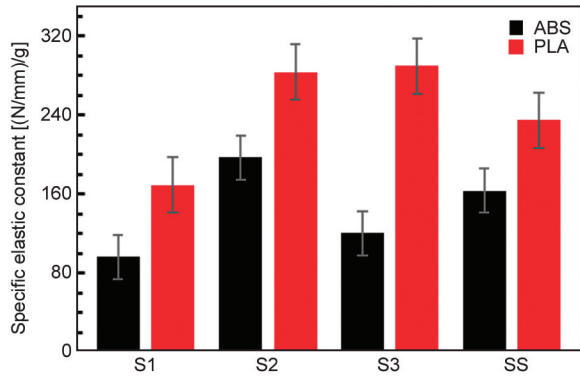


Figure 9. Specific elastic constant under static load calculated from the load-displacement diagrams.

elastic constant values. As the S3 structure with PLA had the highest specific elastic constant, it required the highest amount of force to deform and could absorb more compression energy than the other structures. For the PLA structures, the energy absorption tendency agreed with the specific elastic constant value, but the early delamination for the ABS structures caused a deviation of the stiffness tendency from the energy absorption values.

The structural effect on the materials was also confirmed by the specific modulus and specific initial peak stress, as shown in Figure 10. Table 3 lists the specific values of the respective structures. The structures showed different specific moduli and specific initial peak stresses. From this, a single material could provide several specific modulus and initial peak stress values depending on its structural arrangement. The failure mode of the structures would be the critical criterion for structural performance. The S3 structure with PLA had the highest SEA and

Table 3. Specific modulus and specific initial peak stress under static loading.

Structures	Specific modulus [MPa/g]		Specific initial peak stress [MPa/g]	
	ABS	PLA	ABS	PLA
S1	1.45±0.06	1.53±0.70	0.10±0.01	0.19±0.02
S2	5.10±0.21	6.89±0.62	0.17±0.02	0.26±0.03
S3	3.14±0.03	5.26±0.99	0.27±0.03	0.40±0.06
SS	3.48±0.08	3.47±0.54	0.16±0.01	0.22±0.02

specific initial peak stress. Because the failure was purely dominated by layers collapsing for PLA, the same structure with ABS showed lower energy absorption and modulus values because of delamination. The S2 structure had the highest modulus for the PLA structure, but later little delamination in the structure caused lower energy absorption than S3 in the later stage. The S1 structure showed the lowest specific modulus for both material structures because of the diagonal shear failure.

For further comparisons, all values were normalized with the relative density of the respective structures. Table 4 lists the relative modulus, relative initial peak stress, and relative energy absorption. All structures with ABS showed lower values when compared with the structures with PLA. Structure S3 with PLA absorbed the highest relative energy and showed the highest relative modulus and the highest relative initial peak stress. All other structures S1, S2 and SS provided lower values when compared with the S3 structure of PLA. The cause of the higher performance of the S3 structure with PLA was also described on the base of failure mode, which was a complete layer-wise collapsing failure. All other

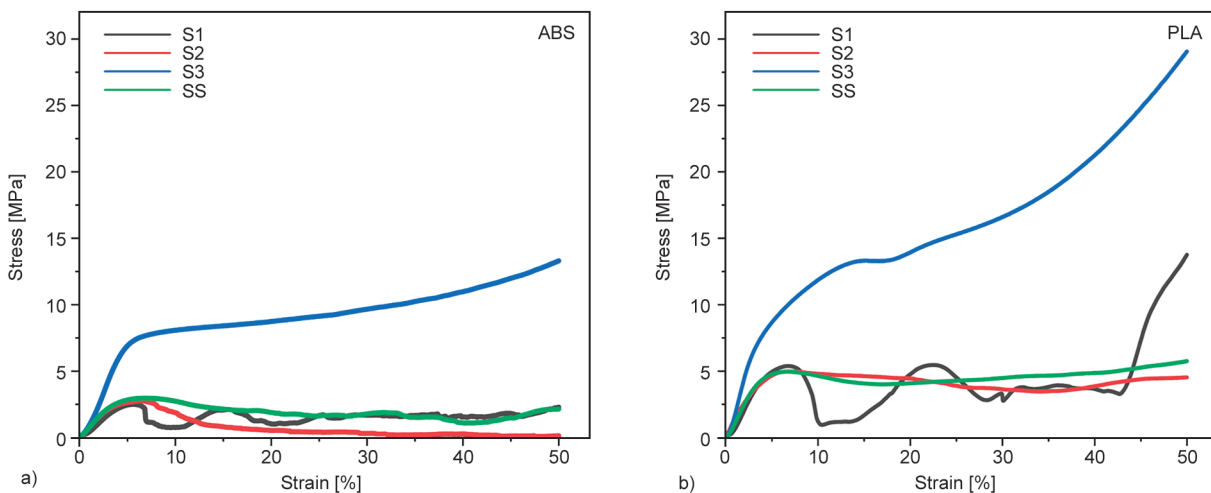


Figure 10. Stress-strain curves of the structures under the static loading. a) ABS, b) PLA.

Table 4. Relative modulus, relative initial peak stress, and relative energy absorption of structures under static loading.

Structures	Relative modulus [MPa]		Relative initial peak stress [MPa]		Relative energy absorption [J]	
	ABS	PLA	ABS	PLA	ABS	PLA
S1	54.70±2.22	67.14±0.55	3.81±0.03	8.17±0.29	74.98±4.08	206.67±2.50
S2	114.84±3.35	181.76 ±0.58	3.85±0.05	6.92±0.04	33.73±0.66	180.81±0.39
S3	137.50±1.18	267.84±0.63	11.60±0.14	20.13±0.05	440.40±2.02	772.35±0.06
SS	88.08±2.55	104.38±0.06	4.01±0.02	6.61±0.06	79.89±0.38	192.25±0.25

structures, showed little delamination in the case of PLA structures and severe delamination was observed with ABS structures.

Overall, from [Figures 5 to 8](#), the load-displacement curve for the ABS structures was lower in all cases. The root cause of the poor performance of the ABS structures was the delamination of the printed layers under compression. The dominant failure mode for ABS structures was cracking, followed by fatal delamination, which was less pronounced in PLA structures. The S3 structures with PLA absorbed the highest energy because the mode failed purely from collapsing layers. Hence, for a good 3D printed structure, better interlayer adhesion is highly necessary. In a general case, ABS is stiffer than PLA, but the structural effect reversed the nature of the materials. All structures absorbed different amounts of energy and showed different elastic moduli and initial peak stresses, regardless of the material, which indicates that a material can have a wide energy absorption capacity range under compression loading that can be altered by changing the structural arrangement. That is, the structure and its integrity can determine the mechanical energy absorption capacity of the constituent materials. For ABS, FDM fails to achieve good layer adhesion, which can be attributed to the rapid consolidation reducing the interfacial layer adhesion ability. However, it is not as pronounced as in the case of crystalline PLA.

3.3. Energy absorption by structures under dynamic displacement

The PLA structure outperformed ABS structures because of better inter-layer adhesion. Hence, only PLA structures were selected for dynamic cyclic compression. [Figure 11](#) shows the 10th load displacement cycles of each structure at the base frequency (1.0 Hz). The other cycles had similar enclosure shapes; hence, for the other two frequencies, only the DER and hysteresis work are reported in [Table 5](#) for the 10th cycle.

As presented in [Table 5](#), PLA showed different DER values for all frequencies, because of the structural effect. Hence, the DER of the materials could be determined by structural arrangement. Here, the structures were first tested at the base frequency of 1.0 Hz. At this frequency, the S3 structure showed the lowest DER, whereas the SS structure provided the highest DER of 96.12%. The S1 and S2 structures had DERs of 92.31 and 95.63%, respectively. DER generally indicates the amount of recovery that occurs after cyclic loading. A higher dynamic recovery means a higher energy-releasing ability, and vice-versa. The S3 structure stored the highest hysteresis work, which indicates that this structure had a higher ability for storing energy than that for release. Moreover, the SS structure was able to release energy better than all other structures and could store only 0.08 J of hysteresis work. By comparing the SS and S2 structures, the difference in DER was 0.50%, and the hysteresis works were the same.

When testing at the low frequency (0.1 Hz), all structures followed the same tendency as with the base frequency in terms of DER and stored hysteresis work. The lowest DER and highest hysteresis work were provided by the S3 structure. The SS structure had the best DER of approximately 96.52% with the lowest hysteresis work of 0.07 J. The S2 and S1 structures had DERs of 94.48 and 93.31% with hysteresis works of 0.09 and 0.17 J. At this frequency, the S3 structures had similar behaviors as those observed at the base frequency. Comparing all structures at 1.0 and 0.1 Hz, all structures demonstrated similar DERs, hence, the frequency change did not significantly affect the DER or the hysteresis work at a larger scale to differ with a small range.

On testing all structures at the high frequency (4.0 Hz), the S3 structure showed the lowest DER again, along with the highest hysteresis work at 1.48 J. The SS structures had a DER of 97.13%, which was the highest among all structures. The S2 and S1 structures had the second and third best

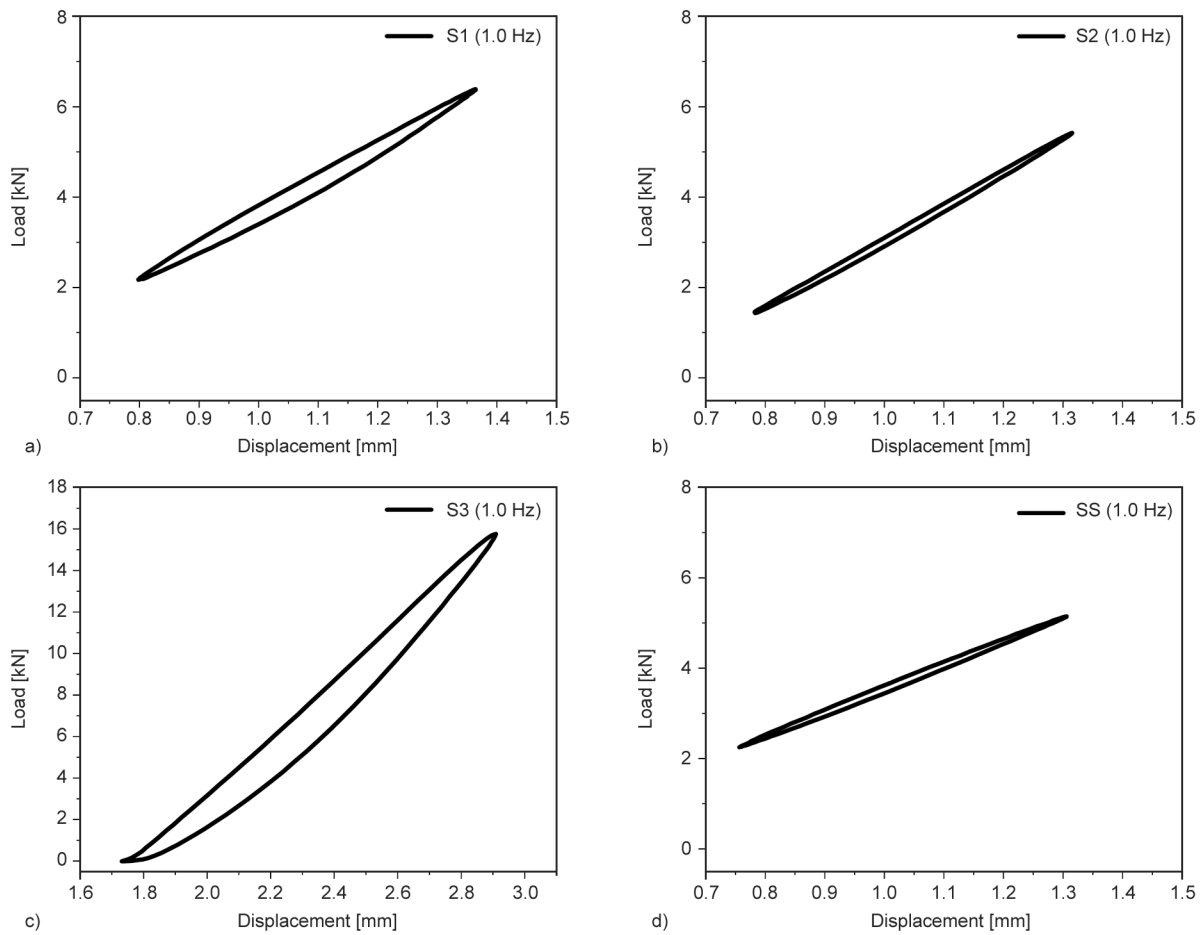


Figure 11. 10th load displacement cycle of each structure under dynamic loading at the base frequency (1.0 Hz). a) S1, b) S2, c) S3, d) SS.

Table 5. DER and hysteresis work of PLA structures under dynamic loading.

Structures	Frequency 0.1 Hz		Frequency 1.0 Hz		Frequency 4.0 Hz	
	DER [%]	Hysteresis work [J]	DER [%]	Hysteresis work [J]	DER [%]	Hysteresis work [J]
S1	93.31	0.17	92.31	0.19	93.46	0.20
S2	94.48	0.09	95.63	0.08	96.81	0.08
S3	80.45	1.14	79.62	1.91	85.94	1.48
SS	96.52	0.07	96.12	0.08	97.13	0.07

DERs of 96.81 and 93.46%, respectively. At this frequency, the DER of all structures was the highest compared with the DER responses at 0.1 and 1.0 Hz. At all frequencies, the S3 structure had the lowest DER but the highest hysteresis work absorbed. The cause of the high value of hysteresis work absorption could be explained based on the free volume of the structures. The S3 structure consisted of the most material, thereby having the lowest free volume. The struts were close to each other, which provided better support for the applied loading. Less free space for the movement of struts in S3 enabled it to sustain a high loading but made its elastic recovery poor. Similarly, the S1 structure had the second heaviest

structure and more free volume than the S3 structure. Owing to the higher free volume, the structure could recover more because of a better release of energy; hence, less hysteresis work was observed than with S3. The S2 structure had the lowest amount of material among the strut-type structures. The additional free volume in the S2 structure provided more movement space for the structures while loading. Because of the additional free space, the struts in the S2 structure were able to recover better for all frequencies. The S2 was the best in terms of DER among the strut-type structures. The SS structure had shell unit cells. The space for movement inside shell is more, which means more

free space for the movement of shells. The free volume of the SS structure enabled them to reach the highest DER with the lowest hysteresis work absorption. For a structure, the free volume is a significant factor in determining the DER and hysteresis work absorption at all frequencies. Here, the S3 structure is recommended for better energy absorption applications. The SS structure is recommended for applications requiring a quicker recovery under dynamic loading conditions. The S3 and SS structures had large DER and hysteresis work differences but a small difference was observed in the DER and hysteresis work when these structures were individually compared at different frequencies. Hence, the DER and hysteresis work was more pronounced with the structural change rather than the frequency change.

3.4. Effect of frequency on the structural damping ability

The damping ability of the structures was calculated from the lag (δ) between the dynamic load and displacement curves, as shown in Figure 12. The tangent of the lag ($\tan \delta$) indicates the damping ability of the structures. Table 6 provides the average $\tan \delta$ of the 10 cycles and the $\tan \delta$ of the strut-structures

Table 6. Average $\tan \delta$ of 10 cycles at different frequencies (0.1, 1.0, 4.0 Hz).

Structures	$\tan \delta \cdot 10^{-2}$		
	0.1 Hz	1.0 Hz	4.0 Hz
S1	2.13	2.43	3.82
S2	2.05	2.99	3.82
S3	3.36	3.61	3.82
SS	1.93	2.43	1.05

(S1, S2, S3) and SSs. For strut-based structures, as the frequency was increased from 0.1 to 4.0 Hz, the $\tan \delta$ increased for the S1, S2, and S3 structures. The S3 structure had the highest $\tan \delta$, indicating that this structure had a more viscous nature and provided the lowest DER because it could dissipate the energy as hysteresis work. The SSs had the lowest $\tan \delta$, which shows that these structures had a more elastic nature and highest DER.

By comparing the frequency effect, based on the viscoelastic nature of materials [42], materials become brittle at high frequencies and viscous at low frequencies. However, owing to the structural effect, strut-based structures (S1, S2, and S3) showed a more viscous nature at a high frequency. This indicates that the nature of the material could be changed

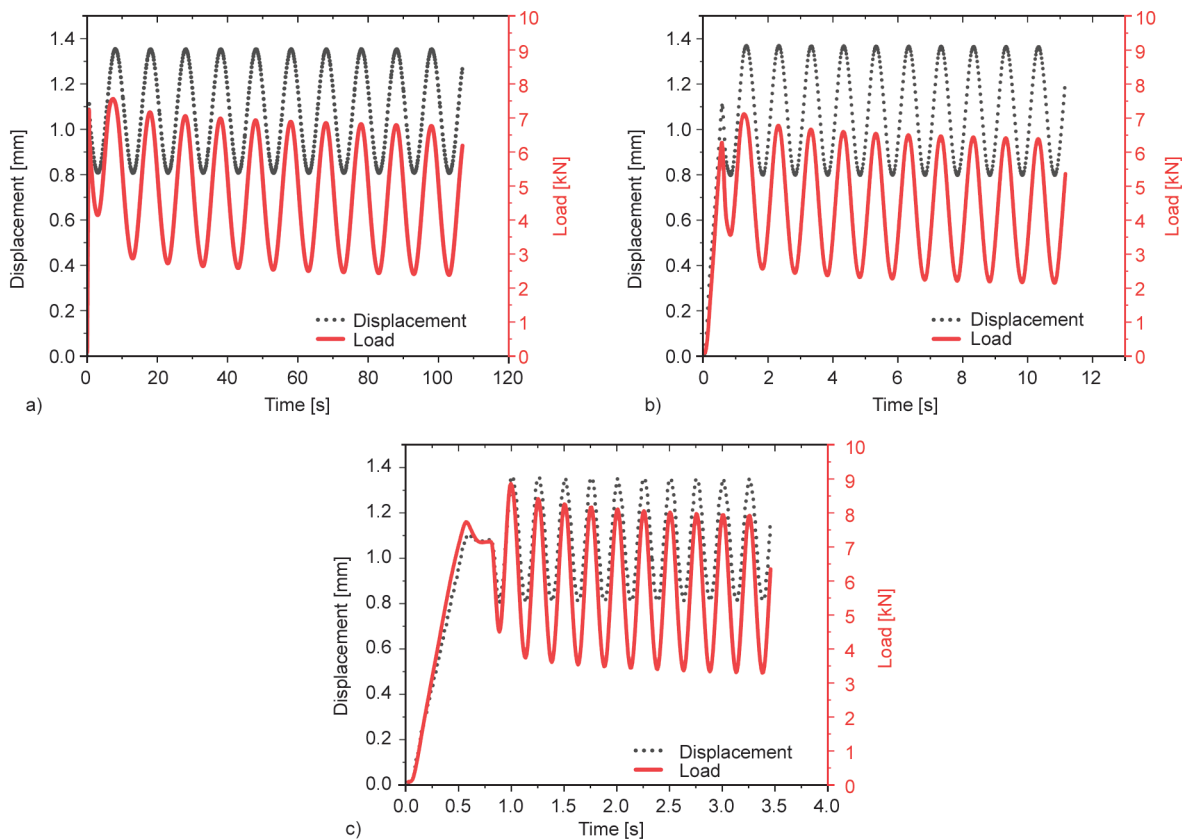


Figure 12. Load-time-displacement diagrams for S1 structures under dynamic loading at a) 0.1 Hz, b) 1.0 Hz, and c) 4.0 Hz.

Table 7. Percentage improvement in energy absorption of S3 (ABS and PLA) structures compared with previously reported FDM fabricated structures.

Structure	Material	Energy absorbed [J/g]	Improvement [%]	References
Honeycomb	ABS	5.43	46	[22]
Hexagonal re-entrant		2.82	72	[41]
Tet oct vertex centroid		2.63	74	[45]
Body center cube-V		0.49	95	[46]
Biomorphic cellular		1.50	85	[47]
Modified octet	PLA	4.50	70	[43]
Bi-graded honeycomb		13.62	10	[48]
Hexagonal prism		10.50	30	[49]
Kelvin foams		11.90	21	[50]
Neovius surface		10.42	31	[51]

by changing the material arrangement in the structures. The structural effect can also be justified by the ability to transmit vibration out of the system. The high $\tan \delta$ indicates a higher damping property. The many interconnected struts composing the structures helped transmit the vibration out of the structures. At the lower frequency, the struts moved slowly; thus, less vibration was transmitted out of the structures and caused less vibration isolation. Therefore, a low $\tan \delta$ was obtained at the high frequency because the fast movement of the struts made the structures transmit more vibration out. The surfaces of the SSs could not provide as much movement as the struts, obtaining a low $\tan \delta$ at the higher frequency. All structures composed of struts could be applied at the higher frequency vibration damping, but the SS structure composed of the surface is better suited for lower frequency vibrational damping applications.

3.5. Comparison of failure mode and energy absorption results

For the S3 structure, PLA absorbed the highest amount of energy because of the full layer collapsing failure. The upper and lower layers started deforming, and this deformation traveled toward the center layer without delamination and ended with densification of the structure without layer debonding during the entire compression period. A comparison of the S3 failure mode with the octet structures with PLA studied by [43] showed that the collapsing deformation of the unstable layer caused the post-yield fluctuation behavior. Hence, the energy absorption was approximately 87% less than that of the S3 structure with PLA. This shows that stability in layer collapsing is essential for structure deformation. Another study reported a re-entrant circular auxetic

honeycomb structure [44] from PLA material, demonstrating non-uniform cross X-like failure during compression. Moreover, owing to this type of failure, the oscillation formed into a stress-strain curve, and the highest SEA was reported at only 2.2 J/g, which is far less than that of the S3 structure. Similarly, another study [35] with a hexagonal open cell structure composed of PLA showed that the best stress-strain curve was obtained with a structure with a layer collapsing failure. These results agree with the cause of the highest energy absorption observed for the S3 structure. The cross failure by the S1 structure for both materials is undesirable, and this also agrees with the deformation behavior explained by [44]. Other structures, S2 and SS, showed minimal delamination with PLA and were severely delaminated with the ABS material which caused the poor SEA results for ABS. This result agrees with [26], which stated that the structure with little debonding had the highest mechanical properties. Comprehensively, the layer collapsing mode with a stable manner is the best deformation mode for 3D-printed structures, whereas debonding always reduces the performance of these types of structures.

To analyze the improvement of the purposed structure, the result of the energy absorption of bending-dominated S3 structures was compared with the results published in the literature, as listed in Table 7 for ABS and PLA.

4. Conclusions

- The structural effect changed the energy absorption of the materials (PLA and ABS). A material can absorb different amounts of energy under compression, which can be determined by structural arrangements.

- For FDM-manufactured structures, interlayer adhesion plays the main role in energy absorption under compression. ABS could not provide better layer adhesion; hence, delamination caused it to absorb less energy than the PLA structures.
- The results show that the energy absorbed by the S3 structure of PLA is the highest, which is 15.16 J/g, the specific strength of the first peak is the highest, which is 0.40 MPa/g, and relative modulus is the highest, which is 267.84 MPa.
- The free volume of the structures resulted in a quick recovery after dynamic loading.
- Under dynamic compression, changes in frequency were less effective for the DER, but the structural change effect was more pronounced on the DER and hysteresis work.
- The SS structure has the best dynamic elastic recovery of 97.13% at 4.0 Hz, while S3 shows the best hysteretic work at 1.91 J.
- All strut-based structures demonstrated a viscous nature at a high frequency, whereas a more elastic nature was observed in the SSs.
- The bending-dominated (S3) structures are recommended for civil engineering applications, such as in load bearing, SS has the highest DER; hence, they can be used for applications requiring quick recovery after loading.

Acknowledgements

This work is partially supported by the Ministry of Science and Technology of Taiwan, R.O.C. under grant numbers MOST 110-2622-E-011-023.

References

- [1] Liu G., Zhang X., Chen X., He Y., Cheng L., Huo M., Yin J., Hao F., Chen S., Wang P., Yi S., Wan L., Mao Z., Chen Z., Wang X., Cao Z., Lu J.: Additive manufacturing of structural materials. *Materials Science and Engineering R: Reports*, **145**, 100596 (2021). <https://doi.org/10.1016/j.msler.2020.100596>
- [2] Maonachie T., Leary M., Lozanovski B., Zhang X., Qian M., Faruque O., Brandt M.: SLM lattice structures: Properties, performance, applications and challenges. *Materials and Design*, **183**, 108137 (2019). <https://doi.org/10.1016/j.matdes.2019.108137>
- [3] Tyagi S., Yadav A., Deshmukh S.: Review on mechanical characterization of 3D printed parts created using material jetting process. *Materials Today: Proceedings*, **51**, 1012–1016 (2021). <https://doi.org/10.1016/j.matpr.2021.07.073>
- [4] Piedra-Cascón W., Krishnamurthy V. R., Att W., Revilla-León M.: 3D printing parameters, supporting structures, slicing, and post-processing procedures of vat-polymerization additive manufacturing technologies: A narrative review. *Journal of Dentistry*, **109**, 103630 (2021). <https://doi.org/10.1016/j.jdent.2021.103630>
- [5] Gupta A. K., Krishnanand, Taufik M.: The effect of process parameters in material extrusion processes on the part surface quality: A review. *Materials Today: Proceedings*, **50**, 1234–1242 (2021). <https://doi.org/10.1016/j.matpr.2021.08.110>
- [6] Chua C. K., Wong C. H., Yeong W. Y.: Material characterization for additive manufacturing. in ‘Standards, quality control, and measurement sciences in 3D printing and additive manufacturing’ (eds.: Chua C. K., Wong C. H., Yeong W. Y.) Academic Press, London, 95–137 (2017). <https://doi.org/10.1016/B978-0-12-813489-4.00005-2>
- [7] Kumaran M., Senthilkumar V., Justus Panicker C. T., Shishir R.: Investigating the residual stress in additive manufacturing of combined process in powder bed fusion and directed energy deposition. *Materials Today: Proceedings*, **47**, 4387–4390 (2021). <https://doi.org/10.1016/j.matpr.2021.05.200>
- [8] Li M., Huang J., Fang A., Mansoor B., Pei Z., Ma C.: Binder jetting additive manufacturing of copper/diamond composites: An experimental study. *Journal of Manufacturing Processes*, **70**, 205–213 (2021). <https://doi.org/10.1016/j.jmapro.2021.08.041>
- [9] Ullsperger T., Wencke Y. L., Yürekli B., Matthäus G., Rettenmayr M., Luinstra G. A., Nolte S.: Laser powder bed fusion of ultra-high molecular weight polyethylene (UHMWPE) using near-infrared ultrashort laser pulses. *Materials and Design*, **210**, 110048 (2021). <https://doi.org/10.1016/j.matdes.2021.110048>
- [10] Rowat S. J., Legge R. L., Moresoli C.: Plant protein in material extrusion 3D printing: Formation, plasticization, prospects, and challenges. *Journal of Food Engineering*, **308**, 110623 (2021). <https://doi.org/10.1016/j.jfoodeng.2021.110623>
- [11] Hanon M. M., Dobos J., Zsidai L.: The influence of 3D printing process parameters on the mechanical performance of PLA polymer and its correlation with hardness. *Procedia Manufacturing*, **54**, 244–249 (2020). <https://doi.org/10.1016/j.promfg.2021.07.038>
- [12] Wang P., Zou B., Ding S., Li L., Huang C.: Effects of FDM-3D printing parameters on mechanical properties and microstructure of CF/PEEK and GF/PEEK. *Chinese Journal of Aeronautics*, **34**, 236–246 (2021). <https://doi.org/10.1016/j.cja.2020.05.040>
- [13] Chikkangoudar R. N., Sachidananda T. G., Pattar N.: Influence of 3D printing parameters on the dimensional stability of polypropylene/clay printed parts using laser scanning technique. *Materials Today: Proceedings*, **44**, 4118–4123 (2020). <https://doi.org/10.1016/j.matpr.2020.10.456>

- [14] Prabhakar M. M., Saravanan A. K., Lenin A. H., Leno I. J., Mayandi K., Ramalingam P. S.: A short review on 3D printing methods, process parameters and materials. *Materials Today: Proceedings*, **45**, 6108–6114 (2020). <https://doi.org/10.1016/j.matpr.2020.10.225>
- [15] Liu Y., Bai W., Cheng X., Tian J., Wei D., Sun Y., Di P.: Effects of printing layer thickness on mechanical properties of 3D-printed custom trays. *Journal of Prosthetic Dentistry*, **126**, 671.e1–671.e7 (2020). <https://doi.org/10.1016/j.prosdent.2020.08.025>
- [16] Fekete I., Ronkay F., Lendvai L.: Highly toughened blends of poly(lactic acid) (PLA) and natural rubber (NR) for FDM-based 3D printing applications: The effect of composition and infill pattern. *Polymer Testing*, **99**, 107205 (2021). <https://doi.org/10.1016/j.polymertesting.2021.107205>
- [17] Park S., Fu K.: Polymer-based filament feedstock for additive manufacturing. *Composites Science and Technology*, **213**, 108876 (2021). <https://doi.org/10.1016/j.compscitech.2021.108876>
- [18] Elmrbet N., Siegkas P.: Dimensional considerations on the mechanical properties of 3D printed polymer parts. *Polymer Testing*, **90**, 106656 (2020). <https://doi.org/10.1016/j.polymertesting.2020.106656>
- [19] Liu C-H., Chen Y., Yang S-Y.: Quantification of hyperelastic material parameters for a 3D-Printed thermo-plastic elastomer with different infill percentages. *Materials Today Communications*, **26**, 101895 (2021). <https://doi.org/10.1016/j.mtcomm.2020.101895>
- [20] Zhang P., Qi D., Xue R., Liu K., Wu W., Li Y.: Mechanical design and energy absorption performances of rational gradient lattice metamaterials. *Composite Structures*, **277**, 114606 (2021). <https://doi.org/10.1016/j.compstruct.2021.114606>
- [21] Kaur M., Yun T. G., Han S. M., Thomas E. L., Kim W. S.: 3D printed stretching-dominated micro-trusses. *Materials and Design*, **134**, 272–280 (2017). <https://doi.org/10.1016/j.matdes.2017.08.061>
- [22] Joseph A., Mahesh V., Mahesh V.: Effect of loading rates on the in-plane compressive properties of additively manufactured ABS and PLA-based hexagonal honeycomb structures. *Journal of Thermoplastic Composite Materials*, **10**, 1–22 (2021). <https://doi.org/10.1177/08927057211051416>
- [23] Sychov M. M., Lebedev L. A., Dyachenko S. V., Nefedova L. A.: Mechanical properties of energy-absorbing structures with triply periodic minimal surface topology. *Acta Astronautica*, **150**, 81–84 (2018). <https://doi.org/10.1016/j.actaastro.2017.12.034>
- [24] Gautam R., Idapalapati S., Feih S.: Printing and characterisation of Kagome lattice structures by fused deposition modelling. *Materials and Design*, **137**, 266–275 (2018). <https://doi.org/10.1016/j.matdes.2017.10.022>
- [25] Ye G., Bi H., Li Z., Hu Y.: Compression performances and failure modes of 3D printed pyramidal lattice truss composite structures. *Composites Communications*, **24**, 100615 (2021). <https://doi.org/10.1016/j.coco.2020.100615>
- [26] Dalaq A. S., Abueidda D. W., Abu Al-Rub R. K.: Mechanical properties of 3D printed interpenetrating phase composites with novel architected 3D solid-sheet reinforcements. *Composites Part A: Applied Science and Manufacturing*, **84**, 266–280 (2016). <https://doi.org/10.1016/j.compositesa.2016.02.009>
- [27] Bates S. R. G., Farrow I. R., Trask R. S.: 3D printed polyurethane honeycombs for repeated tailored energy absorption. *Materials and Design*, **112**, 172–183 (2016). <https://doi.org/10.1016/j.matdes.2016.08.062>
- [28] Li T., Wang L.: Bending behavior of sandwich composite structures with tunable 3D-printed core materials. *Composite Structures*, **175**, 46–57 (2017). <https://doi.org/10.1016/j.compstruct.2017.05.001>
- [29] Abueidda D. W., Bakir M., Abu Al-Rub R. K., Bergström J. S., Sobh N. A., Jasiuk I.: Mechanical properties of 3D printed polymeric cellular materials with triply periodic minimal surface architectures. *Materials and Design*, **122**, 255–267 (2017). <https://doi.org/10.1016/j.matdes.2017.03.018>
- [30] Yazdani S. H., Akbarzadeh A. H., Mirbolghasemi A., Hermenean K.: 3D printed meta-sandwich structures: Failure mechanism, energy absorption and multi-hit capability. *Materials and Design*, **160**, 179–193 (2018). <https://doi.org/10.1016/j.matdes.2018.08.061>
- [31] Al-Ketan O., Rowshan R., Abu Al-Rub R. K.: Topology-mechanical property relationship of 3D printed strut, skeletal, and sheet based periodic metallic cellular materials. *Additive Manufacturing*, **19**, 167–183 (2018). <https://doi.org/10.1016/j.addma.2017.12.006>
- [32] Abueidda D. W., Elhebeary M., Shiang C-S., Pang S., Abu Al-Rub R. K., Jasiuk I. M.: Mechanical properties of 3D printed polymeric Gyroid cellular structures: Experimental and finite element study. *Materials and Design*, **165**, 107597 (2019). <https://doi.org/10.1016/j.matdes.2019.107597>
- [33] Ling C., Cernicchi A., Gilchrist M. D., Cardiff P.: Mechanical behaviour of additively-manufactured polymeric octet-truss lattice structures under quasi-static and dynamic compressive loading. *Materials and Design*, **162**, 106–118 (2019). <https://doi.org/10.1016/j.matdes.2018.11.035>
- [34] Li X., Kawai K., Fujitsuka M., Osakada Y.: COF-based photocatalyst for energy and environment applications. *Surfaces and Interfaces*, **25**, 101249 (2021). <https://doi.org/10.1016/j.surfin.2021.101249>
- [35] Ben Ali N., Khelif M., Hammami D., Bradai C.: Mechanical and morphological characterization of spherical cell porous structures manufactured using FDM process. *Engineering Fracture Mechanics*, **216**, 106527 (2019). <https://doi.org/10.1016/j.engfracmech.2019.106527>

- [36] Baumann A. E., Burns D. A., Liu B., Thoi V. S.: Metal-organic framework functionalization and design strategies for advanced electrochemical energy storage devices. *Communications Chemistry*, **2**, 86 (2019). <https://doi.org/10.1038/s42004-019-0184-6>
- [37] Chen L., Zhang X., Cheng X., Xie Z., Kuang Q., Zheng L.: The function of metal-organic frameworks in the application of MOF-based composites. *Nanoscale Advances*, **2**, 2628–2647 (2020). <https://doi.org/10.1039/D0NA00184H>
- [38] Miralbes R., Ranz D., Pascual F. J., Zouzias D., Maza M.: Characterization of additively manufactured triply periodic minimal surface structures under compressive loading. *Mechanics of Advanced Materials and Structures*, **29**, 1841–1855 (2020). <https://doi.org/10.1080/15376494.2020.1842948>
- [39] Alkateb M., Sapuan S. M., Leman Z., Jawaid M., Ishak M. R.: Quasi-static crush behaviour of environmentally friendly kenaf/wool epoxy composites elliptical tube. *Journal of Mechanical Engineering and Sciences*, **12**, 3671–3688 (2018). <https://doi.org/10.15282/jmes.12.2.2018.13.0325>
- [40] Zeng C., Liu L., Bian W., Leng J., Liu Y.: Bending performance and failure behavior of 3D printed continuous fiber reinforced composite corrugated sandwich structures with shape memory capability. *Composite Structures*, **262**, 113626 (2021). <https://doi.org/10.1016/j.compstruct.2021.113626>
- [41] Choudhry N. K., Panda B., Kumar S.: In-plane energy absorption characteristics of a modified re-entrant auxetic structure fabricated via 3D printing. *Composites Part B: Engineering*, **228**, 109437 (2022). <https://doi.org/10.1016/j.compositesb.2021.109437>
- [42] Mills N., Jenkins M., Kukureka S.: Viscoelastic behaviour. in 'Plastics: Microstructure and engineering applications' (eds.: Mills N., Jenkins M., Kukureka S.) Butterworth-Heinemann, Oxford, 111–125 (2020). <https://doi.org/10.1016/B978-0-08-102499-7.00007-2>
- [43] Sun Z. P., Guo Y. B., Shim V. P. W.: Characterisation and modeling of additively-manufactured polymeric hybrid lattice structures for energy absorption. *International Journal of Mechanical Sciences*, **191**, 106101 (2021). <https://doi.org/10.1016/j.ijmecsci.2020.106101>
- [44] Qi C., Jiang F., Remennikov A., Pei L-Z., Liu J., Wang J-S., Liao X-W., Yang S.: Quasi-static crushing behavior of novel re-entrant circular auxetic honeycombs. *Composites Part B: Engineering*, **197**, 108117 (2020). <https://doi.org/10.1016/j.compositesb.2020.108117>
- [45] Silva R. G., Torres M. J., Viñuela J. Z., Zamora A. G.: Manufacturing and characterization of 3D miniature polymer lattice structures using fused filament fabrication. *Polymers*, **13**, 635 (2021). <https://doi.org/10.3390/polym13040635>
- [46] Fadeel A., Mian A., Al Rifaie M., Srinivasan R.: Effect of vertical strut arrangements on compression characteristics of 3D printed polymer lattice structures: Experimental and computational study. *Journal of Materials Engineering and Performance*, **28**, 709–716 (2019). <https://doi.org/10.1007/s11665-018-3810-z>
- [47] Ufodike C. O., Ahmed M. F., Dolzyk G.: Additively manufactured biomorphic cellular structures inspired by wood microstructure. *Journal of the Mechanical Behavior of Biomedical Materials*, **123**, 104729 (2021). <https://doi.org/10.1016/j.jmbbm.2021.104729>
- [48] Wu Y., Sun L., Yang P., Fang J., Li W.: Energy absorption of additively manufactured functionally bi-graded thickness honeycombs subjected to axial loads. *Thin-Walled Structures*, **164**, 107810 (2021). <https://doi.org/10.1016/j.tws.2021.107810>
- [49] Wang S., Zheng Z., Zhu C., Ding Y., Yu J.: Crushing and densification of rapid prototyping polylactide foam: Meso-structural effect and a statistical constitutive model. *Mechanics of Materials*, **127**, 65–76 (2018). <https://doi.org/10.1016/j.mechmat.2018.09.003>
- [50] Duan Y., Du B., Shi X., Hou B., Li Y.: Quasi-static and dynamic compressive properties and deformation mechanisms of 3D printed polymeric cellular structures with Kelvin cells. *International Journal of Impact Engineering*, **132**, 103303 (2019). <https://doi.org/10.1016/j.ijimpeng.2019.05.017>
- [51] Sychov M. M., Lebedev L. A., Dyachenko S. V., Nefedova L. A.: Mechanical properties of energy-absorbing structures with triply periodic minimal surface topology. *Acta Astronautica*, **150**, 81–84 (2018). <https://doi.org/10.1016/j.actaastro.2017.12.034>

Research article

Photoreversible control over ionic conductivity of coumarin-containing poly(ionic liquid)-based solid electrolyte

Wangjie Xu, Ming Zhang, Yijun Chen, Qinghua Tian, Xianjing Zhou, Li Zhang, Xinping Wang, Wei Zhang* 

Key Laboratory of Surface & Interface Science of Polymer Materials of Zhejiang Province, Department of Chemistry, Zhejiang Sci-Tech University, 310018 Hangzhou, China

Received 19 July 2022; accepted in revised form 11 November 2022

Abstract. Poly(ionic liquid)s (PILs) are promising candidates used as solid electrolytes because of their excellent electrochemical properties and improved processability. Introducing light-sensitive groups to PILs appears as an attractive strategy for developing novel smart PIL-based electronic devices. In this work, a new photoresponsive PIL-based solid electrolyte was prepared by blending PILs containing coumarin groups (COU-PILs) with poly(vinylidene fluoride hexafluoropropylene). It was found that the ionic conductivity of COU-PIL solid electrolytes (COU-PIL SEs) can be reversibly modulated upon alternative 365 and 254 nm light irradiation. In particular, the COU-PIL SEs exhibit a highly reversible and repeatable manipulation of ionic conductivity with a maximum conductivity modulation of 95%. This reversible control over ionic conductivity is attributed to the photodimerization/photocleavage behavior of the coumarin groups.

Keywords: smart polymers, poly(ionic liquid)s, ionic conductivity modulation, polymer membrane, mechanical properties

1. Introduction

Ionic liquids (ILs) exhibit unique properties such as good thermal stability, negligible vapor pressure, high ionic conductivity, and wide electrochemical window. These properties make their corresponding polymers, poly(ionic liquid)s (PILs), promising application in the field of fuel cells, lithium batteries, supercapacitors, and other electrochemical devices [1, 2]. As solid polymer electrolytes in lithium-ion batteries, PILs have been proposed to address the safety issues caused by the leakage of conventional liquid electrolytes [3]. At the same time, light-responsive materials have gained increasing attention as noninvasive, remote, and precise control over their properties can be achieved [4]. These conductive materials with photoresponsive electrochemical properties display potential applications in optical

memories and bio-imaging, photodetectors, photo-controlled electronic circuits, and other fields [5–8]. Introducing light-sensitive groups to PILs appears as an attractive strategy for developing novel smart materials. Several studies indicated that the combination of light-responsive molecules and ILs could endow ILs with controllable ionic conductivity. For example, imidazolium-based ILs containing light-sensitive anions of *trans-ortho*-methoxycinnamic acid displayed a ~130% increase in ionic conductivity under 3 h light irradiation in aqueous solutions [9]. Azobenzene-based ILs exhibited reversible tunable ionic conductivity under UV/visible light irradiation with a maximum conductivity modulation of 10.7% [10]. From the view of practical application, PILs are more attractive candidates used as solid electrolytes when compared to ILs because of their

*Corresponding author, e-mail: zhwei@zstu.edu.cn

© BME-PT

mechanical stability and improved processability. However, few light-responsive PILs with controllable ionic conductivity have been reported [11, 12]. Recently, Sumitani *et al.* [11] synthesized a light-active PILs containing a ruthenium sandwich cation and a polymeric anion and found that the ionic conductivities of those PILs were reversibly tuned by alternately using light and heat due to a coordination structure transformation. Nie *et al.* [12] incorporated imidazolium containing diarylethenes (DAEs) in a poly(ethylene oxide) backbone and investigated the light-induced conductivity manipulation of the obtained PIL systems. Upon UV/visible light irradiation, the imidazolium containing DAEs switched from a ring-open isomer (having delocalized positive charge) to a ring-closed state (having localized positive charge). In this case, the interaction between mobile anions and DAE-based cations was regulated, and accordingly, the ionic conductivity was reversibly adjusted.

Light-sensitive PILs have shown great potential for the fabrication of smart solid electrolytes. Simple synthesis, high reversibility and desirable conductivity modulation need to be considered for designing and developing light-sensitive PILs. Coumarin and its derivatives are widely used as photoresponsive component because of their high-efficiency reversibilities, excellent biocompatibilities and potentials for dimer formation via visible light [13]. Coumarin derivatives undergo [2+2] cycloaddition when irradiated with a 320–365 nm UV light, while the formed cyclobutane structures can be cleaved when exposed to a ~280 nm light. Incorporating coumarin groups into PILs (COU-PILs) enables the transition between crosslinking and decrosslinking among their chains upon irradiation with different light sources, which will cause the change in ion transport behavior through a polymer matrix.

In this work, we designed a photosensitive PIL-based solid electrolyte to achieve reversible conductivity modulation. The photosensitive COU-PILs were prepared by a simple radical polymerization of quaternary ammonium-type IL monomer containing coumarin groups ($[\text{DMAEMA-COU}]^+[\text{Br}]^-$), and subsequently an anion exchange reaction (Figure 1). Since these COU-PILs themselves could hardly form a robust film, they were generally blended with polyvinylidene fluoride hexafluoropropylene (PVDF-HFP) to improve mechanical strength of the blend film [14]. The reversible change in ionic conductivity

of the obtained coumarin-containing PIL solid electrolytes (COU-PIL SE) film was investigated in detail. It was shown that the ionic conductivity of COU-PIL SE films was manipulated with high-efficiency reversibility when irradiating these films with alternative 365 and 254 nm light. The results indicate a novel insight into the fabrication of smart photocontrollable devices and wearable photodetectors.

2. Experimental

2.1. Materials

7-Hydroxycoumarin (99%) was purchased from Meryer Chemical Technology Co., Ltd. (Shanghai, China) 2-(Dimethylamino)ethyl methacrylate (DMAEMA) (99%), azodiisobutyronitrile (AIBN) (99%), and butylated hydroxytoluene (BHT) were obtained from Macklin Inc. (Shanghai, China). 1,3-Dibromopropane (99%), lithium bis(trifluoromethanesulfonimide) (LiTFSI) (99%), potassium carbonate (K_2CO_3) (99%), and magnesium sulfate (MgSO_4) (99%) were supplied by Aladdin Chemistry Co. Ltd. (Shanghai, China). Polyvinylidene difluoroethylene hexafluoropropylene (PVDF-HFP) ($M_w \sim 455\,000$ g/mol) was purchased from Sigma-Aldrich (St. Louis, USA). The monomer of DMAEMA was passed through a column of the neutral aluminum oxide in order to remove the added inhibitors. Solvents, including dichloromethane (DCM), acetone, methanol, dimethyl formamide (DMF), and dimethyl sulfoxide (DMSO), were of analytical grade and were used without further purification.

2.2. Characterization

The chemical structure of products was identified by ^1H and ^{13}C nuclear magnetic resonance spectrometry (NMR) using a BrukerAvance II DMX spectrometer (Bruker, Germany) operating at 400 MHz. Energy-dispersive X-ray spectroscopy (EDX) was used to determine the element content of COU-PILs with field-emission scanning electron microscopy (Hitachi SU8010, Japan). Fourier transform infrared (FTIR) spectra were collected at room temperature using a Nicolet Avatar 370 spectrometer (Thermo Nicolet Co., USA) in the range of $4000\text{--}400$ cm^{-1} . The glass transition temperature (T_g) was obtained with a differential scanning calorimeter (DSC, TA Q2000, TA Instruments, USA) at temperatures ranging from -50 to 180 $^\circ\text{C}$. Samples (5–10 mg) were encapsulated in standard aluminum pans, heated/cooled at a rate of 10 $^\circ\text{C}\cdot\text{min}^{-1}$ under N_2 protection, and the

data during the first cooling were analyzed. Dynamic mechanical analysis (DMA) was conducted with a dynamic mechanical analyzer (Q800, TA Instruments, America) at a fixed frequency of 1 Hz over a temperature range of 20–150 °C with a heating rate of 5 °C·min⁻¹. The mechanical properties of samples were measured on a QL-5 instrument (OBT Testing Equipment, Jinan, China) at room temperature with a stretch speed of 2 mm/min.

The reversible photoresponse of the coumarin-containing PIL system was assessed using UV-Vis absorbance spectroscopy on a UV-Vis spectrophotometer (UV-2600, Shimadzu, Japan) at the scan speed of 200 nm·min⁻¹. An initial spectrum in the unexposed state was collected, and the sample was then irradiated with 365 nm UV light for different periods of time. The UV-Vis spectra were recorded until the equilibrium state was reached, followed by exposure to 254 nm UV light for different periods of time.

The ionic conductivity (σ) of the COU-PIL SE film was tested by impedance spectroscopy measurements with a CHI660D electrochemical workstation (Shanghai Chenhua Instrument, Shanghai, China). The films were sandwiched between two stainless steel (SS) plate electrodes. The spectra were recorded in the frequency range of 0.01 Hz–1 MHz with an alternating current (AC) amplitude of 5 mV. The σ values of the films were calculated according to Equation (1):

$$\sigma = \frac{L}{RS} \quad (1)$$

where R and L are the bulk resistance and film thickness, respectively, and S is the area of the steel electrode. The power of 365 and 254 nm light was 3 and 15 W, respectively.

2.3. Synthesis of 7-(3-bromopropoxy) coumarin

The synthetic route of 7-(3-bromopropoxy) coumarin was shown in Figure 1, and the exact experimental process was conducted according to previous methods [15]. 1,3-Dibromopropane (10 g, 50 mmol) and K₂CO₃ (10 g, 72 mmol) was dissolved in 50 ml acetone in a 200 ml round-bottom flask and started to reflux at 50 °C. Next, 7-hydroxycoumarin (810 mg, 5 mmol) was added dropwise to the obtained mixture within 30 min and refluxed for an additional 2 h. After the reaction was complete, the acetone was evaporated, and the mixture was partitioned between 100 ml DCM and water. The DCM layer was collected, and the water was extracted twice with 100 ml DCM; then, the combined DCM layers were dried with MgSO₄. After drying, the product 7-(3-bromopropoxy) coumarin was obtained (orange powder, yield: 82%). ¹H NMR (400 MHz, CDCl₃) δ : 7.64 (d, J = 9.5 Hz, 1H), 7.38 (d, J = 8.3 Hz, 1H), 6.88–6.81 (m, 2H), 6.26 (d, J = 9.5 Hz, 1H), 4.18 (t, J = 5.8 Hz, 2H), 3.61 (t, J = 6.4 Hz, 2H), 2.36 (p, J = 6.1 Hz, 2H). ¹³C NMR (101 MHz, CDCl₃) δ : 161.9, 161.1, 155.9, 143.4, 128.9, 113.3, 112.9, 112.8, 101.6, 101.5, 66.0, 64.8, 32.0, 29.6.

2.4. Synthesis of quaternary ammonium-type IL monomer ([DMAEMA-COU]⁺[Br]⁻)

7-(3-Bromopropoxy) coumarin (1.558 g, 5.5 mmol), DMAEMA (786 mg, 5 mmol), polymerization inhibitor BHT (22 mg, 0.1 mmol), and 15 ml acetone were added into a 100 ml round bottom flask and were mixed by vigorously stirring. The reaction was carried out at 50 °C for 24 h under a nitrogen atmosphere. The resultant product was thoroughly washed

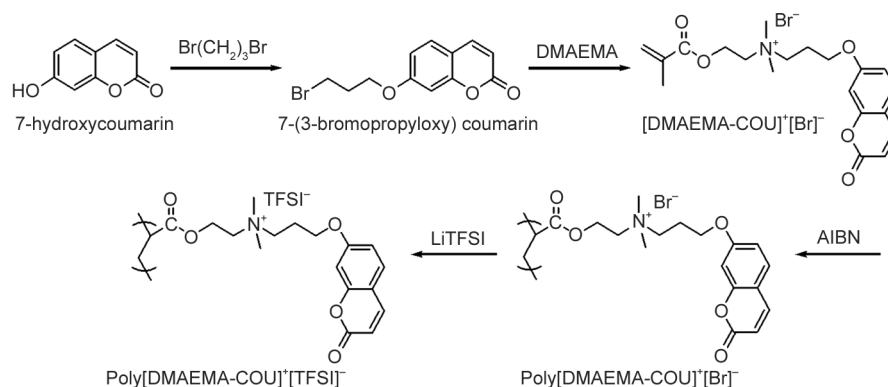


Figure 1. Schematic for the synthesis of photosensitive quaternary ammonium-type poly(ionic liquid)s (PILs) containing coumarin groups, poly([DMAEMA-COU]⁺[TFSI]⁻).

with acetone at least 3 times and dried under vacuum at 40 °C for 24 h. The obtained [DMAEMA-COU]⁺[Br]⁻ is a pale yellow powder with a yield of 69%. ¹H NMR (400 MHz, D₂O) δ: 7.79 (dd, *J* = 9.5, 2.0 Hz, 1H), 7.41 (dd, *J* = 8.8, 2.0 Hz, 1H), 6.83 (dt, *J* = 8.7, 2.3 Hz, 1H), 6.73 (d, *J* = 2.4 Hz, 1H), 6.17 (dd, *J* = 9.5, 2.0 Hz, 1H), 6.06 (s, 1H), 5.63 (d, *J* = 1.8 Hz, 1H), 4.65–4.47 (m, 2H), 4.23–4.02 (m, 2H), 3.79 (dd, *J* = 6.3, 3.5 Hz, 2H), 3.71–3.47 (m, 2H), 3.19 (d, *J* = 2.0 Hz, 6H), 2.37–2.20 (m, 2H), 1.82 (d, *J* = 1.9 Hz, 3H). ¹³C NMR (101 MHz, DMSO-*d*₆) δ: 166.4, 161.8, 160.7, 155.8, 144.8, 135.9, 130.1, 127.2, 113.2, 113.2, 113.1, 101.8, 66.1, 62.5, 61.9, 58.6, 51.2, 22.6, 18.4.

2.5. Synthesis of

poly([DMAEMA-COU]⁺[Br]⁻)

Poly([DMAEMA-COU]⁺[Br]⁻) was prepared via free radical polymerization (Figure 1). IL monomer [DMAEMA-COU]⁺[Br]⁻ (2.203 g, 5 mmol), initiator AIBN (44.1 mg, 0.27 mmol), and methanol (20 ml) were added into a three-necked flask. After the mixtures were completely degassed, the reaction was conducted at 65 °C for 24 h under a nitrogen atmosphere. Since poly([DMAEMA-COU]⁺[Br]⁻) was insoluble in methanol, the precipitation would appear upon polymerization. After polymerization, the obtained products were washed with methanol 3 times and then dried under vacuum at 40 °C for 24 h. Poly([DMAEMA-COU]⁺[Br]⁻) (yield: 80%) is yellow powder. ¹H NMR (400 MHz, DMSO-*d*₆) δ: 7.97 (s, 1H), 7.60 (s, 1H), 6.90 (s, 2H), 6.25 (s, 1H), 4.85 (s, 2H), 4.18 (s, 2H), 3.42 (s, 1H), 3.29 (s, 1H), 2.28 (s, 2H), 1.00 (s, 3H).

2.6. Synthesis of

poly([DMAEMA-COU]⁺[TFSI]⁻)

Poly([DMAEMA-COU]⁺[TFSI]⁻) was prepared via an anion exchange reaction. LiTFSI (3.445 g) and

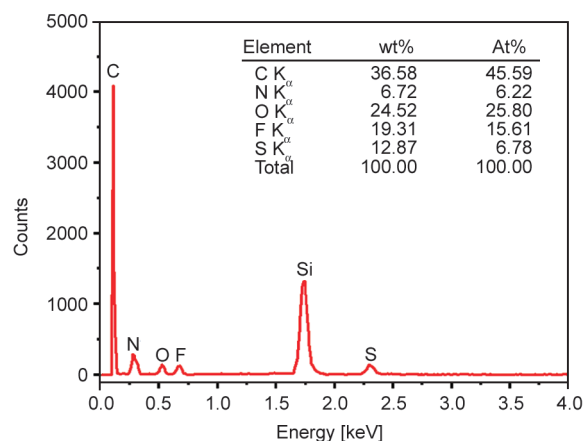


Figure 2. EDX spectra of poly([DMAEMA-COU]⁺[TFSI]⁻).

poly([DMAEMA-COU]⁺[Br]⁻) (4.406 g) were dissolved in 50 ml DMSO, and the solution was stirred at room temperature for 12 h, followed by extraction with excessive deionized water. After drying at 80 °C for 48 h under vacuum, the poly([DMAEMA-COU]⁺[TFSI]⁻) was obtained (yellow powder, yield: 89%). As shown in Figure 2, energy-dispersive X-ray spectroscopy (EDX) revealed that there was no Br⁻ remaining in poly([DMAEMA-COU]⁺[TFSI]⁻), indicating a complete anion exchange reaction.

2.7. Preparation of coumarin-containing PIL solid electrolyte films

In order to prepare photosensitive polymers, coumarin groups were introduced to quaternary ammonium-type poly(ionic liquid)s (PILs). The obtained PILs were denoted as COU-PILs. Since these COU-PILs themselves could hardly form a robust film, they are normally blended with PVDF-HFP, widely used solid electrolyte materials for improving mechanical strength [16, 17]. In this work, the COU-PIL SE films were prepared by blending COU-PILs, PVDF-HFP, and LiTFSI, as shown in Figure 3. The COU-PILs, namely, poly([DMAEMA-COU]⁺[TFSI]⁻) and PVDF-HFP, were dissolved in DMSO, and the

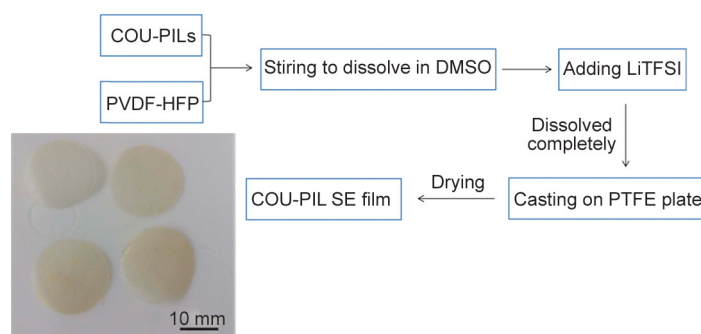


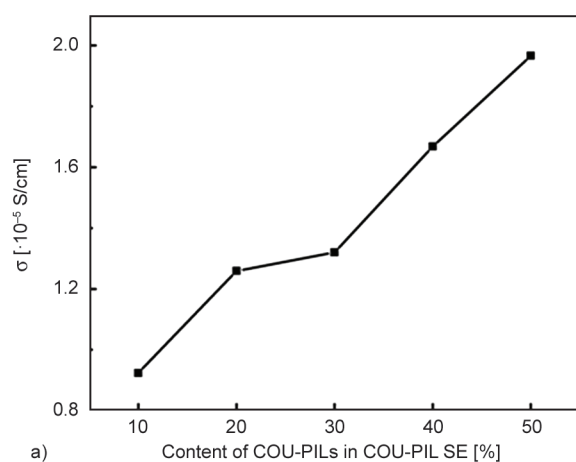
Figure 3. Preparation of the COU-PIL SE film.

blending ratio by weight of COU-PILs to PVDF-HFP was varied from 10/90 to 50/50. Then, LiTFSI (20% of the total weight) was added to the mixture. After complete dissolving, the resulting solution was cast onto a polytetrafluoroethylene (PTFE) plate with a casting knife. The obtained film was further dried in a vacuum oven at 80 °C for 48 h. The thickness of the COU-PIL SE films is 200±20 μm.

3. Result and discussion

3.1. Effect of COU-PILs/PVDF-HFP blending ratio on ionic conductivity and mechanical properties

A series of COU-PIL SE films were prepared by varying the COU-PILs/PVDF-HFP blending ratio while keeping the LiTFSI content unchangeable in order to explore the effect of COU-PILs content on film properties. The effect of COU-PILs content on the ionic conductivity of COU-PIL SE films is presented in Figure 4a. As expected, the ionic conductivity of the COU-PIL SE film increased with increasing COU-PILs content. As shown in Figure 4b, on the other hand, the tensile strength of the COU-PILs SE film decreased while the tensile strain increased as increasing COU-PILs content. This seemed reasonable because COU-PILs themselves have low mechanical strength and even could hardly form a robust film. For example, the film with COU-PILs/PVDF-HFP blending ratio of 50:50, displayed the highest ionic conductivity but lower mechanical properties (tensile strength: 1.86 MPa, Young's modulus: 15.38 MPa) among those SE films. However, this mechanical property was still better than the conventional PEO electrolyte films and other solid electrolyte films reported in the literature [18, 19].



By considering ionic conductivity and mechanical property comprehensively, the COU-PIL SE film with the COU-PILs/PVDF-HFP blending ratio of 50:50 was used for the next investigation.

3.2. Structural photo responsiveness of COU-PIL SE film

The structures of COU-PIL SEs are tuned by taking advantage of the reversible photoresponse of coumarin groups of PILs. Upon 365 nm irradiation, as shown in Figure 5, dimerization occurred between PIL chains to form a cross-linked structure, and the movement of the polymer segments would be hindered. After 254 nm UV irradiation, however, the dimer dissociated to return to the original structure.

The dimerization of COU-PILs can be confirmed by FTIR spectroscopy. Upon 365 nm light irradiation,

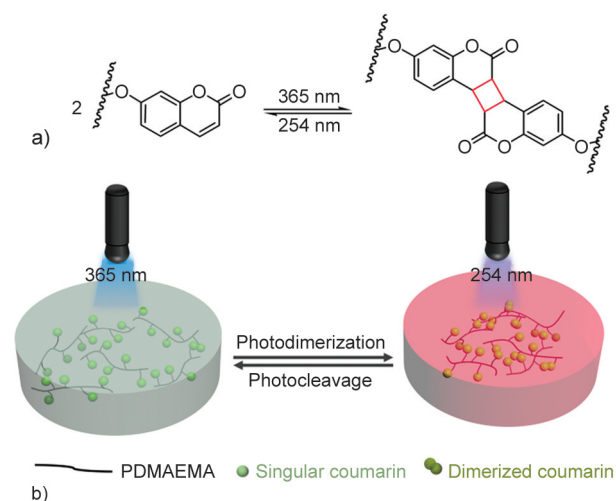


Figure 5. a) Reversible dimerization and cleavage of coumarin groups upon exposure to 365/254 nm light. b) Schematic diagram of crosslinking network formation and dissociation.

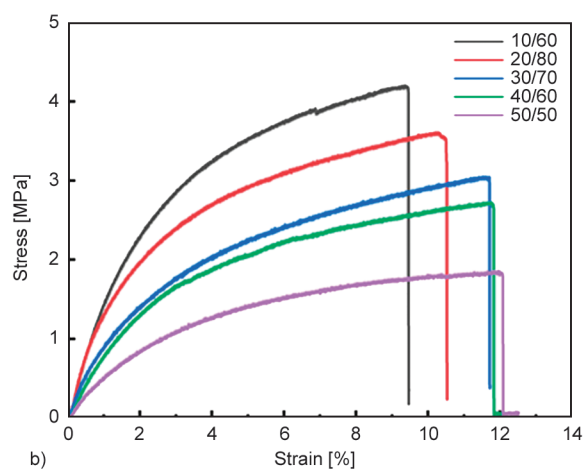


Figure 4. a) Ionic conductivity and b) stress-strain curves of COU-PIL SE films with different COU-PILs/PVDF-HFP blending ratios.

as shown in Figure 6, the intensity of the peak at 1616 cm^{-1} (ring C=C stretching vibration) decreased almost double when compared to the initial samples. In addition, a small shoulder peak appeared at

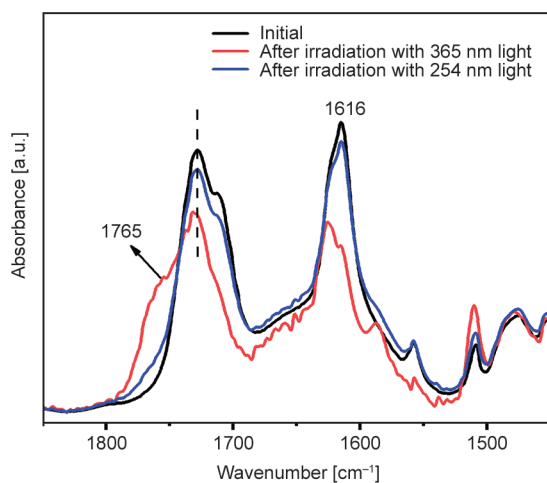


Figure 6. FTIR spectra of COU-PIL SE films after 365/254 nm light irradiation and before 365 nm light irradiation.

1765 cm^{-1} , which was attributed to the carbonyl stretching of the H–H dimer [20]. Upon exposure to 254 nm light, COU-PILs SE films displayed almost the same FTIR spectra as the initial samples, namely, those before 365 nm light irradiation. Those changes in FTIR spectra demonstrate the occurrence of photodimerization and photocleavage of coumarin units in the blending matrix.

Further detection of the photodimerization and photocleavage of coumarins units was conducted by using UV-Vis absorption spectroscopy. As shown in Figure 7a, the maximum absorption peak at 324 nm was attributed to the coumarin double bond. The intensity of this peak gradually decreased when irradiated with a 365 nm light, suggesting the dimerization of coumarin groups [21]. Followed by the exposure to 254 nm light, the absorption intensity at 324 nm increased gradually (Figure 7b), implying that the formed coumarin dimers were cleaved. The change in the maximum absorption peak clearly indicated that the structural transition of COU-PILs

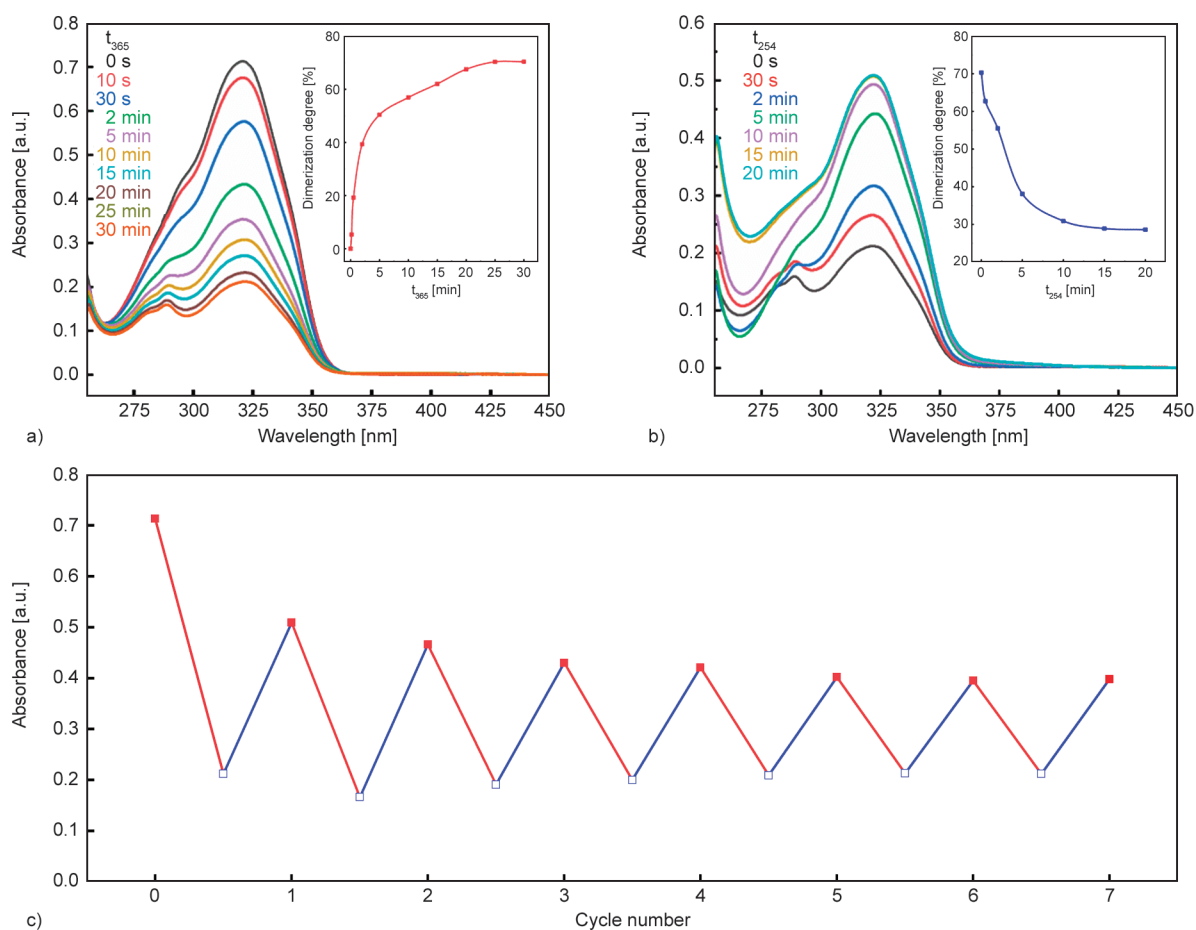


Figure 7. UV-Vis absorption spectra of COU-PIL SE film upon light irradiation at the wavelength of a) 365 nm, b) 254 nm. c) Absorption at 324 nm for COU-PIL SE film during 7 cycles. Insets in a) and b) show the variations of dimerization degree with light irradiation time.

was reversibly tailored under light irradiation, which makes it possible to control the ionic conductivity of the COU-PIL SE film.

The light-induced structural change can also be evaluated by the dimerization degree, D , using Equation (2):

$$D = \frac{A_0 - A_t}{A_0} \cdot 100\% \quad (2)$$

where A_0 is the absorbance at 324 nm of the pristine film and A_t is the absorbance of the film at irradiation time t (t_{365} and t_{254} mean 365 and 254 nm light irradiation, respectively) [22]. It can be seen from the insets of Figure 7 that D gradually increased with t_{365} and finally attained the maximum of 70% within 25 min, while it decreased with t_{254} and reached an equilibrium value of 28% within 20 min.

It was worth noting that D did not attain zero even for prolonging light irradiation at 254 nm because photocleavage and photodimerization of coumarin groups occurred simultaneously upon 254 nm light exposure [22–25]. For convenient comparison, one photodimerization followed by one photocleavage is defined as one cycle. As mentioned above, the absorption at 324 nm could attain equilibrium when exposed to 365 and 254 nm for 25 and 20 min, respectively. Here we employed the equilibrium absorption at 324 nm to evaluate the light-induced reversibility. Figure 7c presents the change in equilibrium absorption at 324 nm during at least 7 cycles. The maximum absorption decreased from 0.7 in the first cycle to 0.5 in the second cycle and finally 0.4 after 7 cycles, implying that some of the formed coumarin dimers were not cleaved. This was possibly

attributed to the asymmetric fission of coumarin dimer during photocleavage under 254 nm light that resulted in irreversible crosslinking [22, 26]. This decay in photoreversibility was unfavorable for the tunable performance modulation. Fortunately, it could be addressed by adding photosensitizer or increasing the power intensity of the light [24, 27].

3.3. Photoresponsiveness of ionic conductivity of COU-PIL SE film

Noticeably, the ionic conductivity varies with irradiation time and finally attains an equilibrium value. For the COU-PIL SE film containing 50% COU-PILs, the time for ionic conductivity to approach equilibrium are 25 and 20 min for 365 and 254 nm irradiation, respectively. The kinetics of ionic conductivity are not listed here, and only the equilibrium values are given in Figure 8 in order to show the repeatable change of ionic conductivity clearly. As presented in Figure 8a, in the first cycle, the ionic conductivity decreased from $1.96 \cdot 10^{-5}$ to $2.32 \cdot 10^{-6} \text{ S} \cdot \text{cm}^{-1}$ at 25 °C after 365 nm light irradiation within 25 minutes, suggesting that light irradiation decreased the ionic conductivity by more than an order of magnitude. When the 254 nm light was employed, the ionic conductivity increased significantly and attained 90% of its original value, which may be due to an incomplete decrosslinking. In fact, the photodimerization and photocleavage of coumarin groups themselves are typically time-dependent, and even 60 min are required for photodimerization to approach equilibrium [22, 25]. This time dependence may be due to the confined light-induced structural evolution caused by the lower mobility of polymer

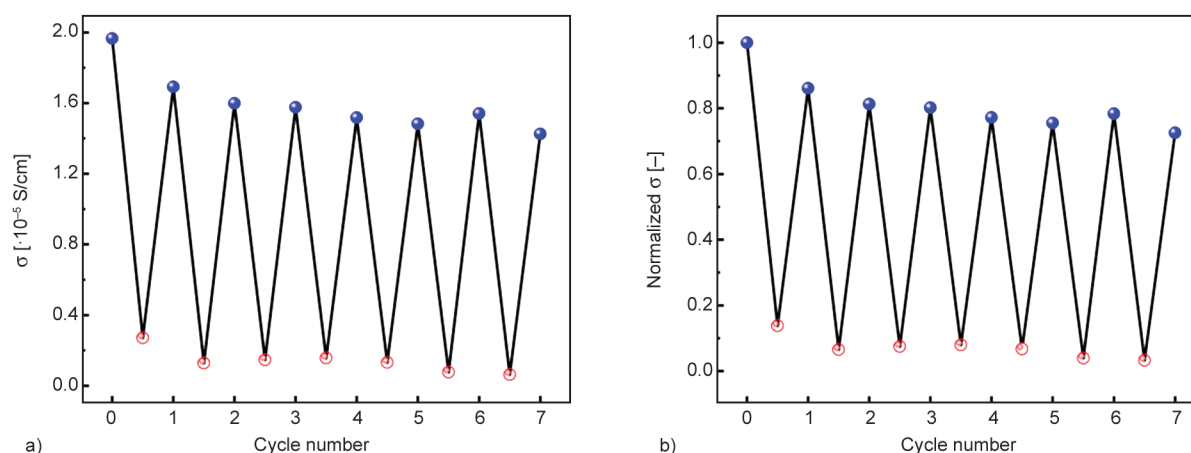


Figure 8. Reversible change in a) the ionic conductivity and b) normalized ionic conductivity of COU-PIL SE film exposed to alternative 365 nm light for 25 min (red hollow symbol) and 254 nm light for 20 min (solid blue symbol). The ratio of COU-PILs and PVDF-HFP in the SE film is 50/50.

chains. In the subsequent cycle, however, the ionic conductivity could be switched back to the starting value, namely about $1.6 \cdot 10^{-5} \text{ S} \cdot \text{cm}^{-1}$, upon 254 nm light irradiation. The change in ionic conductivity with light irradiation can be repeated at least 7 cycles, implying an excellent reversible modulation. The desirable repeatability of conductivity modulation can also be clearly seen in Figure 8b. The normalized σ fluctuated in the range of 0.05~0.9 over 7 cycles, and the maximum conductivity modulation was as high as 95%. Such a high modulation indicates the efficient control of ionic conductivity, which is favorable for various applications. In addition, these results agreed well with those of dimerization as detected by UV-Vis absorption spectroscopy (Figure 7), implying that the photodimerization and photocleavage of coumarin units resulted in the reversible conductivity modulation. It should be pointed out that when the COU-PIL SE films were irradiated by 254 nm light in every cycle, their ionic conductivities can recover to about $(1.5\sim 1.7) \cdot 10^{-5} \text{ S} \cdot \text{cm}^{-1}$ at

room temperature (Figure 8a), which is higher than the minimum value of $10^{-5} \text{ S} \cdot \text{cm}^{-1}$ (at 25 °C) required for acceptable battery performance [28, 29]. This means that the COU-PIL SE film can be reversibly switched between conductive and non-conductive states under alternating illumination of 365 and 254 nm light.

When the ratio of COU-PILs and PVDF-HFP in the blending SE film was varied from 10/90 to 40/60, the reversible behavior of conductivity was still observed (Figure 9). In order to better show the effect of COU-PILs component on reversible conductivity modulation, the magnitude of the modulation of the ionic conductivity ($\Delta\sigma$) was calculated using Equation (3):

$$\Delta\sigma = \frac{\sigma_0 - \sigma_t}{\sigma_0} \quad (3)$$

where σ_0 is the conductivity of the unexposed state and σ_t is the conductivity after 365 nm UV irradiation [10]. It can be observed from Figure 10 that the

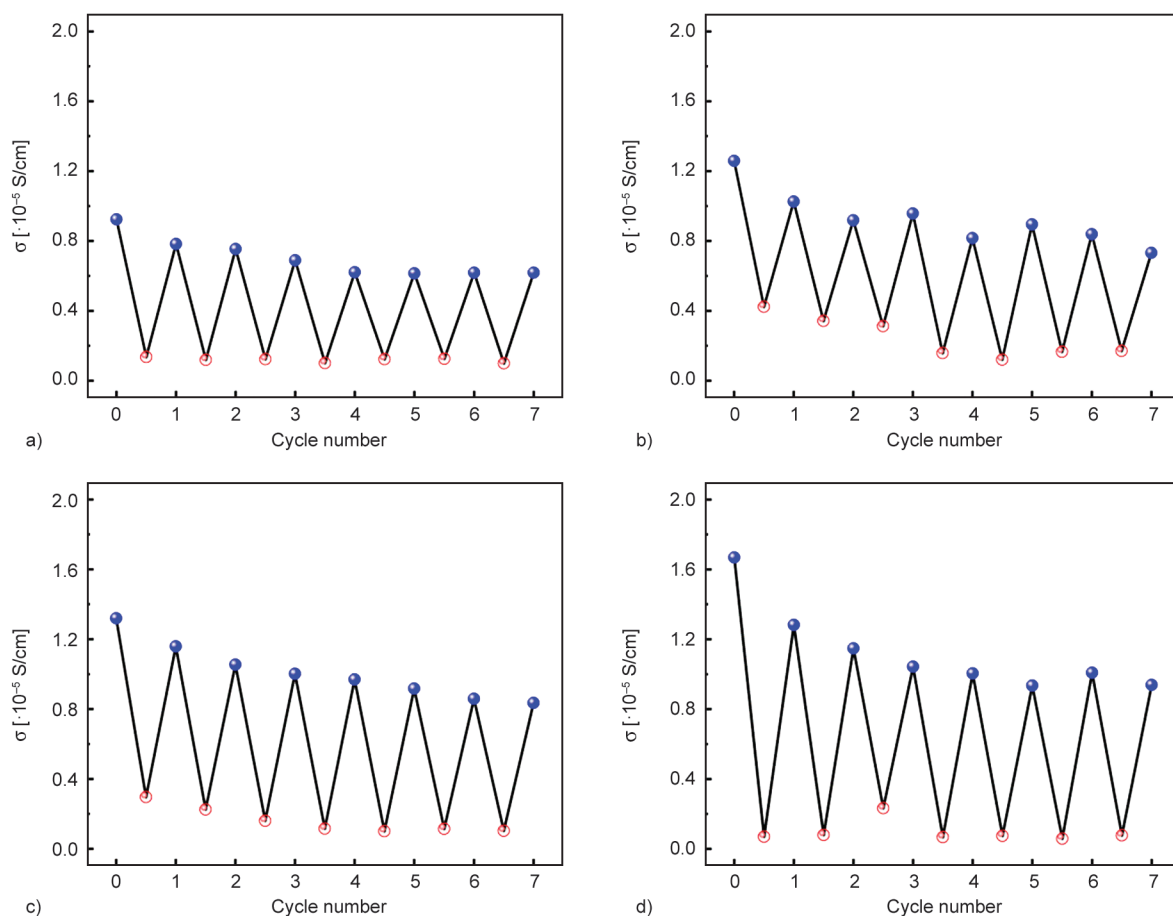


Figure 9. Reversible change in the ionic conductivity of the COU-PIL SE films exposed to alternative 365 nm light for 25 min (solid blue symbol) and 254 nm light for 20 min (red hollow symbol). The weight ratio of COU-PILs and PVDF-HFP is a) 10:90, b) 20:80, c) 30:70, d) 40:60.

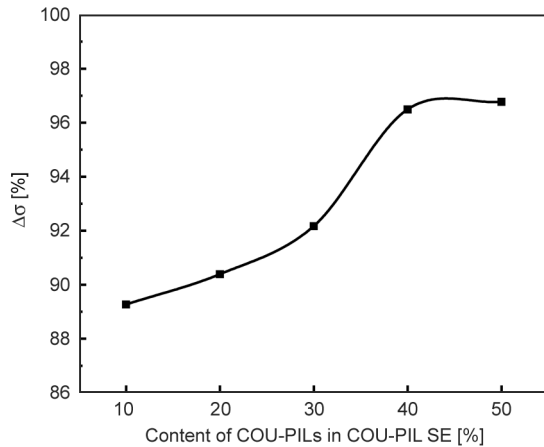


Figure 10. Conductivity modulation of the COU-PIL SE films as a function of the weight ratio of COU-PILs and PVDF-HFP under 7 cycles of illumination.

tunable magnitude of ionic conductivity was enhanced with increasing the COU-PILs content in the blending film, supporting that the COU-PILs components had played an important role in conductivity modulation.

3.4. Reversible manipulation mechanism

It is well documented that Li ions are transported in a polymer matrix via hopping from one coordinating site to another, attaching to polymer backbone or side chains [30, 31]. The segmental motion of polymer chains facilitates the ions' transport, thus improving the ionic conductivity. Conversely, fabricating crosslinking network in a polymer matrix can decrease the ionic conductivity of the polymer electrolyte by restraining the mobility of polymer chains [32]. Incorporating coumarin groups into the polymer

matrix can achieve the reversible formation of crosslinking structures [14, 25], which provides a feasible strategy for reversible photocontrol over ionic conductivity. Herein, the degree of crosslinking of COU-PIL SE film upon successive 365 and 254 nm light irradiation was evaluated by dynamic mechanical analysis (DMA) to understand better the reversible behavior of ionic conductivity in our system. The modulus values shown in Figure 11 are utilized to calculate the crosslinking density, namely, the number of moles of network chains per cubic meter (v_e), using Equation (4) [33]:

$$v_e = \frac{E'}{3RT} \quad (4)$$

where E' is the storage modulus, R is the universal gas constant and T is the temperature ($T > T_g$). As listed in the inset of Figure 11a, there was a significant increase in v_e upon 365 nm light irradiation. Once irradiated by 254 nm light, however, the v_e value decreased dramatically despite the incomplete recovery. Similar behavior was also observed in the first cycle modulation, as shown in Figure 6 and Figure 7. The segmental motion of polymer chains can also be reflected by the change of T_g . In order to clearly show the change in T_g , the DSC curves in the temperature range of -15 to 75 °C are provided. As shown in Figure 11b, the initial COU-PIL SE film without illumination displayed a lower T_g of -0.5 °C, which probably resulted from the plasticization of LiTFSI [14]. The T_g increased to 41.1 °C upon 365 nm light irradiation while decreased to 14.2 °C upon 254 nm light irradiation. The decrease of T_g meant increased free volume, which provided more

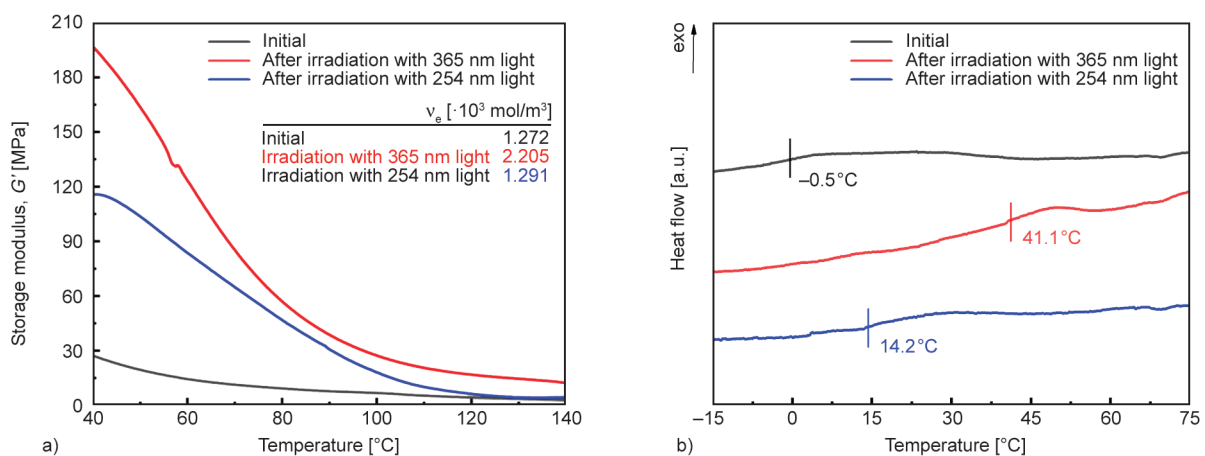


Figure 11. DMA (a) and DSC (b) curves of COU-PIL SE film upon light irradiating at different wavelengths. Inset in a) gives the crosslinking density before and after light irradiation.

free space for Li ions to migrate in the polymer matrix. These results indicated that the photodimerization and photocleavage of coumarin components led to the change of polymer segmental motion, producing reversible conductivity modulation.

4. Conclusions

We have developed a coumarin-containing PIL-based solid electrolyte whose ionic conductivity can be reversibly tailored by photoirradiation. Upon 365 nm light irradiation, the ionic conductivity decreased, whereas it increased upon the subsequent light irradiation at 254 nm. This process can be repeated at least 7 times, within which the maximum conductivity modulation was as high as 95%. The controllable conductivity was attributed to the reversible formation of crosslinking structures caused by photodimerization and photocleavage of coumarin components. This strategy for fabricating a light-responsive PIL-based polymer electrolyte provides a novel idea for the development of functional materials such as smart photo-controllable devices and wearable photodetectors.

Acknowledgements

The authors acknowledge the financial support from the Natural Science Foundation of Zhejiang Province (LY13B040004) and the National Natural Science Foundation of China (21978274 and 21704092).

References

- [1] Zhang S. Y., Zhuang Q., Zhang M., Wang H., Gao Z., Sun J.-K., Yuan J.: Poly(ionic liquid) composites. *Chemical Society Reviews*, **49**, 1726–1755 (2020).
<https://doi.org/10.1039/C8CS00938D>
- [2] Zhang D.-Z., Ren Y.-Y., Hu Y., Li L., Yan F.: Ionic liquid/poly(ionic liquid)-based semi-solid state electrolytes for lithium-ion batteries. *Chinese Journal of Polymer Science*, **38**, 506–513 (2020).
<https://doi.org/10.1007/s10118-020-2390-1>
- [3] Porcarelli L., Shaplov A. S., Salsamendi M., Nair J. R., Vygodskii Y. S., Mecerreyes D., Gerbaldi C.: Single-ion block copoly(ionic liquid)s as electrolytes for all-solid state lithium batteries. *ACS Applied Materials and Interfaces*, **8**, 10350–10359 (2016).
<https://doi.org/10.1021/acsami.6b01973>
- [4] Nie H., Self J. L., Kuenstler A. S., Haywark R. C., de Alaniz J. T.: Multiaddressable photochromic architectures: From molecules to materials. *Advanced Optical Materials*, **7**, 1900224 (2019).
<https://doi.org/10.1002/adom.201900224>
- [5] Mokhtar A., Morinaga R., Akaishi Y., Shimoyoshi M., Kim S., Kurihara S., Kida T., Fukaminato T.: Reversible luminescence photoswitching of colloidal CsPbBr₃ nanocrystals hybridized with a diarylethene photoswitch. *ACS Materials Letters*, **2**, 727–735 (2020).
<https://doi.org/10.1021/acsmaterialslett.0c00131>
- [6] Lin Y.-L., Tseng Y.-H., Ho J.-H., Chen Y.-F., Chen J.-T.: Photoswitchable composite polymer electrolytes using spiropyran-immobilized nanoporous templates. *Chemistry: A European Journal*, **27**, 14981–14988 (2021).
<https://doi.org/10.1002/chem.202102689>
- [7] Wang H., Zhu C. N., Zeng H., Ji X., Xie T., Yan X., Wu Z. L., Huang F.: Reversible ion-conducting switch in a novel single-ion supramolecular hydrogel enabled by photoresponsive host–guest molecular recognition. *Advanced Materials*, **31**, 1807328 (2019).
<https://doi.org/10.1002/adma.201807328>
- [8] Garg S., Schwartz H., Kozłowska M., Kanj A. B., Müller K., Wenzel W., Ruschewitz U., Heinke L.: Conductance photoswitching of metal-organic frameworks with embedded spiropyran. *Angewandte Chemie-International Edition*, **58**, 1193–1197 (2019).
<https://doi.org/10.1002/anie.201811458>
- [9] Yang J., Wang H., Wang J., Zhang Y., Guo Z.: Highly efficient conductivity modulation of cinnamate-based light-responsive ionic liquids in aqueous solutions. *Chemical Communications*, **50**, 14979–14982 (2014).
<https://doi.org/10.1039/c4cc04274c>
- [10] Zhang S., Liu S., Zhang Q., Deng Y.: Solvent-dependent photoresponsive conductivity of azobenzene-appended ionic liquids. *Chemical Communications*, **47**, 6641–6643 (2011).
<https://doi.org/10.1039/c1cc11924a>
- [11] Sumitani R., Mochida T.: Metal-containing poly(ionic liquid) exhibiting photogeneration of coordination network: Reversible control of viscoelasticity and ionic conductivity. *Macromolecules*, **53**, 6968–6974 (2020).
<https://doi.org/10.1021/acs.macromol.0c01141>
- [12] Nie H., Schauer N. S., Dolinski N. D., Hu J., Hawker C. J., Segalman R. A., Read de Alaniz J.: Light-controllable ionic conductivity in a polymeric ionic liquid. *Angewandte Chemie-International Edition*, **59**, 5123–5128 (2020).
<https://doi.org/10.1002/anie.201912921>
- [13] Hughes T., Simon G. P., Saito K.: Chemistries and capabilities of photo-formable and photoreversible cross-linked polymer networks. *Materials Horizons*, **6**, 1762–1773 (2019).
<https://doi.org/10.1039/c9mh00217k>
- [14] Li S., Jiang K., Wang J., Zuo C., Jo Y. H., He D., Xie X., Xue Z.: Molecular brush with dense PEG side chains: Design of a well-defined polymer electrolyte for lithium-ion batteries. *Macromolecules*, **52**, 7234–7243 (2019).
<https://doi.org/10.1021/acs.macromol.9b01641>

- [15] Chadwick R. C., Kardelis V., Liogier S., Adronov A.: Synthesis of conjugated polymers containing DIBAC-derived triazole monomers. *Macromolecules*, **46**, 9593–9598 (2013).
<https://doi.org/10.1021/ma4021467>
- [16] Chen G., Zhang F., Zhou Z., Li J., Tang Y.: A flexible dual-ion battery based on PVDF-HFP-modified gel polymer electrolyte with excellent cycling performance and superior rate capability. *Advanced Energy Materials*, **8**, 1801219 (2018).
<https://doi.org/10.1002/aenm.201801219>
- [17] Mouraliraman D., Shaji N., Praveen S., Nanthagopal M., Ho C. W., Karthik M. V., Kim T., Lee C. W.: Thermally stable PVDF-HFP-based gel polymer electrolytes for high-performance lithium-ion batteries. *Nanomaterials*, **12**, 1056–1069 (2022).
<https://doi.org/10.3390/nano12071056>
- [18] Ye Q., Liang H., Wang S., Cui C., Zeng C., Zhai T., Li H.: Fabricating a PVDF skin for PEO-based SPE to stabilize the interface both at cathode and anode for Li-ion batteries. *Journal of Energy Chemistry*, **70**, 356–362 (2022).
<https://doi.org/10.1016/j.jechem.2022.02.037>
- [19] Rong Z., Sun Y., Zhao Q., Cheng F., Zhang W., Chen J.: UV-cured semi-Interpenetrating polymer networks of solid electrolytes for rechargeable lithium metal batteries. *Chemical Engineering Journal*, **437**, 135329 (2022).
<https://doi.org/10.1016/j.cej.2022.135329>
- [20] Li W., Lynch V., Thompson H., Fox M. A.: Self-assembled monolayers of 7-(10-thiodecoxy)coumarin on gold: Synthesis, characterization, and photodimerization. *Journal of the American Chemical Society*, **119**, 7211–7217 (1997).
<https://doi.org/10.1021/ja970633m>
- [21] Kehrlösser D., Träger J., Kim H-C., Hampp N.: Synthesis and photochemistry of coumarin-based self-assembled monolayers on silicon oxide surfaces. *Langmuir*, **26**, 3878–3882 (2010).
<https://doi.org/10.1021/la903433r>
- [22] Ling J., Rong M. Z., Zhang M. Q.: Photo-stimulated self-healing polyurethane containing dihydroxyl coumarin derivatives. *Polymer*, **53**, 2691–2698 (2012).
<https://doi.org/10.1016/j.polymer.2012.04.016>
- [23] Chen Y., Jean C-S.: Polyethers containing coumarin dimer components in the main chain. I. Synthesis by photopolymerization of 7,7'-(polymethylenedioxy) dicoumarins. *Journal of Applied Polymer Science*, **63**, 1749–1758 (1997).
[https://doi.org/10.1002/\(SICI\)1097-4628\(19970531\)64:9<1749::AID-APP11>3.0.CO;2-T](https://doi.org/10.1002/(SICI)1097-4628(19970531)64:9<1749::AID-APP11>3.0.CO;2-T)
- [24] Chen Y., Jean C-S.: Polyethers containing coumarin dimer components in the main chain. II. Reversible photocleavage and photopolymerization. *Journal of Applied Polymer Science*, **64**, 1759–1768 (1997).
[https://doi.org/10.1002/\(SICI\)1097-4628\(19970531\)64:9<1759::AID-APP12>3.0.CO;2-T](https://doi.org/10.1002/(SICI)1097-4628(19970531)64:9<1759::AID-APP12>3.0.CO;2-T)
- [25] Zhu C. N., Li C. Y., Wang H., Hong W., Huang F., Zheng Q., Wu Z. L.: Reconstructable gradient structures and reprogrammable 3D deformations of hydrogels with coumarin units as the photolabile crosslinks. *Advanced Materials*, **33**, 2008057 (2021).
<https://doi.org/10.1002/adma.202008057>
- [26] Yonezawa N., Yoshida T., Hasegawa M.: Symmetric and asymmetric photocleavage of the cyclobutane rings in head-to-head coumarin dimers and their lactone-opened derivatives. *Journal of the Chemical Society, Perkin Transactions*, **1**, 1083–1086 (1983).
<https://doi.org/10.1039/P19830001083>
- [27] Du Z., Yan X., Dong R., Ke K., Ren B., Tong Z.: Unusual transient network and rheology of a photoresponsive telechelic associative model polymer in aqueous solution induced by dimerization of coumarin end groups. *Macromolecules*, **51**, 1518–1528 (2018).
<https://doi.org/10.1021/acs.macromol.7b01514>
- [28] Xu K.: Nonaqueous liquid electrolytes for lithium-based rechargeable batteries. *Chemical Reviews*, **104**, 4303–4418 (2004).
<https://doi.org/10.1021/cr030203g>
- [29] Armand M., Tarascon J-M.: Building better batteries. *Nature*, **451**, 652–657 (2008).
<https://doi.org/10.1038/451652a>
- [30] Baskoro F., Wong H. Q., Yen H-J.: Strategic structural design of a gel polymer electrolyte toward a high efficiency lithium-ion battery. *ACS Applied Energy Materials*, **2**, 3937–3971 (2019).
<https://doi.org/10.1021/acsaem.9b00295>
- [31] Long L., Wang S., Xiao M., Meng Y.: Polymer electrolytes for lithium polymer batteries. *Journal of Materials Chemistry A*, **4**, 10038–10069 (2016).
<https://doi.org/10.1039/c6ta02621d>
- [32] Chen P., Liu X., Wang S., Zeng Q., Wang Z., Li Z., Zhang L.: Confining hyperbranched star poly(ethylene oxide)-based polymer into a 3D interpenetrating network for a high-performance all-solid-state polymer electrolyte. *ACS Applied Materials and Interfaces*, **11**, 43146–43155 (2019).
<https://doi.org/10.1021/acsaami.9b14346>
- [33] Narayan R., Chattopadhyay D. K., Sreedhar B., Raju K. V. S. N.: Cure, viscoelastic and mechanical properties of hydroxylated polyester melamine high solids coatings. *Journal of Materials Science*, **37**, 4911–4918 (2002).
<https://doi.org/10.1023/A:1020834818562>

Research article

The influence of silicon-doped hydroxyapatite nanoparticles on the properties of novel bionanocomposites based on poly(3-hydroxybutyrate-co-3-hydroxyvalerate)

Mualla Öner^{1*}, Semra Kirboga¹, Emrah Şefik Abamor², Kubra Karadaş², Zeynep Kral¹

¹Yıldız Technical University, Department of Chemical Engineering, Davutpasa Campus, 34210 Esenler, İstanbul Turkey

²Yıldız Technical University, Department of Bioengineering, Davutpasa Campus, 34210 Esenler, İstanbul, Turkey

Received 9 August 2022; accepted in revised form 14 November 2022

Abstract. In this study, silicon-doped hydroxyapatite (SiHAP) nanoparticles and poly(hydroxybutyrate-co-3-hydroxyvalerate, PHBV) were used to develop biodegradable ‘green’ composites due to their intrinsic biodegradability and biocompatibility properties. The novel bionanocomposites were prepared by melt compounding with 0.5, 2, and 3 wt% of SiHAP content. The fracture surface of the bionanocomposites samples from scanning electron microscopy (SEM) exhibited good dispersion of SiHAP in the PHBV matrix at 0.5 wt%. X-ray diffraction (XRD) measurements showed an enhancement of the crystallinity of the PHBV matrix, thereby acting as a nucleating agent, increasing polymer crystallinity from 50 to up to 73% at 3 wt% loadings. Dynamic mechanical analysis (DMA) was used to measure the composite and neat samples’ storage modulus, loss modulus, and damping factor under an oscillating load. DMA analysis showed an increase in storage modulus of 80% at 20 °C and 0.5 wt% SiHAP loadings. Thermal gravimetric analysis (TGA) results showed that the thermal stability of PHBV is slightly decreased by adding 2 and 3 wt% SiHAP. 3-(4,5-dimethylthiazol-2-yl)-2,5-diphenyltetrazolium bromide (MTT) Assay and 4',6-diamidine-2'-phenylindole dihydrochloride (DAPI) staining experiments have demonstrated that PHBV/SiHAP composites exhibit good *in vitro* bioactivity due to the silicon-doped hydroxyapatite nanoparticles. It is concluded that the addition of SiHAP can be a viable strategy for obtaining novel bioactive and biodegradable nanocomposites with improved mechanical and biological properties for potential medical application.

Keywords: biopolymers, biocomposites, biocompatible polymers, biodegradable polymers, reinforcements, mechanical properties

1. Introduction

Biodegradable polymers, which are harmless to the environment, have attracted the attention of many researchers. They are increasingly used in all fields of medicine, especially in applications where biodegradability provides an advantage for the human body. The most widely studied and well-known biodegradable polymers are polyhydroxyalkanoates (PHAs), Poly(lactic acid) PLA, and starch [1–3]. PHAs are a big family of biodegradable and biocompatible microbial biopolyesters from renewable resources [4]. The first PHA identified by the French

bacteriologist Maurice Lemoigne in 1926 was polyhydroxybutyrate (PHB) [5]. The most important features of PHB are its biocompatibility in all environments and its biodegradability. A standard component of human blood is 3-hydroxybutyric acid (3HB), and PHB decomposes into 3HB [6–8]. This proves that the PHB is highly biocompatible and non-toxic. Recently, the number of *in vivo* and *in vitro* studies on PHB has increased. It was shown that by increasing calcium flow in cultured cells, 3HB molecules suppress cell death and prevent serum withdrawal-induced apoptosis [8]. PHB-based biomaterials are

*Corresponding author, e-mail: muallaoner@gmail.com

© BME-PT

piezoelectric that can improve bone growth *in vivo* [8]. It has been observed that PHB is compatible with cells such as epithelium, osteoblast, bone tissue, and blood [9]. Some applications of PHB in biomedical and tissue engineering are drug delivery systems, cardiovascular devices, heart valves, and nerve cuffs, but the difficulty of processing PHB limits its application. To overcome its disadvantages, PHB copolymers can be synthesized with other hydroxyalkanoate monomers, mixtures containing another biopolymer can be prepared, or a PHB-based block can be synthesized. Poly(3-hydroxybutyrate-*co*-3-hydroxyvalerate, PHBV) copolymer is synthesized by the incorporation of 3-hydroxyvalerate (3HV) monomer components of various molar ratios into the 3-hydroxybutyrate (3HB) polymer chain. Some of the shortcomings of PHB improve with the incorporation of 3HV. PHBV has lower melting temperature, stiffness, elasticity modulus, and higher impact strength than PHB [10]. Thus, studies on the poly(3-hydroxybutyrate-*co*-3-hydroxyvalerate) copolymer (PHBV) for biomedical applications have increased. PHBV is obtained by the copolymerization of hydroxybutyrate and hydroxyvalerate. PHBV consists of 0 to 24% hydroxyvalerate (HV) units and hydroxybutyrate (HB) units that appear randomly along the polymer chain. PHBV can promote bone growth *in vivo* due to its degradable, biocompatible, and piezoelectric properties [11, 12]. The properties such as biodegradability and biocompatibility are sufficient for use in PHBV cell culture [13]. It is known that the degradation time of PHBV is longer when compared to other biocompatible polymers [14, 15]. In studies in mice and rats, PHBV was found to be minimally inflammatory in long-term subcutaneous implant applications [15]. Studies show that PHBV is a promising polymer in long-term bone regeneration applications [14]. With the degradation of PHB and PHBV polymers, products that are standard components of human blood are formed, so they give less inflammatory response to the human body than other polymers [16]. The degradation rate of PHBV increases with increasing pH. Hydrolysis of PHBV is slow in the neutral medium at body temperature. At the same temperature and pH, the *in vitro* hydrolysis rate is lower than *in vivo* degradation rate of PHBV [14]. The degradation rates of PHBV and cell/PHBV structures capable of producing neo-cartilage in a heterotopic region continue to be investigated [17]. Therefore, using PHBV as a matrix phase in composite materials is significant potential.

The contribution of nanoscale ceramic fillers in biodegradable polymers to medical applications is undeniable, as they show excellent improvements in material properties, even in low amounts. The most similar ceramic fillers to the mineral part of the bone are hydroxyapatite ($\text{Ca}_{10}(\text{PO}_4)_6(\text{OH})_2$), which exhibits high biocompatibility, bioactivity, osteoconductivity, and an affinity for biopolymers. Therefore, it can be used to repair hard tissues [18].

Synthetic hydroxyapatite (HAP) used in biomedical applications has poor toughness, a low *in vivo* degradation rate, and low mechanical strength. The fact that synthetic HAP has these disadvantages limits its applications. When human bone is examined, it has been observed to contain very few ionic additives such as Si^{4+} , F^- , and Sr^{2+} in its structure. Since ions such as Si and Sr are in natural bone tissues, they were considered dopants and were thought to benefit the biological response of osteoblasts [19, 20]. The main inorganic mineral of bones is hydroxyapatite, doped with various trace elements [19, 20]. The solubility, morphology, surface properties, and particle size of HAP are affected by ion doping in HAP. Ion dopants can also affect the biological activity of HAP. Silicon, which requires small amounts of Si, is found in many animal organs. In the case of Si deficiency, bone and joint diseases are observed. HAP doped with Si can be used in bone repair by improving the functionality of traditional biomaterials [19]. Studies on Si-doped HAP have shown that the crystallinity of Si-doped HAP and the amount of amorphous phase can be affected by high Si-doping content [19]. The expected properties of Si-doped HAP are that it is both biocompatible and has a bone formation-supporting effect [21]. In the literature, in studies with Si-doped HAP materials, cell adhesion and proliferation increase *in vitro* [22]. Si-doped HAP was found to be better biocompatible than undoped HAP when the growth of osteoblastic cells was evaluated [23]. *In vitro*, osteogenic-related gene expressions in human bone marrow cells can be up-regulated by Si-doped HAP [24]. Apatite formation was evaluated by applying Si-doped HAP to the simulated body fluid. Using Si-doped HAP, the appearance of the apatite layer on the surface was significantly improved [25].

PLA, PHB, and PHBV composites with hydroxyapatite have been studied by many researchers. PLA/HAP biocomposite recommended for medical applications has been considered a good alternative to produce bone graft substitutes. Hydroxyapatite, which

has properties close to the structure of bone, has been used to strengthen poly-L-lactic acid (PLA), which is used in many orthopedic applications [26, 27]. The study of Russias *et al.* [26] aimed to combine HAP's bioactivity and mechanical properties with the absorbability of PLA. As a result of the degradation of pure PLA implants in the body, the amount of intermediate acidic products that cause negative inflammatory responses could increase. The addition of HAP may help as a solution to this problem. *in vitro* degradation in body fluid was investigated with PLA/HAP composite by simulating the factors controlling the final properties [26]. It has been found that PHB/HAP composites can be used for rapid bone healing and new bone formation [28]. The biocompatibility of the nanocomposite of PHB with hydroxyapatite is an important area of study [9]. Differentiation was observed in PHB composites with the change in the amount of hydroxyapatite in the composite [29]. The efficiency of a biomaterial depends on the additive's ability to interact with cells, but there is not much data on interaction for the PHB/HAP nanocomposite [30]. In the study of Yuan *et al.* [31], nanoscale hydroxyapatite was incorporated into poly(hydroxybutyrate-co-3-hydroxyvalerate) (PHBV) polymer, and a composite was obtained by solvent casting method. Homogeneous dispersion of HAP nanoparticles on the composite films and good bonding to the polymer was achieved. It has been observed that the ability to adsorb human fibrinogen can be improved with the obtained composite. PHBV/HAP composites were prepared by solvent casting [32]. The material bioactivity increased, and higher glass transition was obtained due to the reinforcement effect of HAP. PHBV/HAP films were produced by surface-treated HAP [33]. The results showed that surface treatment led to higher tensile force. Sadat-Shojai *et al.* [8] prepared PHB/HAP composite by solution casting method. It was observed that HAP strongly affects cell growth and proliferation, enhancing metabolic activity. Öner and İlhan [34] prepared PHBV/HAP composite using the melt extrusion method. The highest tensile properties were obtained for 5 wt% surface-treated HAP loading.

This research aimed to develop and characterize a novel biocomposite using polyhydroxybutyrate-co-valerate (PHBV) and Si-doped HAP for potential medical applications. To the best of our knowledge, the effect of Si-doped HAP on the properties of

PHBV composite has not yet been reported. The biocomposites were prepared using melt extrusion. The composites' physical, thermal, dynamic mechanical, and bioactivity were characterized as a function of the Si-doped loading. This study demonstrates that preparing PHBV composites with Si-doped HAP significantly promotes dynamic mechanical properties and bioactivity.

2. Experimental

2.1. Materials

Under the brand name MAJ'ECO FN000HA, poly(3-hydroxybutyrate-co-3-hydroxyvalerate, or PHBV), with an 8 mol% hydroxyvalerate content, was obtained from ADMajoris Company, France. Hydroxyapatite (HAP) doped with 5% of silicon (SiHAP) was purchased from Sigma-Aldrich Chemicals (St. Louis, USA) (surface area 10–15 m²/g; particle size <200 nm). The human osteoblastic osteosarcoma (SaOs-2) cell line was purchased from American Type Culture Collection (ATCC). 3-(4,5-dimethylthiazol-2-yl)-2,5-diphenyltetrazolium bromide (MTT) and 4',6-diamidine-2'-phenylindole dihydrochloride (DAPI) were purchased from Sigma-Aldrich Chemicals (St. Louis, USA). Dulbecco's modified eagle's medium and Fetal Bovine Serum were purchased from Gibco Life Technologies (Paisley, UK). Penicillin/streptomycin was purchased from Capricorn Scientific (Ebsdorfergrund, Germany).

2.2. Composite preparation

In this work, an extruder was used to prepare PHBV/SiHAP composites. All materials used were dried at 50 °C in a vacuum oven before use. The desired concentrations of SiHAP were added to PHBV in a twin-screw extruder (Rondol Microlab England; L/D: 20). From the feed section to the endpoint, the extruder applied temperatures at 90–135–160–160–150 °C while operating at a screw speed of 80 ppm. Unfilled PHBV was also melt-processed under the same conditions to prepare a reference material. The PHBV nanocomposites films were then compression molded into 0.75 mm thick with a hot-cold press machine (Gülner Makine, Turkey). The obtained composite samples were coded as PHBV-SiHAPX. The number X in the sample represents the percent by weight of SiHAP in the composite. Example, sample PHBV-SiHAP0.5 shows the sample obtained in the presence of 0.5% SiHAP.

2.3. Scanning electron microscopy

Scanning electron microscopy (SEM) was performed using an FEI-Philips XL 30 ESEM-FEG (Thermo Fisher Scientific, Netherlands) scanning electron microscope at an accelerating voltage of 5 kV. Composite samples that had been cryogenically broken were attached to typical SEM stubs and were coated in gold to reduce the sample's charge inside the instrument.

2.4. X-ray diffraction pattern

X-ray diffraction (XRD) measurement with Cu K α source ($\lambda = 0.15418$ nm) was performed at 40 kV and 20 mA using the X'Pert Pro (Philips diffractometer, PANalytical, Denver, Colorado) device. The patterns were recorded for a 2θ range from 4 to 80°. The Scherrer equation is used to determine the crystal size.

2.5. Thermal analysis

A Perkin Elmer TGA analyzer (USA) was used to perform thermogravimetric analysis (TGA) measurements on samples weighing around 10 mg. Each sample was heated at a rate of 10 °C/min under nitrogen at a flow rate of 10 ml/min as the temperature ranged from ambient to 600 °C.

2.6. Fourier transformation infrared spectroscopy

To compare the variation in the functional group of the neat PHBV and its composites, a Bruker ALPHA-P Fourier transformation infrared spectroscope (FTIR, Bruker, Toronto, Canada) was used in transmittance mode at wavelengths ranging from 500 to 4000 cm $^{-1}$.

2.7. Dynamic mechanical analysis of samples

Dynamic mechanical analysis (DMA) was performed using the Perkin-Elmer DMA8000 (PerkinElmer, USA). The dynamic characteristics of samples were examined in single cantilever mode at 1 Hz using film extension mode in the temperature range of –30 to 150 °C at a heating rate of 2 °C/min. The test samples were 10.40 mm \times 10 mm in size. The testing involved determining and recording the storage modulus E' , loss modulus E'' , and $\tan \delta = E''/E'$ values vs. temperature.

2.8. Cell cultivation

Human osteoblastic osteosarcoma (SaOs-2) cells were cultivated in Dulbecco's modified Eagle's medium

(DMEM) supplemented with 10% fetal bovine serum (FBS) and 1% penicillin/streptomycin at 37 °C in an incubator enriched by 5% CO $_2$. The culture medium was refreshed every two days.

2.9. Scaffold sterilization and preparation for cell culture

Before use in cell culture studies, scaffolds were cut into several squares with dimensions of 5 mm \times 5 mm. For sterilization, scaffold pieces were treated with 70% ethanol solution for 30 minutes. After that, scaffold pieces were irradiated with UV light overnight. After sterilization, scaffolds were transferred into test tubes containing 3 ml DMEM medium supplemented with 10% FBS. Then test tubes were incubated at 37 °C for 48 hours. Due to the scope of the extraction method, medium supernatants were collected and used for further cytotoxicity investigation.

2.10. MTT assay

To measure cell viability rates of osteoblast cells after treatment with scaffold extracts, 3-(4,5-dimethylthiazol-2-yl)-2,5-diphenyltetrazolium bromide (MTT assay) was used. Briefly, $1 \cdot 10^4$ osteoblast cells with a final volume of 100 μ l were transferred into each well of the 96 well microplate and incubated at 37 °C overnight. After incubation, 10 μ l of scaffold extracts were included in each well. The wells that were not exposed to extracts were used as the control. After that, microplates were incubated at 37 °C for 96 hours. After incubation, 10 μ l of MTT solution (10 mg/ml) dissolved in phosphate buffer solution (PBS) was added to each well of the microplates. Then microplates were left to incubate for 4 hours. Afterward, formazan crystals in each well were dissolved with the addition of 100 μ l dimethyl sulfoxide (DMSO). Then plates were left to incubate at room temperature in the dark. Finally, the absorbance of each well was read in an ELISA reader at 570 nm. By comparison of absorbance values in control and test groups, cell viability ratios were evaluated following exposure to tissue scaffolds.

2.11. DAPI staining

To determine the biocompatibility of scaffolds, the DAPI staining method was used. For that purpose, sterilized scaffolds were inserted into each well of the 24 well plate and seeded with $1 \cdot 10^4$ osteoblast cells. For a week, the plates were incubated at 37 °C. Every two days, the medium was renewed. Cells

were fixed with 4% paraformaldehyde for 10 minutes after incubation, and they were then washed with PBS. Finally, cells and scaffolds were exposed to DAPI stain for 20 minutes. After exposure, cell-seeded scaffolds were washed with PBS twice, and cell attachment was considered by using a fluorescent microscope.

3. Results and discussion

3.1. Morphological characterization of particles and composites

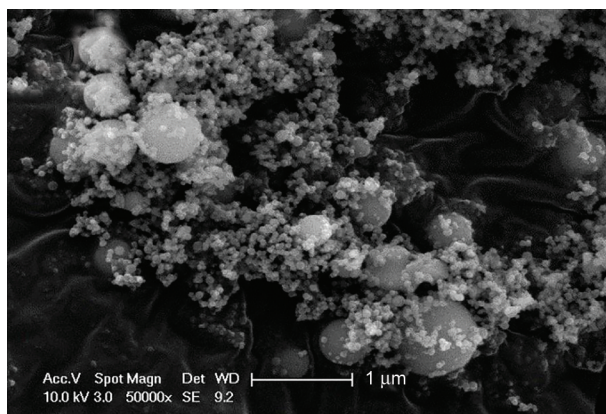
To assess the morphology of SiHAP particles, scanning electron microscopy (SEM) was used, and their micrograph is presented in Figure 1. Through SEM investigation of 210 particles, the distribution of spherical dimensions was determined (Figure 1b). Each distribution curve was fitted using a Gaussian distribution function. The distribution curve appears to have two peaks in the SEM results for these crystals, which demonstrate two size ranges. (Figure 1b). As observed in the particle histogram, most of the uniform spherical SiHAP nanoparticles presented diameter sizes between 35 and 75 nm, with an average diameter of 55 nm. The average diameter of the particles in the second peak, which has a large particle distribution, is about 470 nm.

The melt-processing method was used to prepare PHBV/SiHAP composites. This method does not involve solvent in the process. So, it is greener compared to the solvent casting method. The morphology of the cryo-fractured surface of PHBV and respective composites was examined by scanning electron microscopy (SEM) to investigate the dispersion of the SiHAP particles in the polymer matrix. Figure 2 illustrates the composites at 10 000× magnification. SEM pictures reveal spherical nanoparticles randomly and

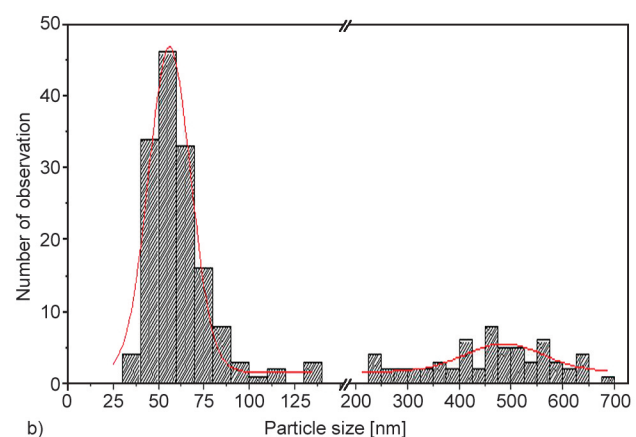
well distributed within the PHBV matrix at 0.5% SiHAP loadings. However, it can be observed that as the nanofillers content increases, the SiHAP nanoparticle dispersion is poorer and has a higher tendency toward aggregation. Therefore, the samples containing 2 and 3 wt% loading (Figures 2b and 2c) showed a biopolymer matrix with filler aggregates of SiHAP. The morphological examination reveals that low concentrations of HAP in PHBV disperse as single particles, but both single particles and tiny clusters appear at greater loadings. This could result from the filler-matrix interface having high surface tension, which results in poor interactions between the polymer and SiHAP particles. Another explanation might be that the extrusion procedure failed to sufficiently break down the HAP aggregate during melt compounding.

3.2. XRD results

In Figure 3a, the XRD pattern shows crystallographic structures of Si-doped HAP particles. Compared to the JCPDS 98-028-9993 standards, each peak of the patterns in Figure 3a corresponds to the hydroxyapatite phase. It has a hexagonal crystal system. The unit cell dimensions are $a = 9.4330 \text{ \AA}$, $b = 9.4330 \text{ \AA}$, and $c = 6.8960 \text{ \AA}$, respectively. There are no additional peaks in the Si-doped HAP patterns compared to the peaks of standard HAP. The silicon-doped HAP samples were prepared using the hydrothermal method [19]. They found that Si doping did not produce a new phase apart from the hydroxyapatite phase. In this work, the characteristic peaks appear at 22.6, 25.6, 30.4, 32.7, 33.6, 39.7, 46.2, 49.1, and 52.8°, corresponding to diffraction planes including (111), (002), (211), (300), (202), (310), (222), (213) and (004) of hydroxyapatite. Three planes (211), (300), and (202) are significant peaks of HAP.



a)



b)

Figure 1. SEM photograph of a) SiHAP and b) particle size distribution of SiHAP.

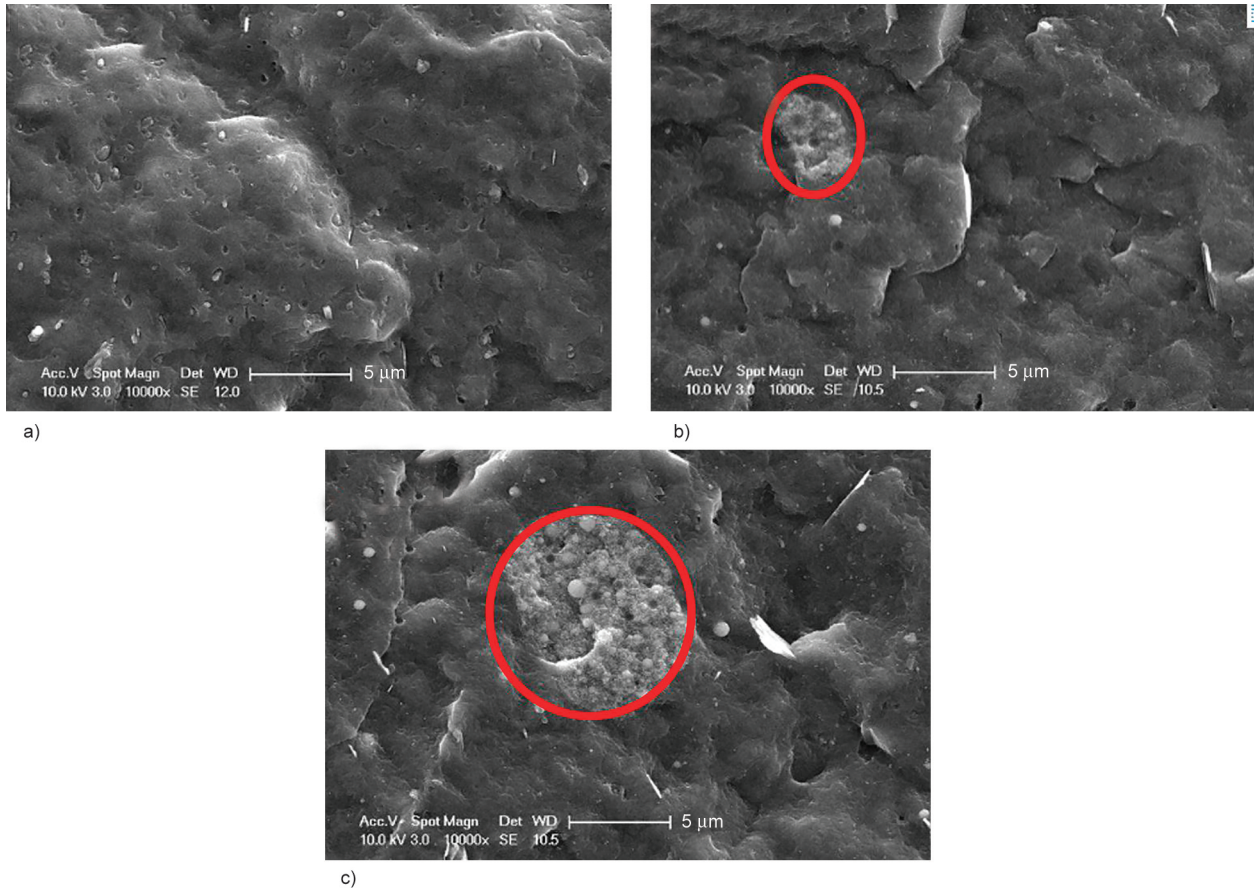


Figure 2. SEM photograph of composites a) PHBV-SiHAP0.5, b) PHBV-SiHAP2.0 and c) PHBV-SiHAP3.0.

Figure 3b displays the XRD spectra of the composites and neat PHBV. Neat PHBV characteristic peaks at $2\theta = 13.3, 16.7, 19.9, 21.2, 25.4, 26.7,$ and 29.8° correspond to (020), (110), (021), (101), (121), (040) and (002) planes with an orthorhombic lattice [35, 36]. The structure of the polymer corresponds to the usual α -form described for P3HB [37]. The same characteristic reflections of the PHBV, which provide detailed information about its crystal structure, were observed after incorporating SiHAP.

This result indicates that the particles did not alter the crystalline structure of the polymer. However, after the addition of SiHAP, the intensity of the PHBV peaks becomes stronger and sharper when compared to the neat PHBV matrix, even in the form of agglomerates at higher concentrations, attributed to SiHAP incorporation, which acts as a nucleating agent tends to increase the ordering level of PHBV molecular chains and to facilitate the crystallization of PHBV, as observed by other researchers.

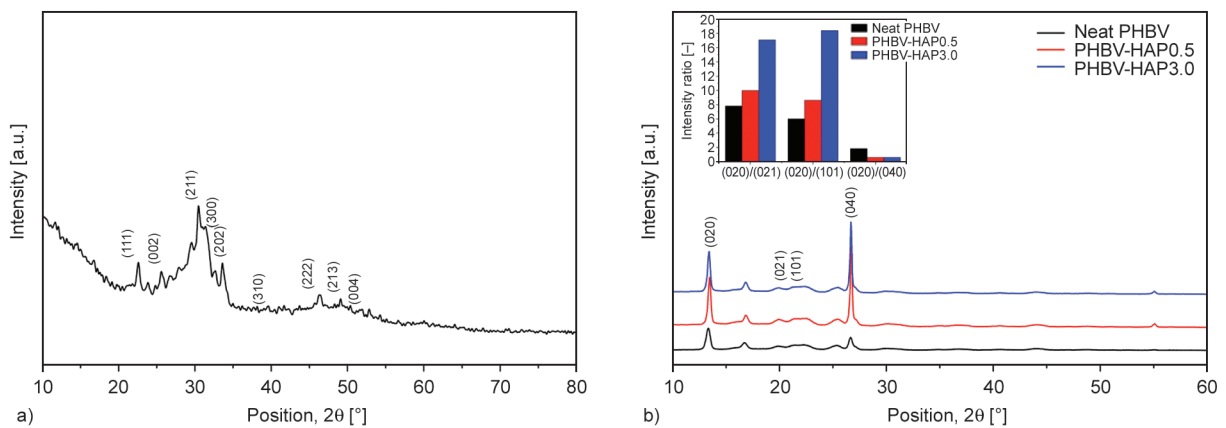


Figure 3. The X-ray diffraction pattern of the a) SiHAP and b) PHBV-SiHAP composites.

In previous studies, PHBV composites using bacterial cellulose [38], boron nitride particles [39], and nanocellulose fillers [40] have all shown a similar effect.

This difference can be explained by analyzing the intensity ratio of the planes (020)/(021), (020)/(101), and (020)/(040) (Table 1). For (020)/(021) planes, the relative intensity ratio of the neat PHBV was 8.56, but for PHBV-SiHAP0.5 and PHBV-SiHAP3 nanocomposites, it was 10.00 and 17.09, respectively. The increase in the relative ratio suggests that the presence of SiHAP particles enhanced crystal formation in the (020) crystal plane. This phenomenon was previously observed by other researchers for PHBV-graphene nanocomposites [41], PHBV-functionalized cellulose nanocrystal composites [42], and PHBV-Boron nitride composites [39]. On the other hand, the intensity ratio of the (020)/(040) decreases from 1.82 to 0.57 for neat PHBV and PHBV-SiHAP3, respectively. The decrease in the (020/040) relative ratio suggests that, despite an increase in both peak intensities due to the addition of SiHAP, the peak intensity of the (040) peak increases more than the intensity of the (020) peak.

The incorporation of SiHAP produced sharper peaks for the (020), (021), and (101) PHBV reflections compared to neat PHBV. The crystallite size dimension L_{020} [nm] was determined using the Scherrer formula for the direction normal to the hkl plane (Equation (1)):

$$L_{(020)} = \frac{k\lambda}{B \cos \theta} \quad (1)$$

where $L_{(020)}$ indicates the average crystallite size in nanometers, k for the shape constant, and B for the diffraction line's broadening as measured at 50% of its highest intensity. B is the diffraction peak under consideration's full width at half maximum intensity (FWHM). When FWHM is utilized for B , the shape factor k becomes 0.9. λ is the X-ray wavelength, and θ is the Bragg diffraction angle.

Table 1 shows the effect of SiHAP on the crystalline lamellae size for the (020) reflection and the crystallinity index. The Equation (2) was used to obtain

the crystallinity index (CI [%]) values for samples based on XRD measurements [43, 44]:

$$CI_{(020)} [\%] = \frac{I_{(020)}}{I_{\text{Total}}} \cdot 100 \quad (2)$$

where $I_{(020)}$ is the intensity of the diffraction peak of the (020) plane, peak at $2\theta = 13.3^\circ$, and I_{Total} is the total intensity value of all crystalline peaks of PHBV. The crystallite size L [nm] calculated for the (020) reflection peak and crystallinity index value was 20.32 nm and 44.70% for neat PHBV, respectively. Addition of SiHAP, both crystallinity and crystal dimensions were increased significantly and varied with SiHAP content. The composites showed higher crystallinity and crystal sizes. The crystallite size and crystallinity values were 35.19 nm and 71.87% for PHBV-SiHAP3 nanocomposites, respectively.

3.3. FTIR results

FTIR spectra of the SiHAP crystals and neat PHBV is given in Figure 4a. In the SiHAP spectrum, the bands at 560 cm^{-1} represent the O–P–O bending mode, and the band at 1036 cm^{-1} corresponds to P–O stretching vibration. No additional peaks were observed for Si-doped HAP. The exhibited peaks also coincide with the structure of HAP, which supports the XRD patterns.

The FTIR transmittance (T) spectra of composites are given in Figure 4b. PHBV composites exhibit the same characteristics peak of neat PHBV. The absorption peaks at around 2977 , 2928 , and 2859 cm^{-1} could be assigned to $-\text{CH}_3$ asymmetric stretching, $-\text{CH}_2$ asymmetric stretching, and $-\text{CH}_3$ symmetric stretching, respectively. The FTIR spectrum showed the characteristic peaks at 1711 cm^{-1} (carbonyl group) and 1170 cm^{-1} (C–O–C asymmetric stretching). The peak is observed at 1711 cm^{-1} due to the C=O stretching vibration in the ester group of PHBV. The peak around 1460 cm^{-1} indicates CH_2 scissoring. The peaks at 1268 and 1170 cm^{-1} may be assigned to C–O–C stretching vibration. The peak in the range of 821 – 972 cm^{-1} could be assigned to C–O–C symmetric stretching. CH_2 wagging may be observed in

Table 1. Values of $L_{(020)}$ [nm], intensity ratios, and CI [%] of composites obtained from the XRD scan.

Sample	$L_{(020)}$ [nm]	(020)/(021) 13.3/19.8	(020)/(101) 13.3/21.2	(020)/(040) 13.3/26.6	$CI_{(020)}$ [%]
Neat PHBV	20.32	8.56	6.01	1.82	44.70
PHBV-SiHAP0.5	30.79	10.00	8.62	0.60	59.45
PHBV-SiHAP3.0	35.19	17.09	18.41	0.57	71.87

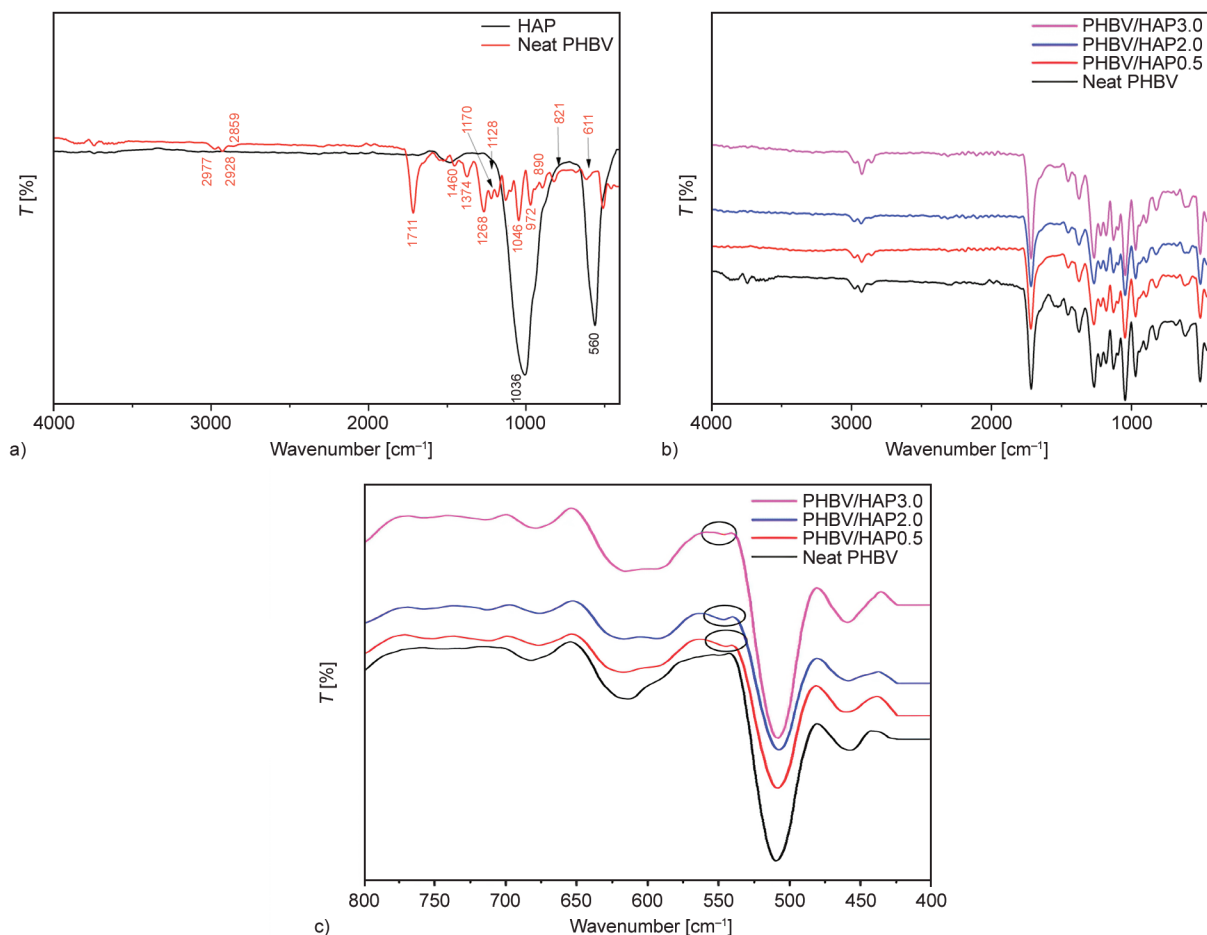


Figure 4. FTIR spectrum of a) SiHAP and neat PHBV at 400–4000 cm^{-1} , b) PHBV-SiHAP composites, and c) PHBV-SiHAP composites at 800–400 cm^{-1} .

the field of 1128–1374 cm^{-1} . Some of the characteristic absorption peaks of SiHAP and the PHBV in the composites overlap. Therefore, it was challenging to demonstrate the distinct differences between PHBV and PHBV-SiHAP composites by FTIR studies. SiHAP has a strong absorption band at 560 cm^{-1} due to the bending vibration of O–P–O bond (Figure 4a). This band is also present at roughly the same location in the spectra of PHBV-SiHAP nanocomposites, and the intensity of the peak increases with the SiHAP content of the composites (Figure 4c). This result validated the inclusion of SiHAP nanoparticles in the PHBV matrix.

3.4. TGA results

Thermogravimetric analyses (TGA) were carried out to evaluate the effect of the addition of the SiHAP on the thermal stability of PHBV nanocomposites. The thermal degradation (TG) and derivative thermogravimetric (DTA) curves of the neat polymer and composites are shown in Figures 5, and representing temperature is given in Table 2. TGA thermograms

show that neat PHBV and composites present one single decomposition step profile. The decomposition step occurs fast, starting at 271.1 °C for neat polymer, and completes at 297.5 °C. The key findings are summarized in Table 2 as the initial degradation temperature (T_i), the degradation temperature T_{10} corresponding to a mass loss of 10 wt%, the mid-point of degradation (T_{50}) recorded at a mass loss of 50 wt%, and the maximum loss temperature (T_{max}).

The initial (T_i) degradation temperatures of the PHBV have not been affected by the addition of 0.5 wt% SiHAP. However, the addition of 2 and 3 wt% SiHAP gently moves the peak of the TGA curves to the left, indicating that the addition of SiHAP in this concentration decreases the thermal stability of PHBV. Figure 5b shows the DTA curve, and the peak represents the temperature corresponding to the maximum degradation rate (DTA_{peak}). For neat PHBV, DTA_{max} occurred at 287.9 °C. However, the addition of SiHAP shifted the DTA_{max} to a lower temperature. The DTA_{max} for PHBV-SiHAP3 occurred at 274.2, which is 13.7 °C lower than the neat PHBV.

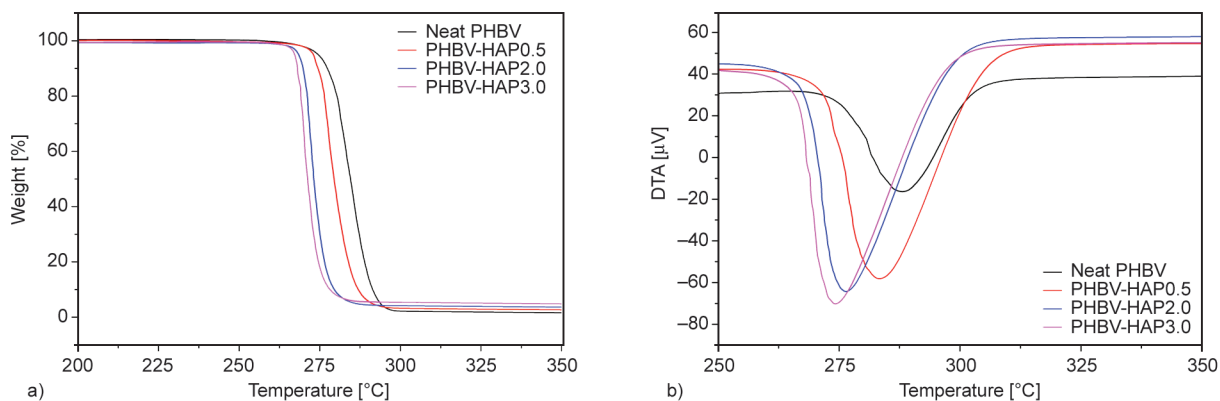


Figure 5. a) TGA and b) DTA curves of neat PHBV and PHBV-SiHAP nano biocomposites.

Table 2. TGA values of PHBV-SiHAP biocomposites.

Sample code	T_i [°C]	T_{10} [°C]	T_{50} [°C]	T_{90} [°C]	T_{max} [°C]	DTA_{peak} [°C]
Neat PHBV	271.14	277.29	284.56	291.28	297.53	287.90
PHBV-HAP0.5	270.37	274.43	279.44	286.82	294.93	283.60
PHBV -HAP2.0	266.28	269.81	273.17	279.25	286.58	276.20
PHBV -HAP3.0	265.24	268.07	271.21	278.04	283.76	274.20

The reduction of T_i and T_{max} values for PHBV was previously reported in the literature for incorporation of lignosulfonate [45], cellulose nanowhiskers [46], lignin [47], nanohydroxyapatite (nHAP) and diamond nanoparticles [48] and graphene nanosheets [41, 49]. The possible reason for this effect was reported as the high thermal conductivity of the particles, which enhanced the heat diffusion throughout the material. Castro-Mayorga *et al.* [50] synthesized ZnO particles by an aqueous precipitation method. They used different methods to fabricate PHBV/ZnO nanocomposites, including melt-mixing and electrospinning. T_{max} value of PHBV was decreased by ZnO particle addition, reducing the thermal stability. This effect was attributed to ZnO's high thermal conductivity and catalytic properties. Chen *et al.* [32] fabricated the PHBV/HAP nanocomposite using the solution casting method with strong ultrasonication. The incorporation of nHAP resulted in the decomposition of the polymer matrix at the initial stage. T_i value for PHBV/HAP (100/50) dropped by 5 °C compared to that for the pure polymer. The composites of polylactide (PLA) or poly(3-hydroxybutyrate-co-3-hydroxyvalerate) (PHBV) were prepared by extrusion and injection molding using ZnO nanoparticles [51]. The results showed that the onset and peak degradation temperature of PLA was shifted towards lower temperatures with the increase of ZnO concentration, while degradation of PHBV showed no dependence on the ZnO concentration

[51]. Braga *et al.* [52] prepared PHBV-TiO₂ composites by using the electrospinning technique, to be used as a scaffold. The decrease in the thermal degradation temperature was observed in the presence of the nanoparticles. This observation was explained due to the presence of agglomerations of the nanocomposites in the fiber; the interactions of the PHBV with TiO₂ were reduced and affected the random chain scission reaction of PHBV during the thermal degradation process [52]. The same argument can be considered in this work since SiHAP particles tend to agglomerate, especially at high concentrations. The aggregation of SiHAP reduced the bonding interactions between PHBV and nanoparticles, thus weakening the thermal stability.

3.5. Dynamic mechanical analysis (DMA) of composites

The mechanical properties of a polymer are strongly influenced by temperature, which affects a decrease in the material's rigidity and an increase in its viscous flow. These variations are reflected in the storage modulus, loss modulus, and loss factor. All samples exhibited a typical behavior of semi-crystalline polymer with a decrease in storage modulus by an increasing temperature. The decline in storage modulus with temperature is due to the increased molecular motion of the matrix molecules. As the temperature rises, the lattice polymer chains can move more freely, reducing the considerable stress within

the polymeric framework resulting in a decrease in modulus.

The storage modulus values against the temperature of PHBV composites are shown in Figure 6a compared to neat PHBV. According to the dynamic mechanical analysis (DMA) results, SiHAP nanocrystals affect the storage modulus of the PHBV overall temperature ranges, as shown in Figure 6a. The strongest reinforcing effect was observed for composites of 0.5 wt% of SiHAP. Figure 6a shows that at -20°C , the E' of PHBV/SiHAP0.5 is 7.4 GPa as opposed to neat PHBV with an E' of 3.9 GPa. For comparison, four temperature settings were used: -20°C as an indicator of the glassy behavior, 20°C for room temperature behavior, 37°C for body temperature behavior, and 80°C as an indicator of the high-temperature behavior of the composite. At -20°C , the highest relative storage modulus increases were obtained compared to the neat PHBV, corresponding to 86, 64, and 42% for 0.5, 2, and 3 wt% SiHAP contents, respectively. The storage modulus of neat PHBV increases by 80% for PHBV-SiHAP0.5 at 20°C . At 37°C , the E' of PHBV increased by 69% for PHBV-SiHAP0.5. On the other hand, a 67% increase in the

storage modulus of PHBV is observed for the sample containing 0.5 wt% SiHAP at 80°C . The storage modulus measures a material's capability to store mechanical energy without dissipating it and to withstand deformation. PHBV composites are more resistant to deformation and, therefore, more rigid than neat polymers. This mechanical reinforcement effect was attributed mainly to the high stiffness and the good affinity through interfacial interaction between the biopolymeric matrix and SiHAP.

The loss modulus, E'' , values of the PHBV and composites as a function of temperature at 1 Hz are presented in Figure 6b. The variation's trend was similar to the E' for loss modulus. This study observed that the loss modulus of neat PHBV was lower than the moduli of all composites, indicating that SiHAP improves the composite materials' damping and internal friction properties. Figure 6b shows the increase in loss modulus as the temperature rises from -30°C to T_g due to molecular friction. The maximum increase was observed with PHBV-SiHAP0.5 followed by PHBV-SiHAP2 and PHBV-SiHAP3. Increased filler loading improved the PHBV composites' capacity to dissipate energy, as indicated by the increase in the

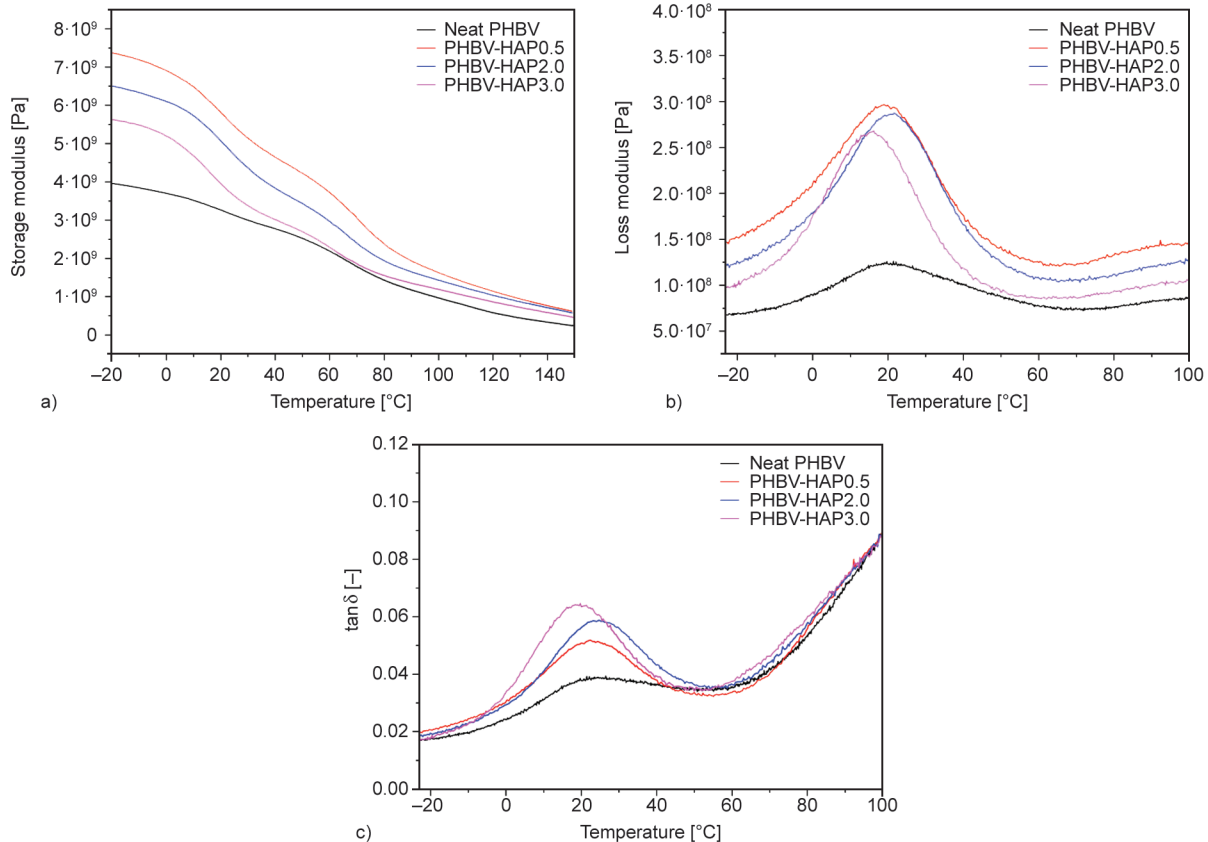


Figure 6. DMA thermographs for PHBV-SiHAP bionanocomposites show a) storage modulus, b) loss modulus, and c) $\tan \delta$.

E'' . However, the loss modulus drops above glass transition temperature (T_g) since less force is needed to cause deformation.

Dynamic mechanical analysis is a valuable tool to determine the material's glass transition temperature, typically taken as the peak of the $\tan \delta$ curve generated through a temperature ramp experiment. Figure 6c shows the temperature-dependent loss tangent ($\tan \delta$) values for the PHBV and composite materials. In viscoelastic materials, internal friction is represented by the loss tangent ($\tan \delta$), which is the ratio of the loss modulus (E'') to the storage modulus (E'). It is an assessment of energy wasted that is expressed in terms of energy recovered. The values of relaxation temperatures connected to the glass transition temperature were taken at the maximum of the peak of the damping factor.

The neat and PHBV composites' glass transition region is between 22–26 °C. The $\tan \delta$ curve of the composites (Figure 6c) showed that the T_g values decreased with the increase in filler loading. T_g of neat PHBV decreases from 26 to 19 °C by incorporating 3 wt% SiHAP.

Srithip et al. [53] prepared poly(3-hydroxybutyrate-co-3-hydroxyvalerate, PHBV) and nanofibrillated cellulose (NFC) nanocomposites by melt compounding. Compared to neat PHBV at 25 °C, the storage modulus for nanocomposite reinforced with 10 wt% NFC increased by 28%. The composite's glass transition temperature slightly increased with increasing NFC. On the other hand, the relaxation process strongly decreased with increasing NFC, which was attributed to the limitation of chain mobility within the polymer matrix. Chen and Wang [54] investigated PHBV/HAP and PHBV/tricalcium phosphate (TCP) biocomposites. The elastic modulus of PHBV at 30% particle loading is reinforced by 21.26 wt% (TCP) and 37.17 wt% of HAP at 37 °C. The addition of bioceramic particles generally reduced $\tan \delta$ for both PHBV/HAP and PHBV/TCP composites [54]. PHBV nanocomposites were fabricated by incorporating nano-sized hydroxyapatite (nHAP) by a solution casting method [32]. The storage modulus of the PHBV/HAP (100/30) nanocomposite was increased by 41.2% at –50 °C and 99.1% at 75 °C at 1 Hz. The neat and PHBV composites glass transition temperature region was found between 17.1–17.6 °C at 1 Hz [32]. PHBV and purified alpha-cellulose fibers were prepared by melt blending. No noticeable changes in T_g values of the composites were found

for low cellulose content with respect to the neat PHBV [55]. PLA nanocomposites were prepared using surface-treated (mNHAP) and untreated nanohydroxyapatite (nNHAP) [56]. Nanocomposites prepared with surface-treated nanohydroxyapatite showed a significant decrease in T_g . They concluded that reduced glass transition temperature is a measure of poor interfacial adhesion between the PLA matrix and mNHAP [56]. Mittal et al. [57] investigated the effect of talc and mica particles on the properties of polypropylene. It was found that when talc and mica loading increased, $\tan \delta$ values decreased. This result was explained by the disruption of the polymer chain packing due to the filling up of the free volume of the polymer by talc and mica particles [57]. PHBV, nanodiamond (nD), and nanohydroxyapatite (nHAP) loaded with vancomycin (VC) nanocomposites were prepared using a rotary evaporator (PHBV/nHAP/VC/nD-R) or spray drying (PHBV/nHAP/VC/nD-SD) [48]. The storage modulus of the composites prepared by the rotary evaporator increased by 51.7% at 37 °C, but T_g value decreased from 17 to 14.8 °C for neat polymer and composite, respectively. This result was explained by the agglomeration of nanoparticles. Since nano HAP particles have the propensity to aggregate, particularly at high concentrations, the same argument can be taken into account in this work.

3.6. Screening of cytotoxicity

Biocompatibility is one of the most significant features of biomaterials that are preferred used in tissue engineering applications. Biomaterials are expected to improve cell attachment, proliferation, and migration. Furthermore, tissue scaffolds should not demonstrate cytotoxicity and prevent the generation of toxic byproducts during degradation [58]. So, within the context of the present study, we explored the possible interactions between osteoblast cells and synthesized composites with variable compositions to understand their probable utilities for biomedical applications. For biological activity experiments, we primarily examined the cytotoxicity of prepared composites.

To evaluate the cellular viability rates of osteoblasts that were treated with neat PHBV and their composites derived with the addition of different values of Si-doped HAP, the MTT method was used. Biocomposites were extracted within a culture medium for 48 hours, and extracts were applied on SaOs-2

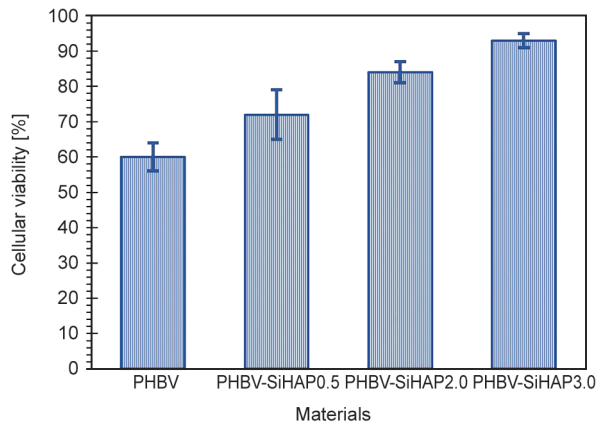


Figure 7. Cellular viability rates of osteoblast cells that were exposed to different biomaterials for 96 hours.

osteoblast cells for 96 hours before measurement of cellular viability degrees. **Figure 7** indicates the cellular viability ratios of osteoblast cells after treatment with extracts. As it is seen in **Figure 7**, neat PHBV leads to a reduction in viability rates. It was detected that PHBV treatment declined cellular viability at 40%. Only 60% of cells were alive after their exposure to PHBV. On the other side, it was also examined from **Figure 7** that the addition of SiHAP into PHBV positively impacts their biocompatibilities since cell vitalities are significantly augmented in contrast to using PHBV alone. Interestingly, it was discovered that there were proportional increases in the numbers of cells according to increasing SiHAP within the composites. The highest cellular viability ratio was measured in the group prepared with 3 wt% SiHAP. Approximately 92% cellular viability was measured in the mentioned group. In contrast, to control, the ratio of viable cells was counted as 72 and 84% in experimental groups prepared by 0.5 and 2 wt% SiHAP, respectively. These results revealed that the toxic feature of PHBV could be reversed by adding SiHAP with enhanced dosages. Numerous studies detected that bioactivity and biocompatibility features of PHBV scaffolds improved remarkably when they were incorporated with other polymers to generate composites. For instance, Degli Esposti, *et al.* [59] synthesized several scaffolds, including PHBV, PHBV-hydroxyapatite, PHBV-calcium silicate, PHBV-bioglass to investigate their possible use for bone tissue engineering. In cytotoxicity assay, researchers determined that the use of a PHBV scaffold decreased cellular viability rates of fibroblast cells to 60%. It was also revealed that the use of combinations of PHBV with bioactive inorganic particles enhanced cellular viabilities significantly, in contrast

to the use of PHBV scaffold alone [59]. In another study, Wu *et al.* [60] discovered that PHBV-bioglass composite scaffolds were more effective in terms of vascularization stimulation for bone tissue recovery when compared with the use of PHBV scaffold. In the scope of mentioned articles, the results of the current study indicate that the PHBV scaffold declined the cell viability rates. At the same time, composites possessed better biocompatibility is consistent with the previous research.

3.7. DAPI staining for determination of biocompatibility

The biocompatibility features of synthesized nanobiomaterials were also explored by visualizing the attachment of cells onto variable composites. The amounts of cells adhered to biomaterials were monitored by DAPI staining. **Figure 8** represents the microscopic views indicating the changes in the amounts of fibroblast cells adhered to biocomposites. As observed, the numbers of attached cells onto samples were at the lowest degree in the group where we used neat PHBV, suggesting that this biomaterial possessed low biocompatibility. In contrast, the numbers of attached cells on samples remarkably lifted when PHBV composites were prepared with different concentrations of SiHAP. The highest biocompatibility property was detected in the group in which the composite was prepared with SiHAP at a 3 wt% concentration. When mentioned biocomposite was applied, the numbers of attached cells on the composite were seen at the highest level. These data showed that the biocompatibility feature of PHBV improved by adding SiHAP at enhanced concentrations. These results are also coherent with the data from cytotoxicity experiments. Both results decipher that composites prepared by PHBV and SiHAP could advance cells' proliferation and migration abilities while massively reducing the toxicity originating from PHBV. Obtained results are also coherent with the data acquired from previous articles. In a similar study, Huang *et al.* [61] conjugated HAP nanoplates with polylactide polymer and investigated the bioavailability of newly synthesized nanocomposites for bone tissue engineering. Authors exhibited that cell proliferation rates of murine preosteoblast cell line (MC3T3-E1) osteoblast cells decreased to 60% at the end of 24 h incubation when polylactide polymer was applied alone. On the other side, adding HAP nanoparticles into the polymeric material enormously

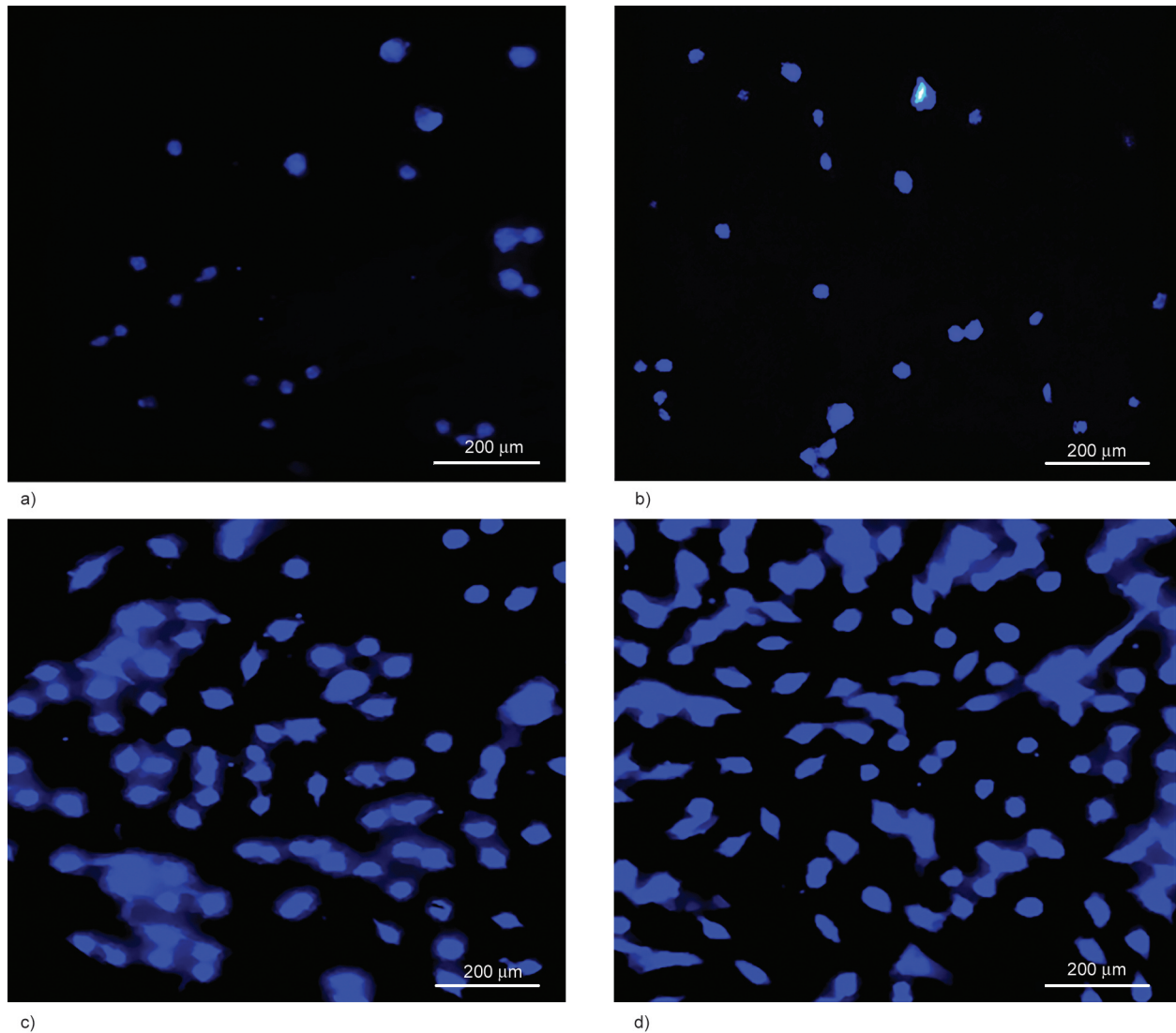


Figure 8. Morphological views of fibroblast cells that were seeded onto a) PHBV, b) PHBV-SiHAP0.5, c) PHBV-SiHAP 2.0, d) PHBV-SiHAP 3.0.

lifted the cellular vitality degrees of osteoblasts following 24 h incubation. Additionally, high osteoblast viability was evaluated in response to the scaffold application, including increased nano-HAP concentrations. At all investigated time intervals, the numbers of osteoblasts were higher in the group in which they were exposed to composites in comparison to the use of polymer alone. In another experiment, researchers accounted for the cell spreading over tested scaffolds. Results showed that approximately 2 mm of scaffolds were covered with osteoblasts in the group in which the composite included 15% HAP. Moreover, it was also determined that the numbers of cells that were adhered to scaffolds were lower in the group in which polylactide was used alone in contrast to the application of polymers incorporated with nano-HAP, according to fluorescence microscopy results. Suslu *et al.* [7] prepared

HAP-PHBV nanofibers as a biocomposite by electrospinning technique in another research similar to ours. They exhibited that these nanofibers, including HAP, synthesized with different surfactants, extensively ameliorated the osteoconductive feature of the PHBV scaffold.

Bioactivity and biocompatibility features of SiHAP were proven in previous studies. In one of them, Sun *et al.* [19] combined HAP and silicone to prepare scaffolds for bone tissue engineering and examined the bioactivity of prepared composites. Outputs showed that adding silicone at various dosages did not influence the cytocompatibility properties of HAP, and both HAP and HAP-silicone composites were found biocompatible at variable concentrations ranging between 25 and 400 $\mu\text{g/ml}$.

This study is the first report indicating that PHBV-SiHAP composites enhance cell proliferation and

migration while decreasing the cytotoxicity of PHBV. In light of this research, we proposed that SiHAP-enriched PHBV could be a promising alternative for using biomedical applications.

4. Conclusions

PHBV reinforced with SiHAP nanocrystals was successfully obtained by melt extrusion using different amounts of particles (0.5, 2, and 3 wt%). We assessed the physical, thermal, thermomechanical, and biological properties of the PHBV-SiHAP bionanocomposites. SiHAP nanoparticles increased the crystallinity of the PHBV matrix, which was confirmed by the XRD analysis. All nanocomposites exhibited improved storage modulus with the addition of SiHAP. The storage modulus of PHBV increases by 80% for PHBV-SiHAP0.5 HAP at 20 °C. This result may be related to the favorable interactions between the polymer matrix and SiHAP that restrict the movement of polymer chains. All these results showed that Si-doped HAP is a very effective reinforcing agent reaching a higher storage modulus with a considerably lower fraction.

We found that the neat PHBV was not tolerable in terms of toxicity since cellular viability rates were assessed as 60% after using sample extracts. However, it was ascertained that adding SiHAP at enhanced concentrations led to noticeable improvements in cellular viability ratios. It was detected that cell viability rates reached 92% when composite including PHBV and SiHAP 3 wt% were performed. These data elicit absolute compatibility between high cell viability rates and advanced SiHAP concentrations. It can be concluded that enrichment of PHBV with increased SiHAP dosages could improve the bioavailability of polymer.

DAPI staining experiments reflected that PHBV-SiHAP composites ensured significant increases in cell attachment, proliferation, and migration in comparison to PHBV polymeric scaffold. In addition, we also established that proliferation and migration levels of osteoblasts markedly augmented as a response to advances in the concentrations of SiHAP within the composites under fluorescence microscope images. Obtained results in the present study reveal that SiHAP reinforced PHBV composites were completely bioavailable and biocompatible. We suggest that

these novel composites that meet the mechanical strength, bioactive, biocompatible, and non-toxic requirements of biomaterials are promising biocomposites for biomedical applications.

Acknowledgements

This research has been supported by the Research Fund of the Yildiz Technical University. Project Number: FYL-2021-4650.

References

- [1] Pantani R., Turg L.-S.: Manufacturing of advanced biodegradable polymeric components. *Journal of Applied Polymer Science*, **132**, 42889 (2015).
<https://doi.org/10.1002/app.42889>
- [2] Silva A. P. B., Montagna L. S., Passador F. R., Rezende M. C., Lemes A. P.: Biodegradable nanocomposites based on PLA/PHBV blend reinforced with carbon nanotubes with potential for electrical and electromagnetic applications. *Express Polymer Letters*, **15**, 987–1003 (2021).
<https://doi.org/10.3144/expresspolymlett.2021.79>
- [3] Jost V.: Packaging related properties of commercially available biopolymers – An overview of the status quo. *Express Polymer Letters*, **12**, 429–435 (2018).
<https://doi.org/10.3144/expresspolymlett.2018.36>
- [4] Khardenavis A. A., Suresh Kumar M., Mudliar S. N., Chakrabarti T.: Biotechnological conversion of agro-industrial wastewaters into biodegradable plastic, poly β -hydroxybutyrate. *Bioresource Technology*, **98**, 3579–3584 (2007).
<https://doi.org/10.1016/j.biortech.2006.11.024>
- [5] Lenz R. W., Marchessault R. H.: Bacterial polyesters: Biosynthesis, biodegradable plastics and biotechnology. *Biomacromolecules*, **6**, 1–8 (2005).
<https://doi.org/10.1021/bm049700c>
- [6] Sadat-Shojai M.: Electrospun polyhydroxybutyrate/hydroxyapatite nanohybrids: Microstructure and bone cell response. *Journal of Materials Science and Technology*, **32**, 1013–1020 (2016).
<https://doi.org/10.1016/j.jmst.2016.07.007>
- [7] Suslu A., Albayrak A. Z., Urkmez A. S., Bayir E., Cocen U.: Effect of surfactant types on the biocompatibility of electrospun HAP/PHBV composite nanofibers. *Journal of Materials Science: Materials in Medicine*, **25**, 2677–2689 (2014).
<https://doi.org/10.1007/s10856-014-5286-1>
- [8] Sadat-Shojai M., Khorasani M.-T., Jamshidi A., Irani S.: Nano-hydroxyapatite reinforced polyhydroxybutyrate composites: A comprehensive study on the structural and *in vitro* biological properties. *Materials Science and Engineering C*, **33**, 2776–2787 (2013).
<https://doi.org/10.1016/j.msec.2013.02.041>

- [9] Panayotidou E., Kroustalli A., Baklavariadis A., Zuburtikudis I., Achilias D. S., Deligianni D.: Biopolyester-based nanocomposites: Structural, thermo-mechanical and biocompatibility characteristics of poly(3-hydroxybutyrate)/montmorillonite clay nanohybrids. *Journal of Applied Polymer Science*, **132**, 41628 (2015). <https://doi.org/10.1002/app.41628>
- [10] Anjum A., Zuber M., Zia K. M., Noreen A., Anjum M. N., Tabasum S.: Microbial production of polyhydroxyalkanoates (PHAs) and its copolymers: A review of recent advancements. *International Journal of Biological Macromolecules*, **89**, 161–174 (2016). <https://doi.org/10.1016/j.ijbiomac.2016.04.069>
- [11] Knowles J. C., Hastings G. W., Ohta H., Niwa S., Boeree N.: Development of a degradable composite for orthopaedic use: *In vivo* biomechanical and histological evaluation of two bioactive degradable composites based on the polyhydroxybutyrate polymer. *Biometaterials*, **13**, 491–496 (1992). [https://doi.org/10.1016/0142-9612\(92\)90099-A](https://doi.org/10.1016/0142-9612(92)90099-A)
- [12] Luzier W. D.: Materials derived from biomass/biodegradable materials. *PNAS*, **89**, 839–842 (1992). <https://doi.org/10.1073/pnas.89.3.839>
- [13] Wang N., Zhou Z., Xia L., Dai Y., Liu H.: Fabrication and characterization of bioactive β -Ca₂SiO₄/PHBV composite scaffolds. *Materials Science and Engineering C*, **33**, 2294–2301 (2013). <https://doi.org/10.1016/j.msec.2013.01.059>
- [14] Sultana N., Khan T. H.: *In vitro* degradation of PHBV scaffolds and nHA/PHBV composite scaffolds containing hydroxyapatite nanoparticles for bone tissue engineering. *Journal of Nanomaterials*, **2012**, 190950 (2012). <https://doi.org/10.1155/2012/190950>
- [15] Gogolewski S., Jovanovic M., Perren S. M., Dillon J. G., Hughes' M. K.: Tissue response and *in vivo* degradation of selected polyhydroxyacids: Polylactides (PLA), poly(3-hydroxybutyrate) (PHB), and poly(3-hydroxybutyrate-co-3-hydroxyvalerate) (PHB/VA). *Journal of Biomedical Materials Research*, **27**, 1135–1147 (1993). <https://doi.org/10.1002/jbm.820270904>
- [16] Bassett D. C.: *Developments in crystalline polymers*. Springer, Dordrecht (1988). <https://doi.org/10.1007/978-94-009-1341-7>
- [17] Liu J., Zhao B., Zhang Y., Lin Y., Hu P., Ye C.: PHBV and predifferentiated human adipose-derived stem cells for cartilage tissue engineering. *Journal of Biomedical Materials Research: Part A*, **94**, 603–610 (2010). <https://doi.org/10.1002/jbm.a.32730>
- [18] Alizadeh-Osgouei M., Li Y., Wen C.: A comprehensive review of biodegradable synthetic polymer-ceramic composites and their manufacture for biomedical applications. *Bioactive Materials*, **4**, 22–36 (2019). <https://doi.org/10.1016/j.bioactmat.2018.11.003>
- [19] Sun T., Wang M., Shao Y., Wang L., Zhu Y.: The effect and osteoblast signaling response of trace silicon doping hydroxyapatite. *Biological Trace Element Research*, **181**, 82–94 (2018). <https://doi.org/10.1007/s12011-017-1031-1>
- [20] Qiao H., Song G., Huang Y., Yang H., Han S., Zhang X., Wang Z., Ma J., Bu X., Fu L.: Si, Sr, Ag co-doped hydroxyapatite/TiO₂ coating: Enhancement of its antibacterial activity and osteoinductivity. *RSC Advances*, **9**, 13348–13364 (2019). <https://doi.org/10.1039/c9ra01168d>
- [21] Arcos D., Rodríguez-Carvajal J., Vallet-Regí M.: Silicon incorporation in hydroxylapatite obtained by controlled crystallization. *Chemistry of Materials*, **16**, 2300–2308 (2004). <https://doi.org/10.1021/cm035337p>
- [22] Botelho C. M., Brooks R. A., Best S. M., Lopes M. A., Santos J. D., Rushton N., Bonfield W.: Human osteoblast response to silicon-substituted hydroxyapatite. *Journal of Biomedical Materials Research: Part A*, **79**, 723–730 (2006). <https://doi.org/10.1002/jbm.a.30806>
- [23] Balamurugan A., Rebelo A. H. S., Lemos A. F., Rocha J. H. G., Ventura J. M. G., Ferreira J. M. F.: Suitability evaluation of sol-gel derived Si-substituted hydroxyapatite for dental and maxillofacial applications through *in vitro* osteoblasts response. *Dental Materials*, **24**, 1374–1380 (2008). <https://doi.org/10.1016/j.dental.2008.02.017>
- [24] Gomes P. S., Botelho C., Lopes M. A., Santos J. D., Fernandes M. H.: Evaluation of human osteoblastic cell response to plasma-sprayed silicon-substituted hydroxyapatite coatings over titanium substrates. *Journal of Biomedical Materials Research Part B: Applied Biomaterials*, **94**, 337–346 (2010). <https://doi.org/10.1002/jbm.b.31656>
- [25] Balas F., Pérez-Pariente J., Vallet-Regí M.: *In vitro* bioactivity of silicon-substituted hydroxyapatites. *Journal of Biomedical Materials Research*, **A66**, 364–375 (2003). <https://doi.org/10.1002/jbm.a.10579>
- [26] Russias J., Saiz E., Nalla R. K., Gryn K., Ritchie R. O., Tomsia A. P.: Fabrication and mechanical properties of PLA/HA composites: A study of *in vitro* degradation. *Materials Science and Engineering C*, **26**, 1289–1295 (2006). <https://doi.org/10.1016/j.msec.2005.08.004>
- [27] Ignjatovic N., Uskokovic D.: Synthesis and application of hydroxyapatite/polylactide composite biomaterial. *Applied Surface Science*, **238**, 314–319 (2004). <https://doi.org/10.1016/j.apsusc.2004.05.227>
- [28] Freier T.: Biopolyesters in tissue engineering applications. *Advances in Polymer Science* **203**, 1–61 (2006). https://doi.org/10.1007/12_073
- [29] Shishatskaya E. I., Khlusov I. A., Volova T. G.: A hybrid PHB–hydroxyapatite composite for biomedical application: Production, *in vitro* and *in vivo* investigation. *Journal of Biomaterials Science, Polymer Edition*, **17**, 481–498 (2006). <https://doi.org/10.1163/156856206776986242>

- [30] Nahanmoghadam A., Asemani M., Goodarzi V., Ebrahimi-Barough S.: *In vivo* investigation of PCL/PHBV/hydroxyapatite nanocomposite scaffold in regeneration of critical-sized bone defects. *Fibers and Polymers*, **22**, 2507–2516 (2021).
<https://doi.org/10.1007/s12221-021-1243-z>
- [31] Yuan J., Zheng Q., Cheng J.: Fabrication, characterization and adsorptive of human fibrinogen of HA/PHBV nanocomposite films. *Advanced Materials Research*, **160–162**, 1325–1330 (2011).
<https://doi.org/10.4028/www.scientific.net/AMR.160-162.1325>
- [32] Chen D. Z., Tang C. Y., Chan K. C., Tsui C. P., Yu P. H. F., Leung M. C. P., Uskokovic P. S.: Dynamic mechanical properties and *in vitro* bioactivity of PHBV/HA nanocomposite. *Composites Science and Technology*, **67**, 1617–1626 (2007).
<https://doi.org/10.1016/j.compscitech.2006.07.034>
- [33] Rai B., Noohom W., Kithva P. H., Grøndahl L., Trau M.: Bionanohydroxyapatite/poly(3-hydroxybutyrate-co-3-hydroxyvalerate) composites with improved particle dispersion and superior mechanical properties. *Chemistry of Materials*, **20**, 2802–2808 (2008).
<https://doi.org/10.1021/cm703045u>
- [34] Öner M., İlhan B.: Fabrication of poly(3-hydroxybutyrate-co-3-hydroxyvalerate) biocomposites with reinforcement by hydroxyapatite using extrusion processing. *Materials Science and Engineering C*, **65**, 19–26 (2016).
<https://doi.org/10.1016/j.msec.2016.04.024>
- [35] Yu H., Sun B., Zhang D., Chen G., Yang X., Yao J.: Reinforcement of biodegradable poly(3-hydroxybutyrate-co-3-hydroxyvalerate) with cellulose nanocrystal/silver nanohybrids as bifunctional nanofillers. *Journal of Materials Chemistry B*, **2**, 8479–8489 (2014).
<https://doi.org/10.1039/c4tb01372g>
- [36] Huang W., Wang Y., Ren L., Du C., Shi X.: A novel PHBV/HA microsphere releasing system loaded with alendronate. *Materials Science and Engineering C*, **29**, 2221–2225 (2009).
<https://doi.org/10.1016/j.msec.2009.05.015>
- [37] Kawamura Y., Gan H., Kabe T., Machara A., Kimura S., Hikima T., Takata M., Iwata T.: Mechanism of elastic properties of biodegradable poly[(R)-3-hydroxybutyrate-co-4-hydroxybutyrate] films revealed by synchrotron radiation. *ACS Omega*, **6**, 7387–7393 (2021).
<https://doi.org/10.1021/acsomega.0c05662>
- [38] Zhijiang C., Guang Y.: Optical nanocomposites prepared by incorporating bacterial cellulose nanofibrils into poly(3-hydroxybutyrate). *Materials Letters*, **65**, 182–184 (2011).
<https://doi.org/10.1016/j.matlet.2010.09.055>
- [39] Öner M., Kızıllı G., Keskin G., Pochat-Bohatier C., Bechelany M.: The effect of boron nitride on the thermal and mechanical properties of poly(3-hydroxybutyrate-co-3-hydroxyvalerate). *Nanomaterials*, **8**, 940 (2018).
<https://doi.org/10.3390/nano8110940>
- [40] Rusmirović J. D., Ivanović J. Z., Pavlović V. B., Rakić V. M., Rančić M. P., Djokić V., Marinković A. D.: Novel modified nanocellulose applicable as reinforcement in high-performance nanocomposites. *Carbohydrate Polymers*, **164**, 64–74 (2017).
<https://doi.org/10.1016/j.carbpol.2017.01.086>
- [41] Ambrosio-Martín J., Gorrasi G., Lopez-Rubio A., Fabra M. J., Mas L. C., López-Manchado M. A., Lagaron J. M.: On the use of ball milling to develop poly(3-hydroxybutyrate-co-3-hydroxyvalerate)-graphene nanocomposites (II) – Mechanical, barrier, and electrical properties. *Journal of Applied Polymer Science*, **132**, 42217 (2015).
<https://doi.org/10.1002/app.42217>
- [42] Yu H., Yan C., Yao J.: Fully biodegradable food packaging materials based on functionalized cellulose nanocrystals/poly(3-hydroxybutyrate-co-3-hydroxyvalerate) nanocomposites. *RSC Advances*, **4**, 59792–59802 (2014).
<https://doi.org/10.1039/c4ra12691b>
- [43] Wei L., McDonald A. G., Stark N. M.: Grafting of bacterial polyhydroxybutyrate (PHB) onto cellulose *via in situ* reactive extrusion with dicumyl peroxide. *Biomacromolecules*, **16**, 1040–1049 (2015).
<https://doi.org/10.1021/acs.biomac.5b00049>
- [44] Díez-Pascual A. M., Díez-Vicente A. L.: ZnO-reinforced poly(3-hydroxybutyrate-co-3-hydroxyvalerate) bionanocomposites with antimicrobial function for food packaging. *ACS Applied Materials and Interfaces*, **6**, 9822–9834 (2014).
<https://doi.org/10.1021/am502261e>
- [45] Lemes A. P., Soto-Oviedo M. A., Waldman W. R.: Innocentini-Mei L. H., Durán N.: Effect of lignosulfonate on the thermal and morphological behavior of poly(3-hydroxybutyrate-co-3-hydroxyvalerate). *Journal of Polymers and the Environment*, **18**, 250–259 (2010).
<https://doi.org/10.1007/s10924-010-0170-7>
- [46] Ten E., Turtle J., Bahr D., Jiang L., Wolcott M.: Thermal and mechanical properties of poly(3-hydroxybutyrate-co-3-hydroxyvalerate)/cellulose nanowhiskers composites. *Polymer*, **51**, 2652–2660 (2010).
<https://doi.org/10.1016/j.polymer.2010.04.007>
- [47] Wang S., Xiang H., Wang R., Zhou Z., Zhu M.: Influence of amorphous alkaline lignin on the crystallization behavior and thermal properties of bacterial polyester. *Journal of Applied Polymer Science*, **132**, 41325 (2015).
<https://doi.org/10.1002/app.41325>
- [48] de Almeida Neto G. R., Barcelos M. V., Ribeiro M. E. A., Folly M. M., Rodríguez R. J. S.: Formulation and characterization of a novel PHBV nanocomposite for bone defect filling and infection treatment. *Materials Science and Engineering C*, **104**, 110004 (2019).
<https://doi.org/10.1016/j.msec.2019.110004>
- [49] Ambrosio-Martín J., Gorrasi G., Lopez-Rubio A., Fabra M. J., Mas L. C., López-Manchado M. A., Lagaron J. M.: On the use of ball milling to develop PHBV–graphene nanocomposites (I) – Morphology, thermal properties, and thermal stability. *Journal of Applied Polymer Science*, **132**, 42101 (2015).
<https://doi.org/10.1002/app.42101>

- [50] Castro-Mayorga J. L., Fabra M. J., Pourrahimi A. M., Olsson R. T., Lagaron J. M.: The impact of zinc oxide particle morphology as an antimicrobial and when incorporated in poly(3-hydroxybutyrate-co-3-hydroxyvalerate) films for food packaging and food contact surfaces applications. *Food and Bioproducts Processing*, **101**, 32–44 (2017).
<https://doi.org/10.1016/j.fbp.2016.10.007>
- [51] Anžlovar A., Kržan A., Žagar E.: Degradation of PLA/ZnO and PHBV/ZnO composites prepared by melt processing. *Arabian Journal of Chemistry*, **11**, 343–352 (2018).
<https://doi.org/10.1016/j.arabjc.2017.07.001>
- [52] Braga N. F., Vital D. A., Guerrini L. M., Lemes A. P., Formaggio D. M. D., Tada D. B., Arantes T. M., Cristovan F. H.: PHBV-TiO₂ mats prepared by electrospinning technique: Physico-chemical properties and cytocompatibility. *Biopolymers*, **109**, e23120 (2018).
<https://doi.org/10.1002/bip.23120>
- [53] Srithep Y., Ellingham T., Peng J., Sabo R., Clemons C., Turng L-S., Pilla S.: Melt compounding of poly(3-hydroxybutyrate-co-3-hydroxyvalerate)/nanofibrillated cellulose nanocomposites. *Polymer Degradation and Stability*, **98**, 1439–1449 (2013).
<https://doi.org/10.1016/j.polymdegradstab.2013.05.006>
- [54] Chen L. J., Wang M.: Production and evaluation of biodegradable composites based on PHB-PHV copolymer. *Biomaterials*, **23**, 2631–2639 (2002).
[https://doi.org/10.1016/S0142-9612\(01\)00394-5](https://doi.org/10.1016/S0142-9612(01)00394-5)
- [55] Sánchez-Safont E. L., González-Ausejo J., Gámez-Pérez J., Lagarón J. M., Cabedo L.: Poly(3-hydroxybutyrate-co-3-hydroxyvalerate)/ purified cellulose fiber composites by melt blending: Characterization and degradation in composting conditions. *Journal of Renewable Materials*, **4**, 123–132 (2016).
<https://doi.org/10.7569/JRM.2015.634127>
- [56] Michael F. M., Khalid M., Raju G., Ratnam C. T., Walvekar R., Mubarak N. M.: Viscoelastic properties and thermal stability of nanohydroxyapatite reinforced poly(lactic acid) for load bearing applications. *Molecules*, **26**, 5852 (2021).
<https://doi.org/10.3390/molecules26195852>
- [57] Mittal P., Naresh S., Luthra P., Singh A., Dhaliwal J. S., Kapur G. S.: Polypropylene composites reinforced with hybrid inorganic fillers: Morphological, mechanical, and rheological properties. *Journal of Thermoplastic Composite Materials*, **32**, 848–864 (2019).
<https://doi.org/10.1177/0892705718785674>
- [58] Jack K. S., Velayudhan S., Luckman P., Trau M., Grøndahl L., Cooper-White J.: The fabrication and characterization of biodegradable HA/PHBV nanoparticle-polymer composite scaffolds. *Acta Biomaterialia*, **5**, 2657–2667 (2009).
<https://doi.org/10.1016/j.actbio.2009.03.017>
- [59] Esposti M. D., Changizi M., Salvatori R., Chiarini L., Cannillo V., Morselli D., Fabbri P.: Comparative study on bioactive filler/biopolymer scaffolds for potential application in supporting bone tissue regeneration. *ACS Applied Polymer Materials*, **4**, 4306–4318 (2022).
<https://doi.org/10.1021/acsapm.2c00270>
- [60] Wu J., Wu Z., Xue Z., Li H., Liu J.: PHBV/bioglass composite scaffolds with co-cultures of endothelial cells and bone marrow stromal cells improve vascularization and osteogenesis for bone tissue engineering. *RSC Advances*, **7**, 22197–22207 (2017).
<https://doi.org/10.1039/c7ra02767b>
- [61] Huang Z., Wan Y., Peng M., Yang Z., Luo H.: Incorporating nanoplate-like hydroxyapatite into polylactide for biomimetic nanocomposites *via* direct melt intercalation. *Composites Science and Technology*, **185**, 107903 (2020).
<https://doi.org/10.1016/j.compscitech.2019.107903>

Research article

Dual effect of wood fiber as bio-nucleating agent and reinforcement material in wood fiber/poly(lactic acid) composites

Chao Lv^{ID}, Shupin Luo^{*ID}, Wenjing Guo

Research Institute of Wood Industry, Chinese Academy of Forestry, No. 2 Dongxiaofu, Haidian District, 100091 Beijing, China

Received 9 September 2022; accepted in revised form 19 November 2022

Abstract. Biodegradable plastics such as poly(lactic acid) (PLA) are gaining considerable interest as promising substitutes for conventional petroleum-based plastics due to ecological, health, and environmental concerns. PLA possesses good biodegradability and biocompatibility but is limited by its slow crystallization rate, low impact resistance, and high costs. In this study, a small amount of natural wood fiber (WF) was incorporated into PLA to improve mechanical and crystallization properties as well as cost reduction. The effects of WF size (20–40, 80–100, and 140–160 mesh) and loading content (0.5–8 wt%) on the mechanical and crystallization properties were investigated and compared. Results indicated that WF of 80–100 mesh (WF₈₀₋₁₀₀) exhibited a better reinforcement effect on PLA than the other two sizes of WF. The optimal loading content for WF₈₀₋₁₀₀ was 1 wt%, at which the flexural and tensile strength increased by about 18% compared to neat PLA, and the elongation at break increased by 27%. Moreover, the degree of crystallinity and crystallization rate significantly increased with the addition of WF₈₀₋₁₀₀. Polarized optical microscopy observation revealed that the number of spherulites increased in 1WF₈₀₋₁₀₀/PLA composite and the spherulite size decreased compared to neat PLA. These findings confirmed that WF, even at a low addition level, could act as both a reinforcement material and an efficient nucleating agent for PLA, which is closely related to its size.

Keywords: biocomposites, mechanical properties, reinforcements, poly(lactic acid), bio-nucleating agent

1. Introduction

In recent years, the disposal of plastic waste has become a serious environmental issue. Biodegradable plastics from renewable resources have been receiving increasing attention as potential alternatives to petroleum-based plastics [1]. Poly(lactic acid) (PLA) is a fully bio-based and bio-degradable plastic produced completely from renewable resources and can be degraded into carbon dioxide and water without any pollution. It shows great superiority in the aspect of biodegradability, biocompatibility, and processability, which makes it a promising alternative to traditional petroleum-based polymers in

fields of medical, packaging, cutleries, *etc.* [2, 3]. However, PLA is limited by its low crystallization rate, brittleness, and high production price for specific fields of applications [4, 5]. Also, PLA has a lower crystallization rate as compared to conventional synthetic plastics such as polypropylene and polyethylene, which requires longer molding cycle time and leads to low productivity [6, 7]. Another major drawback of PLA is its poor toughness, with low elongation at break and relatively poor impact strength, thereby limiting its applications as films, fiber or biomedical materials that require plastic deformation [8, 9].

*Corresponding author, e-mail: luosp@caf.ac.cn
© BME-PT

Various strategies, including blending with other polymers, adding nucleating agents, incorporating fillers, compounding with plasticizers, and copolymerizing chemicals, have been investigated to overcome the aforementioned drawbacks of PLA [10–12]. Among all these technologies, adding a nucleating agent is a simple but effective method to facilitate the crystallization process and improve crystallization temperature during cooling [6]. Nucleating agents could increase the number of primary nucleation sites and accelerate nucleation by reducing the surface free energy nuclei barrier [13]. The common nucleating agents used in PLA mainly include mineral, organic, bio-based, and stereocomplex categories. Previous studies have identified some effective nucleating agents for PLA, such as talc [14], calcium carbonate [15, 16], and silica [17]. The nucleation effect largely depends on the properties of the nucleating agent including types, particle size, geometry, and dispersion in the matrix [18, 19]. Recently, introducing bio-based nucleating agents have attracted more interest owing to preserving the green properties of PLA, which is attractive for broadening the utilization of PLA for biodegradable product development. For instance, starch [20], cellulose [4], and lignin [21] have been evaluated as heterogeneous nucleating agents to improve the crystallization rate of PLA. Wood filler (wood flour and fiber) is also a promising natural bio-nucleating agent for PLA. It was found that the addition of 4 wt% wood flour increased the nucleation density of PLA and reduced half-crystallization time [22].

As the most widely known and used natural filler, wood filler has raised a lot of interest in recent years, and its composite with other polymers is extensively investigated. Many researchers have investigated the use of wood filler as reinforcement of PLA due to its low cost, easy availability, and bio-based nature [23]. In these studies, a high amount of wood filler was often incorporated into PLA for the purpose of cost reduction and achieving a balance between sustainability and performance. Previous studies on wood filler/PLA composites show differences in their mechanical properties. Huda *et al.* [24] found that the incorporation of 20 wt% wood fiber (WF) into PLA resulted in a considerable increase in the tensile strength and modulus but a decrease in notched Izod impact strength. Dobrzyńska-Mizera *et al.* [25] prepared PLA-based composites with WF content of 30 wt% and found that the tensile strength was decreased

while Young's modulus was improved. Petinakis *et al.* [26] found that the addition of up to 40 wt% wood flour into PLA caused a significant decrease in break elongation. Generally, under the same manufacturing parameters, the effect of wood filler on the physical and mechanical properties of PLA depends largely on the nature of wood filler, such as the size and distribution of wood particles, wood filler species, and contents [27]. For instance, wood fiber provides higher plastic reinforcement than wood flour [19]. Moreover, a high amount of fillers cause difficulties in fabrication and may not generate a significant reinforcement effect.

A review of the literature shows that the comparative studies of the PLA-based composites containing different sizes of WF are very limited. Moreover, few studies pay attention to the effect of a small amount of WF as a reinforcement and bio-nucleating agent for PLA. Therefore, the aim of this study was to systematically evaluate the role of a small amount of WF with different sizes and contents in WF/PLA composites. Herein, poplar WF was sieved into three distinct size grades and respectively compounded with PLA. The mechanical properties of PLA composites with three sizes of WF were comparatively studied, and the optimal WF size was determined. After that, a small amount of WF with the selected size was incorporated with PLA to prepare WF/PLA composites. The crystallization behavior, crystalline morphology, and structure of WF/PLA composites with different WF contents were further investigated. This work indicates that WF at appropriate size and content plays the role of both reinforcement material and nucleating agent for PLA, which promotes producing completely biodegradable PLA-based composite and broadening application fields of PLA.

2. Experimental

2.1. Materials

Extrusion grade PLA 2002D, Natureworks, Minnesota, USA) was used as the polymer matrix. It's comprised of 4% D-lactic, and its melt flow index is 4–8 g/10 min (210 °C, 2.16 kg). Poplar (*Populus tomentosa* Carr.) WF was provided by Yongdeshun mineral processing factory (Hebei Province, China). The WF was sieved to three sizes: 20–40 mesh (WF₂₀₋₄₀), 80–100 mesh (WF₈₀₋₁₀₀), and 140–160 mesh (WF₁₄₀₋₁₆₀) by using an automatic vibratory sieve shaker (JEL 200, Engelsmann, Ludwigs-hafen, Germany).

2.2. Preparation of WF/PLA composites with varying WF sizes

After drying in an oven at 103 °C for 6–8 h, 1 wt% WF of each size was mixed with PLA in a high-speed mixer. Then the mixture was extruded using a single-screw extruder (SJ35, Orodes machinery Co. Ltd, Zhangjiagang, China) and crushed into about 4 mm long granules. The extrusion temperature was 180 °C, and the screw speed was 20 rpm. Then the pellets were molded using a hydraulic press (type 3889, Carver Inc., USA) at 190 °C with a pressure of 4 MPa for 5 min. After that, the samples were cold pressed at 6 MPa for another 5 min at room temperature to obtain WF/PLA composites (1WF₂₀₋₄₀/PLA, 1WF₈₀₋₁₀₀/PLA, and 1WF₁₄₀₋₁₆₀/PLA).

2.3. Preparation of WF/PLA composites with varying WF contents

According to our preliminary experiment results, WF₈₀₋₁₀₀ was selected to explore the optimum WF content for reinforcing and nucleating PLA. Subsequently, 0.5, 1, 2, 4, and 8 wt% of WF₈₀₋₁₀₀ were compounded with PLA for preparing 0.5WF₈₀₋₁₀₀/PLA, 1WF₈₀₋₁₀₀/PLA, 2WF₈₀₋₁₀₀/PLA, 4WF₈₀₋₁₀₀/PLA, and 8WF₈₀₋₁₀₀/PLA composites, respectively. WF/PLA composites containing 0.5–8.0 wt% WF₈₀₋₁₀₀ were mixed, extruded, crushed, and molded using the same procedures as mentioned above. Figure 1 shows the process of preparing WF₈₀₋₁₀₀/PLA composites containing varying contents of WF₈₀₋₁₀₀.

2.4. WF morphology and size distribution

The microscopic morphology of WF₂₀₋₄₀, WF₈₀₋₁₀₀, and WF₁₄₀₋₁₆₀ was observed by optical microscope (BX53, Olympus, Japan). The length and diameter distributions of WF₂₀₋₄₀ and WF₈₀₋₁₀₀ were measured by an optical lab fiber screen analyzer (FIBERCAM 100, IMAL-PAL Group, Italy). The wood fibers were separated using compressed air and imaged by

a digital camera, and the length and diameter of individual fibers were measured. Approximately 100 000 fibers were evaluated for each size of WF. This method was inapplicable for fibers below 1 mm. Therefore, the size distribution of WF₁₄₀₋₁₆₀ was determined by a laser diffraction particle size analyzer (Mastersizer 2000, Malvern Panalytical, UK). The surface of WF/PLA composites containing different sizes of WF was observed by an optical microscope to investigate the distribution of WF in the PLA matrix.

2.5. Scanning electron microscopy (SEM)

The fracture surface of the WF/PLA composites after impact tests was gold sputter-coated and observed using a field emission scanning electron microscopy (Gemini 300, ZEISS, UK) with an accelerating voltage 3 kV. The overall morphology of the composites and the interaction of WF with PLA was investigated.

2.6. Mechanical properties

Izod notched impact strength was measured using a HIT50P pendulum impact tester (Zwick/Roell, German) referred to ISO 180:2000. The 80×10×4 mm standard specimens were notched for impact tests. The flexural properties of samples were tested on a 5582 Universal mechanical testing machine (Instron, USA) for three-point bending at a 2 mm/min loading rate referred to ISO 178:2001. The standard specimens of 80×10×4 mm dimensions were placed between two supports at a distance of 64 mm for the flexural test. Tensile properties were tested on a 5582 Universal mechanical testing machine (Instron, USA) at a crosshead speed of 5 mm/min, referred to ISO 527:2012. Samples for tensile tests were molded into dog-bone-shaped specimens with a thickness of 4 mm. Tensile properties including elongation at break, tensile strength, and modulus, were measured. All presented results are the average values of ten measurements.

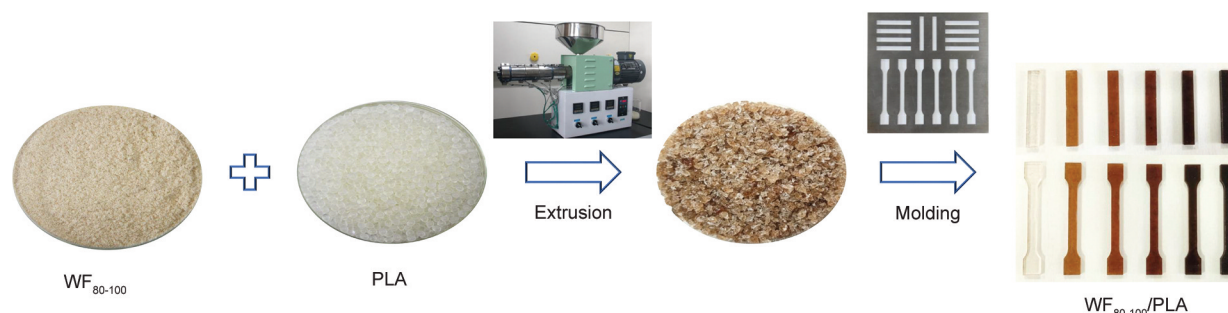


Figure 1. Process of preparing WF₈₀₋₁₀₀/PLA composites containing varying contents of WF₈₀₋₁₀₀.

2.7. Differential scanning calorimetry (DSC)

The melting and crystallization behavior of the samples were performed on a DSC apparatus (DSC8000, PerkinElmer, USA) under a nitrogen atmosphere. Fragment-shaped samples of 5–6 mg were cut from neat PLA and WF/PLA composite films and placed into sealed aluminum pans with lids. For non-isothermal crystallization, samples were firstly heated to 200 °C at a heating rate of 20 °C/min and held for 5 min to eliminate thermal history. Then samples were cooled to 30 °C at a cooling rate of 10 °C/min and reheated to 200 °C at a heating rate of 10 °C/min. In the analysis of isothermal crystallization, the sample was heated from room temperature to 200 °C at a heating rate of 20 °C/min and held for 5 min to eliminate thermal history. Then it was rapidly cooled to 120, 110, and 100 °C at a cooling rate of 50 °C/min and held at this temperature until crystallization was completed, respectively. After that, the samples were reheated to 200 °C at a heating rate of 10 °C/min. The degree of crystallinity (X_c) was calculated according to Equation (1) [14]:

$$X_c = \frac{\Delta H_m - \Delta H_{cc}}{f \cdot \Delta H_m^0} \cdot 100\% \quad (1)$$

where ΔH_m and ΔH_{cc} are the melting enthalpy and cold crystallization enthalpy of the samples, respectively. ΔH_m^0 is the standard melting enthalpy of 100% crystalline PLA, which value is 93.6 J/g [14]. f is the weight fraction of PLA in the WF/PLA composite.

2.8. Polarized optical microscope (POM)

Crystalline morphology of PLA and WF/PLA composite were observed by a polarized optical microscope (BX53, Olympus, Japan) equipped with a hot stage. The samples were firstly pressed into films of about 20 μm thickness. Then each film was put into between two cover glasses and placed in the hot stage. The sample was first heated to 200 °C at a heating rate of 20 °C/min and maintained for 5 min, then cooled to 110 °C at a rate of 50 °C/min and maintained at this temperature until the crystallization was completed. Images were taken automatically by a digital camera during the isothermal crystallization process.

2.9. Wide angle X-ray diffraction (WAXD)

WAXD was used to probe the crystalline structure of neat PLA and WF/PLA composite. The experiment was performed using a D8 Advance X-ray diffraction

(Bruker, Germany) under a voltage of 40 kV and current of 40 mA with Cu-K α tube ($\lambda = 1.5418 \text{ \AA}$) between $2\theta = 5\text{--}40^\circ$ at a scan rate of 6 °/min.

3. Results and discussion

3.1. Morphology and size distribution of WFs

Figure 2 shows the morphology of WF₂₀₋₄₀, WF₈₀₋₁₀₀, and WF₁₄₀₋₁₆₀ and their size distributions. The WF₂₀₋₄₀ and WF₈₀₋₁₀₀ exhibited a slim shape, whereas the WF₁₄₀₋₁₆₀ appeared as a fine powder. The average length/diameter ratio was determined to be 13, 10, and 5 for WF₂₀₋₄₀, WF₈₀₋₁₀₀, and WF₁₄₀₋₁₆₀, respectively. WF₂₀₋₄₀ exhibited the highest length/diameter ratio. For fiber length distribution (Figures 2b and 2e), in comparison to WF₂₀₋₄₀, WF₈₀₋₁₀₀ showed lower amounts of longer fibers (>3 mm) and higher amounts of shorter fibers (<3 mm). In the case of diameter distribution (Figures 2c and 2f), in comparison to WF₂₀₋₄₀, WF₈₀₋₁₀₀ showed higher amounts of fibers with smaller diameters (<0.16 mm). For WF₁₄₀₋₁₆₀ (Figure 2h), the average particle size was 51 μm , which was much lower than that of WF₂₀₋₄₀ and WF₈₀₋₁₀₀.

3.2. Microstructure of WF/PLA composites containing varying sizes of WF

Figure 3 shows the distribution of three sizes of WF in the PLA matrix observed under an optical microscope. It was clearly seen that the small-sized WF (WF₁₄₀₋₁₆₀) did not distribute evenly in the PLA matrix and formed agglomerates, as indicated by the dark area in Figure 3c. Figure 4 shows the fracture surface of 1WF/PLA composites containing three different sizes of WF. The fiber size has a direct influence on the microstructure of composites. The microstructure of the failure surface in Figure 4a suggested weak interfacial adhesion between large-sized WF and PLA matrix. It is evident that fiber/matrix debonding and fiber pull-out occurred at the interface of large fibers (WF₂₀₋₄₀) with the matrix, which indicated weak points in the composite. The composites prepared with the medium-sized fibers (WF₈₀₋₁₀₀) show a better cohesive structure between the fibers and the PLA compared to WF₂₀₋₄₀; however, fiber fracture and pull-out remained to be visible (Figure 4b). The composites prepared with the small-sized fibers (WF₁₄₀₋₁₆₀) show a more homogeneous and compacted structure compared to the larger fibers, with the small fibers embedded into the PLA (Figure 4c).

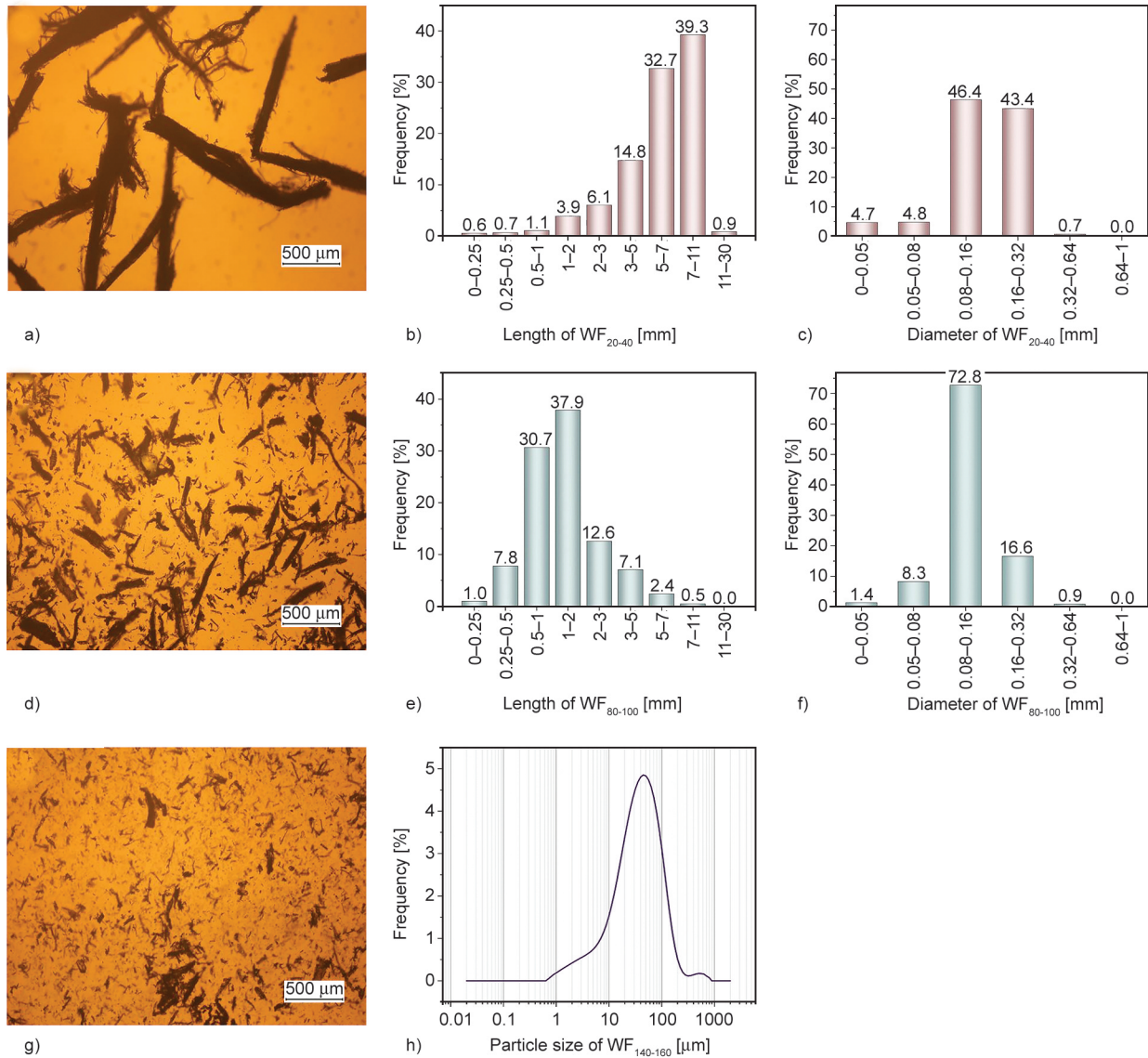


Figure 2. Optical micrograph and size distribution of WF with three sizes: a)–c) WF₂₀₋₄₀, d)–f) WF₈₀₋₁₀₀, g) and h) WF₁₄₀₋₁₆₀.

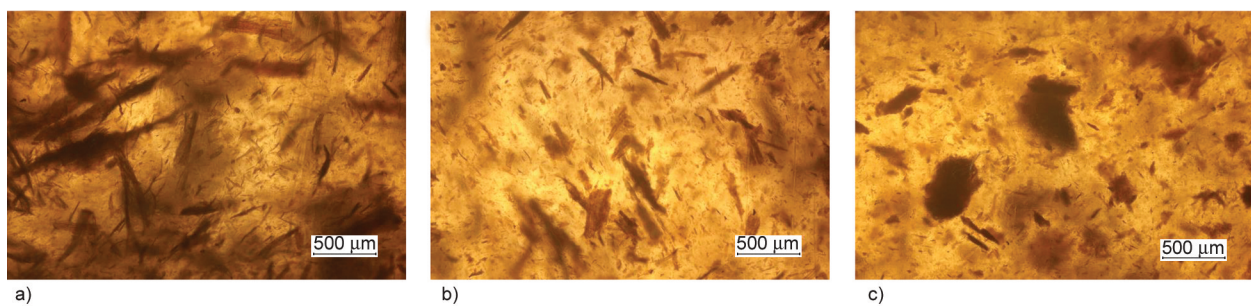


Figure 3. Distribution of three sizes of WF in PLA matrix observed under optical microscopy: a) WF₂₀₋₄₀/PLA, b) WF₈₀₋₁₀₀/PLA, c) WF₁₄₀₋₁₆₀/PLA.

3.3. Mechanical properties of the composite containing varying sizes of WF

Notched impact strength represents the energy absorbed by a material when it is ruptured [28]. The variation in notched impact strength with varying WF sizes is shown in Figure 5a. It is clearly seen that neat PLA shows lower notched impact strength of

1.49 kJ/m². Adding 1 wt% WF₂₀₋₄₀ or WF₁₄₀₋₁₆₀ had no remarkable effect on the notched impact strength of PLA. The notched impact strength of 1WF₈₀₋₁₀₀/PLA composite significantly increased by 14% compared with neat PLA, indicating WF₈₀₋₁₀₀ exhibits a better toughening effect than the other two sizes of WF. The value of elongation at break also reflects

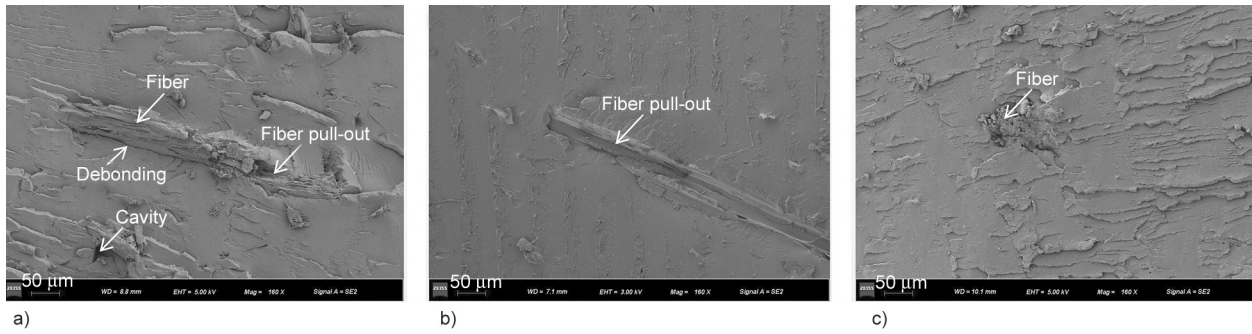


Figure 4. Scanning electron micrographs of the fracture surface of WF/PLA composite with varying WF sizes: a) WF₂₀₋₄₀/PLA, b) WF₈₀₋₁₀₀/PLA, c) WF₁₄₀₋₁₆₀/PLA.

the toughness of the composite. **Figure 5b** shows the elongation at break of neat PLA and 1WF/PLA composites containing three sizes of WF. The elongation at break for neat PLA, 1WF₂₀₋₄₀/PLA, 1WF₈₀₋₁₀₀/PLA, and 1WF₁₄₀₋₁₆₀/PLA was 1.63, 1.57, 2.07, and 1.60%, respectively. Among the three sizes of WF, the incorporation of 1 wt% WF₈₀₋₁₀₀ resulted in the highest elongation at break, which increased by 27% compared with neat PLA. Adding 1 wt% WF₂₀₋₄₀ or WF₁₄₀₋₁₆₀ had no significant effect on elongation at

break. According to the above results, the addition of WF₈₀₋₁₀₀ contributed to enhancing the toughness of PLA.

The flexural test measures the force required to bend a beam under the action of the applied load [29]. The variation of flexural strength and modulus for varying WF sizes is shown in **Figure 5c**. The flexural strength and modulus of neat PLA were 71.6 and 2788 MPa, respectively. In comparison to neat PLA, the highest elevation in flexural strength (13.1 MPa)

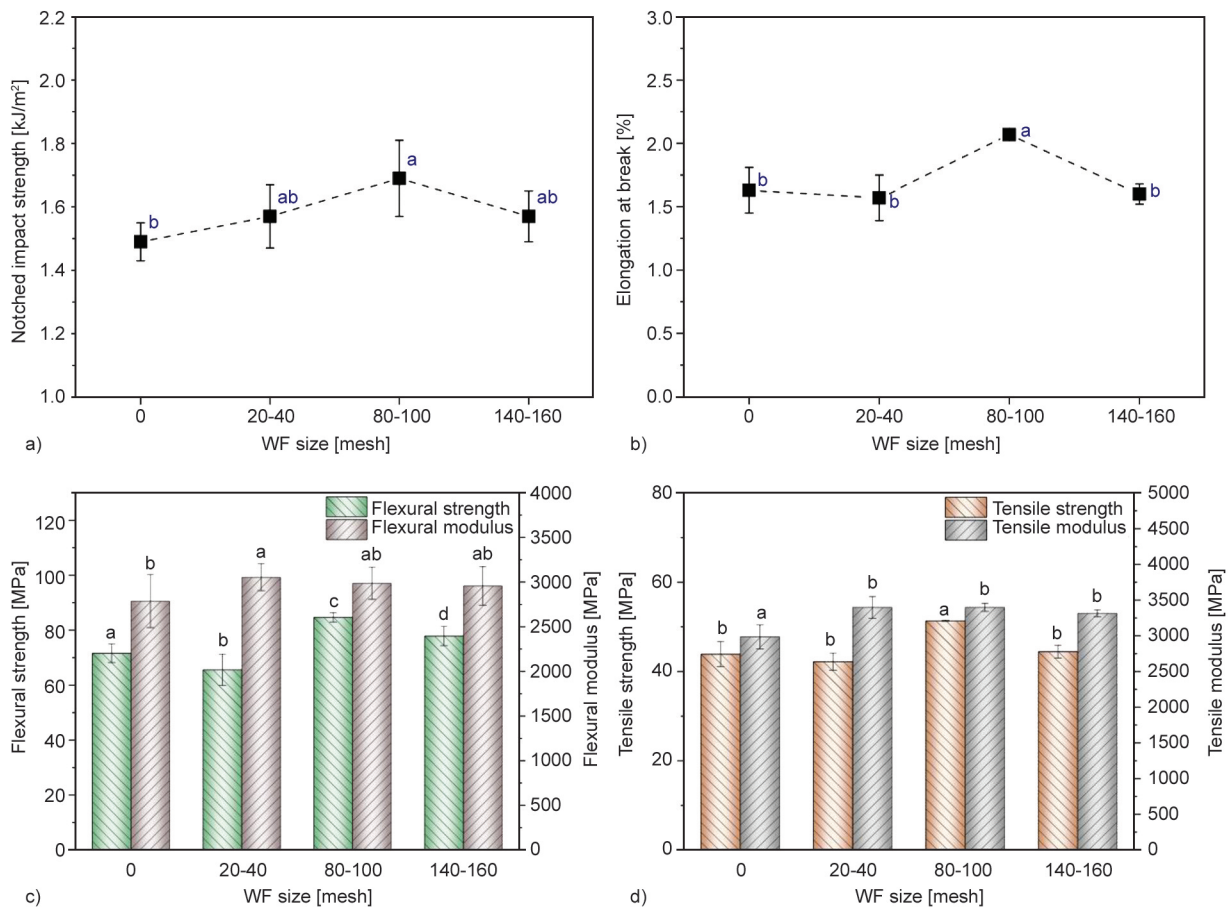


Figure 5. Mechanical properties of neat PLA and WF/PLA composite containing 1 wt% of WF with three sizes: a) Notched impact strength, b) elongation at break, c) flexural properties, d) tensile properties. Samples with the same alphabetical designation are not significantly different using Tukey paired t-tests ($P > 0.05$).

was observed with the addition of 1 wt% WF₈₀₋₁₀₀. The flexural strength of WF₂₀₋₄₀/PLA and WF₁₄₀₋₁₆₀/PLA composites was inferior to that of WF₈₀₋₁₀₀/PLA composite. In the case of flexural modulus, the incorporation of WF increased the modulus compared to neat PLA, but the difference between the three sizes of WF was not statistically significant.

The tensile properties exhibited the ability of a material to withstand the applied pulling force [30]. Figure 5d displays the tensile properties of PLA and WF/PLA composite containing 1 wt% WF of various sizes. Neat PLA exhibited tensile strength and modulus of 43.9 and 2985 MPa, respectively. The presence of WF resulted in an increasing tensile modulus. The size of WF did not have a remarkable influence on the tensile modulus. In the case of tensile strength, the incorporation of WF₂₀₋₄₀ and WF₁₄₀₋₁₆₀ had no significant influence compared to neat PLA. However, the tensile strength of WF₈₀₋₁₀₀/PLA (51.4 MPa) was significantly higher than the other groups. This indicated that medium-sized WF (WF₈₀₋₁₀₀) showed better reinforcing potential in PLA than the other two sizes of WF.

Through a comprehensive comparison of WF/PLA made with three sizes of WF, WF of medium size (WF₈₀₋₁₀₀) had the greatest reinforcing effect on PLA. Similarly, a previous study by Golmakani *et al.* [31] prepared wood flour-reinforced polyethylene composites using three different sizes of wood flour (30–40,

70–80, and 100–120 mesh). They also found that the maximum tensile strength and flexural strength were related to the composites comprised of 70–80 mesh wood flour. The better reinforcing effect of medium-sized WF (WF₈₀₋₁₀₀) than the other two sizes of WF is due to several factors. On the one hand, when using the larger fibers (WF₂₀₋₄₀), the fractured composite showed discontinuous microstructure with fiber/matrix debonding and fiber pull-out, which indicated weak interfacial bonding. On the other hand, the aspect ratio of WF₁₄₀₋₁₆₀ was the lowest among the three sizes of WF, indicating an inferior strengthening effect. Besides, WF₁₄₀₋₁₆₀ did not disperse evenly in the PLA matrix (as shown in Figure 3c), resulting in inefficient stress transfer and reduced strength.

3.4. Microstructure of WF/PLA composites containing varying contents of WF

Figure 6 shows the SEM images taken from the fracture surface of composites containing varying contents of WF₈₀₋₁₀₀. More fibers were visible with the increasing WF content in the composite. The composites prepared with lower contents of WF (0.5 and 1 wt%) exhibited a more homogeneous and continuous microstructure, with few small holes and cracks visible. As the WF content increased to 2 wt%, the cavities caused by fibers being pulled out of the matrix during the impact test were seen clearly. With the WF further increased to 8 wt%, more traces of

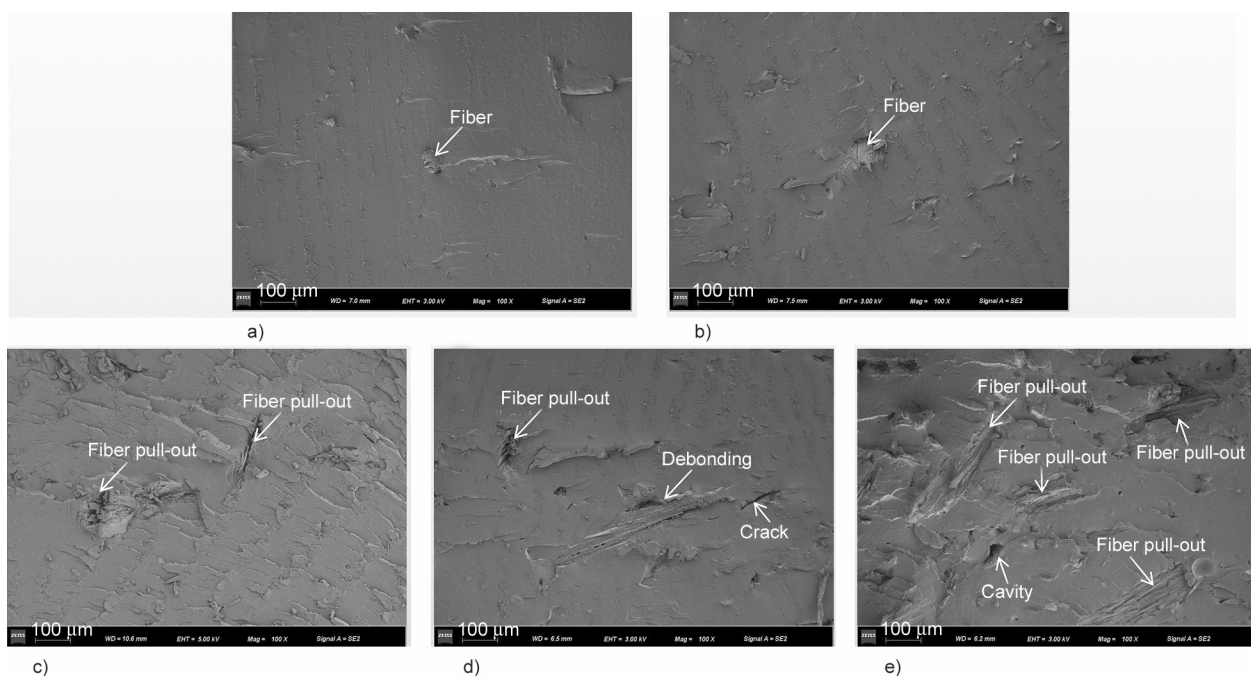


Figure 6. Scanning electron micrographs of the fracture surface of WF₈₀₋₁₀₀/PLA composite with varying WF contents: a) 0.5 wt% WF₈₀₋₁₀₀; b) 1 wt% WF₈₀₋₁₀₀; c) 2 wt% WF₈₀₋₁₀₀; d) 4 wt% WF₈₀₋₁₀₀; e) 8 wt% WF₈₀₋₁₀₀.

WF pull-out from the matrix could be observed, and the fracture surface was less continuous than the lower WF contents. These results suggested that when more WF was incorporated, there were more weak points caused by the weak interfacial adhesion between WF and the PLA matrix.

3.5. Mechanical properties of the composite containing varying contents of WF₈₀₋₁₀₀

Based on previous experiments, WF₈₀₋₁₀₀ was selected to further investigate the effects of varying WF contents on the mechanical properties of WF/PLA composite. The notched impact strength of WF/PLA composite as a function of WF₈₀₋₁₀₀ contents is shown in Figure 7a. The notched impact strength of WF/PLA composite containing 0.5–4.0 wt% WF₈₀₋₁₀₀ had a significant improvement compared to neat PLA. However, the addition of 8 wt% WF₈₀₋₁₀₀ caused a reduction in impact strength, and the difference between neat PLA and PLA composites with 8 wt% WF₈₀₋₁₀₀ was not significant. For elongation at break, the maximum value of 2.46% was obtained by adding

0.5 wt% WF₈₀₋₁₀₀ (Figure 7b). Beyond 0.5 wt% WF₈₀₋₁₀₀ loading, the elongation at break of WF/PLA composite gradually decreased with increasing WF₈₀₋₁₀₀ contents. When WF₈₀₋₁₀₀ content increased to 4 wt%, the elongation at break of the composite decreased to the same level of neat PLA. With the further increase in WF₈₀₋₁₀₀ content to 8 wt%, the elongation at break was significantly lower than that of neat PLA. This result indicated that lower content of WF₈₀₋₁₀₀ improved the toughness of the WF/PLA composite.

The variation in the flexural strength and modulus of the WF/PLA composite as a function of WF₈₀₋₁₀₀ content is shown in Figure 7c. The addition of 0.5–2 wt% WF₈₀₋₁₀₀ significantly increased the flexural strength compared to neat PLA, but the difference between composites of these WF₈₀₋₁₀₀ loadings was not statistically significant. Flexural strength reached a maximum of 84.7 MPa in composites containing 1 wt% WF₈₀₋₁₀₀. Beyond 2 wt% WF₈₀₋₁₀₀ loading, a steady decrease in flexural strength was observed with the increasing WF₈₀₋₁₀₀ loading up to 8 wt%.

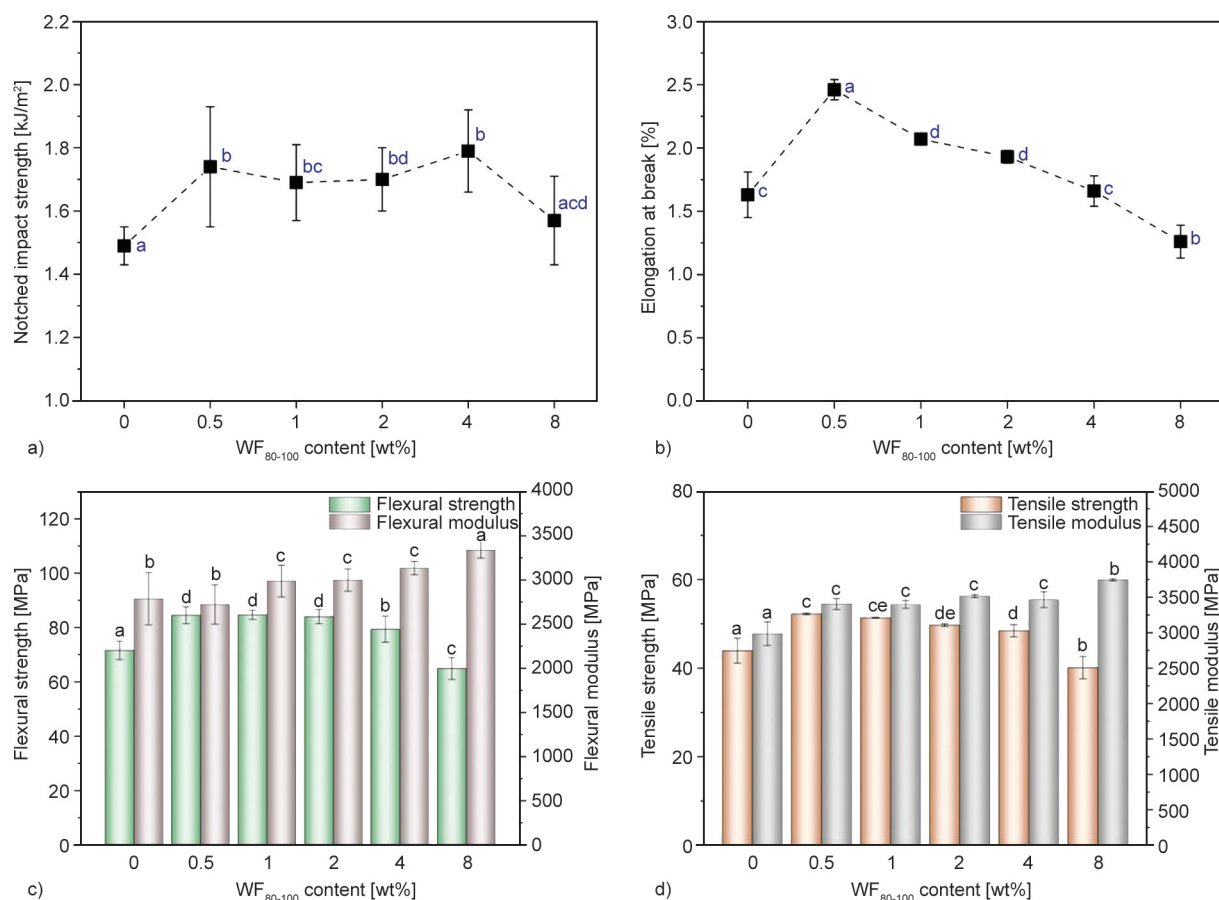


Figure 7. Mechanical properties of WF/PLA composite with varying WF₈₀₋₁₀₀ contents: a) Notched impact strength, b) elongation at break, c) flexural properties, d) tensile properties. Samples with the same alphabetical designation are not significantly different using Tukey paired t-tests ($P > 0.05$).

For flexural modulus, adding 0.5 wt% WF had no significant effect on PLA. Adding 1–8 wt% WF₈₀₋₁₀₀ into PLA significantly increased the flexural modulus, and the highest flexural modulus was observed for composites containing 8 wt% WF₈₀₋₁₀₀. The results of flexural properties indicated that WF₈₀₋₁₀₀ at appropriate loadings (1–2 wt%) played a reinforcing effect on PLA, which increased flexural strength as well as stiffness.

The tensile strength and tensile modulus of the WF/PLA composite are displayed in Figure 7d. Neat PLA possessed a tensile strength and modulus of 43.9 and 2985 MPa, respectively. The incorporation of 0.5–1 wt% WF₈₀₋₁₀₀ into the PLA matrix significantly increased the tensile strength, which ranged from 43.9 to 52.2 MPa. Tensile strength of 0.5WF₈₀₋₁₀₀/PLA reached the highest value of 52.2 MPa with an insignificant difference with 1WF₈₀₋₁₀₀/PLA composite. Beyond 1 wt% WF₈₀₋₁₀₀ loading content, tensile strength decreased significantly with increasing WF₈₀₋₁₀₀ content up to 8 wt%. Higher content of WF₈₀₋₁₀₀ resulted in lower tensile strength may be due to mingling or agglomeration of WF in PLA. Adding 0.5–8 wt% WF₈₀₋₁₀₀ significantly improved the tensile modulus of PLA. The difference between composites of 0.5–4 wt% WF₈₀₋₁₀₀ loadings was not statistically significant. But the addition of 8 wt% WF₈₀₋₁₀₀ effectively improved the tensile modulus of PLA, which is similar to the results of flexural modulus. The tensile results showed 0.5-1WF₈₀₋₁₀₀/PLA composite has a better tensile strength through tensile properties analysis.

Through a comprehensive comparison of the above mechanical properties, the optimal loading of WF₈₀₋₁₀₀ was found to be 1 wt% among the loadings used in this study. At this WF₈₀₋₁₀₀ addition level, the overall mechanical properties of WF/PLA composite were significantly enhanced compared to neat PLA. The mechanical test results suggested that WF₈₀₋₁₀₀, even at low dosages, can play the role of reinforcement in WF/PLA composites.

3.6. Non-isothermal crystallization behaviors

Non-isothermal crystallization behaviors of neat PLA and WF/PLA composite were analyzed by DSC. The second heating curves of WF/PLA composites containing different contents of WF₈₀₋₁₀₀ are presented in Figure 8. The characteristic parameters, including glass transition temperature (T_g), cold crystallization temperature (T_{cc}), melting temperature

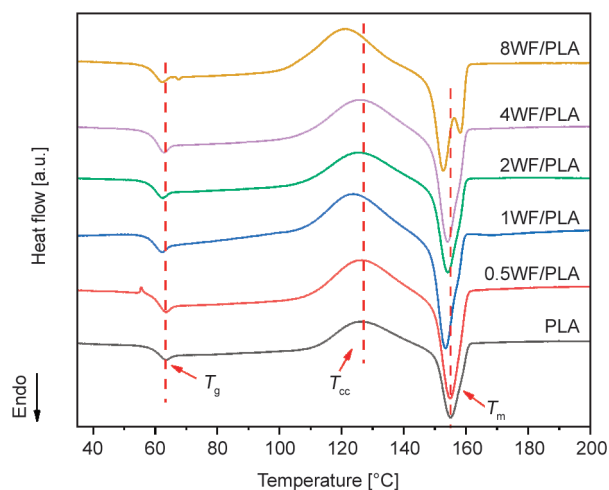


Figure 8. Melting curves after non-isothermal crystallization of WF/PLA composite with varying WF₈₀₋₁₀₀ contents.

(T_m), ΔH_m , ΔH_{cc} , and X_c derived from DSC, are listed in Table 1. The melting curves displayed three main transitions, which were related to T_g around 62–63°C, T_{cc} around 121–126°C, and T_m around 152–155°C. There was an exothermic peak in the melting curves belonging to the cold crystallization of PLA. The cold crystallization peak reflects the ability of a material to crystallize below the melting temperature [32]. The incorporation of WF₈₀₋₁₀₀ slightly decreased the T_{cc} , indicating the crystallization window was moving to a lower temperature. For processing, the decrease of T_{cc} is desirable as by expanding this window, the crystallinity for the material can be increased, or the processing temperature can be lowered, leading to more efficient processes [33]. The DSC curves of neat PLA and WF₈₀₋₁₀₀/PLA composite containing 0.5–4.0 wt% WF₈₀₋₁₀₀ exhibited a single melting peak belonging to the α -crystal [34], indicating the addition of WF₈₀₋₁₀₀ did not change the crystal form of PLA. However, there was a double melting peak in 8WF₈₀₋₁₀₀/PLA composite. The melting peak at lower temperatures corresponded to the melting of less ordered α' -crystal,

Table 1. Non-isothermal crystallization parameters of WF/PLA composite with varying WF₈₀₋₁₀₀ contents.

Samples	T_g [°C]	T_m [°C]	ΔH_m [J/g]	T_{cc} [°C]	ΔH_{cc} [J/g]	X_c [%]
PLA	63.3	155.1	21.2	126.2	−18.8	2.6
0.5WF ₈₀₋₁₀₀ /PLA	63.3	154.9	29.1	126.3	−24.4	5.0
1WF ₈₀₋₁₀₀ /PLA	62.1	153.4	23.4	124.0	−18.0	5.8
2WF ₈₀₋₁₀₀ /PLA	62.3	154.1	23.5	125.3	−18.6	5.3
4WF ₈₀₋₁₀₀ /PLA	62.7	154.1	25.2	125.9	−19.3	5.0
8WF ₈₀₋₁₀₀ /PLA	62.1	152.8	29.4	121.6	−24.9	5.3

and the peak at higher temperatures corresponded to the melting of the thermodynamically more stable α -crystal [35]. Furthermore, it was found that adding WF₈₀₋₁₀₀ into PLA increased the crystallinity. The crystallinity of 1WF₈₀₋₁₀₀/PLA composite reached 5.8%, exceeding by 3.2% that of neat PLA (2.6%). Non-isothermal crystallization behaviors of the WF/PLA composite indicated WF improved the crystallinity and heterogeneous nucleation ability of PLA.

3.7. Isothermal crystallization behaviors

Isothermal crystallization analysis was performed to further study the effect of WF₈₀₋₁₀₀ on the crystallization of PLA. Figures 9a and 9b displays the isothermal crystallization behaviors under certain crystallization temperatures (100, 110, and 120 °C) for neat PLA and 1WF₈₀₋₁₀₀/PLA composite. The width of the exothermic peak reflects the crystallization rate. The wider the exothermic peak, the slower the crystallization rate [22]. The exothermic peak of the isothermal crystallization of PLA was flatter than

that of the WF/PLA composite under the same crystallization temperature, indicating that WF accelerated the crystallization of PLA. For the same sample, the exothermic peak of isothermal crystallization at 110 °C was sharper than that at 100 and 120 °C. It can be concluded that the optimal isothermal crystallization temperature of PLA and WF/PLA composite was 110 °C in this study. The isothermal crystallization kinetics can be analyzed by the Avrami model, which describes the change of relative crystallinity (X_t) with crystallization time t [36] (Equation (2)):

$$1 - X_t = \exp(-kt^n) \quad (2)$$

where X_t is time-dependent relative crystallinity, n is Avrami exponent, and k is the overall crystallization rate constant related to nucleation and crystal growth. Avrami model can be expressed in linear form and is given by the Equation (3):

$$\lg[-\ln(1 - X_t)] = \lg k + n \lg t \quad (3)$$

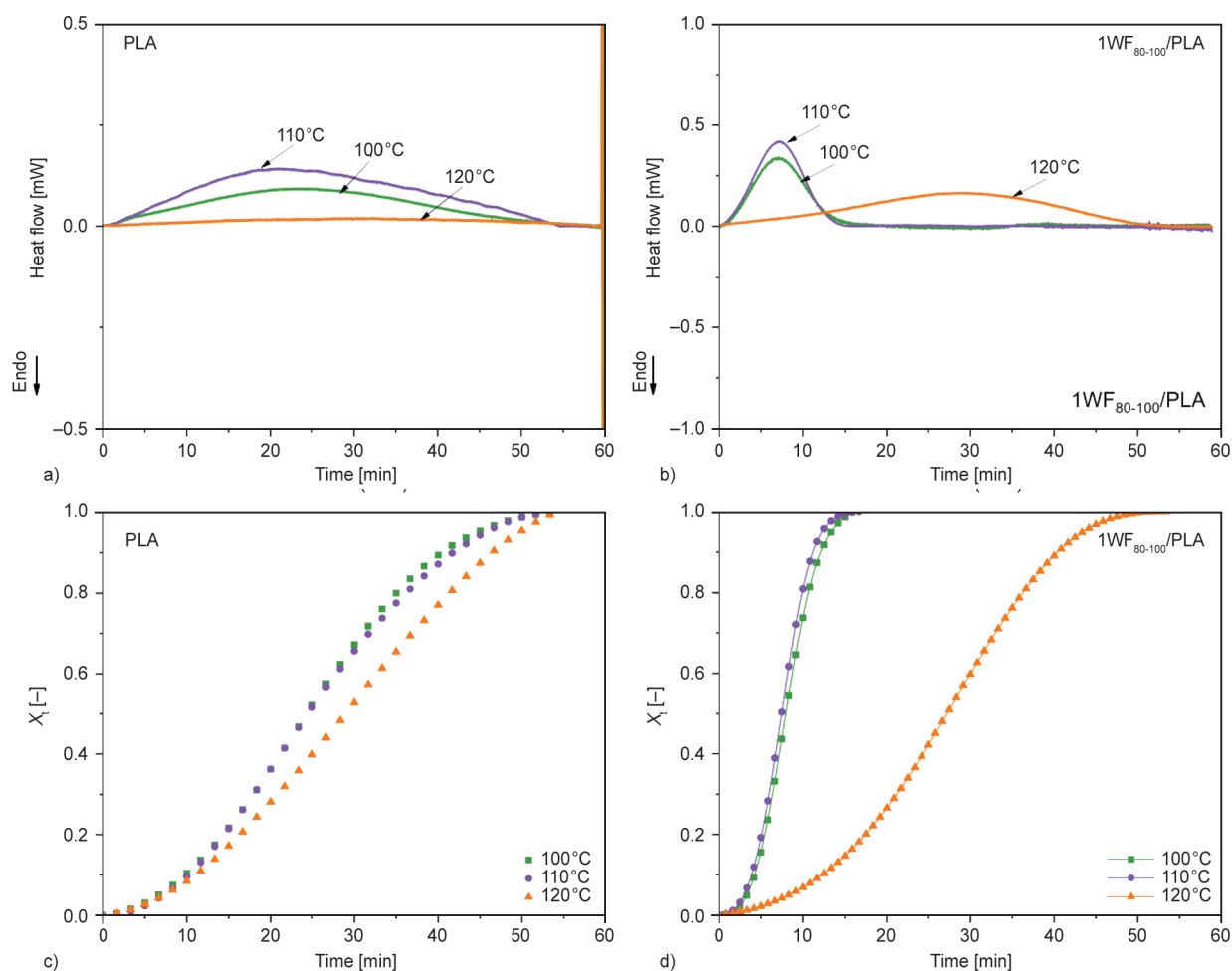


Figure 9. a) and b) isothermal crystallization exotherms and c) and d) relative crystallinity (X_t) versus crystallization time at different isothermal crystallization temperatures for neat PLA and 1WF₈₀₋₁₀₀/PLA.

X_t can be calculated from the isothermal DSC heat flow curve as Equation (4) [37]:

$$X_t = \frac{\int_0^t \frac{dH}{dt} dt}{\int_0^\infty \frac{dH}{dt} dt} \quad (4)$$

where dH/dt is the respective heat flow; the sum of dH/dt from 0 to t is the enthalpy at time t ; and the sum of dH/dt from 0 to t^∞ is the enthalpy at time t^∞ , which can be obtained as the total area under the crystallization DSC curve. The half-crystallization time ($t_{1/2}$) is another important crystallization kinetics parameter, which is defined as the time of achieving 50% crystallinity of samples. It can be calculated by the Equation (5) [38]:

$$t_{1/2} = \left(\frac{\ln 2}{k}\right)^{1/n} \quad (5)$$

Avrami parameters calculated from the isothermal curves were summarized in Table 2. For the ideal isothermal crystallization process, n should be an integer, which depends on the nucleation mechanism and the growth mode. The n value ranged from 1.8 to 2.7 due to the heterogeneous nucleation mechanism [22]. Figures 9c and 9d shows the relative crystallinity X_t versus crystallization time t for neat PLA and 1WF₈₀₋₁₀₀/PLA composite, which exhibited typical S-type curves. The X_t versus t curve of 1WF₈₀₋₁₀₀/PLA composite extraordinarily shifted to the left

compared with neat PLA at 100 and 110 °C. At the same isothermal crystallization temperature, neat PLA showed longer $t_{1/2}$ than that of 1WF₈₀₋₁₀₀/PLA composite. As listed in Table 2, $t_{1/2}$ of neat PLA was 23.6 min at 110 °C. A shorter $t_{1/2}$ of 7.2 min was observed for 1WF₈₀₋₁₀₀/PLA composite isothermally crystallized at 110 °C, which indicated that 1 wt% WF₈₀₋₁₀₀ was efficient in promoting crystallization rate. Figure 10 shows the $t_{1/2}$ plots as a function of WF₈₀₋₁₀₀ contents for WF/PLA composite at three crystallization temperatures. The crystallinity of 1WF₈₀₋₁₀₀/PLA composite after isothermal crystallization at 100, 110, and 120 °C were 30.1, 31.7, and

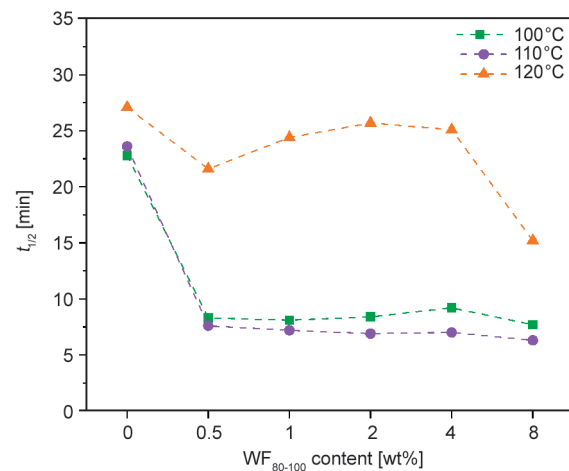


Figure 10. Half-crystallization time ($t_{1/2}$) at different isothermal crystallization temperatures for WF/PLA composite with varying WF₈₀₋₁₀₀ contents.

Table 2. Isothermal crystallization kinetic parameters of WF/PLA composite with varying contents of WF₈₀₋₁₀₀.

Samples	T_c [°C]	n	k [min ⁻ⁿ]	$t_{1/2}$ [min]	ΔH_m [J/g]	X_c [%]
PLA	100	2.0	$1.5 \cdot 10^{-3}$	22.8	28.6	30.6
	110	2.1	$8.9 \cdot 10^{-4}$	23.6	29.7	31.7
	120	1.8	$1.7 \cdot 10^{-3}$	27.1	13.7	14.6
0.5WF ₈₀₋₁₀₀ /PLA	100	2.7	$2.1 \cdot 10^{-3}$	8.3	27.8	29.9
	110	2.3	$5.9 \cdot 10^{-3}$	7.6	29.6	31.8
	120	2.4	$4.3 \cdot 10^{-4}$	21.6	27.4	29.4
1WF ₈₀₋₁₀₀ /PLA	100	2.5	$4.0 \cdot 10^{-3}$	8.1	27.9	30.1
	110	2.4	$5.9 \cdot 10^{-3}$	7.2	29.4	31.7
	120	2.0	$1.1 \cdot 10^{-3}$	24.4	29.7	32.1
2WF ₈₀₋₁₀₀ /PLA	100	2.6	$2.8 \cdot 10^{-3}$	8.4	27.2	29.7
	110	2.6	$4.9 \cdot 10^{-3}$	6.9	29.6	32.3
	120	2.3	$4.5 \cdot 10^{-4}$	25.7	29.5	32.2
4WF ₈₀₋₁₀₀ /PLA	100	2.6	$2.2 \cdot 10^{-3}$	9.2	28.0	31.2
	110	2.5	$5.6 \cdot 10^{-3}$	7.0	30.7	34.2
	120	2.5	$2.0 \cdot 10^{-4}$	25.1	30.3	33.7
8WF ₈₀₋₁₀₀ /PLA	100	2.6	$3.8 \cdot 10^{-3}$	7.7	28.4	33.0
	110	2.6	$6.1 \cdot 10^{-3}$	6.3	28.9	33.6
	120	2.3	$1.2 \cdot 10^{-3}$	15.2	28.3	32.9

32.1%, respectively. In comparison to neat PLA, the incorporation of 1% WF₈₀₋₁₀₀ resulted in a higher

level of crystallinity. The reduced crystallization half-time and cold crystallization temperature, as well as

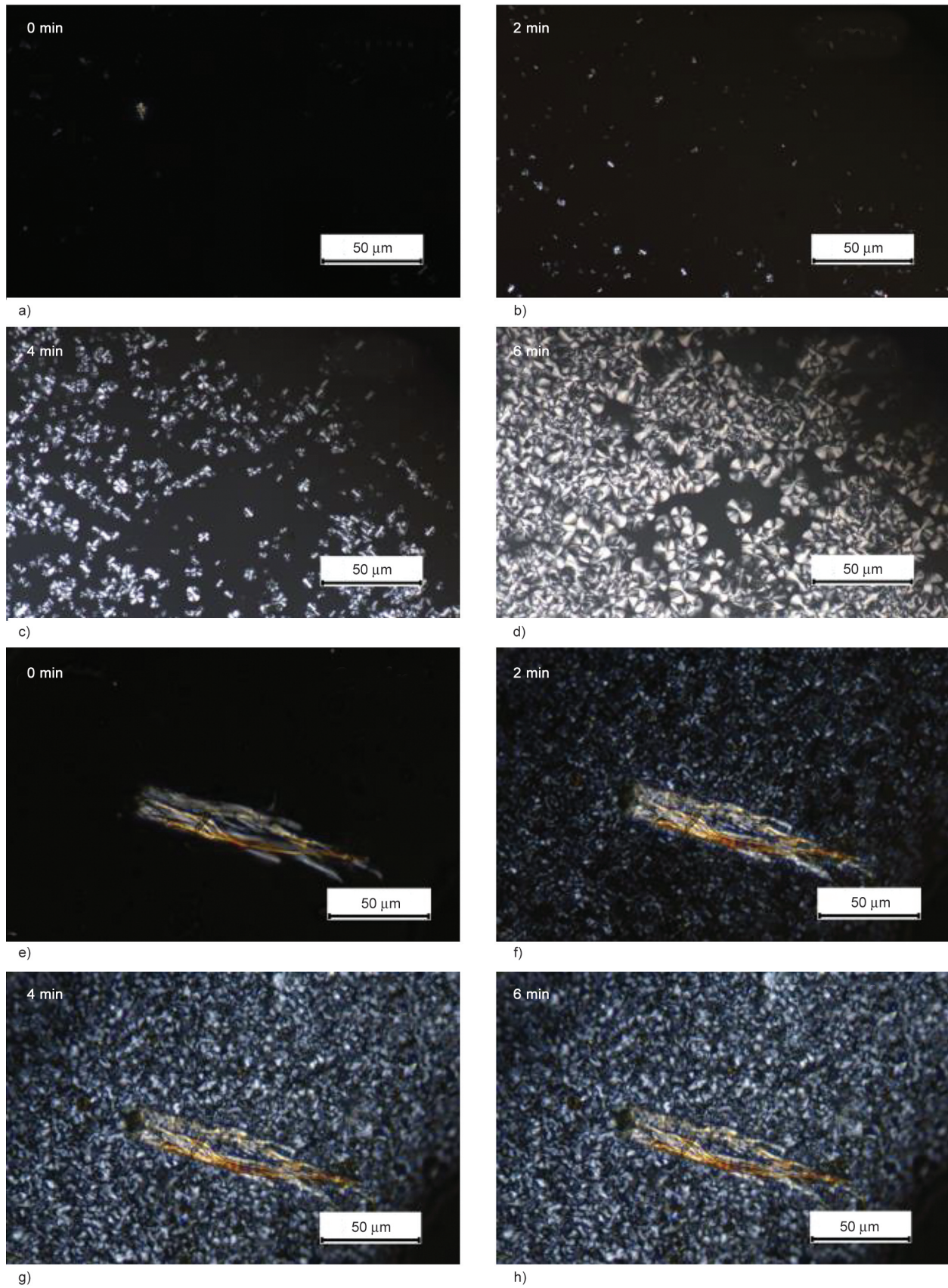


Figure 11. Crystalline morphology evolution observed by polarized optical microscope (POM) during isothermal crystallization at 110 °C of a)–d) neat PLA and e)–h) 1WF₈₀₋₁₀₀/PLA.

increased crystallinity, suggested that 1% WF₈₀₋₁₀₀ promoted the nucleation and crystallization process of the PLA matrix.

3.8. Crystalline morphology

Crystalline morphological evolution for neat PLA and 1WF₈₀₋₁₀₀/PLA composite under POM observation during isothermal crystallization at 110 °C was shown in Figure 11. The spherulites in neat PLA slowly grew with time. Relatively large spherulites with a diameter of about 20 μm were observed for neat PLA until isothermal crystallization was completed. Neat PLA exhibited a typical maltase cross phenomenon. In the presence of WF₈₀₋₁₀₀, the spherulite size was smaller, and the crystal growth rate was much faster. This result is consistent with the $t_{1/2}$ results of the DSC analysis. It was also noticed that the crystals of 1WF₈₀₋₁₀₀/PLA composite were denser than neat PLA, which was attributed to the increasing nucleation density of PLA [22]. The spherulite sizes of 1WF₈₀₋₁₀₀/PLA composite were so fine that it was hard to be figured out, indicating WF₈₀₋₁₀₀ provided more nucleation sites for PLA. PLA crystals grew along the WF until WF was coated with crystals completely. Such a phenomenon further demonstrated that WF₈₀₋₁₀₀ was an effective nucleating agent for PLA.

3.9. Crystalline structure

Diffraction peaks of WAXD spectra reflect the crystalline structure of WF and WF/PLA composite with varying WF₈₀₋₁₀₀ contents shown in Figure 12. WF

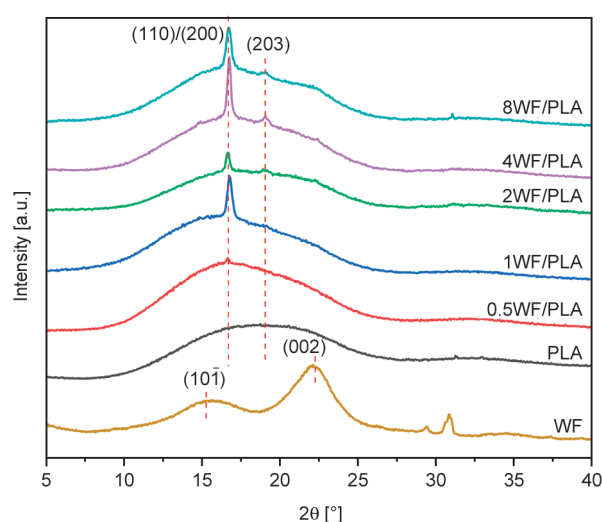


Figure 12. Wide angle X-ray diffraction (WAXD) spectra of WF and WF/PLA composite with varying WF₈₀₋₁₀₀ contents.

showed obvious diffraction peaks at $2\theta = 15.7$ and 22.2° corresponding to $(10\bar{1})$ and (002) lattice planes, respectively, which indicated a typical cellulose I structure with high crystallinity of 66.7%. Neat PLA is amorphous, as evidenced by a broad WAXD curve. The WAXD pattern of WF/PLA composites with varying WF₈₀₋₁₀₀ contents shows obvious diffraction peaks around $2\theta = 16.6$ and 19.0° , which was associated with $(110)/(200)$ and (203) lattice planes of α -crystal in PLA. In 1WF₈₀₋₁₀₀/PLA composite, a shift of the above-mentioned lattice planes towards higher 2θ values (16.8°) attributed to the crystalline structure of PLA transformed from a disorder α' -crystal to an ordered α -crystal [25]. This phenomenon indicated WF₈₀₋₁₀₀ contributed to enhancing PLA crystallization, which is consistent with DSC results.

4. Conclusions

The effect of a small amount of WF on the mechanical and crystallization properties of PLA was investigated in this study. WF/PLA composite containing 1 wt% WF₈₀₋₁₀₀ exhibited better mechanical properties in notched impact strength and flexural and tensile properties compared to neat PLA, 1WF₂₀₋₄₀/PLA, and 1WF₁₄₀₋₁₆₀/PLA composite. Thus, WF₈₀₋₁₀₀ was determined as the optimal size of WF for reinforcing PLA. Then the mechanical properties of WF₈₀₋₁₀₀/PLA composites containing varying WF₈₀₋₁₀₀ contents (0.5, 1, 2, 4, and 8 wt%) were further studied. The optimal loading content for WF₈₀₋₁₀₀ was 1 wt%, at which the notched impact strength, flexural and tensile strength increased by 14, 18, and 18%, respectively. Elongation at break of 1WF₈₀₋₁₀₀/PLA composite significantly increased by 27% compared to neat PLA. Furthermore, adding WF₈₀₋₁₀₀ could significantly reduce half-crystallization time, meanwhile improving crystallinity. The phenomenon indicated WF accelerated crystallization and contributed to the heterogeneous nucleation of PLA. Crystalline morphology evolution of WF/PLA composite observed by polarized optical microscope showed that WF increased the nucleation sites companies with decreasing the size of spherulites. Meanwhile, WF₈₀₋₁₀₀ significantly enhanced the formation of α -crystal of PLA based on wide-angle X-ray diffraction results. These results indicated that the presence of a small amount of WF with appropriate size acted as both a bio-nucleating agent and reinforcement material for the PLA matrix. This study provides a

simple and feasible strategy for enhancing the processing and properties of PLA and ensures its complete biodegradability.

Acknowledgements

The authors gratefully acknowledge the support from the National Natural Science Foundation of China (grant number 31901250).


References

- [1] Joseph S., Deenadayalan E., Mahanwar P. A.: Studies on melt processable biocomposites of polylactic acid. *Journal of Polymers and the Environment*, **23**, 321–333 (2014).
<https://doi.org/10.1007/s10924-014-0668-5>
- [2] Xu T., Zhang A., Zhao Y., Han Z., Xue L.: Crystallization kinetics and morphology of biodegradable poly (lactic acid) with a hydrazide nucleating agent. *Polymer Testing*, **45**, 101–106 (2015).
<https://doi.org/10.1016/j.polymertesting.2015.05.009>
- [3] Ujčić A., Fortelny I., Krejčíková S., Pavlova E., Hodan J., Slouf M.: Effects of thermal treatment and nucleating agents on crystallinity, toughness, and stiffness of PLA/PCL blends. *Express Polymer Letters*, **16**, 221–233 (2022).
<https://doi.org/10.3144/expresspolymlett.2022.18>
- [4] Zhai S., Liu Q., Zhao Y., Sun H., Yang B., Weng Y.: A review: Research progress in modification of poly (lactic acid) by lignin and cellulose. *Polymers*, **13**, 776 (2021).
<https://doi.org/10.3390/polym13050776>
- [5] Zhao L., Kong J., Tian X., Zhang J., Qin S.: Isothermal crystallization of poly(L-lactide) and poly(butylene adipate) crystalline/crystalline blends. *Polymer Journal*, **46**, 323–329 (2014).
<https://doi.org/10.1038/pj.2014.8>
- [6] Mileva D., Tranchida D., Gahleitner M.: Designing polymer crystallinity: An industrial perspective. *Polymer Crystallization*, **1**, e10009 (2018).
<https://doi.org/10.1002/pcr2.10009>
- [7] Suryanegara L., Okumura H., Nakagaito A. N., Yano H.: The synergetic effect of phenylphosphonic acid zinc and microfibrillated cellulose on the injection molding cycle time of PLA composites. *Cellulose*, **18**, 689–698 (2011).
<https://doi.org/10.1007/s10570-011-9515-1>
- [8] Liu H., Chen F., Liu B., Estep G., Zhang J.: Super toughened poly(lactic acid) ternary blends by simultaneous dynamic vulcanization and interfacial compatibilization. *Macromolecules*, **43**, 6058–6066 (2010).
<https://doi.org/10.1021/ma101108g>
- [9] Zhao X., Hu H., Wang X., Yu X., Zhou W., Peng S.: Super tough poly(lactic acid) blends: A comprehensive review. *RSC Advances*, **10**, 13316–13368 (2020).
<https://doi.org/10.1039/d0ra01801e>
- [10] Cheng Y., Deng S., Chen P., Ruan R.: Polylactic acid (PLA) synthesis and modifications: A review. *Frontiers of Chemistry in China*, **4**, 259–264 (2009).
<https://doi.org/10.1007/s11458-009-0092-x>
- [11] Shi X., Zhang G., Phuong T. V., Lazzeri A.: Synergistic effects of nucleating agents and plasticizers on the crystallization behavior of poly(lactic acid). *Molecules*, **20**, 1579–1593 (2015).
<https://doi.org/10.3390/molecules20011579>
- [12] Rangavar H., Taghiyari H. R., Oromiehie A., Gholipour T., Safarpour A.: Effects of nanoclay on physical and mechanical properties of wood-plastic composites. *Wood Material Science and Engineering*, **12**, 211–219 (2016).
<https://doi.org/10.1080/17480272.2016.1156743>
- [13] Saeidlou S., Huneault M. A., Li H., Park C. B.: Poly (lactic acid) crystallization. *Progress in Polymer Science*, **37**, 1657–1677 (2012).
<https://doi.org/10.1016/j.progpolymsci.2012.07.005>
- [14] Chen L., Dou Q.: Influence of the combination of nucleating agent and plasticizer on the non-isothermal crystallization kinetics and activation energies of poly (lactic acid). *Journal of Thermal Analysis and Calorimetry*, **139**, 1069–1090 (2019).
<https://doi.org/10.1007/s10973-019-08507-y>
- [15] Aliotta L., Sciara L. M., Cinelli P., Canesi I., Lazzeri A.: Improvement of the PLA crystallinity and heat distortion temperature optimizing the content of nucleating agents and the injection molding cycle time. *Polymers*, **14**, 977 (2022).
<https://doi.org/10.3390/polym14050977>
- [16] Petchwattana N., Naknaen P., Narupai B.: Combination effects of reinforcing filler and impact modifier on the crystallization and toughening performances of poly (lactic acid). *Express Polymer Letters*, **14**, 848–859 (2020).
<https://doi.org/10.3144/expresspolymlett.2020.70>
- [17] Zuo Y., Chen K., Li P., He X., Li W., Wu Y.: Effect of nano-SiO₂ on the compatibility interface and properties of polylactic acid-grafted-bamboo fiber/polylactic acid composite. *International Journal of Biological Macromolecules*, **157**, 177–186 (2020).
<https://doi.org/10.1016/j.ijbiomac.2020.04.205>
- [18] Li Y., Han C., Yu Y., Xiao L., Shao Y.: Effect of content and particle size of talc on nonisothermal melt crystallization behavior of poly(L-lactide). *Journal of Thermal Analysis and Calorimetry*, **135**, 2049–2058 (2018).
<https://doi.org/10.1007/s10973-018-7365-x>
- [19] Peltola H., Pääkkönen E., Jetsu P., Heinemann S.: Wood based PLA and PP composites: Effect of fibre type and matrix polymer on fibre morphology, dispersion and composite properties. *Composites Part A: Applied Science and Manufacturing*, **61**, 13–22 (2014).
<https://doi.org/10.1016/j.compositesa.2014.02.002>
- [20] Kulkarni A. N. R., Narayan R.: Effects of modified thermoplastic starch on crystallization kinetics and barrier properties of PLA. *Polymers*, **13**, 4125 (2021).
<https://doi.org/10.3390/polym13234125>

- [21] Wang N., Zhang C., Weng Y.: Enhancing gas barrier performance of polylactic acid/lignin composite films through cooperative effect of compatibilization and nucleation. *Journal of Applied Polymer Science*, **138**, 50199 (2020).
<https://doi.org/10.1002/app.50199>
- [22] Wu W., Wu G., Zhang H.: Effect of wood flour as nucleating agent on the isothermal crystallization of poly(lactic acid). *Polymers for Advanced Technologies*, **28**, 252–260 (2017).
<https://doi.org/10.1002/pat.3881>
- [23] La Mantia F. P., Morreale M.: Green composites: A brief review. *Composites Part A: Applied Science and Manufacturing*, **42**, 579–588 (2011).
<https://doi.org/10.1016/j.compositesa.2011.01.017>
- [24] Huda M. S., Drzal L. T., Misra M., Mohanty A. K.: Wood-fiber-reinforced poly(lactic acid) composites: Evaluation of the physicomechanical and morphological properties. *Journal of Applied Polymer Science*, **102**, 4856–4869 (2006).
<https://doi.org/10.1002/app.24829>
- [25] Dobrzyńska-Mizera M., Knitter M., Woźniak-Braszak A., Baranowski M., Sterzyński T., Di Lorenzo M. L.: Poly(L-lactic acid)/pine wood bio-based composites. *Materials*, **13**, 3776 (2020).
<https://doi.org/10.3390/ma13173776>
- [26] Petinakis E., Yu L., Edward G., Dean K., Liu H., Scully A. D.: Effect of matrix–particle interfacial adhesion on the mechanical properties of poly(lactic acid)/wood-flour micro-composites. *Journal of Polymers and the Environment*, **17**, 83–94 (2009).
<https://doi.org/10.1007/s10924-009-0124-0>
- [27] Özdemir F., Ayırlım N., Yurttaş E.: Mechanical and thermal properties of biocomposite films produced from hazelnut husk and polylactic acid. *Wood Material Science and Engineering*, in press (2022).
<https://doi.org/10.1080/17480272.2021.1955972>
- [28] Sathishkumar G. K., Gautham G., Shankar G. G., Rajkumar G., Karpagam R., Dhivya V., Zacharia G., Gopinath B., Karthik P., Charles M. M.: Influence of lignite fly ash on the structural and mechanical properties of banana fiber containing epoxy polymer matrix composite. *Polymer Bulletin*, **79**, 285–306 (2021).
<https://doi.org/10.1007/s00289-020-03524-6>
- [29] Ahmad J., Martínez-García R., de-Prado-Gil J., Pasha A. A., Irshad K., Bourchak M.: Mechanical performance of sustainable high strength ductile fiber reinforced concrete (HSDFRC) with wooden ash. *Scientific Reports*, **12**, 4306 (2022).
<https://doi.org/10.1038/s41598-022-08134-y>
- [30] Rajkumar G., Sathishkumar G. K., Srinivasan K., Karpagam R., Dhivya V., Sakthipandi K., Sivakumar R., Ibrahim M., Akheel M. M.: Structural and mechanical properties of lignite fly ash and flax-added polypropylene polymer matrix composite. *Journal of Natural Fibers*, **19**, 6534–6552 (2022).
<https://doi.org/10.1080/15440478.2021.1927929>
- [31] Golmakani M. E., Wiczenbach T., Malikan M., Aliakbari R., Eremeyev V. A.: Investigation of wood flour size, aspect ratios, and injection molding temperature on mechanical properties of wood flour/polyethylene composites. *Materials*, **14**, 3406 (2021).
<https://doi.org/10.3390/ma14123406>
- [32] Nagarajan V., Zhang K., Misra M., Mohanty A. K.: Overcoming the fundamental challenges in improving the impact strength and crystallinity of PLA biocomposites: Influence of nucleating agent and mold temperature. *ACS Applied Materials and Interfaces*, **7**, 11203–11214 (2015).
<https://doi.org/10.1021/acsami.5b01145>
- [33] Clarkson C. M., El Awad Azrak S. M., Schueneman G. T., Snyder J. F., Youngblood J. P.: Crystallization kinetics and morphology of small concentrations of cellulose nanofibrils (CNFs) and cellulose nanocrystals (CNCs) melt-compounded into poly(lactic acid) (PLA) with plasticizer. *Polymer*, **187**, 122101 (2020).
<https://doi.org/10.1016/j.polymer.2019.122101>
- [34] Zhang X., Yang B., Fan B., Sun H., Zhang H.: Enhanced nonisothermal crystallization and heat resistance of poly(L-lactic acid) by D-sorbitol as a homogeneous nucleating agent. *ACS Macro Letters*, **10**, 154–160 (2021).
<https://doi.org/10.1021/acsmacrolett.0c00830>
- [35] Le Marec P. E., Ferry L., Quantin J-C., Bénézet J-C., Bonfils F., Guilbert S., Bergeret A.: Influence of melt processing conditions on poly(lactic acid) degradation: Molar mass distribution and crystallization. *Polymer Degradation and Stability*, **110**, 353–363 (2014).
<https://doi.org/10.1016/j.polymdegradstab.2014.10.003>
- [36] Xu C., Zhang J., Bai J., Ding S., Wang X., Wang Z.: Two-stage crystallization kinetics and morphological evolution with stereocomplex crystallite-induced enhancement for long-chain branched polylactide/poly(D-lactic acid) blends. *Industrial and Engineering Chemistry Research*, **60**, 5319–5329 (2021).
<https://doi.org/10.1021/acs.iecr.1c00377>
- [37] Haeldermans T., Samyn P., Cardinaels R., Vandamme D., Vanreppelen K., Cuypers A., Schreurs S.: Poly(lactic acid) bio-composites containing biochar particles: Effects of fillers and plasticizer on crystallization and thermal properties. *Express Polymer Letters*, **15**, 343–360 (2021).
<https://doi.org/10.3144/expresspolymlett.2021.30>
- [38] Li M-X., Ren Y., Lee D., Choi S-W.: Crystallization behavior and electrical properties of nanoparticle-reinforced poly(lactic acid)-based films. *Polymers*, **14**, 177 (2022).
<https://doi.org/10.3390/polym14010177>

Research article

Modification of PEDOT:PSS films using ZnI₂ additive for power conversion efficiency enhancement of organic solar cells

Sucheewan Krobthong¹, Sutthipoj Wongrerkdee^{1*}, Sawitree Wongrerkdee²,
Khathawut Lohawet³, Anusit Kaewprajak³, Pisist Kumnorkaew³

¹Department of Physics, Faculty of Liberal Arts and Science, Kasetsart University Kamphaeng Saen Campus, Kamphaengsaen, 73140 Nakhon Pathom, Thailand

²Faculty of Engineering, Rajamangala University of Technology Lanna Tak, Muang, 63000 Tak, Thailand

³National Nanotechnology Center, National Science and Technology Development Agency, Thailand Science Park, Khlong Luang, 12120 Pathum Thani, Thailand

Received 13 September 2022; accepted in revised form 24 November 2022

Abstract. Organic solar cells (OSCs) fabricated with poly(3,4-ethylenedioxythiophene) polystyrene sulfonate (PEDOT:PSS) films often have limited performance due to high sheet resistances since commercial PEDOT:PSS contains a high insulating PSS to conducting PEDOT ratio. To resolve this issue, zinc iodide (ZnI₂) additive was utilized to modify PEDOT:PSS films, which was carried out by mixing ZnI₂ with PEDOT:PSS solution. The mixture was deposited on a fluorine-doped tin oxide substrate to derive the modified PEDOT:PSS films for application as a hole-transporting layer in OSCs. This resulted in an enhanced power conversion efficiency for OSCs fabricated with modified PEDOT:PSS films. The enhancement was primarily due to the improved PEDOT:PSS/PCDTBT:PC₇₀BM (poly[*N*-9'-heptadecanyl-2,7-carbazole-alt-5,5-(4',7'-di-2-thienyl-2',1',3'-benzothiadiazole)] – PCDTBT, [6,6]-phenyl-C₇₁-butyric acid methyl ester – PC₇₀BM) interfaces, which facilitates enhanced hole collection performance and results in a high current density for OSC devices. Moreover, the ZnI₂ plays a role in the depletion of insulating PSS from the film's surface. This behavior causes lower sheet resistance and results in an increased J_{sc} and V_{oc} for OSC devices. Therefore, the improved interfacial contact and depletion of PSS are considered synergistic functions for OSC enhancement.

Keywords: *nanomaterials, zinc iodide, hole transporting layers, organic solar cells*

1. Introduction

Energy is a vital factor for consumption and development. The usability of conventional energy resources, including coal, oils, and natural gases, is associated with limited reserves and pollution. Therefore, alternative energy has been extensively investigated and developed for next-generation energy consumption. Solar cells are an interesting alternative technology and have been considered a candidate for sustainable technology since they are inexpensive and can be installed anywhere. The electricity

generated from solar cells not only has on-grid usability but can also be stored by batteries for off-grid or hybrid systems. Furthermore, no pollution emission is associated with generating electricity using solar cells. In comparison to silicon solar cells, organic solar cells (OSCs) are developed based on a low-temperature process, no vacuum system requirements, and flexible thin film deposition, which can be easily fabricated [1–4]. A conductive polymer, poly(3,4-ethylenedioxythiophene)-poly(styrene sulfonate) (PEDOT:PSS), has been widely investigated

*Corresponding author, e-mail: sutthipoj.s@gmail.com

© BME-PT

in OSCs, attributable to its high electrical conductivity and transparency [5, 6]. However, PEDOT:PSS chains contain high ratios of insulating PSS to conducting PEDOT, which may potentially limit the conductivity for optoelectronic device applications, including OSCs [7, 8]. Moreover, the formation of PEDOT:PSS chains might be shortly formed by thin film fabrication. To solve this issue, many researchers have focused on the development and optimization of PEDOT:PSS films. Hussain *et al.* [9] developed MXene/ WO_3 embedded PEDOT:PSS hole transporting layers (HTLs) and applied them to perovskite solar cells. They prepared the MXene/ WO_3 hybrid structure using a solution process. The hybrid structure was used to modify PEDOT:PSS for applying HTLs of PSCs. The PSC devices demonstrated a power conversion efficiency (*PCE*) enhancement of 12.26%. This is caused by the appropriate energy band alignment in the modified HTLs, which results in a more efficient charge transfer and a shorter carrier lifetime. Gemeiner *et al.* [10] modified PEDOT:PSS using secondary dopants of ethylene glycol (EG), polyethylene glycol (PEG), and dimethyl sulfoxide (DMSO) for dye-sensitized solar cells (DSSCs). The dopants were added to PEDOT:PSS inks and printed on fluorine-doped tin oxide (FTO) substrates. The secondary dopants caused low sheet resistance and better wettability and electrochemical activity for PEDOT:PSS films. This demonstrated efficiency enhancement for DSSCs fabricated with PEDOT:PSS counter electrodes. Wan *et al.* [11] reported an enhancement of OSCs using thionyl chloride (SOCl_2) treatment. PEDOT:PSS films were soaked onto SOCl_2 . After 10 min of soaking, the PEDOT:PSS was washed with de-ionized water and isopropanol, followed by baking at 80 °C for 15 min. The SOCl_2 -treated PEDOT:PSS was then applied as the HTL layer for the OSCs within a high *PCE* of 15%. The *PCE* enhancement was due to the SOCl_2 treatment, which caused an improvement in optical transparency, electrical conductivity, Seebeck coefficient, and work function. Moreover, Xu *et al.* [12] demonstrated that a co-development of an engineering fabrication using layer-by-layer and solvent treatment greatly enhanced OSC performance. The *PCEs* of fabricated OSC devices using layer-by-layer fabrication and treatment with 1-chloronaphthalene (CN) can be enhanced from 13.67 to 15.81%. These results suggest that the development strategy, including the method and treatment of

PEDOT:PSS HTL, can potentially enhance OSC performance.

In this work, PEDOT:PSS films were modified using a ZnI_2 additive. The ZnI_2 is easily soluble in water to form Zn^{2+} and I^- ions, that could react with PEDOT:PSS molecules. Due to the insulating PSS parts of PEDOT:PSS causing low electrical properties, the reaction between the ZnI_2 additive and PEDOT:PSS reduces the PSS parts for passivating and improving the electrical properties of PEDOT:PSS films [13, 14]. OSCs fabricated with modified PEDOT:PSS are expected to be enhanced. PEDOT:PSS film preparation can be performed using several techniques such as dip-coating, spin-coating, and convective deposition [15, 16]. The dip-coating process requires large initial materials, while spin-coating causes a high loss of initial material by spinning out. On the other hand, the convective deposition can solve these problems. It requires low initial materials and causes low material loss; hence, its application to prepare PEDOT:PSS films.

2. Experiments

Starting materials, including poly(3,4-ethylenedioxythiophene)-poly(styrene sulfonate) (PEDOT:PSS, PH1000), poly[*N*-9'-heptadecanyl-2,7-carbazole-alt-5,5-(4',7'-di-2-thienyl-2',1',3'-benzothiadiazole)] (PCDTBT), and phenyl C_{70} butyric acid methyl ester (PC $_{70}$ BM), were purchased from Ossila, UK. ZnI_2 ($\geq 98\%$) was purchased from Sigma-Aldrich, Singapore. All chemicals were used as received.

Fluorine doped-tin oxide (FTO, Sigma-Aldrich, Singapore, surface resistivity $\sim 7 \Omega/\text{sq}$) substrates were cleaned withalconox detergent, de-ionized (DI) water, and isopropanol for 30 min each using an ultrasonic cleaner. Prior to deposition, the cleaned substrates underwent surface treatment with oxygen plasma (Ossila, Pathum Thani, Thailand). The ZnI_2 additive was dissolved into DI water for an initial concentration of 0.1 M, followed by stirring for 1 h, to obtain the final ZnI_2 solution. The ZnI_2 solution was then mixed into PEDOT:PSS for 0, 1, 2, and 4 vol%. The mixture was stirred for 30 min to form a homogeneous PEDOT:PSS aqueous solution. For PEDOT:PSS film deposition, 20 μl of the aqueous solution was deposited onto FTO substrates using a convective deposition technique, followed by heating at 120 °C for 30 min, to obtain PEDOT:PSS films. These films were then used as HTL for OSC application. The OSC structures of PEDOT:PSS/

PCDTBT:PC₇₀BM/TiO_x/Al were fabricated as described in prior work [15].

Current density-voltage (J - V) characteristics of OSCs were measured under the standard irradiation of 100 mW/cm² from a solar simulator (G2V pico, Pathum Thani, Thailand) to evaluate OSC performance. A cross-sectional image was acquired by a scanning electron microscope (SEM, JSM-6610 LV, JEOL, Bangkok, Thailand). The root-mean-square (RMS) surface roughness was examined by an atomic force microscope (AFM, Asylum Research MFP-3D, Bangkok, Thailand). The surface chemical element was investigated using X-ray photoelectron spectroscopy (XPS, Kratos, Axis ultra DLD, Bangkok, Thailand). Sheet resistance was measured using a four-point probe measurement (Ossila, Pathum Thani, Thailand). The contact angle was measured using a contact angle measurement system (a homemade setup with 500× microscope, Nakhon Pathom, Thailand). The optical transmittance was recorded by an ultraviolet-visible (UV-Vis) spectrophotometer (UV-3101 PC, Shimadzu, Nakhon Pathom, Thailand). The chemical structure was investigated using Fourier transform infrared (FTIR) spectroscopy (Spectrum Two, PerkinElmer, Nakhon Pathom, Thailand). Crystalline structures were characterized using X-ray diffractometry (XRD, D8 Advance, Bruker, Nakhon Pathom, Thailand) using a Cu K_α radiation wavelength (λ) of 1.5406 Å.

3. Results and discussion

The photovoltaic characteristics of OSCs fabricated with PEDOT:PSS films were analyzed by measuring current density – voltage (J - V) curves, as shown in Figure 1. The measurement was carried out using at least three repeated samples for each condition. The power conversion efficiency (PCE) was then calculated using the Equations (1) and (2) [15–17]:

$$PCE [\%] = \frac{J_{sc} \cdot V_{oc} \cdot FF}{P_{in}} \cdot 100 \quad (1)$$

$$FF = \frac{J_{max} \cdot V_{max}}{J_{sc} \cdot V_{oc}} \quad (2)$$

where J_{sc} is the short-circuit current density, V_{oc} is the open-circuit voltage, FF is the fill factor, P_{in} is the incident solar power from the solar simulator, J_{max} is current density at the maximum power point, and V_{max} is the voltage at the maximum power point. All photovoltaic parameters are summarized in Table 1.

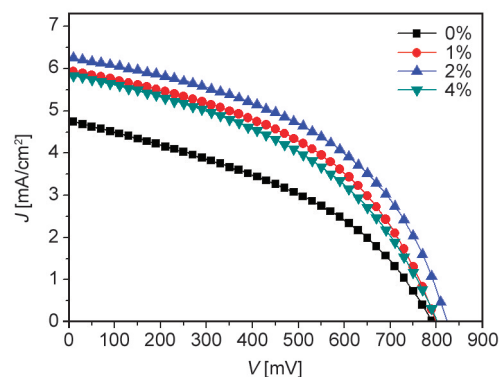


Figure 1. J - V curves of OSCs fabricated with PEDOT:PSS films at different ZnI₂ additive volumes.

It was found that OSC devices fabricated with ZnI₂-mixing PEDOT:PSS films demonstrate higher PCE s compared with the pristine PEDOT:PSS films. The PCE s slightly increase as ZnI₂ additive increases for 1–2 vol%, whereas 4 vol% ZnI₂ additive results in decreased PCE and J_{sc} . To investigate the correlation between photovoltaic parameters, plots of J_{sc} , V_{oc} , FF , and PCE as a function of ZnI₂ additive volume are shown in Figure 2. PCE trends are consistent with J_{sc} , V_{oc} , and FF , indicating that all photovoltaic parameters were improved for PEDOT:PSS mixed with ZnI₂ additive. This improvement is due to the reduced recombination in OSC devices [18], which is caused by the efficient hole transport efficiency. Note that the increase in V_{oc} , might also be attributed to the small change in the chemical structure of PEDOT:PSS in the presence of the ZnI₂ additive. In comparison with the other works mentioned above [9–12], the PCE of OSC in this work demonstrates low PCE s, which might be due to different fabrication methods [19]. However, the ZnI₂-mixing condition can enhance PCE for OSC application. For the 2 vol% ZnI₂-mixing conditions, it reveals the maximum PCE for OSC devices, implying the optimum condition. Therefore, it was further investigated as a representative of the modified PEDOT:PSS films in comparison with the pristine PEDOT:PSS films.

Table 1. Photovoltaic parameters of OSCs fabricated with PEDOT:PSS films at a different volumetric percentage of ZnI₂ additive mixtures.

ZnI ₂ additive volume [%]	J_{sc} [mA/cm ²]	V_{oc} [mV]	FF [-]	PCE [%]
0	4.77±0.94	785±19	0.41±0.01	1.52±0.35
1	5.96±0.76	793±15	0.46±0.01	2.18±0.33
2	6.28±0.72	818±5	0.47±0.01	2.42±0.35
4	5.86±0.57	797±12	0.44±0.01	2.03±0.25

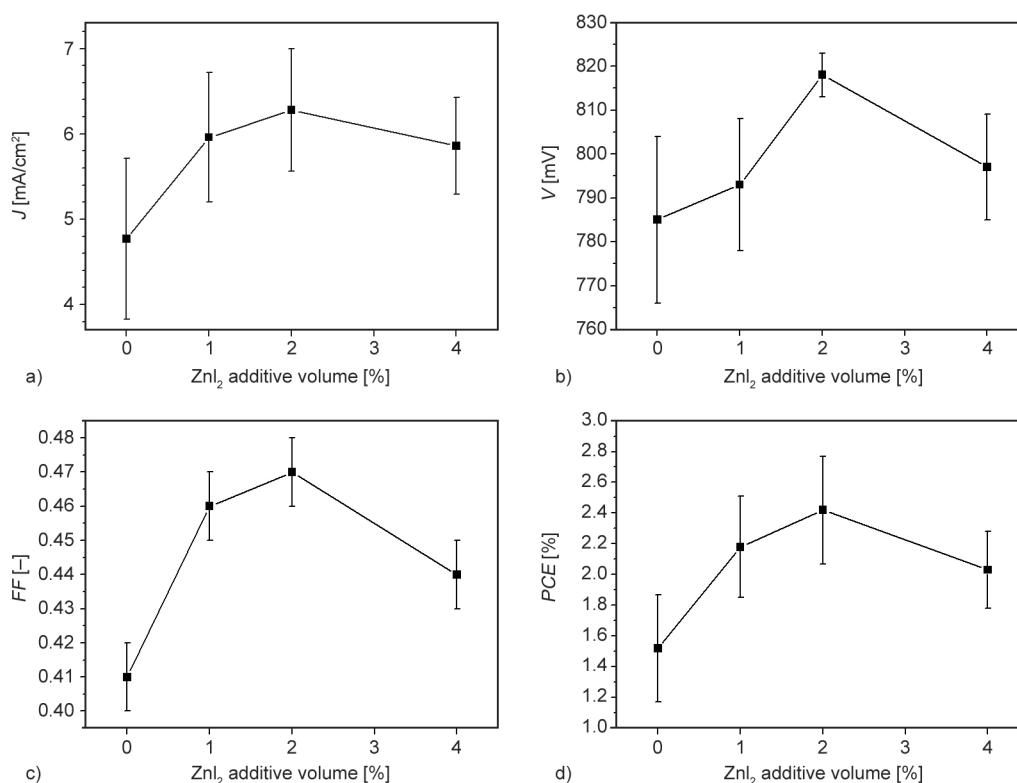


Figure 2. Photovoltaic parameters of OSCs fabricated with PEDOT:PSS films as function of ZnI₂ additive volume: a) J_{sc} , b) V_{oc} , c) FF , and d) PCE .

The cross-sectional SEM images in Figure 3 demonstrate that the interfaces between pristine PEDOT:PSS films and FTO substrates were not found. On the other hand, the junction between modified PEDOT:PSS and FTO layers was clearly observed. This indicates the different dynamic coating nature for pristine and modified PEDOT:PSS. To examine the surface roughness of PEDOT:PSS films, AFM was carried out. RMS roughness values of 8.80 and 15.03 nm were obtained for pristine and modified films, respectively. The roughness for modified films shows a higher value than that for the pristine films, indicating a higher surface area for modified films in comparison to the pristine films. The results imply that the interfacial contact has increased for OSC fabrication. This improvement leads to the high

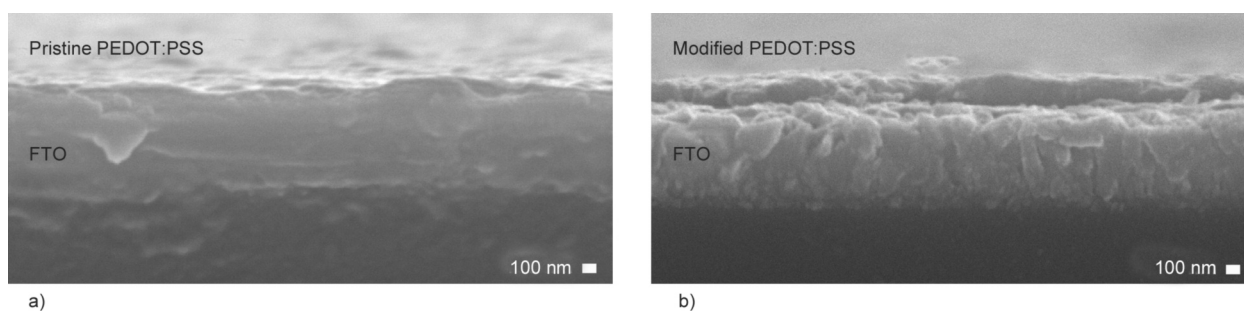


Figure 3. Cross-sectional images of a) FTO/pristine PEDOT:PSS and b) FTO/modified PEDOT:PSS.

hole transport pathway and facilitates enhanced hole collection performance between PEDOT:PSS/PCDTBT:PC₇₀BM interfaces [20], which causes a higher current density for OSC devices.

The XPS measurement in Figure 4 shows the S(2p) peak of PEDOT:PSS films. The binding energy peak at around 167.8 eV corresponds to the sulfur atoms in PSS, whereas the peaks at around 163.5–164.7 eV represent the sulfur atoms in PEDOT [21, 22]. The intensity of S(2p) peaks for modified films is higher than that of pristine films, indicating that PEDOT:PSS chains reorient and change to compact layered PEDOT:PSS films. To examine the change of modified PEDOT:PSS films, PSS to PEDOT ratios were analyzed by calculating the peak areas for PSS and PEDOT peaks. The integrated S(2p) peak

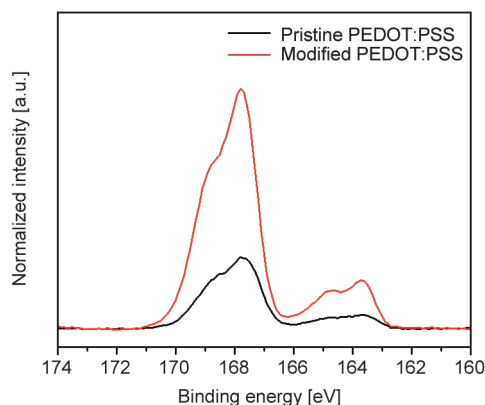


Figure 4. XPS spectra of pristine and modified PEDOT:PSS films.

areas were 4.69:1 and 4.15:1 for pristine and modified films, respectively. The decrease in integrated S(2p) peak areas for modified films points to the depletion of PSS from the surface of modified films by around 12% compared with pristine films [23]. This behavior implies re-orientation and re-interaction of PEDOT:PSS in the presence of the ZnI_2 additive. It can be interpreted that PEDOT:PSS films modified with ZnI_2 additive were changed as the compact formation and PSS depletion from the film's surfaces. This behavior can enhance hole transport efficiency in OSC devices, primarily due to the increase of hole-conducting PEDOT to insulating PSS ratios. The efficient hole transport behavior also suppresses the recombination effect, which results in an increased J_{sc} and V_{oc} for OSC devices [24].

To investigate the impact of PSS depletion on electrical property, sheet resistance was measured using a four-point probe measurement. The measurement presents the sheet resistance value of 81.16 ± 1.96 and $69.59 \pm 3.78 \Omega/sq$ for the pristine and modified films, respectively. The modified films exhibit a 14% decrease in sheet resistance in comparison with the pristine one, which nearly correlates to the decrease in PSS to PEDOT ratios. Moreover, the decrease in sheet resistance corresponds to the increase in J_{sc} value for OSC devices. Therefore, the improved electrical property of the modified films is considered an effective factor for enhancing the *PCE* of OSCs in this work. Moreover, PSS depletion also changes the surface wettability of PEDOT:PSS films as shown by the contact angle measurement results in Figure 5. The contact angle measured within a drop of DI water features hydrophilic properties for both pristine and modified films, and it slightly decreases for longer intervals. The contact angle of modified films,

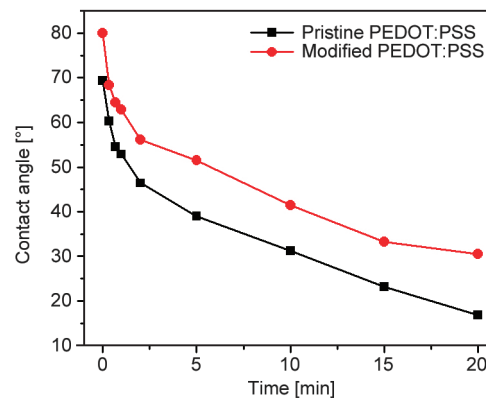


Figure 5. Contact angle measurement of pristine and modified PEDOT:PSS films.

however, demonstrates a higher value compared to that of pristine films. This is due to the depletion of water-soluble PSS parts from the surface of modified PEDOT:PSS films, leaving higher ratios of non-soluble PEDOT parts at the film's surfaces and causing a higher contact angle.

The transmittance spectra in Figure 6 were measured to evaluate the optical impact on OSC performance. The transmittance spectra significantly decrease for the modified films in comparison with the pristine ones. This feature could be affected by the incorporation of ZnI_2 , which is caused by the dense and compact structure of PEDOT:PSS in accordance with XPS results. Although low transmittance was obtained for the modified films, the *PCE* of the OSC device increased. This may be due to the fact that the active layer (PCDTBT:PC₇₀BM) can respond to the incident light, even with a low intensity [25]. Note that the low intensity of incident light also prevents the burn-in loss of V_{oc} , which maintains stability for OSC devices. This result suggests that the significant

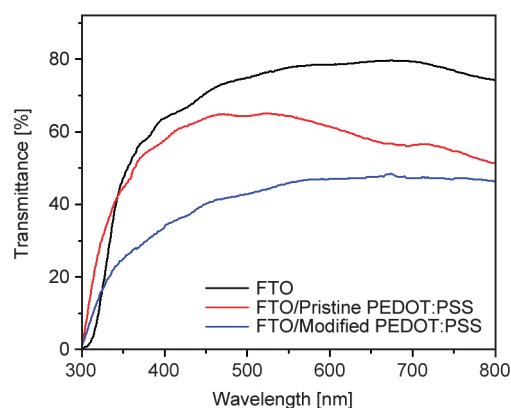


Figure 6. Optical transmittance of FTO, FTO/pristine PEDOT:PSS films, and FTO/modified PEDOT:PSS films.

factor for enhanced OSC devices is not transmittance but resistance.

To analyze the structures of the PEDOT:PSS films, FTIR spectra, and XRD patterns were performed. The observation of the PEDOT:PSS structures were determined from the FTIR peaks (Figure 7a) at 1010 and 665 cm^{-1} for the SO_3^- symmetric stretching of PSS and the C–S stretching of PEDOT, respectively [26]. The results confirm the PEDOT:PSS structure for both pristine PEDOT:PSS and modified PEDOT:PSS films. In terms of the other peaks, the broad peaks at 3860–3670 and 1440 cm^{-1} were assigned to the O–H stretching and bending vibrations, respectively. The peak at 1725 cm^{-1} represents the C=O stretching vibration of the COOH group. The peaks at 1365 and 1220 cm^{-1} represent the C–O stretching vibration. Figure 7b shows the XRD patterns of pristine PEDOT:PSS and modified PEDOT:PSS films deposited on FTO substrates. The XRD peak of PEDOT:PSS at $2\theta \sim 17.10^\circ$ was found for both pristine and modified PEDOT:PSS films contributed from PSS, indicating PEDOT:PSS crystalline structures [27]. The small XRD peak corresponds to PEDOT ($2\theta \sim 25.80^\circ$), which was found for only pristine PEDOT:PSS films but disappeared for the modified PEDOT:PSS films. This is due to the interaction between the ZnI_2 additive and PEDOT:PSS molecules. Note that the ZnI_2 structures were not detected by XRD characterization [28]. This is possibly due to the insufficient ZnI_2 additive for PEDOT:PSS- ZnI_2 mixtures or to ZnI_2 being distributed into the PEDOT:PSS matrices.

4. Conclusions

PEDOT:PSS were modified with the ZnI_2 solution and coated onto an FTO substrate for application as a hole transporting layer in OSCs. The average

power conversion efficiency was enhanced from 1.52 to 2.42%. This enhancement was found to be in correspondence with the rough surface of modified PEDOT:PSS, which improves the interfacial contact between PEDOT:PSS and PCDTBT:PC₇₀BM. This improvement leads to the high hole transport pathway and facilitates improved hole collection performance, which thus leads to a higher current density for OSC devices. Moreover, the ZnI_2 plays a role in the depletion of insulating PSS from the film's surface. This behavior causes lower sheet resistance and results in an increased J_{sc} and V_{oc} for OSC devices. Therefore, the improved interfacial contact and depletion of PSS are considered a synergistic function for OSC enhancement.

Acknowledgements

This work was supported by the Research Promotion and Technology Transfer Center (RPTTC), Faculty of Liberal Arts and Science, Kasetsart University Kamphaeng Saen Campus; and the Department of Physics, Faculty of Liberal Arts and Science, Kasetsart University Kamphaeng Saen Campus.

References

- [1] Xu W., Ma X., Son J. H., Jeong S. Y., Niu L., Xu C., Zhang S., Zhou Z., Gao J., Woo H. Y., Zhang J., Wang J., Zhang F.: Smart ternary strategy in promoting the performance of polymer solar cells based on bulk-heterojunction or layer-by-layer structure. *Small*, **18**, 2104215 (2022).
<https://doi.org/10.1002/smll.202104215>
- [2] Xu C., Jin K., Xiao Z., Zhao Z., Yan Y., Zhu Z., Li X., Zhou Z., Jeong S. Y., Ding L., Woo H. Y., Yuan G., Zhang F.: Efficient semitransparent layer-by-layer organic photovoltaics via optimizing wide bandgap and narrow absorption polymer layer thickness. *Solar RRL*, **6**, 2200308 (2022).
<https://doi.org/10.1002/solr.202200308>

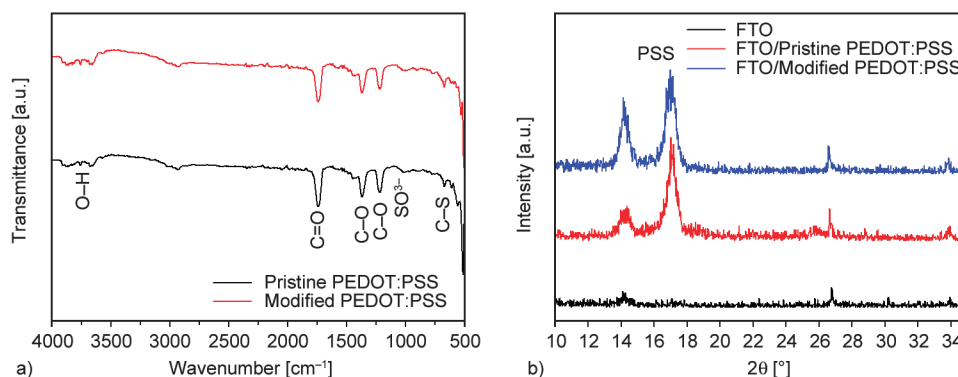


Figure 7. Structural analysis of pristine and modified PEDOT:PSS films: a) FTIR spectra and b) XRD patterns.

- [3] Zhao X., Liu M., Yang K., Zhao Z., Wang J., Zhou Z., Ma X., Zhang F.: Photomultiplication type organic photodetectors with different response characteristics under forward or reverse bias. *Organic Electronics*, **108**, 106587 (2022).
<https://doi.org/10.1016/j.orgel.2022.106587>
- [4] Wang X., Sun Q., Gao J., Wang J., Xu C., Ma X., Zhang F.: Recent progress of organic photovoltaics with efficiency over 17%. *Energies*, **14**, 4200 (2021).
<https://doi.org/10.3390/en14144200>
- [5] Alamer F. A., Beyari R. F.: Overview of the influence of silver, gold, and titanium nanoparticles on the physical properties of PEDOT:PSS-coated cotton fabrics. *Nanomaterials*, **12**, 1609 (2022).
<https://doi.org/10.3390/nano12091609>
- [6] Ong G. L., Ong T. S., Yap S. L., Liaw D-J., Tou T. Y., Yap S. S., Nee C. H.: A brief review of nanoparticles-doped PEDOT:PSS nanocomposite for OLED and OPV. *Nanotechnology Reviews*, **11**, 1870–1889 (2022).
<https://doi.org/10.1515/ntrev-2022-0104>
- [7] Liu X., Shi X-L., Zhang L., Liu W-D., Yang Y., Chen Z-G.: One-step post-treatment boosts thermoelectric properties of PEDOT:PSS flexible thin films. *Journal of Materials Science and Technology*, **132**, 81–89 (2023).
<https://doi.org/10.1016/j.jmst.2022.05.047>
- [8] Hu L., Song J., Yin X., Su Z., Li Z.: Research progress on polymer solar cells based on PEDOT:PSS electrodes. *Polymers*, **12**, 145 (2020).
<https://doi.org/10.3390/polym12010145>
- [9] Hussain S., Liu H., Hussain M., Mehran M. T., Kim H-S., Jung J., Vikraman D., Kang J.: Development of MXene/WO₃ embedded PEDOT:PSS hole transport layers for highly efficient perovskite solar cells and X-ray detectors. *International Journal of Energy Research*, **46**, 12485–12497 (2022).
<https://doi.org/10.1002/er.8020>
- [10] Gemeiner P., Pavličková M., Hatala M., Hvojník M., Homola T., Mikula M.: The effect of secondary dopants on screen-printed PEDOT:PSS counter-electrodes for dye-sensitized solar cells. *Journal of Applied Polymer Science*, **139**, 51929 (2022).
<https://doi.org/10.1002/app.51929>
- [11] Wan J., Fan X., Li Y., Li P., Zhang T., Hui K. N., Huang H., Kang K., Qian L.: High-efficiency flexible organic photovoltaics and thermoelectricities based on thionyl chloride treated PEDOT:PSS electrodes. *Frontiers in Chemistry*, **9**, 807538 (2022).
<https://doi.org/10.3389/fchem.2021.807538>
- [12] Xu W., Zhu X., Ma X., Zhou H., Li X., Jeong S. Y., Woo H. Y., Zhou Z., Sun Q., Zhang F.: Achieving 15.81% and 15.29% efficiency of all-polymer solar cells based on layer-by-layer and bulk heterojunction structures. *Journal of Materials Chemistry A*, **10**, 13492–13499 (2022).
<https://doi.org/10.1039/D2TA02914F>
- [13] Zhang S., Hu J., Huang S., Zhang J., Lyu M., Lu H., Zhu J.: ZnI₂ post-processing of CsPbBr₃ quantum dots for red, stable, and low-threshold amplified spontaneous emission. *Applied Physics Letters*, **120**, 221101 (2022).
<https://doi.org/10.1063/5.0091905>
- [14] Tian C., Han X., Zhao Y., Sun Z., Hou C., Wang H., Qi J., Li Y., Jia W., Zhang Q.: Anion effect on properties of Zn-doped CH₃NH₃PbI₃ based perovskite solar cells. *Solar Energy Materials and Solar Cells*, **233**, 111400 (2021).
<https://doi.org/10.1016/j.solmat.2021.111400>
- [15] Ritruksa M., Wongrerkdee S., Lohawet K., Kaewprajak A., Kumnorkaew P., Wongrerkdee S.: Surface modification of PEDOT: PSS film by chemical vapor texturing process for enhanced organic photovoltaics. *Surfaces and Interfaces*, **21**, 100716 (2020).
<https://doi.org/10.1016/j.surfin.2020.100716>
- [16] Wongrerkdee S., Ritruksa M., Phattum S., Lohawet K., Kaewprajak A., Kumnorkaew P., Wongrerkdee S.: PEDOT:PSS film preparation and characterization using convective deposition system controlled by arduino microcontroller for organic photovoltaic application. *Engineering Journal*, **25**, 335–341 (2021).
<https://doi.org/10.4186/ej.2021.25.2.335>
- [17] Wongrerkdee S., Moungrsrijun S., Pimpang P., Hongsith K., Choopun S.: Linking bridge improvement of ZnO/N719 interfaces *via* ammonia treatment for efficiency enhancement of dye-sensitized solar cell. *Surfaces and Interfaces*, **23**, 100991 (2021).
<https://doi.org/10.1016/j.surfin.2021.100991>
- [18] Niu Z., Zheng E., Dong H., Tosado G. A., Yu Q.: Manipulation of PEDOT:PSS with polar and nonpolar solvent post-treatment for efficient inverted perovskite solar cells. *ACS Applied Energy Materials*, **3**, 9656–9666 (2020).
<https://doi.org/10.1021/acsaem.0c01194>
- [19] Neukom M., Züfle S., Jenatsch S., Ruhstaller B.: Optoelectronic characterization of third-generation solar cells. *Science and Technology of Advanced Materials*, **19**, 291–316 (2018).
<https://doi.org/10.1080/14686996.2018.1442091>
- [20] Ge B., Zhou Z. R., Wu X. F., Zheng L. R., Dai S., Chen A. P., Hou Y., Yang H. G., Yang S.: Self-organized Co₃O₄-SrCO₃ percolative composites enabling nano-sized hole transport pathways for perovskite solar cells. *Advanced Functional Materials*, **31**, 2106121 (2021).
<https://doi.org/10.1002/adfm.202106121>
- [21] Reza K. M., Gurung A., Bahrami B., Mabrouk S., Elbohy H., Pathak R., Chen K., Chowdhury A. H., Rahman M. T., Letourneau S., Yang H-C., Saianand G., Elam J. W., Darling S. B., Qiao Q.: Tailored PEDOT:PSS hole transport layer for higher performance in perovskite solar cells: Enhancement of electrical and optical properties with improved morphology. *Journal of Energy Chemistry*, **44**, 41–50 (2020).
<https://doi.org/10.1016/j.jechem.2019.09.014>

- [22] Zhao Z., Wu Q., Xia F., Chen X., Liu Y., Zhang W., Zhu J., Dai S., Yang S.: Improving the conductivity of PEDOT:PSS hole transport layer in polymer solar cells via copper(II) bromide salt doping. *ACS Applied Materials and Interfaces*, **7**, 1439–1448 (2015).
<https://doi.org/10.1021/am505387q>
- [23] Mengistie D. A., Wang P-C., Chu C-W.: Effect of molecular weight of additives on the conductivity of PEDOT:PSS and efficiency for ITO-free organic solar cells. *Journal of Materials Chemistry A*, **1**, 9907–9915 (2013).
<https://doi.org/10.1039/c3ta11726j>
- [24] Syed A. A., Poon C. Y., Li H. W., Zhu F.: A sodium citrate-modified-PEDOT:PSS hole transporting layer for performance enhancement in inverted planar perovskite solar cells. *Journal of Materials Chemistry C*, **7**, 5260–5266 (2019).
<https://doi.org/10.1039/C8TC06043F>
- [25] Züfle S., Hansson R., Katz E. A., Moons E.: Initial photo-degradation of PCDTBT:PC₇₀BM solar cells studied under various illumination conditions: Role of the hole transport layer. *Solar Energy*, **183**, 234–239 (2019).
<https://doi.org/10.1016/j.solener.2019.03.020>
- [26] Paul G., Verma S., Jalil O., Thakur D., Pandey C. M., Kumar D.: PEDOT: PSS-grafted graphene oxide-titanium dioxide nanohybrid-based conducting paper for glucose detection. *Polymers for Advanced Technologies*, **32**, 1774–1782 (2021).
<https://doi.org/10.1002/pat.5213>
- [27] Rwei S-P., Lee Y-H., Shiu J. W., Sasikumar R., Shyr U. T.: Characterization of solvent-treated PEDOT:PSS thin films with enhanced conductivities. *Polymers*, **11**, 134 (2019).
<https://doi.org/10.3390/polym11010134>
- [28] Kariper I. A.: Optical and structural properties of zinc iodine thin films. *Optical Materials*, **44**, 78–83 (2015).
<https://doi.org/10.1016/j.optmat.2015.03.012>